Expanding the Scope of Powerful Electrochemical Methods by Exploiting Nanoconfined Cascade Catalysis



Ryan A. Herold

Department of Chemistry
Trinity College, University of Oxford

Thesis submitted for the degree of Doctor of Philosophy

Trinity Term 2023

© Ryan A. Herold 2023

DEDICATION

I dedicate this thesis to my dad and to my mom.

ACKNOWLEDGEMENTS

Firstly, I would like to thank my supervisor, Fraser Armstrong. Working with Fraser has truly been an honor, and I will forever be grateful for his mentorship.

Secondly, I would like to thank my collaborating supervisor, Chris Schofield, for his unwavering support over the past four years. I am also particularly grateful to Clare Megarity, who trained me on the e-Leaf when I first joined the group, and whom I am glad to have as a friend. I thank my main collaborator, Raphael Reinbold, for generously sharing his IDH1 enzyme with me and for joining me on weekends to run NMR experiments. I am also grateful for all of the former members of the Armstrong group with whom I have had the pleasure of working alongside: Beichen, Lei, Giorgio, and Non. I would also like to thank the members of the Schofield group with whom I have collaborated: Lennart, Martine, Xiao, Ziggy, and Patrick. I thank the members of the Vincent group who kindly invited me to their events over the past year when I was the last remaining Armstrong group member: Sofia, Tim, Wangzhe, Sam, Lucy, Chris, Liz, Maya, and Zehui. I am also grateful to several members of the ICL staff who helped to facilitate my research; most notably, I thank our resident scientific glassblower Terri Adams, who created beautiful custom glass electrochemical cells in which I performed all of my electrochemical experiments. I also thank Alex Gonzalez for designing a custom 10-channel electrical feedthrough which enabled me to perform multiple anaerobic electrochemistry experiments in parallel.

I am extremely grateful to the Clarendon Fund and Trinity College for funding. Without their support, I would not have been able to undertake this DPhil.

Finally, I would like to thank my family. I am especially grateful to my amazing wife, Lizzie, who made the big move from America to England with me, and who has always supported and encouraged me over the last eleven years. I thank my mom and dad for helping to shape me into who I am, and my brother, Jordan, for all of the experiences we have shared. Finally, I would like to thank my extended family, especially my grandparents, for being such a positive presence in my life.

PUBLICATIONS

(8) **Herold, R. A.**; Schofield, C. J.; Armstrong, F. A. Electrochemical Nanoreactor Provides a Comprehensive View of Isocitrate Dehydrogenase Cancer-drug Kinetics. *Angewandte Chemie Int. Ed.* **2023**, *62* (42), e202309149.

Results appear in Chapter IV. Contribution: conceptualization, design and execution of all experiments, methodology, data analysis, validation, visualization, equation derivation, writing: original draft preparation & review and editing.

(7) Liu, X.; Reinbold, R.; *****Liu, S.; ***Herold, R. A.**; *****Rabe, P.; Duclos, S.; Yadav, R. B.; Abboud, M. I.; Thieffine, S.; Armstrong, F. A.; Brewitz, L.; Schofield, C. J. Natural and Synthetic 2-Oxoglutarate Derivatives Are Substrates for Oncogenic Variants of Human Isocitrate Dehydrogenase 1 and 2. *Journal of Biological Chemistry*. **2023**, *299* (2), 102873.

Results appear in Chapter II. Contribution: design and execution of experiments, methodology, data analysis, validation, visualization, writing: original draft preparation & review and editing.

(6) **Herold, R. A.**; Reinbold, R.; Schofield, C. J.; Armstrong, F. A. NADP(H)-dependent Biocatalysis without adding NADP(H). *Proceedings of the National Academy of Sciences.* **2023**, *120* (1), e2214123120.

Results appear in Chapter III. Contribution: conceptualization, design and execution of all experiments, methodology, data analysis, validation, visualization, equation derivation, writing: original draft preparation & review and editing.

(5) †Armstrong, F. A.; †Cheng, B.; †**Herold, R. A.**; †Megarity, C. F.; †Siritanaratkul, B. From Protein Film Electrochemistry to Nanoconfined Enzyme Cascades and the Electrochemical Leaf. *Chemical Reviews.* **2023**, *123* (9), 5421–5458.

Review Article. Contribution: visualization, writing: original draft preparation & review and editing.

(4) Reinbold, R.; Hvinden, I. C.; Rabe, P.; **Herold, R. A.**; Finch, A.; Wood, J.; Morgan, M.; Staudt, M.; Clifton, I. J.; Armstrong, F. A.; McCullagh, J. S. O.; Redmond, J.; Bardella, C.; Abboud, M. I.; Schofield, C. J. Resistance to the Isocitrate Dehydrogenase 1 Mutant Inhibitor Ivosidenib Can Be Overcome by Alternative Dimer-Interface Binding Inhibitors. *Nature Communications.* **2022**, *13* (1), 4785.

Results appear in Chapter II. Contribution: design and execution of experiments, methodology, data analysis, validation, visualization, writing: review and editing.

(3) **Herold, R. A.**; Reinbold, R.; Megarity, C. F.; Abboud, M. I.; Schofield, C. J.; Armstrong, F. A. Exploiting Electrode Nanoconfinement to Investigate the Catalytic Properties of Isocitrate Dehydrogenase (IDH1) and a Cancer-Associated Variant. *Journal of Physical Chemistry Letters.* **2021**, *12* (26), 6095–6101.

Results appear in Chapters II and IV. Contribution: conceptualization, design and execution of experiments, methodology, data analysis, validation, visualization, writing: original draft preparation & review and editing.

(2) Wan, L.; Heath, R. S.; Megarity, C. F.; Sills, A. J.; **Herold, R. A.**; Turner, N. J.; Armstrong, F. A. Exploiting Bidirectional Electrocatalysis by a Nanoconfined Enzyme Cascade to Drive and Control Enantioselective Reactions. *ACS Catalysis.* **2021**, *11* (11), 6526–6533.

Contribution: design of experiments, methodology, visualization, writing: review and editing.

(1) Megarity, C. F.; Siritanaratkul, B.; **Herold, R. A.**; G. Morello, F. A. Armstrong. Electron flow between the worlds of Marcus and Warburg. *Journal of Chemical Physics.* **2020**, 153 (22), 225201.

Review Article. Contribution: visualization, writing: original draft preparation & review and editing.

*****contributed equally

†alphabetical order

TABLE OF CONTENTS

Dedication 1
Acknowledgements 2
Publications 4
Table of Contents 6
Abstract 11
Chapter I 13
1 Introduction: Protein Film Electrochemistry and the Electrochemical Leaf 14
1.1 Scope and Structure of this Thesis 14
1.2 A Brief Introduction to Electrochemical Methods 15
1.2.1 Standard Three-electrode System 15
1.2.2 Chronoamperometry and the Current-Rate Relationship 17
1.2.3 Cyclic Voltammetry 18
1.3 Protein Film Electrochemistry 22
1.3.1 Requirements for Direct Electrochemical Study of Proteins 22
1.3.2 Direct versus Mediated Protein Electrochemistry 23
1.3.3 Bidirectional, Reversible, Irreversible, and Unidirectional Catalysis 25
1.4 The Electrochemical Leaf 26
1.4.1 Ferredoxin-$NADP^+$ Reductase (FNR) 26
1.4.1.1 Electrochemistry of Ferredoxin-$NADP^+$ Reductase (FNR) 28
1.4.2 The Electrochemical Leaf Extends Electrochemical Methods to Non-electroactive Enzymes 30
Chapter II 33
2 Rendering Isocitrate Dehydrogenases Electroactive 34
2.1 Abstract 34
2.2 Introduction 35
2.2.1 Physical and Biochemical Properties of Isocitrate Dehydrogenase 35
2.2.2 Cancer-associated Isocitrate Dehydrogenase Variants 38
2.2.3 Aims of this Chapter 39
2.3 Results and Discussion 40
2.3.1 Wildtype and Variant IDH1 Activity in the e-Leaf 40
2.3.1.1 Rates of Activation of IDH1 Catalysis in the e-Leaf 40
2.3.1.2 Reversible Inactivation of IDH1 R132H by Metal Chelation 42
2.3.1.3 Enzymes in the e-Leaf Exhibit Michaelis-Menten Kinetics with Some Caveats 43
2.3.2 Wildtype and Variant IDH1 Cyclic Voltammetry at different pH 46
2.3.2.1 Interpreting Waveforms of Coupled Cyclic Voltammograms 47
2.3.2.2 IDH1 Double Mutant Variant Voltammetry 49

2.3.2.3 Thermodynamic vs Kinetic pH Bias of IDH1 Catalysis 49
2.3.3 Wildtype IDH1 as a Reversible Electrocatalyst 52
2.3.3.1 Electrochemically Driving and Measuring IDH1-catalyzed Reductive Carboxylation 53
2.3.3.2 Determining the Formal Reduction Potential of the 2OG, CO_2/Isocitrate Reaction 55
2.3.4 Thermodynamics Governing the Production of 2-hydroxyglutarate 56
2.3.5 Measuring Isocitrate Oxidation Catalyzed by IDH1 Variants 58
2.3.5.1 Decoupling Isocitrate Oxidation from 2OG Reduction 58
2.3.5.2 Understanding the Effects of Different Mutations on IDH1 Catalysis 61
2.3.6 IDH1 R132H Reduction of 2OG Derivative Substrates 66
2.3.6.1 IDH1 R132H is More Active with Some 2OG Derivatives than with 2OG 66
2.3.6.2 IDH1 R132H is Enantioselective for 2OG Derivative Substrates 67
2.3.6.3 Observation of Substrate Competition Between 2OG and 3-methyl-2OG 69
2.3.7 Complex Interactions between IDH1 R132C/S280F and Mg^{2+} 71
2.4 Conclusions 76
Chapter III 78
3 NADP(H)-dependent Biocatalysis Using only Enzyme-copurified NADP(H) 79
3.1 Abstract 79
3.2 Introduction 81
3.2.1 Biological Nanoconfinement 81
3.2.2 Enzyme Copurification with Bound Nicotinamide 81
3.2.3 Aims of this Chapter 83
3.3 Results and Discussion 84
3.3.1 IDH1 Enzymes Copurify with Bound NADP(H) 84
3.3.2 Copurified NADP(H) is Sufficient for Nanoconfined Enzyme Catalysis 87
3.3.2.1 IDH1-Copurified NADP(H) is Detectable by Cyclic Voltammetry 90
3.3.3 Bulk Synthesis Using Only Enzyme-copurified NADP(H) 90
3.3.4 Quantification of FNR, IDH1, and NADP(H) in the Electrode Nanopores 92
3.3.4.1 The Longstanding Challenge of Non-electroactive Enzyme Quantification 92
3.3.4.2 Thin-film Voltammetry Quantification of NADP(H) and IDH1 93
3.3.4.3 Estimating Enzyme and NADP(H) Concentrations in the Electrode Nanopores 99
3.3.5 Estimating NADP(H) and Enzyme Total Turnover Numbers 101
3.3.5.1 A New Metric for Comparing the Efficiency of Cofactor Recycling Systems: the “Total Turnover Product” 102
3.3.6 Enzymes *and* NADP(H) remain Nanoconfined Following Buffer Exchanges 103
3.3.6.1 Wildtype IDH1 Tightly Rebinds both $NADP^+$ and NADPH while IDH1 R132H only Rebinds NADPH 106

3.3.7 Nanoconfinement Greatly Enhances NADP(H) Recycling Efficiency 110
3.3.8 IDH1-FNR Cascade Nanoconfined versus in Dilute Solution 115
3.4 Conclusions 118
Chapter IV 120
4 Investigating the Kinetic Mechanism of Isocitrate Dehydrogenase Inhibition 121
4.1 Abstract 121
4.2 Introduction 123
4.2.1 Isocitrate Dehydrogenase as a Drug Target 123
4.2.2 Current Knowledge of the Mechanism of Allosteric IDH1 Inhibition 124
4.2.3 IDH1 Inhibition Kinetics 126
4.2.4 The Importance of Enzyme Inhibition Kinetics 127
4.2.5 Advantages of the e-Leaf for Measuring Inhibition Kinetics 128
4.2.6 Aims of this Chapter 130
4.3 Results and Discussion 131
4.3.1 Measuring Real-time Inhibition of IDH1 R132H by an FDA-approved Drug.. 131
4.3.2 Dual Enzyme Monitoring: Selective Inhibition of "side-by-side" Enzymes..... 132
4.3.3 Comparing Rates of Inhibition with Inhibitor Potency 136
4.3.4 Real-time Measurement of Inhibitor Binding *and* Dissociation in a Single Experiment 141
4.3.5 Obtaining Pseudo First-order Kinetics at Nanomolar Inhibitor Concentrations 144
4.3.6 Obtaining k_{on}, k_{off}, and K_d Values from Timecourse Data 146
4.3.6.1 IDH1 Variant Inhibitors are Competitive with 2OG and Mg^{2+} 148
4.3.7 IDH1 Variant Inhibitors Bind the Enzyme Before Inhibiting 151
4.3.8 Enzyme Inhibition Kinetics Under Concentrated versus Dilute Enzyme Conditions 155
4.3.9 Comparison of e-Leaf Kinetic Data with Other Kinetic Data for IDH1/2 Inhibitors 158
4.3.10 Further Testing the Proposed Model 159
4.3.11 Bringing the Data Together: A Kinetic Mechanism of IDH1 Inhibition 160
4.3.11.1 Timeline for an Average IDH1 R132H Molecule in the Inhibition Cycle . 161
4.3.12 Discussion on General Mechanistic Features of IDH1/2 Variant Inhibition ... 162
4.3.12.1 Does the Oxidation State of IDH1-bound NADP(H) Affect Rates of Inhibition? 162
4.3.12.2 Does the Reaction Being Catalyzed Affect Inhibition? 164
4.3.12.3 Inhibitor Binding Stoichiometry 165
4.3.13 *This redacted material will be publicly available in December 2029* 166
4.4 Conclusions 172
Chapter V 174
5 *This redacted material will be publicly available in December 2029* 175
5.1 175

5.2 176
5.2.1 176
5.2.2 177
5.2.3 178
5.3 179
5.3.1 179
5.3.2 181
5.3.3 187
5.3.4 190
5.3.5 192
5.4 196
Chapter VI 198
6 Conclusions and Future Perspectives 199
6.1 Nanoconfined Cascade Catalysis 199
6.2 The Kinetic Mechanism of Isocitrate Dehydrogenase Inhibition 201
6.3 The e-Leaf as an Analytical Tool for Investigating Enzyme Mechanisms 203
6.4 *This redacted material will be publicly available in December 2029* 205
Chapter VII 206
7 Methods and Derivation of Equations 207
7.1 Materials and Methods 207
7.1.1 Enzyme Expression and Purification 207
7.1.2 Expression and Purification of Recombinant *Hs* IDH1 and *Hs* IDH1 Variants 208
7.1.3 ITO/PGE Electrode Fabrication 209
7.1.4 Enzyme Loading (Dropcasting) 209
7.1.5 Electrochemical Quantification of Adsorbed FNR 210
7.1.6 Electrochemical Experiments 210
7.1.7 Live Buffer Exchange Protocol 211
7.1.8 Enzyme Reactions in Homogeneous Solution 212
7.1.8.1 Wildtype IDH1 and IDH1 R132H Spectrophotometric Assays 212
7.1.8.2 IC_{50} Measurement 212
7.1.8.3 IDH1-FNR Experiments in Homogeneous Solution 213
7.1.8.4 FNR Solution Assay 214
7.1.8.5 Solution Enzyme Inhibition Kinetic Assays 214
7.1.9 e-Leaf Inhibition Kinetic Experiments 215
7.1.9.1 Treatment of Primary Data: Assumptions Required for Obtaining Inhibition Kinetic Parameters 215
7.1.9.2 Determining k_{obs} From Timecourse Experiments 216
7.1.9.3 Film Loss Correction 217

7.1.10 ^{1}H Nuclear Magnetic Resonance (NMR) Experiments 219
7.1.11 Non-denaturing Mass Spectrometry Experiments 220
7.1.12 Data Smoothing 220
7.2 Derivation of Equations 221
7.2.1 Derivation of Equations for Chapter III 221
7.2.2 Derivation of Equations for Chapter IV 222
7.2.2.1 Derivation of the Pseudo First-order Reversible Integrated Rate Law 222
7.2.2.2 Derivation of Rate Law for Competition Between Ivosidenib and 2OG/Mg^{2+} 224
7.2.2.3 Relating the Observed Rate Constant to Pre-equilibrium Binding and the Rate-determining Inhibition Step 226
7.2.2.4 Derivation of Equations Describing the Hyperbolic Dependence of the Inhibition Rate on [I] 227
Appendix 233
References 235

ABSTRACT

The Electrochemical Leaf (e-Leaf) extends powerful electrochemical methods, historically only applicable to a relatively small group of "electroactive" enzymes (i.e., enzymes that can directly exchange electrons with an electrode), to non-electroactive enzymes. The technology works by trapping enzymes inside a nanoporous electrode and linking the reaction(s) catalyzed by the enzyme(s) of interest to an NADP(H)-recycling enzyme, ferredoxin $NADP^+$-reductase (FNR), which is controlled electrochemically; the outcome is that the catalytic activity of the overall enzyme cascade is simultaneously energized (via the applied electrode potential) and monitored (as electrical current) in real time. Much of this work focuses on using the e-Leaf to study wildtype isocitrate dehydrogenase 1 (IDH1) and several cancer-associated IDH1 variants. Exploiting the unique advantages of the e-Leaf for investigating slow, tight-binding inhibitors, a method and analytical framework are developed to investigate the kinetics of inhibition of a cancer-associated IDH1 variant by multiple FDA-approved drugs. Implementation of this method leads to a proposed general kinetic mechanism for allosteric IDH inhibition. Notably, the inhibition kinetics are very slow, and the data show that inhibitors can bind in both inhibitory and non-inhibitory modes. Separately, the ability of IDH1 to copurify from cells with bound NADP(H) is used to "shuttle" NADP(H) into a nanoporous electrode to create a nanoconfined NADP(H)-dependent system which can be run without any external NADP(H), i.e., only the NADP(H) that copurified bound to IDH1 is required for cascade catalysis. The system is extraordinarily stable and is able to carry out bulk electrolysis over a five-day period with an NADP(H) total turnover number of ~160,000. The presence of a finite quantity of NADP(H) in the electrode (without any NADP(H) in the bulk solution) is used to quantify

concentrations of NADP(H) and IDH1 in the electrode nanopores. Together with values obtained for FNR, total nonconfined enzyme concentrations ([FNR] + [IDH1]) are shown to be ~2 mM, approaching the physical limit. At such concentrations, the average center-to-center distance between enzymes is just 9.4 nm; this leads to a "cluster channeling" effect that increases the overall enzyme cascade efficiency by preventing cascade intermediates from escaping the nanoporous electrode. Together, this work demonstrates the power of electrochemical methods for enzyme mechanistic studies and quantifies the benefits of nanoconfinement for increasing the efficiency of cascade catalysis.

CHAPTER I

INTRODUCTION: PROTEIN FILM ELECTROCHEMISTRY AND THE ELECTROCHEMICAL LEAF

1 Introduction: Protein Film Electrochemistry and the Electrochemical Leaf

1.1 Scope and Structure of this Thesis

This thesis focuses on the electrochemical study of enzymes that have been trapped at high concentration inside a nanoporous electrode. **Chapter I** begins with a brief introduction to the electrochemical methods most frequently used in this work, followed by an introduction to protein film electrochemistry, i.e., the direct electrochemical study of proteins. Most enzymes cannot be studied using electrochemical methods; however, this work utilizes a new technology called the Electrochemical Leaf (e-Leaf), which extends powerful electrochemical methods to many new enzyme classes as described at the end of **Chapter I**.

Chapter II establishes the electrochemistry of the isocitrate dehydrogenase I (IDH1) enzymes in the e-Leaf, demonstrating how the application of electrochemical methods to previously inaccessible enzymes allows facile extraction of useful thermodynamic and kinetic information while giving tight control over the rates and direction of enzyme catalysis. **Chapter III** explores a special case of extreme enzyme cascade efficiency in which a recycled cofactor, NADP(H), is trapped inside the electrode nanopores alongside the cascade enzymes, enabling unique and highly informative experiments to be carried out. **Chapter IV** investigates the kinetic mechanism of inhibition of a high-profile cancer-associated IDH1 variant by several inhibitors, two of which are FDA-approved and are in clinical use. To obtain such detailed kinetic information, a new electrochemical method and analytical framework for investigating enzyme inhibition kinetics was developed; this

important advance is described in detail in **Chapter IV**. Finally, **Chapter VI** summarizes the research carried out in this work, and **Chapter VII** describes the experimental methods used and the equations which were derived to analyze the experimental data.

This page contains redacted material that will become publicly available in December 2029.

1.2 A Brief Introduction to Electrochemical Methods

The majority of the data presented in this work are electrochemical. It is therefore important to briefly describe the most common methods used and to explain the basic principles for their interpretation. Throughout this text, it will be assumed that the reader has a general understanding of thermodynamics, chemical/enzyme kinetics, and basic electrochemistry.

1.2.1 Standard Three-electrode System

For a simple experiment using a three-electrode setup (**Figure 1**), a working electrode (WE), i.e., the electrode of study, is placed into an electrolyte solution alongside two other electrodes: a counter electrode (CE) and a reference electrode (RE). Using a potentiostat, a potential (voltage) is applied across the WE and the RE—the reference electrode will have a well-established and stable reduction potential whereas the working electrode potential

varies depending on the applied potential. Importantly, no current flows between these electrodes as this would change the potential (voltage) at the WE according to:

$$E_{WE} = E_{Cell} + E_{RE} + iR, \qquad \text{(Eq. 1)}$$

where E_{cell} represents the *applied* potential (voltage) difference between the two electrodes, E_{WE} is the working electrode potential, E_{RE} is the reference electrode potential, i is the current that flows between the WE and RE, and R is the resistance of the electrolyte solution between the surfaces of the WE and RE. In actuality, an infinitesimally small current does flow

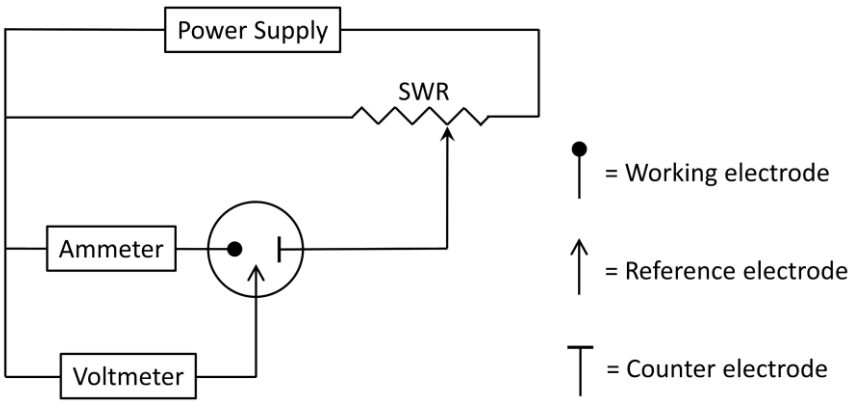


Figure 1. Simplified circuit diagram for a potentiostat with a three-electrode system. A voltmeter measures the potential difference (voltage) between the WE and RE without allowing current to flow between the two (very high resistance). An ammeter measures the flow of current (very low resistance) between the WE and CE. A slide-wire resistor (SWR) is connected between the WE and CE which allows the resistance between the WE and CE to be adjusted.

between the WE and RE; however, this current (i) is minimized by the use of a high resistance circuit connecting the two electrodes. This is important because the iR term in Eq. 1 represents the cell "potential drop", which is the difference between the actual and expected potential at the working electrode surface when current flows between the WE and RE (thus keeping i extremely small means this difference is insignificant). To facilitate the flow of electrical current at the WE, a low resistance circuit is used to connect the WE and CE.

Furthermore, the potential applied to the CE is modulated by the potentiostat to drive essentially all of the anodic/cathodic current through the CE to balance the reaction occurring at the WE—note that the CE reaction type will be the opposite (anodic (oxidation)/cathodic (reduction)) to that occurring at the WE.

Put simply, the WE potential is measured against the RE potential, and no current flows between the two electrodes. Current *does* flow between the WE and CE, but the potential of the CE does not affect the potential of the WE. All of the electrochemical experiments carried out in this work utilized a three-electrode system.

1.2.2 Chronoamperometry and the Current-Rate Relationship

Chronoamperometry is perhaps the simplest type of dynamic electrochemical method. In essence, a fixed potential is applied to the working electrode and the resulting current is measured over time. It is important to note that electrical current, *I*, is the measurement of the amount of charge, *q*, passed over time, *t*. For an electrochemical reaction, the measured current results from the flow of electrons into/out of the electrode (across the electrode-solution interface) over time, which is directly proportional to the consumption/production of a chemical species over time, i.e., the *rate of reaction*, according to:

$$\text{Rate} = \frac{I}{nF}, \qquad \text{(Eq. 2)}$$

where *I* is the current, *F* is the Faraday constant (96485 C per mole of electrons), and *n* is the number of electrons transferred per molecule of reactant. Therefore, each electrical current data point measured in an electrochemical experiment is a measurement of the rate of the

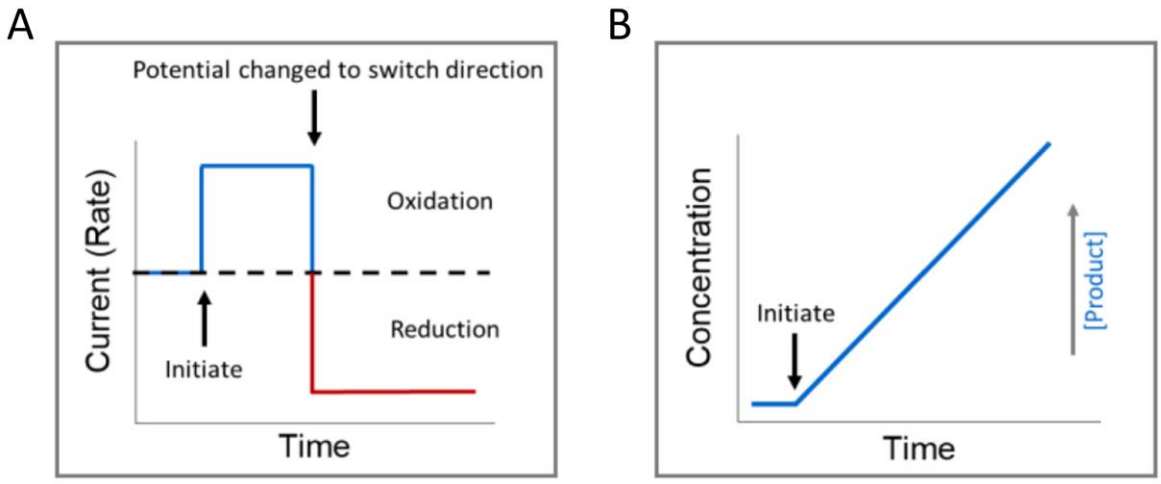


Figure 2. Comparisons between the different information readouts for (A) an electrochemical reaction (measuring electrical current over time) versus (B) an experiment carried out in homogeneous solution (measuring concentration over time). Adapted with permission from ref.[1]

reaction at that timepoint (**Figure 2A**). Thus, a flat line in a chronoamperometry experiment equates to steady-state catalysis. By contrast, rising or falling currents represent the *transient kinetics* of a process in an approach to steady-state or equilibrium. This concept constitutes a major difference between electrochemical reactions and reactions occurring in homogeneous solution; the latter are generally studied by measuring the change in concentration of a reactant/product over time (**Figure 2B**). The rate of a reaction occurring in solution is therefore obtained by taking the first derivative of the data at the start of the experiment when the reaction is under pseudo steady-state conditions (i.e., roughly linear) (**Figure 2B**).

1.2.3 Cyclic Voltammetry

Unlike chronoamperometry, cyclic voltammetry experiments are less intuitive, having more subtle features that require careful interpretation. However, these subtle features are

also what make it such a powerful method for various applications. Here, only a basic description of the technique will be given.

Whereas chronoamperometry measures the current at a fixed electrode potential, cyclic voltammetry measures the current as the electrode potential is swept from one potential limit to another potential limit. The scan direction is then switched, and the current is measured until the first potential limit is reached again (**Figure 3**). The rate at which the potentials are cycled is determined by the scan rate, ν, measured in units of V s^{-1}, which can help resolve

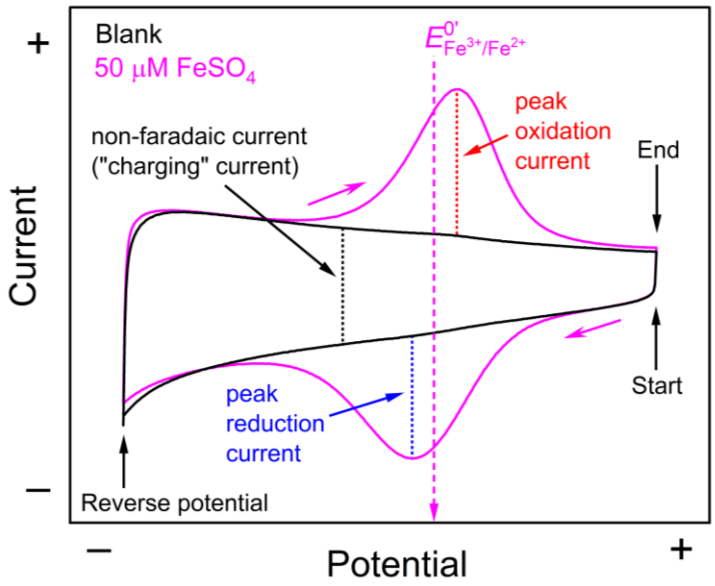


Figure 3. Cyclic voltammetry of $FeSO_4$ at a stationary mesoporous indium tin oxide electrode.

time-dependent events. **Figure 3** shows two cyclic voltammograms: one was measured for an electrode in an electrolyte solution without an electroactive species present (black), and the other was measured using the same electrode after $FeSO_4$ was added to the solution (magenta). In both cases, the scans start at a positive potential limit (start arrow), and the electrode potential is progressively lowered until the negative potential limit is reached. Once

at the negative potential limit, the electrode potential is raised again until the starting potential is reached (end arrow).

Three important features of a cyclic voltammogram are shown in **Figure 3**: (1) the peaks of the magenta trace are the result of the single-electron reversible oxidation and reduction of Fe^{2+} and Fe^{3+}, respectively, at the electrode surface (Eq. 3). This type of current

$$Fe^{3+} + e^- \rightleftharpoons Fe^{2+} \qquad \text{(Eq. 3)}$$

is referred to as "faradaic" current, in which electrons pass across the electrode-solution interface. Importantly, the positive peak (red dotted line) is the oxidation peak, and the negative peak (blue dotted line) is the reduction peak. (2) The average of the oxidation and reduction peak potentials is equivalent to the formal reduction potential ($E^{0'}$) of the reaction when the oxidized and reduced species are present at equal concentrations in solution.[2] This is a very important concept because reduction potentials are intensive thermodynamic properties from which other values such as the Gibbs free energy (ΔG) can be *directly* obtained. (3) The black dotted line shows the "non-faradaic" current that is measured during cyclic voltammetry. Importantly, the current measured using cyclic voltammetry consists of a combination of "faradaic" and "non-faradaic" components. Faradaic current is measured from an oxidation or reduction reaction occurring at the electrode surface (i.e., electrons must cross the electrode-solution interface). Non-faradaic current, also called "capacitive" or "charging" current, results from the "charging" and "discharging" of the electrode in the same way that a capacitor works. In the latter case, electrons are "pushed into" or "pulled out of" the electrode depending on the potential applied, causing it to build up a net charge. This process is measured as current because electrons are flowing through the wire into/out of the electrode. To balance the net charge (positive or negative) on the electrode, oppositely

charged ions in the electrolyte solution adsorb onto the electrode surface; this plane of ions is then itself stabilized by a more loosely associated plane of oppositely charged electrolyte ions (now the same sign as the charge on the electrode) forming what is referred to as the "electrical double layer". Because the electrolyte ions stabilize a net charge at the electrode surface without electrons crossing the electrode-solution interface, the electrical double layer can be treated as a capacitor. Capacitance, *C*, is dependent on the charge on the electrode and the potential applied according to:

$$C = \frac{q}{E}, \qquad \text{(Eq. 4)}$$

where *q* is the charge (coulombs) and *E* is the potential (volts) across the capacitor. Because the current is the flow of charge over time,

$$I = \frac{dq}{dt}, \qquad \text{(Eq. 5)}$$

Eq. 4 and Eq. 5 can be combined to give:

$$I_C = C\frac{dE}{dt} = C\nu, \qquad \text{(Eq. 6)}$$

where I_c is the capacitive (non-faradaic) current and ν the scan rate. Importantly, this means that the capacitive current is directly proportional to the scan rate. The practical importance of this relationship is that, for experiments with a reactant in solution, slower scan rates will yield a better signal-to-noise ratio by disproportionally reducing the capacitive (non-faradaic) current relative to the faradaic current.

1.3 Protein Film Electrochemistry

1.3.1 Requirements for Direct Electrochemical Study of Proteins

As will be shown throughout this work, electrochemical methods offer a powerful way to study enzymes by providing direct thermodynamic (via the electrode potential) and kinetic (via the measured current) information. Protein film electrochemistry (PFE) encompasses a suite of methodologies to study films of proteins adsorbed on electrode surfaces.[3–10] However, only proteins containing redox-active groups are electroactive, i.e., able to directly exchange electrons with an electrode. Even if a protein does contain a redox-active group, the protein scaffold is electrically insulating, and redox-active sites are often deeply buried in the protein preventing facile electron exchange with an electrode. Interestingly, the protein scaffold itself does not intrinsically hinder electron transfer because electrons can pass through the polypeptide and solvent via quantum mechanical tunneling with relative ease in many cases.[2] The issue is rather the electron tunneling *distance*, whereby the protein will not be electroactive if the distance between the redox-active site and the electrode exceeds 14 Å.[11,12]

A further requirement is the ability to form a film of protein on the electrode. Electrodes can be modified to facilitate this, or in some cases, this is not required.[11] In either case, the protein must be adsorbed onto the electrode in an orientation which allows facile electron transfer. If the protein is present in many different orientations, some of which do not facilitate rapid electron transfer (**Figure 4**), then the protein signal may be too small to be practically studied or the protein redox peaks may be broadened as a result of a "dispersion" effect, i.e., the spectrum of differently oriented enzymes will be oxidized/reduced according to a spectrum of electron transfer rate constants, broadening

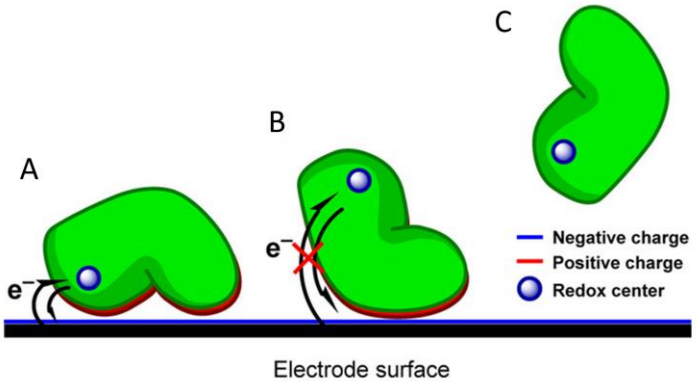


Figure 4. Non-specific protein adsorption on an electrode. (A) Electrostatic attraction allows the protein to adsorb in an orientation which facilitates direct electron transfer between the protein redox center and the electrode. (B) The protein adsorbs in an orientation which does not facilitate electron transfer. (C) The protein does not adsorb to the electrode. Adapted with permission from ref.[11]

measured redox peaks.[3,11,13] A final, and perhaps obvious, requirement is that the protein must be stable (i.e., remain folded) on the electrode long enough for a measurement to take place.

1.3.2 Direct versus Mediated Protein Electrochemistry

In addition to studying proteins via direct enzyme-electrode interaction, redox mediators can be used to oxidize/reduce protein active sites. Mediated electron transfer can take several forms: (1) the mediator can be present in homogeneous solution whereby the mediator reacts at the electrode surface before reacting with the protein, (2) the mediator can be covalently attached to the protein forming a "wire" through which electron transfer is achieved, or (3) the mediator can be present in a redox hydrogel or conductive polymer in which the protein is also embedded.[14]

In comparing direct versus mediated electrode-protein electron transfer, it is generally agreed upon that direct electron transfer is preferrable. Mediators mask important information because they inherently have different redox properties than the protein under

study. The result is that measured potentials and rates of protein redox processes become controlled by the properties of the mediator rather than those of the protein/enzyme.[4,14]

Without the requirement for mediators, direct protein electrochemical methods make it possible to "talk" directly to the active sites of proteins in real time, revealing important details about enzyme catalysis (e.g., reactive intermediate states) that may be very difficult

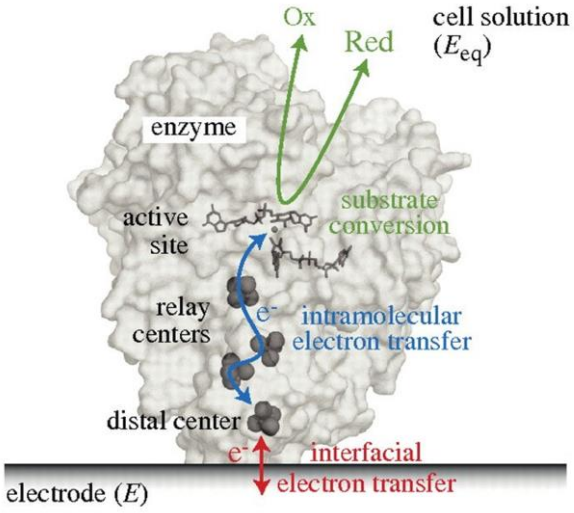


Figure 5. A metalloenzyme adsorbed on an electrode allowing it to function as an electrocatalyst. Adapted with permission from ref.[6]

to study using other methods.[2] As a visual representation of such direct interaction, **Figure 5** shows a generic electroactive enzyme (containing multiple redox-active sites) adsorbed to an electrode. Close to the electrode surface and within electron tunneling distance (≤14 Å),[11,12] a series of four FeS clusters form an extended electron relay chain leading to the enzyme active site where catalysis can be driven electrochemically. Such relay chains are common in large metalloproteins as it allows electrons to rapidly move across long distances.[15] Significantly, distinct electron transfer steps can often be detected, and changes to the electrode potential give real-time feedback from the enzyme allowing catalytic properties and reactive enzyme intermediates to be studied.[2]

1.3.3 Bidirectional, Reversible, Irreversible, and Unidirectional Catalysis

A notable advantage of using electrochemical methods to study enzymes is the ability to control the redox state of the enzyme and thus the direction in which catalysis proceeds. This makes studying bidirectional enzyme catalysis more straightforward than practically any other method. As previously mentioned, the electrode potential is an important measurement from which a host of useful thermodynamic information can be obtained.

Electrochemistry has proven to be a powerful tool for investigating the efficiency with which enzymes catalyze reactions. An efficient enzyme in electrochemical terms is one which requires only a minimal overpotential to drive the reaction in either direction (blue line, **Figure 6**). This type of reaction is termed *reversible*; in such a case, the rates at potentials close to the x-axis crossover (equilibrium) potential represent the system trying to achieve the concentrations of species which would be predicted by the Nernst equation (Eq. 7) at each potential.

$$E = E^{0'} - \frac{RT}{nF}\ln(Q) \qquad \text{(Eq. 7)}$$

Therefore, if a 1:1 mixture of oxidized and reduced forms of a redox couple are present in solution, the current cuts sharply through the potential axis at the formal reduction potential ($E^{0'}$) of the redox couple. In the case where the reaction is not reversible, i.e., it does not cut sharply through the potential axis, but it can still be driven in both directions with an overpotential (red line, **Figure 6**), the reaction is considered to be *irreversible*—note that the reaction is still considered bidirectional and that bidirectional catalysis encompasses both reversible and irreversible catalysis. Irreversible catalysis is thus less efficient because an overpotential (extra driving force) is required to drive the reaction in either direction. Finally,

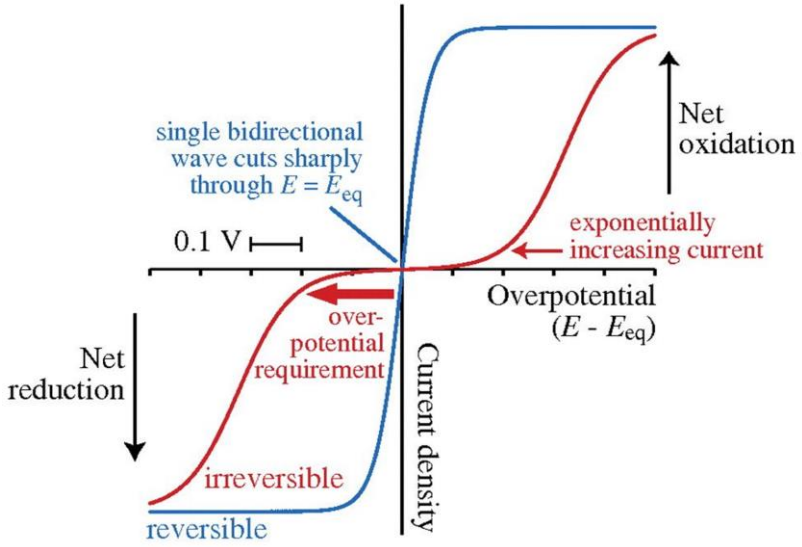


Figure 6. Reversible versus irreversible catalysis visualized using cyclic voltammetry. The reversible trace (blue) cuts sharply across the x-axis without inflection. In contrast, the irreversible trace (red) exhibits an inflection point at the zero current potential (x-axis) indicating that an overpotential is required to drive the reaction in either direction. Note that both the reversible and irreversible traces are bidirectional; a unidirectional reaction is one in which only one of the two half reactions (oxidation or reduction) can occur. Adapted with permission from ref.[6]

a reaction which can only be driven in one direction (i.e., either oxidation or reduction) is termed unidirectional.

1.4 The Electrochemical Leaf

1.4.1 Ferredoxin-NADP$^+$ Reductase (FNR)

The electrochemical Leaf (e-Leaf) is a technology that extends electrochemical methods to non-electroactive enzymes which have been trapped inside a nanoporous metal oxide electrode. At the center of the technology is the terminal enzyme in the photosynthetic electron transport chain, ferredoxin-NADP$^+$ reductase (FNR), which is responsible for storing the low potential (high energy) electrons produced by photosystem I in the form of

NADPH.[15] In photosynthetic organisms, FNR accepts two sequential electrons at its flavin adenine dinucleotide (FAD) active site from its redox partner, ferredoxin, via long range electron transfer when the two proteins physically associate (**Figure 7A**; **Scheme 1**). Notably, the two reduction potentials of FNR are "crossed" ($E_2 > E_1$), meaning once the first electron transfer from ferredoxin to FNR occurs, the second electron transfer event is much more favorable, i.e., electron transfer is cooperative.[15] This has the effect of suppressing the

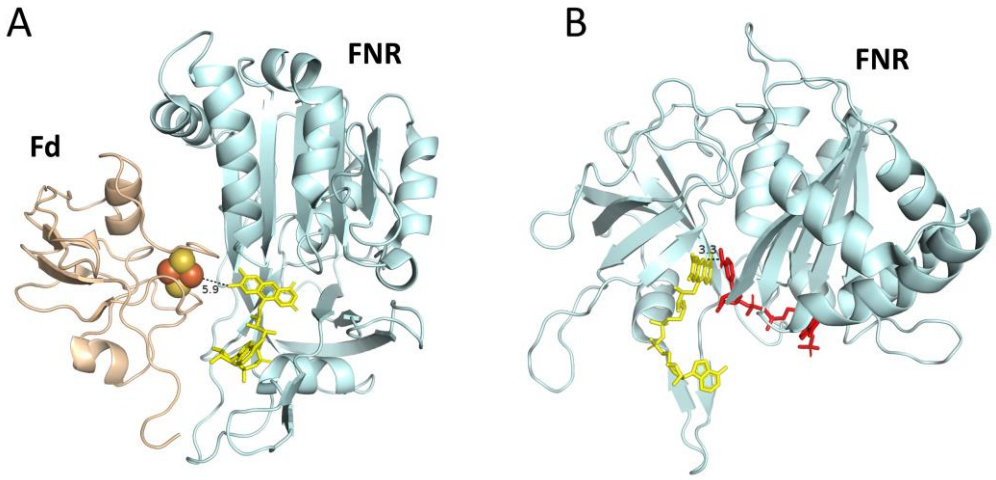
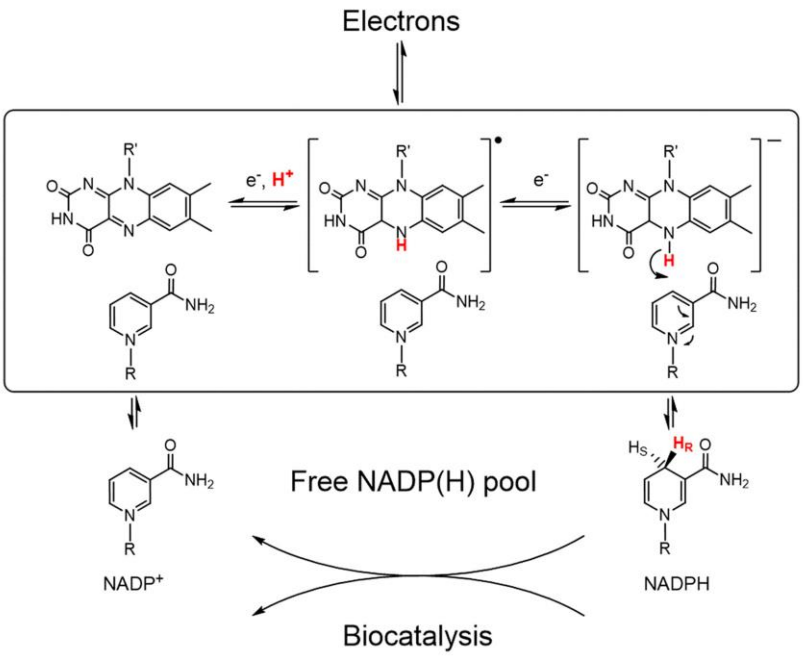


Figure 7. Crystal structure views of FNR and ferredoxin. (A) FNR in complex with ferredoxin showing the close approach (5.9 Å) between the [2Fe-2S] cluster of ferredoxin and the FAD group (yellow) of FNR (PDB: 1GAQ).[16] (B) FNR with $NADP^+$ (red) bound at the FAD (yellow) active site (PDB 1QFZ).[17]

semiquinone form of FAD, facilitating the role of FNR as a translator between $1e^-$ (ferredoxin) and $2e^-$ (NADP(H)) reactions. When fully reduced (hydroquinone), FNR is able to reduce $NADP^+$ to NADPH via a hydride transfer reaction, reforming the fully oxidized quinone form of FAD (**Scheme 1**). **Figure 7B** shows FNR in complex with $NADP^+$ where the two groups are 3.3 Å apart. While this is well within the distance in which electron tunneling can take place, hydride tunneling can only occur over much shorter distances (< 1 Å).[15] Thus, an enzyme conformational change is required to bring the FAD and $NADP^+$ groups close enough for them to react.



Scheme 1. Tightly-bound flavin (FAD) in FNR (here, represented as the rectangle) accumulates two electrons and a proton to generate reduced nicotinamide (NAD(P)H) for use in downstream reactions. Only the nicotinamide ring is shown; R is the nucleotide side chain which contains an additional phosphate group in NADP(H) compared to NAD(H). R′ is the nucleotide side chain of the flavin. Adapted with permission from ref.[15]

1.4.1.1 Electrochemistry of Ferredoxin-NADP⁺ Reductase (FNR)

Having an exposed FAD active site and naturally performing long-range electron transfer in vivo, FNR is a good candidate enzyme to be studied electrochemically. When loaded onto a nanoporous indium tin oxide (ITO) electrode, formed by the electrophoretic deposition of ITO nanoparticles on a conductive support, the surface-bound FAD group of FNR can directly exchange electrons with an electrode.[18] Cyclic voltammograms with FNR show peaks corresponding to the oxidation and reduction of its FAD active site (non-turnover peaks) at an average value of –0.38 V vs SHE at pH = 8 (**Figure 8A**).[18] In the presence of NADP(H), FNR exhibits quasi-reversible $NADP^+$/NADPH interconversion whereby, depending on the electrode potential applied, FNR can be driven efficiently in either

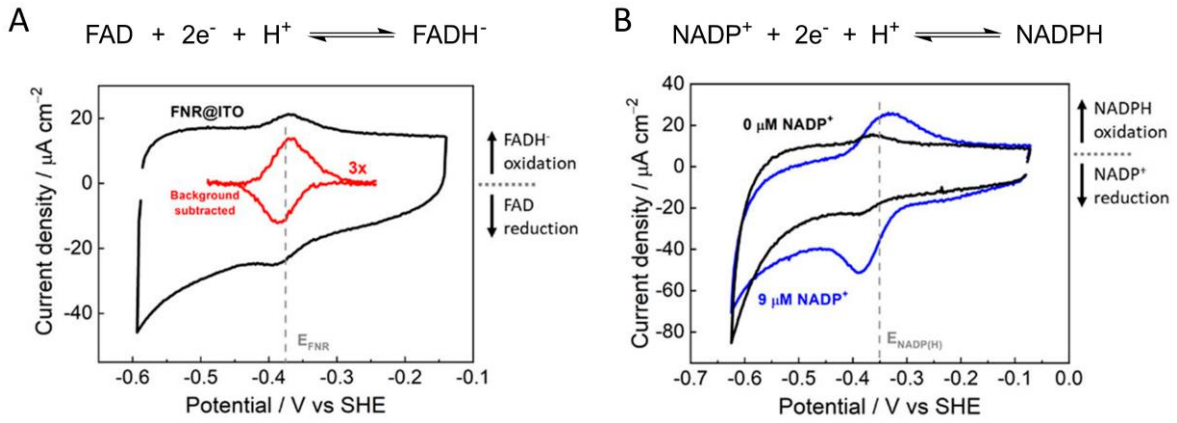


Figure 8. Cyclic voltammograms with FNR loaded onto a nanoporous indium tin oxide (ITO) electrode. (A) Non-turnover redox peaks (raw voltammogram (black) and background subtracted (red)) show the direct oxidation/reduction of the FAD prosthetic group of FNR. (B) Turnover peaks (blue) showing FNR-catalyzed $NADP^+$ reduction (just negative of the NADP(H) formal reduction potential) and NADPH oxidation (just positive of the NADP(H) formal reduction potential). Adapted with permission from ref.[15]

direction (oxidation or reduction) with catalysis requiring almost no overpotential beyond the –0.35 V vs SHE (at pH = 8) $NADP^+$/NADPH formal reduction potential (**Figure 8B)**.[18]

Reversible electrochemistry for $NAD(P)^+$/NAD(P)H has been a topic of intensive research for many decades. However, non-enzymatic NAD(P)(H) electrochemistry is very difficult because the single-electron reduction potentials are extremely crossed (E_1 = −1.16 V and E_2= +0.81 V),[19] resulting in the production of highly reactive radical intermediates which can dimerize and become inactive.[19–21] Furthermore, direct electrochemical reduction is non-specific, which can result in a hydride group being added to the wrong carbon atom yielding the inactive 1,6-NAD(P)H instead of the biologically active 1,4-NAD(P)H.[20–22] Notably, even if electrochemical NAD(P)(H) recycling were to have a fidelity of 99% (it is generally much lower), this would result in 87% of the cofactor being inactivated after just 200 cycles. In contrast, FNR catalyzes the interconversion of $NADP^+$/NADPH with essentially 100% fidelity[4,15] making it possible to achieve very high turnover numbers.[23] The

relative inefficiency of direct NAD(P)(H) electrochemistry at an electrode surface can be visualized by overlaying such results on the same plot as a cyclic voltammogram obtained using FNR adsorbed on an electrode (**Figure 9**). As is clearly visible, FNR catalyzes NADPH oxidation or $NADP^+$ reduction at potentials just beyond the formal reduction potential of the $NADP^+$/NADPH redox couple; in other words, almost no energy is wasted when driving these reactions. By contrast, NAD^+ reduction at a gold electrode or NADH oxidation at a pyrolytic graphite edge (PGE) electrode require very large overpotentials to drive either reaction at a significant rate resulting in wasted energy and lower efficiency.

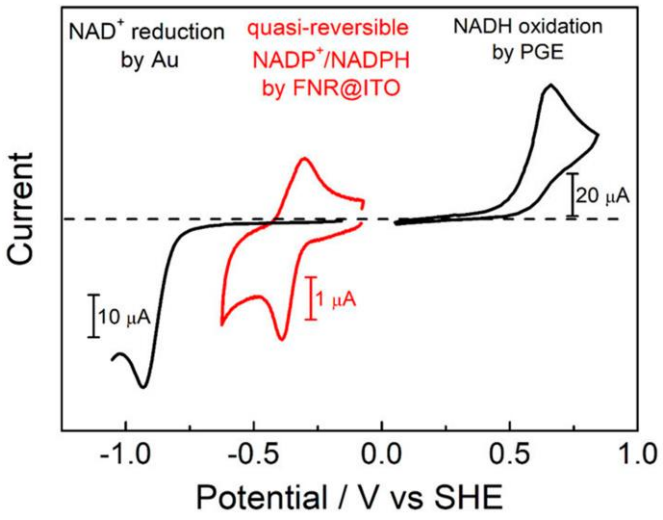
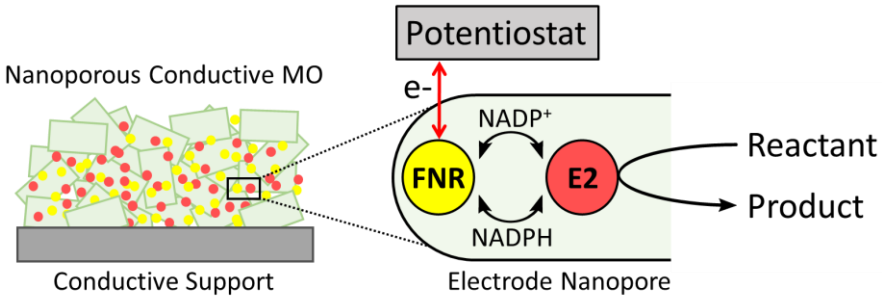


Figure 9. Visual representation of the efficiency of FNR as an electrocatalyst for performing NADP(H) electrochemistry compared to bare Au and pyrolytic graphite edge (PGE) electrodes. Adapted with permission from ref.[15]

1.4.2 The Electrochemical Leaf Extends Electrochemical Methods to Non-electroactive Enzymes

The exchange of electrons between FNR (E1) and the electrode is both driven and measured by a potentiostat; therefore, FNR-catalyzed NADP(H) oxidation or reduction can be visualized on a computer screen with rates measured as electrical current in real time.

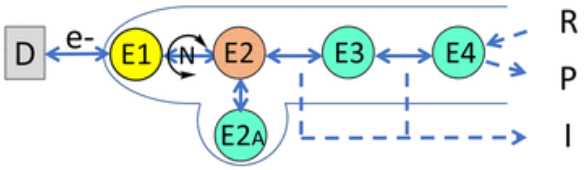
When an NADP(H)-dependent dehydrogenase (E2) is trapped inside the nanoporous indium tin oxide (ITO) electrode *alongside* FNR, in the presence of the substrate for E2, NADP(H) is recycled rapidly between E2 and FNR (E1) as E2 converts its substrate into product, giving a "coupled" current signal (**Scheme 2**). The combination of FNR and an NADP(H)-dependent dehydrogenase in a nanoporous electrode is referred to as the Electrochemical Leaf (e-Leaf),[4] named for the analogous process linking FNR-catalyzed NADPH chemistry to downstream reactions in photosynthetic organisms.[24]



Scheme 2. The Electrochemical Leaf (e-Leaf). Enzymes are trapped in a nanoporous electrode (pore sizes range from 20–200 nm) formed from electrophoretic deposition of indium tin oxide (ITO) nanoparticles (<50 nm) onto a conductive support (other conductive metal oxides (MO) can be used in place of ITO). FNR catalyzes $NADP^+$/NADPH interconversion and is controlled by the potential applied to the electrode. E2 is an NADP(H)-dependent dehydrogenase. In the presence of E2 substrate, NADP(H) is rapidly recycled between FNR and E2 giving rise to a "coupled" current that is directly proportional to the rate of E2 turnover (assuming the rate of FNR turnover is not limiting).

Importantly, once the enzymes are present in the electrode, they become trapped, i.e., exchange of enzyme molecules between the electrode nanopores and the bulk solution is extremely low.[4,23] This "nanoconfinement" effect is crucial—real-time E2 activity can only be observed when FNR and E2 are close enough to facilitate rapid NADP(H) exchange.[4,23,25] The extremely close proximity and rapid recycling of NADP(H) between enzymes means that only catalytic amounts of NADP(H) (1–30 μM) are required to facilitate E2 catalysis.[4,23] So long as FNR activity is not limiting, the electric current measured for a coupled reaction (E1 + E2) is directly proportional to the rate of E2 turnover. Thus, the e-Leaf

is able to render NADP(H)-dependent enzymes "electroactive";[26] notably, such enzymes constitute one-sixth of all enzymes.[27] Enzymes which are catalytically linked to the NADP(H)-dependent dehydrogenase (E2) i.e., enzymes which utilize an E2 product or produce an E2 substrate, can be loaded into the electrode nanopores alongside FNR (E1) and E2 (**Scheme 3**).[1,28] In this way, cascades can be formed which extend electrochemical methods to many other enzyme classes.[4]



Scheme 3. Cartoon showing an extended e-Leaf cascade inside an electrode nanopore. E1 = FNR, E2 = an NADP(H)-dependent dehydrogenase, E3 and E4 are enzymes in a linear cascade with activities linked to E2. E2A is a "service branch" enzyme supplying/consuming a substrate/product of E2. "N" is NADP(H); "R", "P", and "I" are reactants, products, and intermediates, respectively. "D" represents the dashboard, which includes a potentiostat and an electrode rotator, used to control and monitor the cascade. Adapted with permission from ref.[4]

CHAPTER II

RENDERING ISOCITRATE DEHYDROGENASES ELECTROACTIVE

2 Rendering Isocitrate Dehydrogenases Electroactive

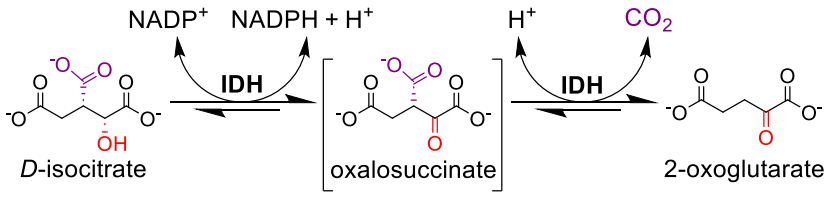
2.1 Abstract

Human isocitrate dehydrogenase I (IDH1) and several cancer-associated IDH1 variants are rendered electroactive through co-entrapment inside electrode nanopores alongside the NADP(H)-recycling enzyme, ferredoxin-$NADP^+$ reductase (FNR). In the e-Leaf electrode, IDH1 activities are measured as electric current, and rates of activation (by the essential Mg^{2+} cofactor or substrate) are directly observed in real time. Despite the unusual environment, enzyme activity profiles resemble those expected by Michaelis-Menten kinetics. Tight electrochemical control over the redox environment inside the electrode nanopores, where the enzymes reside, is easily achieved via the applied potential; this is exploited to drive wildtype IDH1 reversibly and to investigate the underlying thermodynamics of the reactions catalyzed by the wildtype and several variant IDH1 enzymes. Redox control is also exploited to measure the rates of formation of a cascade intermediate that cannot easily be measured using standard methods but which is accessible by cyclic voltammetry. Other fundamental properties of enzyme catalysis are investigated, including the kinetic and thermodynamic pH biases of wildtype and variant IDH1 enzymes and the rates of catalysis using alternative substrates. The “electrification” of enzymes using the e-Leaf offers a new perspective on enzyme catalysis by extending powerful electrochemical methods to previously inaccessible enzymes which can now be controlled with ease, yielding direct thermodynamic and kinetic information.

2.2 Introduction

2.2.1 Physical and Biochemical Properties of Isocitrate Dehydrogenase

Isocitrate dehydrogenase (IDH) enzymes are required by all aerobic organisms. Humans possess three isoforms of IDH: the more closely related homodimeric IDH1 and IDH2 (~70% identity) and the more distantly related heterotetrameric IDH3.[29] All three IDH enzymes catalyze the Mg^{2+}-dependent oxidative decarboxylation of isocitrate to 2-oxoglutarate (2OG) and carbon dioxide coupled to the reduction of $NAD(P)^+$. IDH1 and IDH2 both use $NADP^+$ and are capable of performing the reductive carboxylation of 2OG (using NADPH) to isocitrate (**Scheme 4**), i.e., they can be driven in either direction.[30] In



Scheme 4. Bidirectional oxidative decarboxylation of *D*-isocitrate to 2-oxoglutrate catalyzed by isocitrate dehydrogenase showing the transient oxalosuccinate intermediate. Molecules are presented as the forms dominating at pH = 7.

contrast, IDH3 uses NAD^+ and is not capable of reducing 2OG to isocitrate.[29] IDH2 and IDH3 are mitochondrial enzymes linked to the tricarboxylic acid (TCA) cycle, while IDH1, the primary focus of this work, is located in the cytoplasm where it helps to maintain $NADP^+$/NADPH ratios as well as supply 2OG for use by other enzymes/pathways.[31]

IDH1 is a highly dynamic enzyme which undergoes large conformational changes during its catalytic cycle.[32,33] The two most well-characterized conformations of homodimeric (2 x 47 kDa) IDH1 are shown in **Figure 10**. When heterologously expressed and purified, IDH1 copurifies and crystallizes in an “open inactive” conformation with one

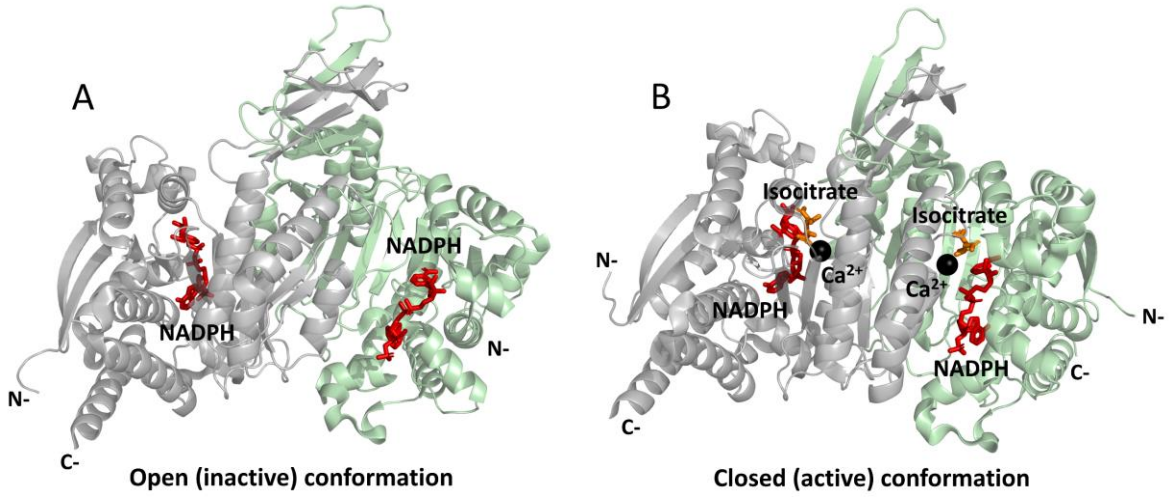


Figure 10. Crystal structure views of dimeric wildtype IDH1. (A) IDH1 crystallized "as purified" (i.e., without added NADP(H)) showing the copurified NADP(H) bound at each monomer active site. IDH1 is purified in the open inactive conformation (PDB: 1T09).[34] (B) IDH1 in the closed active conformation with NADP(H), isocitrate, and inhibitory Ca^{2+} (substituting for Mg^{2+} to prevent turnover) bound at each monomer active site (PDB: 1T0L).[34]

molecule of NADP(H) bound to the active site of each monomer (**Figure 10A**)[23,32,34–37] (this property will be exploited later, see **Chapter III**). Upon binding of isocitrate and Mg^{2+}, likely together as the isocitrate-Mg^{2+} complex is proposed to be the true substrate,[35] IDH1 undergoes a large conformational change to the "closed active" conformation (**Figure 10B**). This conformational shift pulls the nicotinamide ring of the bound $NADP^+$ toward the center of the enzyme by ~6 Å, putting it into close proximity with isocitrate to facilitate hydride transfer from the C_2 of isocitrate to the C_4 of the $NADP^+$ nicotinamide ring (**Figure 11B**). Significantly, the crystal structure representing the closed active conformation of IDH1 was crystallized with inhibitory Ca^{2+} in place of Mg^{2+} in order to prevent turnover. While this likely provides a good approximation of the pre-turnover complex, the structure of the active site shown in **Figure 11B** shows a distance of 3.3 Å between the C_2 of isocitrate and the C_4 of the nicotinamide ring, meaning further conformational changes are required to bring the two atoms into close enough proximity (< 1 Å) for hydride transfer (via quantum mechanical

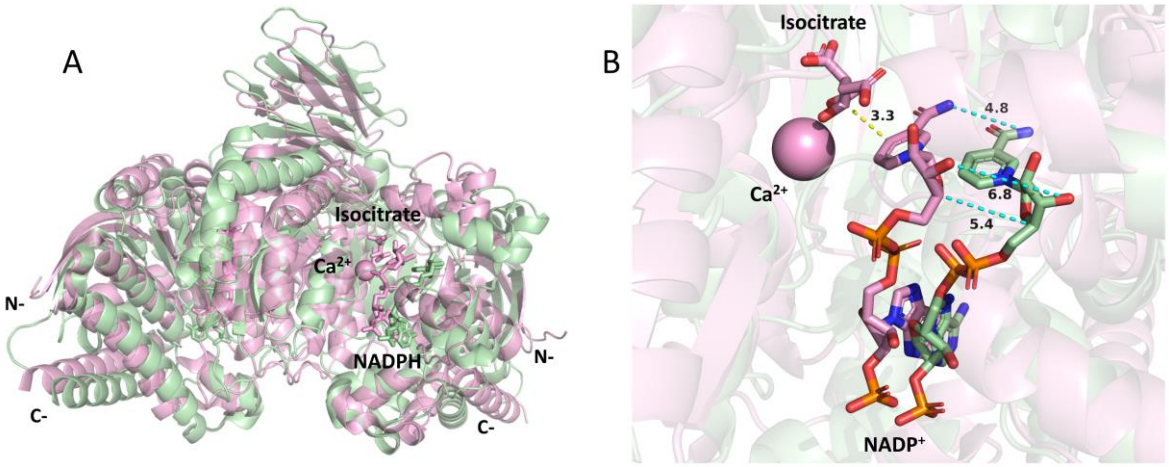


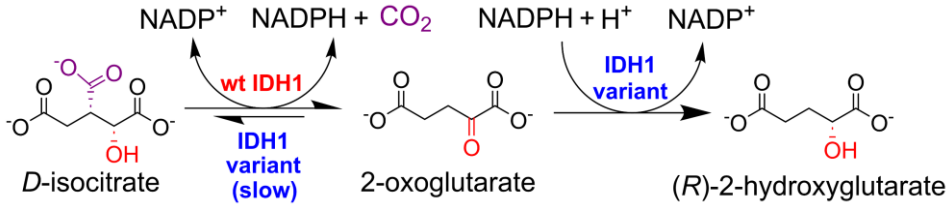
Figure 11. Substrate binding induces large conformational changes in IDH1. (A) Native IDH1 (i.e., IDH1 apoenzyme crystallized without added NADP(H)) shown in green (PDB: 1T09)[34] overlaid with "activated" IDH1 (crystallized with $NADP^+$, isocitrate, and inhibitory Ca^{2+} in place of Mg^{2+}) shown in pink (PDB: 1T0L).[34] (B) IDH1 active site showing how isocitrate/Ca^{2+} (and presumably Mg^{2+}) binding results in the $NADP^+$ nicotinamide ring being pulled toward the center of the enzyme. Note that the distance between the nicotinamide C_4 and the isocitrate C_2 is too far for hydride transfer to occur and therefore additional enzyme motion is required for turnover.[15]

tunneling) to occur.[15] The significance of the different conformations of IDH1, within and outside of the catalytic cycle, will be addressed in more detail in **Chapters III** and **IV**.

IDH1 catalysis (and by analogy IDH2) is complex and not fully understood despite its prominent role in central carbon metabolism; complicating factors are (1) its highly dynamic nature and (2) the fact that the monomers of dimeric IDH1 appear to be catalytically dependent on one another, leading to the proposal that IDH1 exhibits half-site reactivity, i.e., the monomers "take turns" performing catalysis.[32] Because of this possible ambiguity, enzyme concentrations and kinetic parameters, such as the enzyme turnover frequency (k_{cat}), will be based on the dimeric form of the enzyme in this work.

2.2.2 Cancer-associated Isocitrate Dehydrogenase Variants

Human IDH1/2 are the most frequently mutated metabolic genes associated with cancer.[29,38] Although the association between IDH mutations and cancer had been known for some time, it was not until 2009 when it was reported by Dang et al. that a naturally occurring IDH1 variant (IDH1 R132H) no longer efficiently catalyzed the $NADP^+$-dependent wildtype isocitrate oxidation reaction and instead catalyzed the NADPH-dependent reduction of 2OG, producing the oncometabolite (*R*)-2-hydroxyglutarate (2HG) (**Scheme 5**).[39] Subsequent research showed that other naturally occurring mutations at the arginine 132 residue of IDH1 (and the structurally analogous 172 residue of IDH2)[29] also conferred variants with this neomorphic (gain of function) activity with a concomitant reduction in isocitrate oxidation activity.[29,40–42] In cells, these mutations cause 2HG—normally present at low concentrations—to accumulate to millimolar levels,[39] inhibiting 2OG/Fe(II)-dependent oxygenases and disrupting processes including DNA repair and histone and DNA demethylation.[43,44]



Scheme 5. Reactions of wildtype IDH1 and 2HG-producing IDH1 variants. The variant IDH1 enzymes also can catalyze the wildtype reaction but at a much lower rate.[35,39,40] Molecules are presented as the forms dominating at pH = 7.

In the case of IDH1, substitution of arginine-132 by histidine or cysteine (IDH1 R132H and R132C, respectively) are the most common cancer-associated variants.[30,45,46] IDH1 R132 variant enzymes have been linked to numerous cancers including acute myeloid leukemia, gliomas, chondrosarcoma, and cholangiocarcinoma.[30] Notably, IDH1 R132H alone is

present in >80% of grade II/III gliomas.[30,47–49] To suppress the in vivo production of the oncometabolite 2HG, small-molecule inhibitors selective for IDH1 and IDH2 variants have been developed,[29,44,50] with three drugs having been FDA-approved: Ivosidenib[51] and Olutasidenib[52] for IDH1-associated acute myeloid leukemia (AML) and Enasidenib[53] for treating IDH2-associated AML. Further discussion of IDH1 inhibitors will be given in **Chapter IV**.

2.2.3 Aims of this Chapter

Due to their association with many types of cancer and their importance in central carbon metabolism, understanding the complex, highly dynamic catalytic mechanisms of the isocitrate dehydrogenase enzymes are of great importance. This chapter aims to study the catalytic properties of wildtype IDH1 and several IDH1 variants using electrochemical methods via incorporation into the e-Leaf. Unlike other techniques used to investigate biocatalytic reactions, the e-Leaf provides *both* thermodynamic and kinetic information, allowing IDH1 catalysis to be studied interactively and in real time, thus offering a new perspective on enzyme activity.

2.3 Results and Discussion

2.3.1 Wildtype and Variant IDH1 Activity in the e-Leaf

2.3.1.1 Rates of Activation of IDH1 Catalysis in the e-Leaf

To assess the activities of wildtype IDH1 and IDH1 R132H in the e-Leaf, concentrated solutions of purified FNR and IDH1 were mixed (4–7 µL total volume) and loaded onto nanoporous indium tin oxide (ITO) rotating disc electrodes via dropcasting (enzyme solutions were pipetted onto electrodes and incubated for ~45 minutes at room temperature; see Methods, **Chapter VII** for further detail). The electrodes were rinsed with buffer to remove any excess enzyme that had not been trapped in the electrode nanopores prior to placing them in the reaction buffer.

Using chronoamperometry (measuring current at a constant electrode potential), IDH1 activity, which is directly proportional to the electrical current, can be measured under steady state conditions making it possible to observe changes in enzyme activity in real time as live interventions are made. **Figure 12** shows normalized enzyme activities and rates of activation of wildtype IDH1 catalyzing isocitrate oxidation (panel A) and IDH1 R132H catalyzing 2OG reduction (panel B) following injections of the Mg^{2+} cofactor and the substrate for each enzyme. Initiation of the reaction was rapid for both enzymes following the addition of substrate or Mg^{2+}, with >75% of the total activity appearing within seconds, indicating facile mass transport of small molecule substrates into the electrode nanopores from the bulk solution. This immediate increase in current was then followed by a slower increase, indicating further activation of the system, which is hypothesized to be due to the nicotinamide (NADP(H)) cofactor concentrating in the electrode pores following initiation of the coupled reaction. Note that for the red trace in **Figure 12A**, where the reaction was

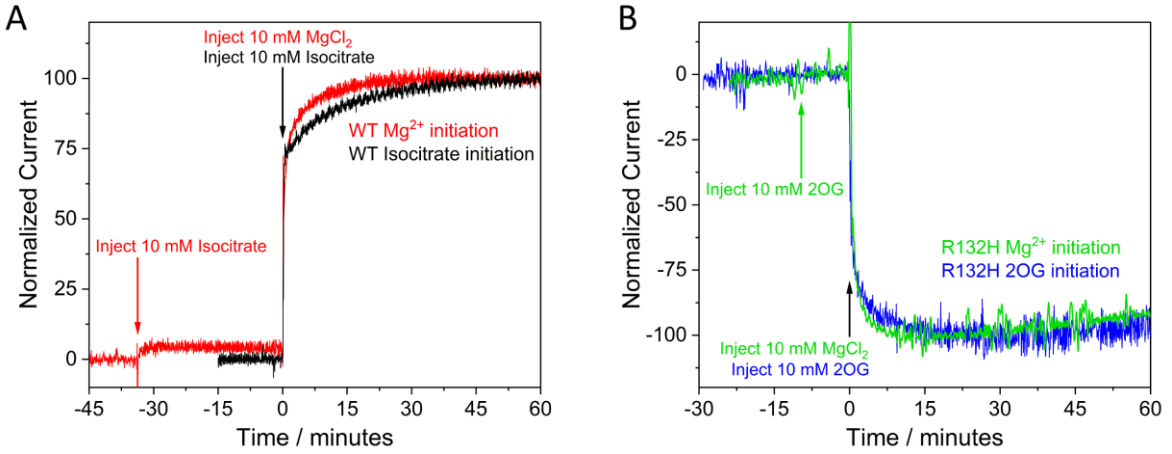


Figure 12. Chronoamperometry showing rates of activation of wildtype IDH1 (A) and IDH1 R132H (B) following injection of their respective substrates (isocitrate for wildtype and 2OG for IDH1 R132H) with Mg^{2+} already present versus rates of activation following injection of Mg^{2+} with substate already present. Current was normalized to allow direct comparison between experiments, but the wildtype enzyme was much more active. Conditions: 0.06 cm^2 FNR@ITO/PGE electrode, 25 °C, 1000 rpm, *E* (vs SHE) = –0.188 V for wildtype and –0.513 V for R132H; pH = 8 (20 mM each: MES, TAPS, CHES), 10 mM $MgCl_2$ (for experiments not initiated with Mg^{2+}), NADP(H): 10 µM $NADP^+$ for wildtype IDH1 and 10 µM NADPH for R132H; 4 mL volume. Enzyme loading ratios (molar): (A) FNR/$IDH1_{WT}$; 2/1 and (B) FNR/$IDH1_{R132H}$; 2/5.

initiated by the addition of Mg^{2+}, there was a small increase in current upon the addition of isocitrate at approximately 32 minutes prior to Mg^{2+} addition. This small current was due to wildtype IDH1 isocitrate oxidation activity resulting from a very slight amount of Mg^{2+} impurity present in the enzyme preparation that was not removed following EDTA treatment. This result indicates the extreme sensitivity of the e-Leaf for measuring enzyme activity as this very minor activity is not detected in standard solution assays. Interestingly, wildtype IDH1 has an approximately 200-fold greater affinity for Mg^{2+} than the R132H variant (K_m = 0.018 mM for wildtype vs K_m = 4.0 mM for R132H)[40], which explains why a small percentage of residual Mg^{2+} remains bound to wildtype IDH1 but not IDH1 R132H after treatment with EDTA (and thus why no activity is observed for R132H following injection of 2OG without added Mg^{2+}). Importantly, neither isocitrate nor 2OG are electroactive on their own at the potentials relevant to this work.[26]

2.3.1.2 Reversible Inactivation of IDH1 R132H by Metal Chelation

Taking advantage of the relatively low affinity of IDH1 R132H for Mg^{2+} (K_m = 4.0 mM)[40], an experiment was carried out to see if the essential Mg^{2+} cofactor could be removed via chelation, forming the inactive apoenzyme, live during the experiment as a means of chemically stopping turnover (**Figure 13**). When the 2OG reduction reaction had reached a steady state following the addition of substrate, 10 mM EDTA (equal to the

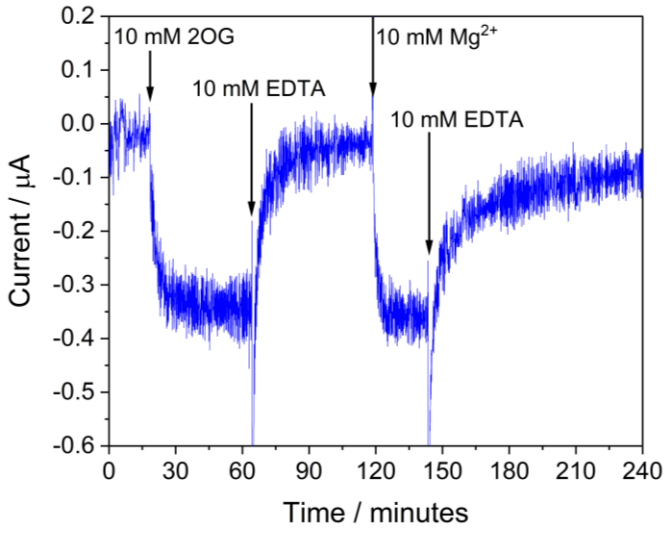


Figure 13. IDH1 R132H reaction initiated by 2OG injection followed by demonstration of reversible generation of apoenzyme and holoenzyme by chelation of Mg^{2+} using EDTA and addition of Mg^{2+}. Conditions: 0.06 cm^2 FNR@ITO/PGE electrode, 25 °C, 1000 rpm, *E* (vs SHE) = –0.513 V, pH = 8 (20 mM each: MES, TAPS, CHES), 10 mM $MgCl_2$ at start of experiment, 10 µM NADPH, 4 mL volume. Enzyme loading ratio (molar): $FNR/IDH1_{R132H}$; 2/5.

concentration of $MgCl_2$ already present) was injected into the reaction solution. The rate of IDH1 R132H turnover quickly dropped following injection of EDTA, falling to a current of roughly 0 A after approximately 20 minutes indicating that the inactive apo form of the R132H enzyme had indeed been produced inside the electrode. To test the reversibility of this process, an additional 10 mM $MgCl_2$ was injected into the reaction solution (now 20 mM final concentration with 10mM chelated by EDTA), and an immediate increase in catalytic activity was observed. Notably, the rate of increase in current upon injection of Mg^{2+} was

much faster than the decrease following injection of EDTA; since EDTA is a small molecule and thus rapidly equilibrates within the electrode nanopores, this difference must reflect the kinetic differences between the formation and dissociation of the R132H-Mg^{2+} complex.

2.3.1.3 Enzymes in the e-Leaf Exhibit Michaelis-Menten Kinetics with Some Caveats

Enzymes in the e-Leaf appear to exhibit near-ideal Michaelis-Menten kinetics, that is, their catalytic rates (v), measured as electrical current (*I*), have a hyperbolic dependence on the substrate concentration ([S]) allowing plots of steady-state current vs [S] to be fit directly by the Michaelis-Menten equation (Eq. 8) (**Figure 14**). When the equation is fitted, V_{max} is

$$\nu = \frac{V_{max}[S]}{K_m + [S]} \qquad \text{(Eq. 8)}$$

equivalent to the maximum current, I_{max}, as the two are directly related. In the case of IDH1 R132H, a timecourse experiment in which increasing concentrations of 2OG substrate were titrated into the reaction solution resulted in a "textbook" Michaelis-Menten plot, yielding a nanoconfined Michaelis constant ($K_{m(nano)}$) value of 0.616 mM, which is in good agreement with values obtained by standard spectrophotometric assays in dilute solution (dilute solution K_m = 0.40–0.85 mM).[35,40,54]

Despite the apparently ideal Michaelis-Menten fit obtained for IDH1 R132H activity, it should be borne in mind that electrochemical experiments are heterogeneous (surface-solution), and therefore enzyme substrate mass transport limitations may affect measured constants, particularly for enzymes with high turnover rates. For example, when a similar experiment was performed with an electrode loaded with only FNR (**Figure 15**), this time titrating NADPH into solution for FNR-catalyzed NADPH oxidation, the activity vs [*S*]

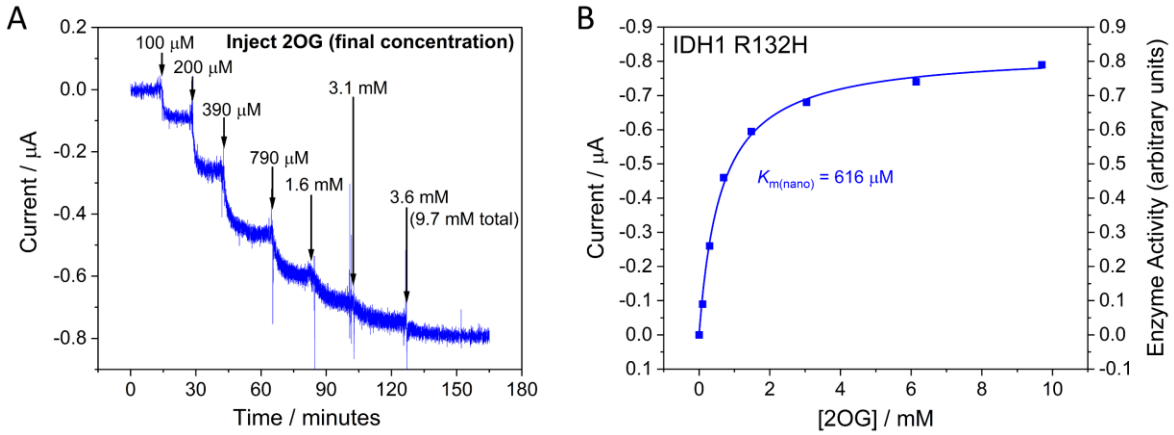


Figure 14. IDH1 R132H exhibits Michaelis-Menten kinetics in the e-Leaf. (A) Chronoamperometry showing IDH1 R132H activity as 2OG is titrated into the reaction solution at increasing concentrations (arrows show the final concentration of each 2OG each injection, not the cumulative concentration). (B) Plot showing the steady-state R132H activity at each 2OG concentration fitted by the Michaelis-Menten equation (K_m = 0.616 mM). Conditions: 25 °C, pH = 8.0: mixed buffer (20 mM each: MES, TAPS, CHES), 10 mM $MgCl_2$, 10 µM NADPH, 4 mL cell volume, (FNR+$IDH1_{R132H}$)@ITO/PGE electrode, electrode area 0.06 cm^2, rotated at 1000 rpm, E = –0.513 V vs SHE, enzyme loading ratios (molar): FNR/$IDH1_{R132H}$; 2/5.

profile again exhibited Michaelis-Menten behavior, but the measured $K_{m(nano)}$ was 5.69 mM—two orders of magnitude higher than that observed in dilute solution (K_m = 0.049 mM).[23] This large difference is explained by the well-established fact that heterogeneous catalytic systems are often limited by mass transport (i.e., the rate of re-supply of fresh reactant to the immobilized catalyst on a planar surface). In the case of FNR, it's relatively high turnover frequency (k_{cat} = 51 s^{-1})[23] coupled with a high affinity for NADPH (K_m = 49 µM),[23] explains the observed difference between e-Leaf and dilute (homogeneous) solution measured K_m values. In contrast, IDH1 R132H, for which the $K_{m(nano)}$ was representative of the dilute solution K_m, is a much slower enzyme (dilute solution k_{cat} = 1–2 s^{-1})[35,40,54] with a substrate affinity that is an order of magnitude lower than FNR in dilute solution. In this case, it appears that substrate mass transport is not the limiting factor determining the rate of IDH1 R132H turnover.

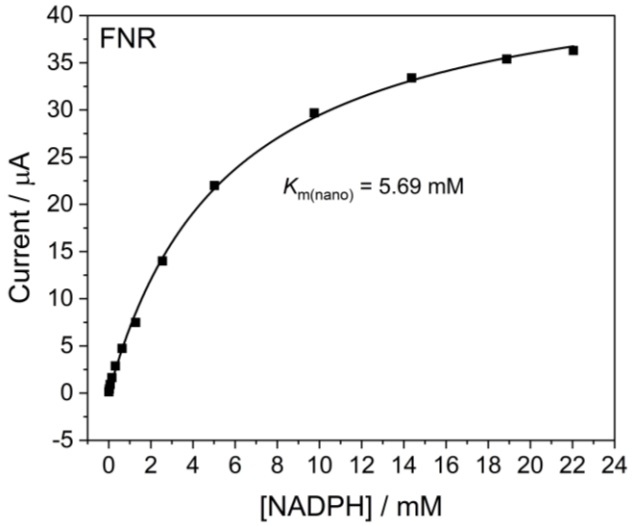


Figure 15. FNR exhibits Michaelis-Menten kinetics in the e-Leaf but yields different Michaelis constant values compared to measurements in dilute solution. The plot shows steady-state FNR activity at different NADPH concentrations fitted by the Michaelis-Menten equation ($K_{m(nano)}$ = 5.69 mM). Current (directly proportional to enzyme activity) values were obtained from a chronoamperometry experiment where NADPH was titrated into the reaction solution at increasing concentrations. Conditions: (FNR)@ITO/PGE electrode, electrode area 0.06 cm^2, rotated at 3000 rpm, E = +0.2 V vs SHE, temperature 25 °C, pH = 8 (100 mM HEPES), 3.4 mL cell volume.

In addition to potentially being limited by mass transport, the e-Leaf operates with enzymes that are concentrated to millimolar levels inside the electrode nanopores (this will be shown in **Chapter III**), a very different environment than those found in standard solution assays where enzyme concentrations are often at nanomolar levels. Noting that Michaelis Menten kinetics assumes that the enzyme concentration is much lower than the substrate concentration (i.e., [E] << [S]) and that this is not always true in the e-Leaf, care was taken in deciding how to interpret measured Michaelis-Menten constants such as $K_{m(nano)}$ and $k_{cat(nano)}$ from experiments with the e-Leaf. This topic will be further explored in **Chapter III**.

2.3.2 Wildtype and Variant IDH1 Cyclic Voltammetry at different pH

Following several experiments confirming activity for wildtype and variant IDH1, enzyme activity in the e-Leaf was measured at four different pH values (6.0, 7.0, 8.0, and 9.0) by cyclic voltammetry to test the pH-dependence of both the wildtype and variant IDH1 enzyme-catalyzed reactions (**Figure 16**). Background traces (shown in black) were recorded with 30 µM NADP(H) in the reaction solution to establish a baseline prior to the addition of

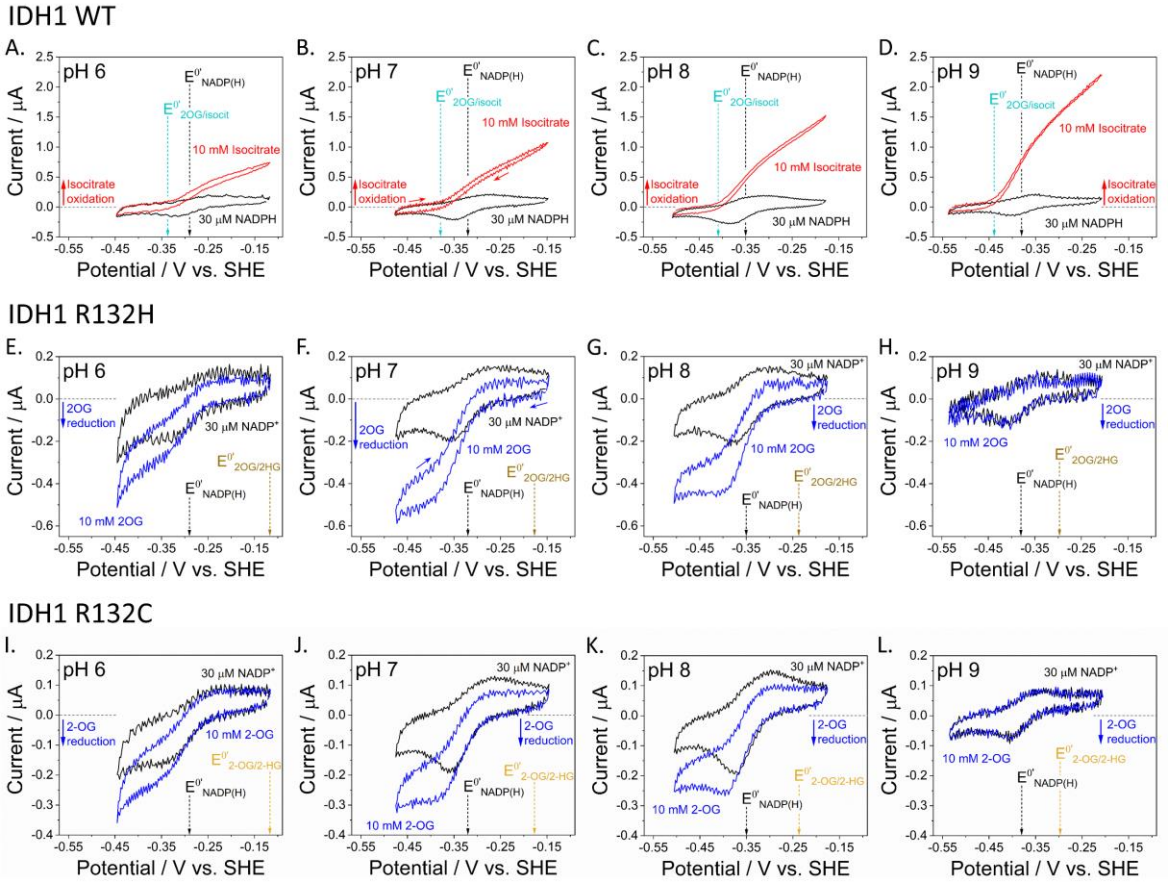


Figure 16. Cyclic voltammograms of wildtype IDH1 (**A–D**) and the single mutant IDH1 variants: IDH1 R132H (**E–H**) and IDH1 R132C (**I–L**) at different pH. Experiments were performed using a 0.03 cm^2 (FNR+E2)@ITO/PGE stationary electrode (E2 is an IDH1 enzyme). Conditions: 1 mV s^{-1}, 25 °C, 60 mM mixed buffer (20 mM of each: MES, TAPS, CHES), 10 mM $MgCl_2$, 30 µM NADP(H), 10 mM substrate (*DL*-isocitrate or 2-oxoglutarate), 4 mL volume. Enzyme loading ratios (molar): $FNR/IDH1_{WT}$; 2/1 and $FNR/IDH1_{R132H}$; 1/2. $E^{0'}{}_{NADP(H)}$, $E^{0'}{}_{2OG/isocit}$, and $E^{0'}{}_{2OG/2HG}$ denote the formal reduction potentials of the $NADP^+$/NADPH, 2OG/isocitrate, and 2OG/2HG reactions, respectively, at each pH.[26] $E^{0'}{}_{2OG/isocit}$ was calculated from the crossover potential (E_{eq}) shown in **Figure 22**, and $E^{0'}{}_{2OG/2HG}$ was calculated using experimentally derived equilibrium constant data.[55,56] Isocitrate formal potentials at each pH were estimated assuming a slope of -60 mV/pH.

substrate. The black traces show reversible $NADP^+$/NADPH electrochemistry at a stationary electrode catalyzed by FNR and exhibit characteristic peaks for NADPH oxidation (just positive of the $NADP^+$/NADPH redox potential) and $NADP^+$ reduction (just negative of the $NADP^+$/NADPH redox potential) (**Figure 16**). In the presence of IDH1 substrate (isocitrate for wildtype or 2OG for IDH1 variants), cyclic voltammograms (measuring activity as a function of applied potential) clearly show activity for both enzyme reactions and that the rates of both enzyme-catalyzed reactions are pH-dependent (**Figure 16**).

2.3.2.1 Interpreting Waveforms of Coupled Cyclic Voltammograms

The direction for which each enzyme is coupled to FNR is dependent on the dominant reaction it performs: wildtype IDH1 **Figure 16A–D** performs isocitrate oxidation using $NADP^+$ (yielding an oxidation current), while the two IDH1 single-mutant variants, IDH1 R132H and IDH1 R132C (**Figure 16E–H** and **I–L**, respectively), catalyze the reduction of 2OG using NADPH (yielding a reduction current). Notably, unlike the background voltammograms (black traces) which show clear $NADP^+$/NADPH peaks resulting from the 30 μM NADP(H) becoming depleted locally at the electrode, IDH1-FNR coupled current is observed as catalytic waves—substrate depletion is not observed because the measured current is now dependent on the IDH1 substrate concentration (millimolar levels) while the NADPH (present at micromolar levels) is rapidly recycled within the electrode pores.

It had been noted for other enzymes in the e-Leaf, studied over several years, that coupled E2-FNR stationary cyclic voltammograms sometimes yielded potential-dependent (roughly linear) waves and sometimes sigmoidal waves (no significant potential-dependence), but the reasons for these differences were unknown. While applying

different enzyme loading ratios (i.e., how much FNR vs IDH1 was loaded onto the electrode), I made the important observation that changing the amount of each enzyme loaded resulted in changes to the shape of the coupled trace. This relationship implies that the different catalytic waveforms are dependent on the degree to which the coupled current is limited by the overall turnover rate of either FNR or E2. Subsequent experiments revealed that a system limited by FNR turnover will show coupled current waveforms with linear potential dependence, i.e., increasing the applied overpotential increases current, as is the case for the wildtype IDH1 experiments (**Figure 16A–D**). In contrast, a system limited by E2 turnover will display a sigmoidal coupled current (no potential dependence) as is seen for both of the IDH1 variants (**Figure 16E–L**).[26] This relationship between the shape of the coupled voltammogram and the rate-limiting enzyme was subsequently confirmed definitively by experiments using a different E2 enzyme, alcohol dehydrogenase, in the e-Leaf.[57]

Due to the large differences in the turnover rates of each IDH1 enzyme,[40] four-fold more FNR was loaded onto the electrode for wildtype experiments (FNR/$IDH1_{WT}$; 2/1) compared to those for the variants (FNR/$IDH1_{R132H/C}$; 1/2), meaning there was less wildtype enzyme in the electrode even though the initial number of moles of each IDH1 enzyme loaded was the same (a method for quantifying IDH1 in the electrode confirms this, see **Chapter III**). This adjustment was necessary because more FNR was required to match the high rate of substrate turnover by the wildtype compared to variants. Experiments with higher IDH1 variant loading ratios (same amount of R132H/C but less FNR) gave enhanced but more FNR-limited coupled current as well as lower total FNR coverages in the electrode, implying that there is competition between enzymes for space within the electrode pores and emphasizing the importance of enzyme loading ratios despite the final amount of IDH1

enzyme loaded in the electrode being unknown.

2.3.2.2 IDH1 Double Mutant Variant Voltammetry

Cyclic voltammetry experiments were also performed using the double mutant IDH1 variant, IDH1 R132H/S280F (**Figure 17**), which shows resistance to the FDA-approved drug, Ivosidenib, that inhibits the single mutant IDH1 variants (IDH1 R132H/C).[40,58] These experiments demonstrate that the double mutant variant is able to carry out 2OG reduction at a higher rate than either of the single mutants variants as can be seen by comparing both the shapes of the CVs (double mutant exhibits greater potential dependence and is thus more FNR-limited) and the magnitude of the coupled catalytic currents.

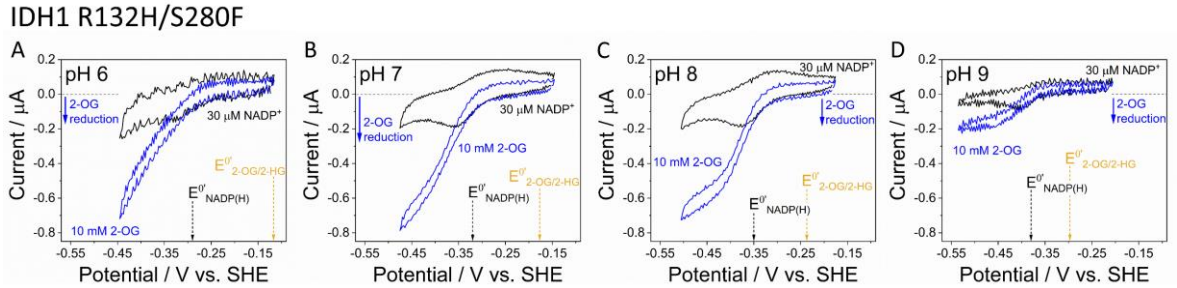


Figure 17. Cyclic voltammograms of the double mutant IDH1 variant, IDH1 R132H/S280F at different pH. Experiments were performed using a 0.03 cm^2 FNR@ITO/PGE stationary electrode. Conditions: 0.03 cm^2 (FNR+IDH1$_{R132H/S280F}$)@ITO/PGE stationary electrode, 1 mV s^{-1}, 25 °C, 60 mM mixed buffer (20 mM of each: MES, TAPS, CHES), 10 mM $MgCl_2$, 30 μM $NADP^+$,10 mM 2-oxoglutarate, 4 mL volume. Enzyme loading ratios (molar): FNR/IDH1$_{R132H/S280F}$; 1/2.

2.3.2.3 Thermodynamic vs Kinetic pH Bias of IDH1 Catalysis

Because wildtype IDH1 and the variants are coupled to NADP(H) in opposite directions, the thermodynamically expected pH bias of the wildtype reaction is also opposite of that for the variants. The reaction driving force in each direction depends on the gap (ΔE) between the reduction potentials of $NADP^+$/NADPH and the 2OG/isocitrate and 2OG/2HG

redox couples. Because the reduction potentials of $2e^-$, $2H^+$ redox reactions (most organic redox reactions including 2OG/2HG) are affected by pH differently than $NADP^+$/NADPH, which is $2e^-$, $1H^+$, reactions coupled to NADP(H) more strongly thermodynamically favor oxidation at higher pH, while low pH values more strongly thermodynamically favor reduction reactions (**Figure 18**). Notably, the 2OG/isocitrate redox couple is $2e^-$, $1H^+$ above pH = 6.4 but changes to a $2e^-$, $2H^+$ reaction below pH = 6.4 (see **Figure 23** for further details).

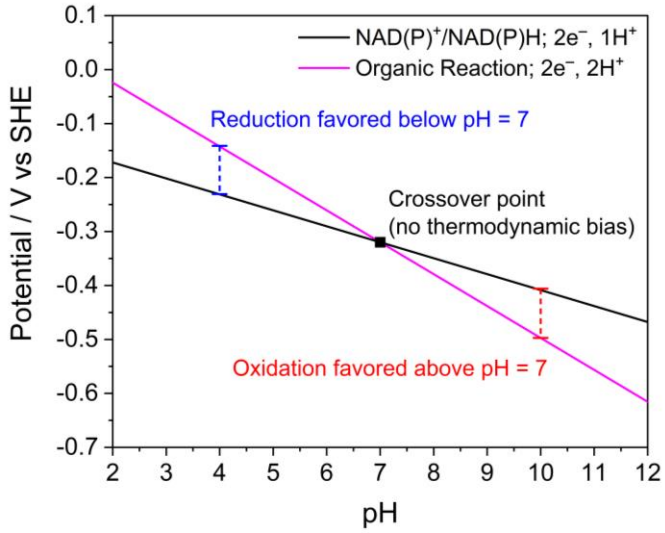


Figure 18. Pourbaix diagram showing the different potential/pH relationships for $NAD(P)^+$/NAD(P)H versus that for a generic organic redox reaction with a formal reduction potential that is equal to the $NAD(P)^+$/NAD(P)H redox couple at pH = 7 ($E^{0'}$ = –0.32 V vs SHE). As defined by the Nernst equation, reduction potentials for $2e^-$, $1H^+$ reactions decrease by ~30 mV per increase in pH unit, while $2e^-$, $2H^+$ reactions decrease by ~60 mV per increase in pH unit. The result is that reversible organic reactions coupled to NADP(H) will more strongly thermodynamically favor oxidation at higher pH and reduction at lower pH—note that enzyme *kinetics* will not always reflect this thermodynamic rule due to properties of the enzyme at different pH.

Figure 16 and **Figure 17**, which note the reduction potentials for the reactions at each pH, show that these predictions (oxidation favored at high pH; reduction favored at low pH) are largely borne out based on the differences in the magnitude of the coupled currents. Interestingly, the wildtype IDH1 current is higher at pH 8.0 and 9.0 compared to pH 7.0 despite no change in ΔE between the 2OG/isocitrate and $NADP^+$/NADPH redox couples

above pH 6.4 (i.e., faster isocitrate oxidation turnover is observed despite there being no increase in the thermodynamic driving force).

To compare to the results with wildtype and R132H IDH1 using the e-Leaf, enzyme assays were carried out in dilute solution at different pH (**Figure 19**). The overall trends are the same as the e-Leaf data, showing increasing activity at higher pH for the wildtype and at

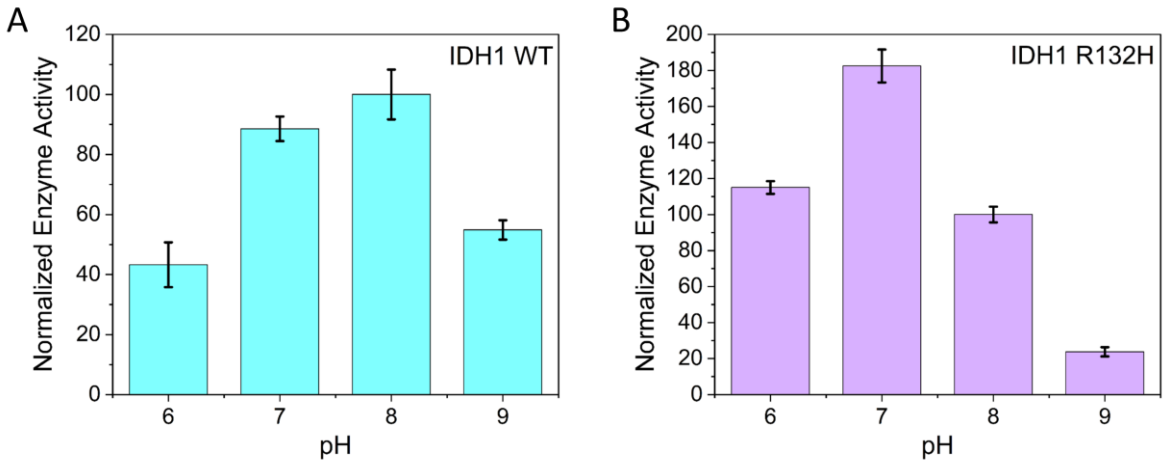


Figure 19. Spectrophotometric solution assays showing the effect of pH on the catalytic rate of wildtype IDH1 (A) and IDH1 R132H (B) coupled to $NADP^+$ and NADPH, respectively. Rates were normalized to the activity at pH 8 for each enzyme. Error bars represent the standard deviation of three technical replicates. Note: these experiments were carried out by Raphael Reinbold.

lower pH for R132H. However, the extreme pH values (pH 9 for wildtype and pH 6 for R132H) disagree with the expected trends indicating an optimal pH value for each enzyme-catalyzed reaction. This trend break is also visible in the e-Leaf data for the IDH1 variants at pH 6 (**Figure 16E, I**) but not for wildtype IDH1 at pH 9 (**Figure 16D**). This difference is explained by the fact that the currents measured for the wildtype voltammograms are limited by the turnover rate of FNR—this is known from the steep potential dependence of the wildtype traces compared to the plateaued currents for the IDH1 variant traces. Importantly, more FNR adsorbs to an ITO electrode at higher pH;[18] therefore, for an FNR-limited system, greater current is measured at pH 9 even though the maximum

turnover rate of the wildtype enzyme is lower at pH 9 as is seen from the experiments carried out in dilute solution (**Figure 19A**).

2.3.3 Wildtype IDH1 as a Reversible Electrocatalyst

Although it is known that wildtype IDH1 carries out the bidirectional oxidative decarboxylation of isocitrate, it is experimentally difficult to measure the reverse reaction (reductive carboxylation) under controlled conditions due to the need to supply CO_2 in situ and the strong effect that dissolved CO_2 has on pH (which significantly influences the thermodynamics/kinetics of NADP(H)-dependent enzyme reactions as shown in the previous section (**Figure 16, Figure 19**)).

Electrochemical methods are ideally suited for studying bidirectional enzymes because both thermodynamic and kinetic information can be efficiently extracted directly from the data.[4,7,59,60] For example, the reaction equilibrium point of a cyclic voltammogram, represented as the zero current (crossover) potential, is equivalent to the formal reduction potential of the reaction (E^{0}') when the ratio of oxidized/reduced substrate is 1/1.[4] If the reaction is thermodynamically biased toward either oxidation or reduction, the oxidized/reduced substrate ratio need only be adjusted until the oxidation and reduction currents are roughly equivalent; the formal reduction potential can then be calculated from the equilibrium (crossover) potential using the Nernst equation.[26] The e-Leaf, which extends electrochemical methods to non-electroactive enzymes such as IDH1, offers a further advantage for investigating difficult-to-study reactions requiring in situ production of a (co)substrate: other enzymes can be loaded into the electrode nanopores alongside the enzyme(s) of interest in order to produce the required (co)substrate inside the electrode.[1,26]

2.3.3.1 Electrochemically Driving and Measuring IDH1-catalyzed Reductive Carboxylation

To measure the reductive carboxylation reaction catalyzed by IDH1, carbonic anhydrase (CA), a highly active Zn^{2+} enzyme which interconverts bicarbonate and carbon dioxide, was co-loaded into the electrode nanopores alongside FNR and IDH1. In the presence of bicarbonate (100 mM) in the buffered reaction solution, CO_2 was produced in situ in the electrode, and wildtype IDH1 reduction activity (2OG and CO_2 to isocitrate) was able to be measured without significantly affecting the pH during the reaction (the pH was measured before and after experiments to confirm) (blue trace, **Figure 20**). Following addition of isocitrate to the reaction buffer, 2OG reductive carboxylation activity was no longer observed as the enzyme began to catalyze the thermodynamically favored isocitrate

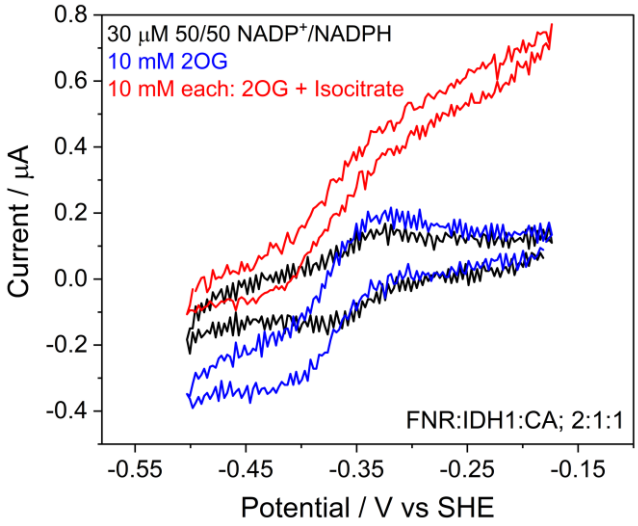


Figure 20. Cyclic voltammogram showing both wildtype IDH1 reactions: reductive carboxylation of 2OG to isocitrate (blue trace) and oxidative decarboxylation of isocitrate to 2OG (red trace). The black trace shows background NADP(H) cycling (oxidation and reduction) catalyzed by FNR. To facilitate IDH1-catalyzed 2OG reductive carboxylation, carbonic anhydrase (CA) was co-loaded in the electrode alongside IDH1 and FNR to supply CO2 in situ (blue trace). The addition of an equal concentration of isocitrate (i.e., [2OG]/[isocitrate]; 1/1) to the reaction solution completely eliminates any measured 2OG reduction activity catalyzed by IDH1 (isocitrate oxidation is the dominant reaction). Conditions: stationary (FNR+IDH1+CA)@ITO/PGE electrode, electrode area 0.06 cm^2, scan rate 1 mV s^{-1}, temperature 25°C, volume 4 mL, 10 mM $MgCl_2$, 15μM $NADP^+$, 15μM NADPH, pH = 7.5 (HEPES and $NaHCO_3$ at 0.10 M), enzyme loading ratios (molar): FNR/IDH1/CA; 2/1/1.

oxidation reaction (red trace, **Figure 20**). Note that the blue trace in **Figure 20**, showing IDH1-catalyzed 2OG reductive carboxylation, has an oxidation peak (at a potential just positive of –0.35 V) that is greater than the background $NADP^+$/NADPH turnover peaks (black trace); this difference is due to the IDH1 enzyme reoxidizing the isocitrate produced during the reductive scan that remained at the surface/inside the nanopores of the *stationary* electrode. Repeat experiments with more active IDH1 electrodes showed even larger isocitrate oxidation peaks even though no isocitrate had been added (**Figure 21**), demonstrating the strong bias of wildtype IDH1 for catalyzing isocitrate oxidation over 2OG reductive carboxylation.

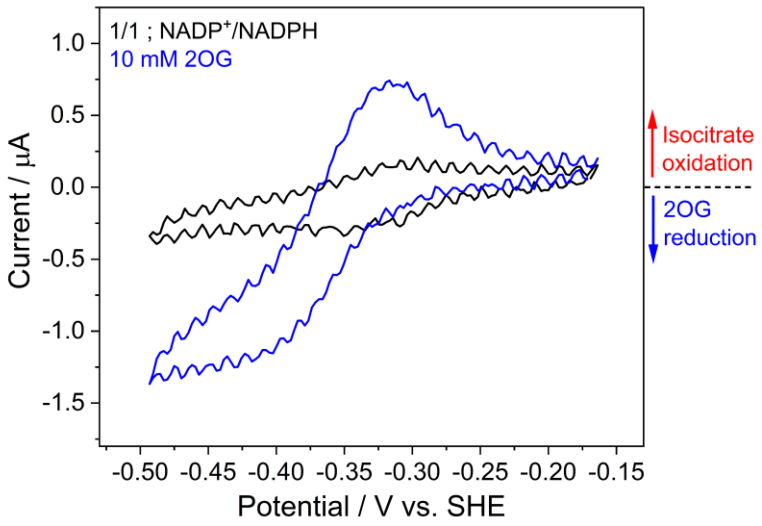


Figure 21. Stationary cyclic voltammogram showing the strong bias of wildtype IDH1 for catalyzing isocitrate oxidation over 2OG reductive carboxylation. Conditions: stationary (FNR+IDH1+CA)@ITO/PGE electrode, electrode area 0.06 cm^2, scan rate 1 mV s^{-1}, temperature 25°C, volume 4 mL, 10 mM $MgCl_2$, 10 mM 2OG, 15µM $NADP^+$, 15µM NADPH, pH = 7.6 (HEPES and $NaHCO_3$ at 0.10 M), enzyme loading ratios (molar): FNR/IDH1/CA; 2/1/1.

2.3.3.2 Determining the Formal Reduction Potential of the 2OG, CO_2/Isocitrate Reaction

A reversible cyclic voltammogram, showing roughly equal oxidation and reduction currents, was obtained for wildtype IDH1 by slowly titrating isocitrate into solution after 2OG reductive carboxylation activity had been established (**Figure 22**). Notably, a 50/1; 2OG/isocitrate ratio was required to achieve roughly equal oxidation and reduction currents indicating the strong bias of IDH1 for catalyzing isocitrate oxidation. Altering the oxidized/reduced substrate ratio to drive reversible catalysis has the effect of shifting the

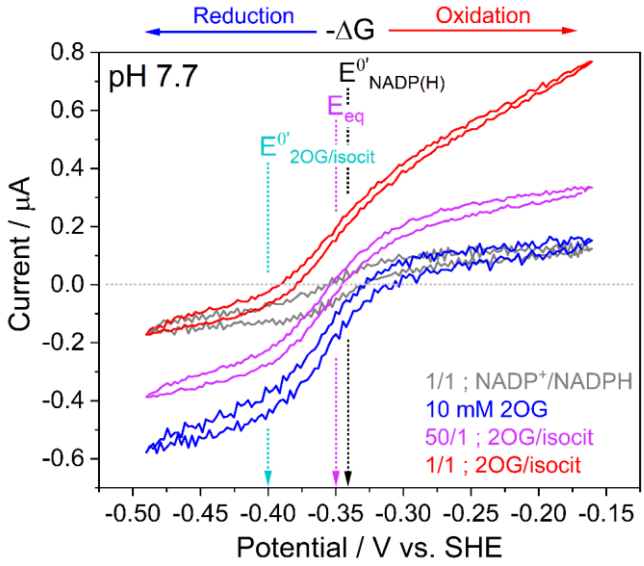


Figure 22. Cyclic voltammetry measuring the bidirectionality of IDH1-catalyzed 2OG/isocitrate interconversion at different 2OG/isocitrate ratios. Conditions: electrode area 0.03 cm^2, scan rate 1 mV s^{-1}, temperature 25°C, volume 4 mL, 10 mM $MgCl_2$. (FNR+IDH1+CA)@ITO/PGE electrode, 15µM $NADP^+$, 15µM NADPH; HEPES and $NaHCO_3$ at 0.10 M (pH = 7.7); electrode rotated at 1000 rpm. Magenta trace: 10 mM 2OG + 200 µM isocitrate; red trace: 10 mM each: 2OG, isocitrate. Enzyme loading ratios (molar): FNR/IDH1/CA; 4/2/1

equilibrium (crossover) potential of the cyclic voltammogram close enough to the $NADP^+$/NADPH redox couple such that it cuts through the zero-current line (x-axis) sharply and without inflection. Using the Nernst equation, which takes into account the oxidized/reduced substrate ratio, the formal reduction potential of the 2OG, CO_2/isocitrate

reaction (E^{0}'$_{2OG/isocit}$) was calculated, using the equilibrium potential, to be –0.40 V vs SHE at pH = 7.7 and under the condition of in situ CO_2 production by carbonic anhydrase. A repeat experiment gave a formal potential of the same value with an error of roughly 1 mV. The 2OG/isocitrate formal reduction potential is thus 60 mV more negative than the $NADP^+$/NADPH reduction potential of –0.34 V at pH = 7.7, indicating a thermodynamic bias (ΔG = –11.6 kJ mol^{-1}) for the oxidation of isocitrate in agreement with other experiments.

2.3.4 Thermodynamics Governing the Production of 2-hydroxyglutarate

Having established the reversibility of wildtype IDH1 and measured the formal reduction potential for the 2OG/isocitrate reaction, experiments were carried out to do the same for the IDH1 variant neomorphic reaction (2OG/2HG) with the goal of determining the conditions under which the oncometabolite 2HG would be produced and persist in cells possessing an IDH1 variant enzyme. However, the 2HG oxidation reaction could not be measured either electrochemically using the e-Leaf or spectroscopically in homogeneous solution despite several attempts using high $NADP^+$ and IDH1 variant concentrations. This result is consistent with the fact the oxidation of 2HG to 2OG using $NAD(P)^+$ is not observed biologically; instead, a flavoenzyme, *D*-2HG dehydrogenase (D2HGDH), is required to catalyze the oxidation of 2HG to 2OG in vivo.[44,56,61] Together, these facts imply that the reduction potential of the 2OG/2HG redox couple must be much more positive than the $NADP^+$/NADPH couple (i.e., $NADP^+$ is not a strong enough oxidant to efficiently drive 2HG oxidation).

Because IDH1 R132H could not be driven reversibly, a formal reduction potential of −0.177 V vs SHE was calculated for the 2OG/2HG reaction using solution-based equilibrium data.[55,56] Using these data, along with the measured 2OG/isocitrate formal potential (**Figure 22**) and the well-known chemistry of NAD(P)(H), a Pourbaix diagram (potential vs pH plot) was constructed across the pH range 6–9, assuming a $2e^-/2H^+$ ratio (−60 mV/pH slope) for the 2OG/2HG reaction and a $2e^-/1H^+$ ratio (–30 mV/pH slope) for the 2OG/isocitrate and $NADP^+$/NADPH reactions (**Figure 23**). Note that the slope of the 2OG/isocitrate line shifts from –30 mV/pH to –60 mV/pH at pH = 6.4: this is due to one of

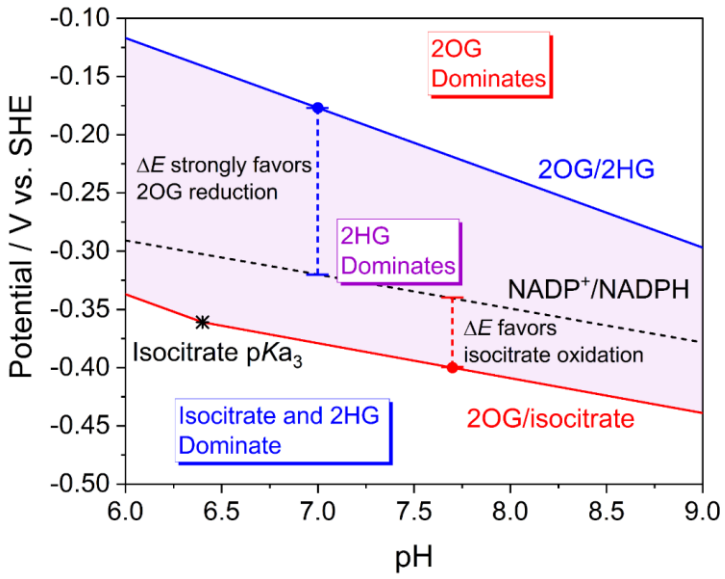


Figure 23. Pourbaix diagram showing the species that are stable in different regions of potential and pH. The central shaded region shows conditions where isocitrate will be spontaneously converted to 2HG. The slope of the 2OG/isocitrate reaction increases to −60 mV/pH below pH 6.4 as it becomes a $2e^-/2H^+$ reaction: the third isocitrate carboxylate group becomes protonated whereas 2OG is a dianion above pH 4.8. The Δ*E* values show the thermodynamic driving force for 2OG reduction or isocitrate oxidation when coupled to NADPH oxidation or $NADP^+$ reduction, respectively.

the carboxylate groups of isocitrate becoming protonated (pKa_3 = 6.4) whereas 2OG is a dianion above a pH of 4.8 (i.e., the 2OG/isocitrate reaction becomes $2e^-/2H^+$ from pH 4.8−6.4).

The Pourbaix diagram (**Figure 23**) shows the thermodynamic relationships between each of the redox reactions, i.e., which reactions are favorable and thus which redox species should be stable in different regions of potential and pH. For example, within a cell containing only wildtype IDH1, isocitrate will be spontaneously oxidized to 2OG, and 2OG will be stable at potentials above the 2OG/isocitrate potential couple (red line). However, the introduction (via mutation) of a 2HG-forming IDH1 variant into a cell changes the redox potentials at which 2OG is thermodynamically stable; in this case, 2OG is only stable above the 181 mV more positive 2OG/2HG potential couple (blue line), and 2HG dominates below the 2OG/2HG (blue) line. In other words, the very positive potential of the 2OG/2HG redox couple means that both 2OG and isocitrate will be spontaneously converted to 2HG, mediated by NADP(H), with free energy (ΔG) values (at pH = 7) of –27.6 kJ mol^{-1} for the reduction of 2OG to 2HG using NADPH and –39.0 kJ mol^{-1} for the overall conversion of isocitrate to 2HG (the isocitrate to 2HG reaction is redox neutral). The purple shaded region in the diagram indicates the regions of potential and pH where isocitrate will be spontaneously converted to 2HG. Based on the intracellular potential of a living cell typically being more negative than –0.2 V at neutral pH,[62] these results indicate that 2HG should be spontaneously produced and accumulate in living cells whenever an IDH1 variant is present.

2.3.5 Measuring Isocitrate Oxidation Catalyzed by IDH1 Variants

2.3.5.1 Decoupling Isocitrate Oxidation from 2OG Reduction

Production of 2HG from isocitrate occurs via a redox-neutral cascade reaction that involves but does not consume $NADP^+$: isocitrate is oxidized to 2OG using $NADP^+$, producing NADPH, which is oxidized back to $NADP^+$ when 2OG is reduced to 2HG

(**Scheme 5**). Importantly, the IDH1 variant enzymes retain some of their wildtype isocitrate oxidation activity, albeit at a reduced rate,[35,39,40] meaning they can perform the full cascade reaction independent of the wildtype enzyme. Although it is known that the variant IDH1 enzymes perform isocitrate oxidation, the second reaction (2OG reduction) is faster than the first reaction (isocitrate oxidation) making it very difficult to measure rates of isocitrate oxidation independently—measuring NADPH formation using UV/Vis spectroscopy or 2OG formation by NMR both show NADPH and 2OG as low-concentration intermediates during catalysis[40] and thus rates cannot be obtained.

Taking advantage of the unique ability of the e-Leaf to rapidly regenerate NADP(H) locally within the electrode nanopores while simultaneously monitoring activity, an experiment was conducted to see if the two IDH1 variant reactions could be decoupled (**Figure 24**). As shown in **Figure 24**, the addition of 10 mM isocitrate produces a small increase in oxidation current positive of the $NADP^+$/NADPH couple, confirming the ability

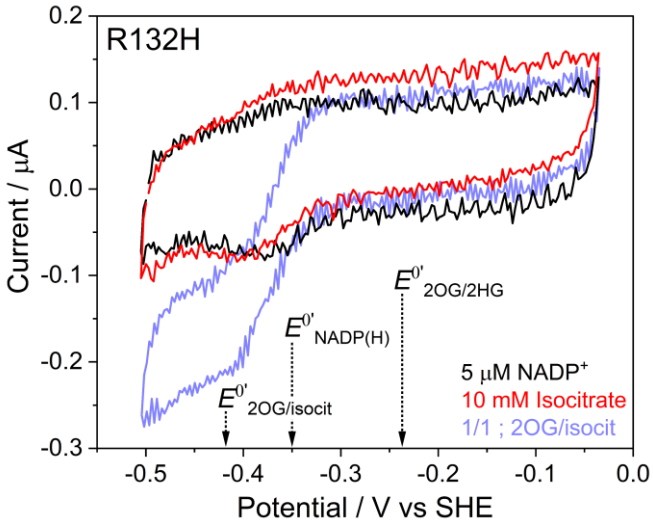


Figure 24. Cyclic voltammogram showing the ability of IDH1 R132H to catalyze isocitrate oxidation. Conditions: 0.03 cm^2 FNR@ITO/PGE RDE electrode, 25 °C, 4 mL volume, 10 mM $MgCl_2$, 5 µM $NADP^+$, pH 8 (20 mM each: MES, TAPS, CHES). Molar enzyme loading ratio: $FNR/IDH1_{R132H}$; 2/5.

of IDH1 R132H to oxidize isocitrate. This experiment also indicates that the NADPH intermediate (formed from isocitrate oxidation) must be released by R132H between cycles of isocitrate oxidation and 2OG reduction otherwise no oxidation activity would be observed. Addition of an equal amount of 2OG then results in a much larger reduction current negative of the $NADP^+$/NADPH potential, demonstrating the strong bias of the enzyme for catalyzing the neomorphic reduction reaction. The ability to separately measure IDH1 R132H-catalyzed oxidation of isocitrate to 2OG is possible because any NADPH formed and released from the R132H enzyme is immediately reoxidized by an adjacent FNR molecule (measured as current) when an oxidizing potential is applied to the electrode, i.e., NADPH is removed from the system by the much faster FNR as quickly as it is formed by R132H. Under these conditions, the rate of isocitrate oxidation by IDH1 R132H (without 2OG present) is approximately 18% the rate of 2OG reduction with 1/1; 2OG/isocitrate present (**Figure 24**). Significantly, this result indicates that IDH1 R132H is much better at performing the wildtype reaction than a previous study that had attempted to measure isocitrate oxidation using spectroscopic methods which concluded that the rate of isocitrate oxidation was only ~3.7% that of the rate of 2OG reduction.[39] This difference highlights the fact that standard methods are unreliable for measuring the rates of IDH variant-catalyzed isocitrate oxidation (or the formation of any cascade intermediate where the rate-limiting step is not dramatically slower than all other steps) for the reasons aforementioned. Despite showing that isocitrate oxidation is more efficient than previously reported, the experiment confirms that IDH1 R132H reduces 2OG at a higher rate than it oxidizes isocitrate, preventing 2OG and NADPH from accumulating and instead resulting in the accumulation of the oncometabolite 2HG.

2.3.5.2 Understanding the Effects of Different Mutations on IDH1 Catalysis

After establishing that the two IDH1 variant reactions could be decoupled using the e-Leaf, the same experiment was performed with several other cancer-associated IDH1 variants to investigate the effect of different mutations on the rates at which each variant carries out the two reactions. **Figure 25** shows cyclic voltammograms for four IDH1 variants (including R132H, which was repeated) catalyzing isocitrate oxidation under identical conditions. Rates of isocitrate oxidation (red traces) are clearly visible as catalytic waves above the background NADP(H) turnover peaks (black traces) and positive of the

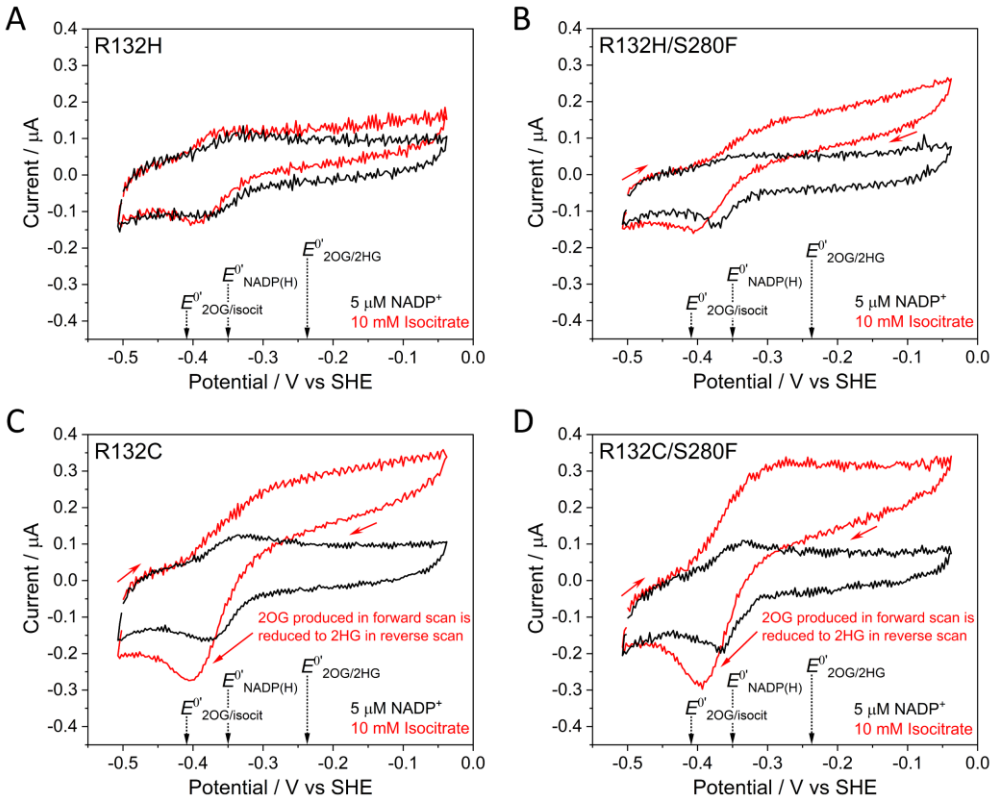


Figure 25. Stationary cyclic voltammograms showing the rates at which four different IDH1 variants catalyze the wildtype isocitrate oxidation reaction. Note that the peak negative of the $NADP^+$/NADPH redox potential (in the reverse scan of the red traces) is due to reduction of 2OG which was formed from the oxidation of isocitrate during the forward scan. Conditions: stationary (FNR+vIDH1)@ITO/PGE electrode, electrode area 0.03 cm^2 , scan rate 1 mV s^{-1}, temperature 25 °C, volume 4 mL, pH 8 (20 mM each: MES, TAPS, CHES), 10 mM $MgCl_2$, 5 µM $NADP^+$. Enzyme loading ratios (molar): FNR/vIDH1; 2/5 (vIDH1 represents any of the neomorphic IDH1 variants).

2OG/isocitrate formal reduction potential. Cyclic voltammetry experiments were carried out using a stationary electrode, and peaks negative of the $NADP^+$/NADPH reduction potential (red traces) are clearly visible: these peaks are *not* observed for voltammograms carried out with wildtype IDH1 (**Figure 16A–D**) and are due to the reduction of 2OG (forming 2HG) that remained at the stationary electrode surface/in the electrode pores after being formed during the forward (oxidative) scan. These peaks are especially large for experiments carried out with IDH1 R132C and R132C/S280F (panels C and D) and indicate the strong bias of these variant enzymes for catalyzing 2OG reduction over isocitrate oxidation.

Upon comparing the two single mutant variants, IDH1 R132H and R132C (**Figure 25** panels A and C, respectively), it is clear that IDH1 R132C retains much more wildtype activity, catalyzing isocitrate oxidation 4-fold faster than R132H (**Table 1**). The two single mutant variants, IDH1 R132H and R132C are plotted next to their respective double mutant

Table 1. Comparing Rates of Isocitrate Oxidation vs 2OG Reduction for IDH1 Variants

IDH1 Enzyme	Isocitrate Ox Current/ µA	Isocitrate Ox Rate/ nmoles min^{-1} cm^{-2}	2OG Red Current/ µA	2OG Red Rate/ nmoles min^{-1} cm^{-2}	Ratio Ox vs Red Rates
Wildtype	1.41	14.6	–	–	–
S280F	3.02	31.3	–	–	–
R132H	0.06	0.62	–0.32	3.32	1 : 5.3
R132H S280F	0.19	1.97	–0.77	7.98	1 : 4.1
R132C	0.24	2.49	–0.57	5.91	1 : 2.4
R132C S280F	0.24	2.49	–1.27	13.2	1 : 5.3
R132S	0.49	5.08	–0.49	5.08	1 : 1.0

Note: Currents represent the maximum coupled currents measured by stationary cyclic voltammetry with the background current subtracted out. Values were obtained from **Figure 25**–**Figure 28**.

variant equivalents, R132H/S280F and R132C/S280F. Understanding the effect of the S280F mutation on IDH1 catalysis (for both reactions) is of great interest because this mutation confers resistance to the FDA-approved inhibitor, Ivosidenib, and has been observed to emerge spontaneously in tumors with little known about the effect it has on the biochemistry of the IDH1 enzymes.[40,58,63,64] Interestingly, the S280F substitution only appears to increase the rate of isocitrate oxidation for the R132H variant (3-fold increase in rate), while the R132C variant oxidizes isocitrate at roughly the same rate as the R132C/S280F variant (**Table 1**).

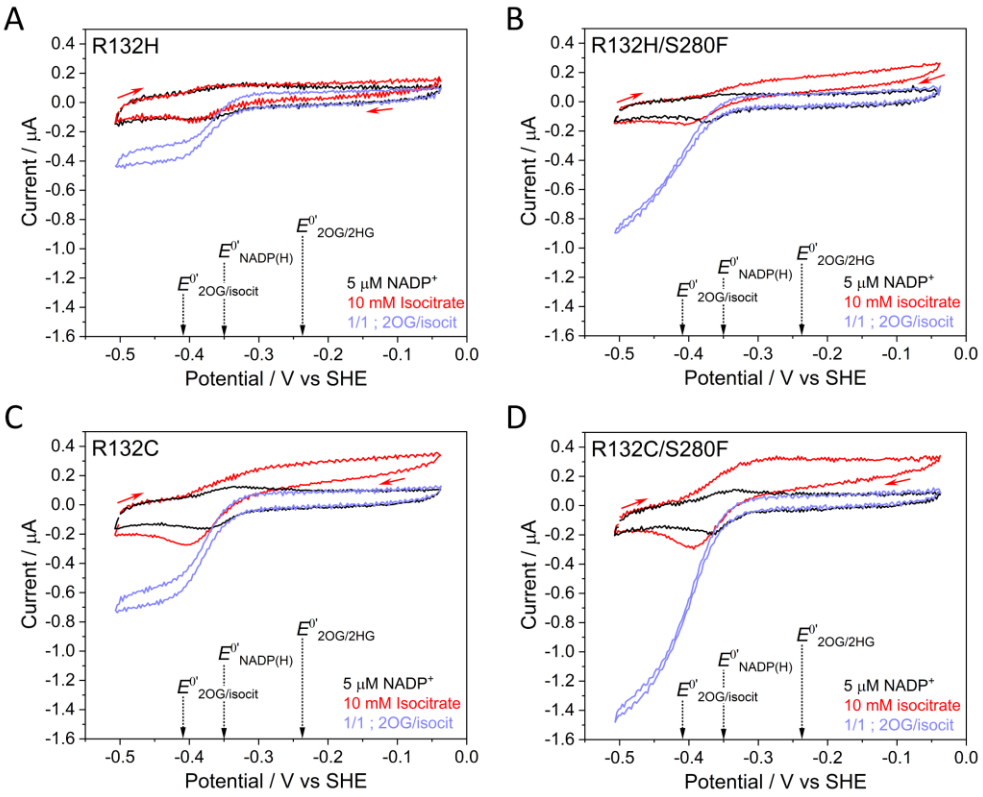


Figure 26. Stationary cyclic voltammograms showing the rates at which four different IDH1 variants catalyze isocitrate oxidation vs 2OG reduction. Purple traces (1/1; 2OG/isocitrate) correspond to reactions with 10 mM 2OG + 10 mM isocitrate. Conditions: stationary (FNR+vIDH1)@ITO/PGE electrode, electrode area 0.03 cm^2, scan rate 1 mV s^{-1}, temperature 25 °C, volume 4 mL, pH 8 (20 mM each: MES, TAPS, CHES), 10 mM $MgCl_2$, 5 µM $NADP^+$. Enzyme loading molar ratios: FNR/vIDH1; 2/5 (vIDH1 represents any of the neomorphic IDH1 variants). Note that the 2OG reduction reaction is not inhibited by the presence of isocitrate.

Figure 26 reshows the data in **Figure 25** with an additional trace recorded for each experiment after injecting 10 mM 2OG (final concentration) into the reaction solution. In the presence of 2OG, isocitrate oxidation is no longer observed; instead, large catalytic waves, due to 2OG reduction to 2HG, appear at potentials negative of the $NADP^+$/NADPH formal potential (**Figure 26**). Similar to isocitrate oxidation, rates of 2OG reduction are faster for IDH1 R132C compared to IDH1 R132H (but to a lesser extent). Significantly, the S280F mutation results in a large increase in the rate of 2OG reduction relative to both single mutant variants: IDH1 R132H/S280F and R132C/S280F reduce 2OG 2.4-fold and 2.2-fold faster than IDH1 R132H and R132C, respectively (**Figure 26**, **Table 1**). Interestingly, the S280F mutation alone (without R132H or R132C) also significantly enhances the rate of isocitrate oxidation compared to the wildtype (**Figure 27**, **Table 1**). Neither the wildtype nor the IDH1 S280F variant reduce 2OG to 2HG at an appreciable rate. Though it is beyond the scope of this thesis, insight from these experiments helped to uncover the mechanism by which the

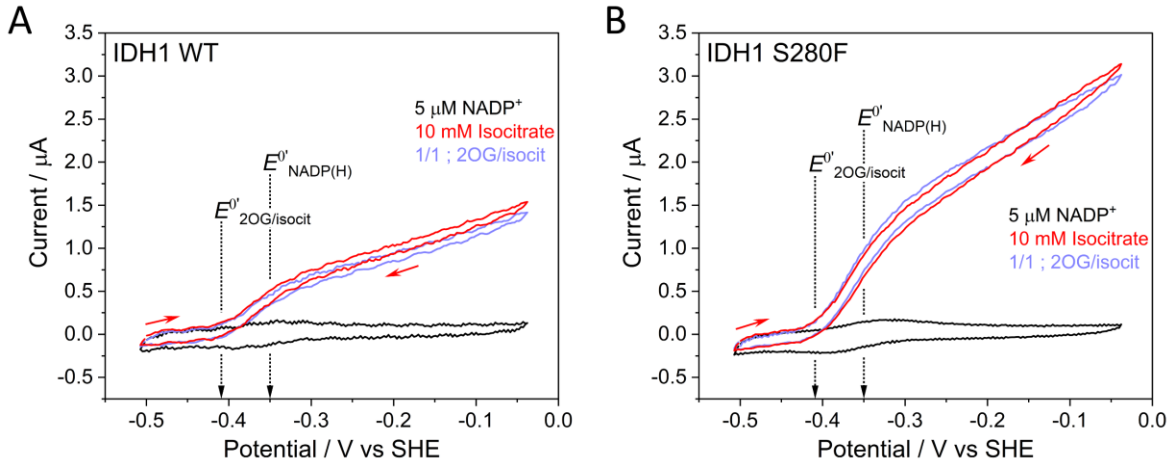


Figure 27. Stationary cyclic voltammograms measuring the ability of wild-type IDH1 and IDH1 S280F to catalyze the oxidation of isocitrate. Purple traces (1/1; 2OG/isocitrate) correspond to reactions with 10 mM 2OG + 10 mM isocitrate—note that isocitrate oxidation is not inhibited by the presence of 2OG. Conditions: stationary (FNR+IDH1)@ITO/PGE electrode, electrode area 0.03 cm^2, scan rate 1 mV s^{-1}, temperature 25 °C, volume 4 mL, pH 8 (20 mM each: MES, TAPS, CHES), 10 mM $MgCl_2$, 5 μM $NADP^+$. Enzyme loading molar ratios: $FNR/IDH1_{WT}$ or $IDH1_{S280F}$; 8/1.

second site mutation (S280F) increases the rate of formation of the oncometabolite, 2HG, compared to the single mutant variants and how Ivosidenib resistance is achieved.[40]

A less commonly occurring cancer-associated single mutant IDH1 variant, IDH1 R132S,[46] was also tested (**Figure 28**). Like IDH1 R132H and R132C, the R132S variant performs the neomorphic 2OG reduction reaction. Interestingly, the R132S variant retained the most wildtype activity of all neomorphic variants, catalyzing isocitrate oxidation at a rate

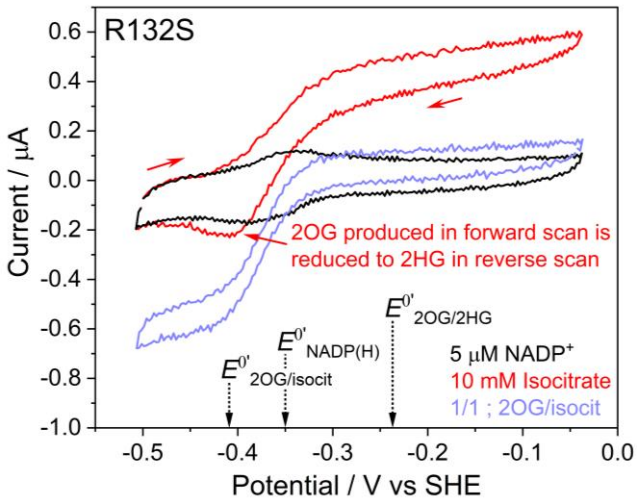


Figure 28. Stationary cyclic voltammogram showing the rates at which IDH1 R132S catalyzes isocitrate oxidation vs 2OG reduction. Purple traces (1/1; 2OG/isocitrate) correspond to reactions with 10 mM 2OG + 10 mM isocitrate. Conditions: stationary (FNR+IDH1$_{R132S}$)@ITO/PGE electrode, electrode area 0.03 cm^2 , scan rate 1 mV s^{-1}, temperature 25 °C, volume 4 mL, pH 8 (20 mM each: MES, TAPS, CHES), 10 mM $MgCl_2$, 5 µM $NADP^+$. Enzyme loading molar ratios: FNR/IDH1$_{R132S}$; 2/5. Note that the 2OG reduction reaction is not inhibited by the presence of isocitrate.

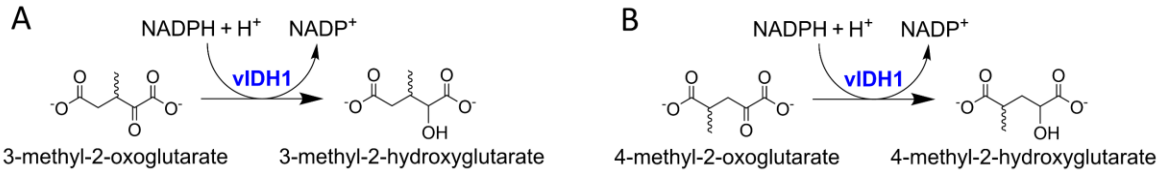
more than 2-fold greater than any other neomorphic IDH1 enzyme (**Table 1**). Notably, the red trace in **Figure 28**, for which only $NADP^+$ and isocitrate are present, has a much smaller peak negative of the $NADP^+$/NADPH formal potential resulting from reduction of 2OG formed during the forward scan, i.e., the enzyme is less biased toward catalyzing 2OG reduction compared to other neomorphic IDH1 variants. This was confirmed by the addition of 2OG to the reaction solution (purple trace, **Figure 28**): R132S appears to catalyze

isocitrate oxidation and 2OG reduction with roughly equal efficiency in contrast to every other IDH1 enzyme tested (**Figure 28**, **Table 1**).

2.3.6 IDH1 R132H Reduction of 2OG Derivative Substrates

2.3.6.1 IDH1 R132H is More Active with Some 2OG Derivatives than with 2OG

In addition to measuring rates of IDH1 variant-catalyzed isocitrate oxidation, it was of interest to test if the IDH enzymes can use other substrates which are structurally similar to 2OG and whether such molecules might be competitive inhibitors. A large number of C3 and C4-alkylated 2OG derivatives were synthesized, primarily by Lennart Brewitz of the Chris Schofield group, and tested as substrates against IDH1 R132H, wildtype IDH1/2, and two IDH2 variants.[54] Of these 2OG derivatives, I performed electrochemical experiments testing two derivates as potential substrates of IDH1 R132H: 3-methyl-2-oxoglutarate (3-methyl-2OG) and 4-methyl-2-oxoglutarate (4-methyl-2OG) (**Scheme 6**).



Scheme 6. 2OG derivatives as IDH1 R132H substrates

As shown in **Figure 29**, and confirmed by experiments in homogenous solution,[54] both 3-methyl-2OG and 4-methyl-2OG are substrates of IDH1 R132H and are reduced by NADPH to form methylated 2-hydroxyglutarate analogues (**Scheme 6**). Interestingly, both 2OG derivates yield coupled currents of roughly the same magnitude as 2OG at lower concentrations (2 mM) but give greater currents compared to 2OG at high concentrations of substrate (8 mM) (**Figure 29**). This indicates that both substrates have higher k_{cat} and K_m

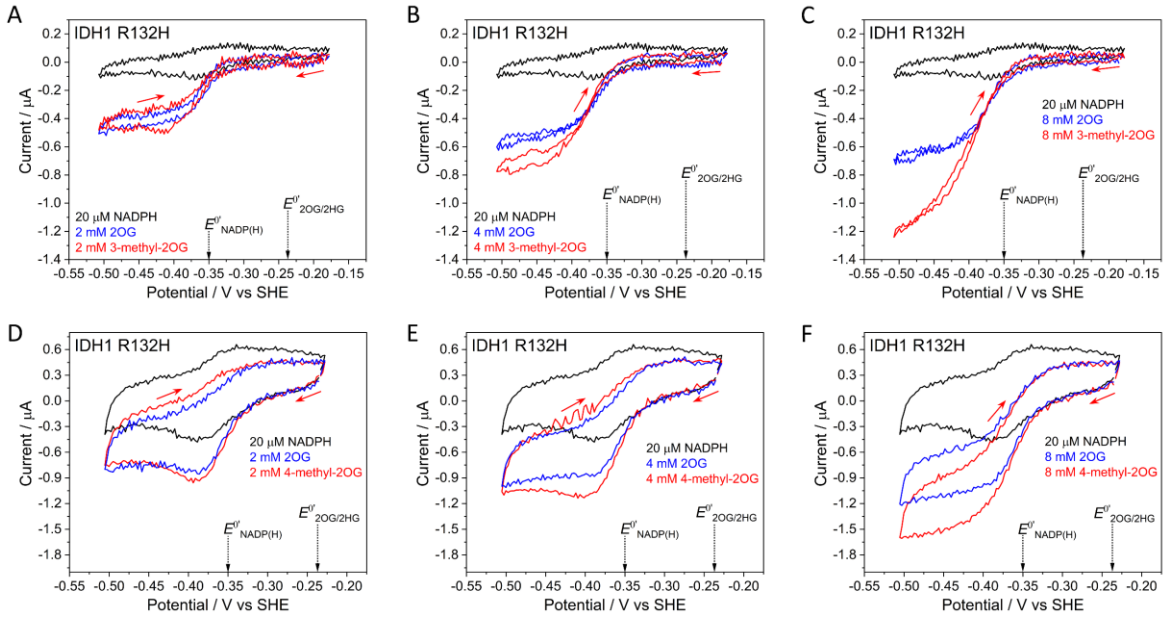


Figure 29. Stationary cyclic voltammetry showing IDH1 R132H activity with 2OG compared with two racemic 2OG derivatives, 3-methyl-2OG (A–C) and 4-methyl-2OG (D–F), at different concentrations (2 mM, 4 mM, 8 mM). Conditions (A–F): Stationary (FNR+IDH1$_{R132H}$)@ITO/PGE electrode, temperature 25 °C, pH = 8 (100 mM HEPES, 150 mM NaCl), 10 mM $MgCl_2$, 20 μM NADPH, 2.5 mL cell volume, Enzyme loading ratios (molar): FNR/IDH1$_{R132H}$; 1/2. (A–C) electrode area 0.03 cm^2, scan rate 1 mV s^{-1}; (D–F) electrode area 0.06 cm^2, scan rate 2 mV s^{-1}. $E^{0\prime}_{NADP(H)}$ and $E^{0\prime}_{2OG/2HG}$ denote formal potentials for the $NADP^+$/NADPH and 2OG/2HG couples, respectively.

values than 2OG, i.e., they are more active substrates than 2OG but have weaker binding affinities. These interesting results, along with solution results testing a further 30 2OG derivatives as substrates,[54] suggest the possibility that IDH1 variants may catalyze other reactions in vivo beyond the established 2OG to 2HG reaction.

2.3.6.2 IDH1 R132H is Enantioselective for 2OG Derivative Substrates

While testing IDH1 R123H activity with the 2OG derivatives in the e-Leaf, I noticed that the 2OG derivatives appeared to deplete more rapidly than 2OG at an equivalent concentration; in other words, during cyclic voltammetry at a stationary electrode, the current would decrease at a faster rate for 2OG derivatives compared to 2OG during the course of each scan (**Figure 30A**). Although surface depletion during stationary cyclic voltammetry is

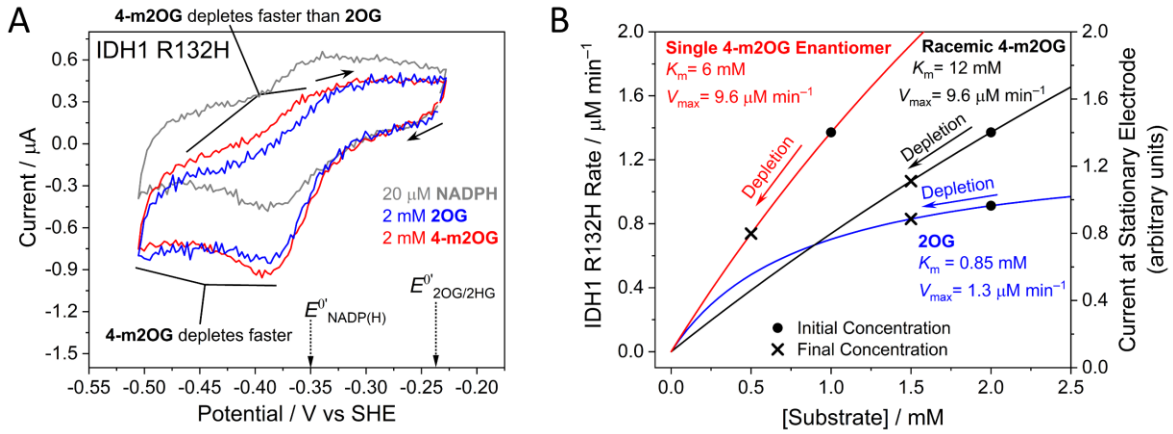


Figure 30. 4-methyl-2OG depletes at the electrode surface much faster than 2OG. (A) Stationary cyclic voltammetry for IDH1 R132H in the presence of 2 mM 2OG and 2 mM of a racemic 2OG derivative, 4-methyl-2OG. 4-methyl-2OG depletes at the electrode surface faster than 2OG at similar current magnitudes: R132H faradaic "coupled" current[26] dropped by 43% for 4-methyl-2OG compared to 10% for 2OG during each scan. (B) Simulated Michaelis-Menten curves showing the expected enzyme activity (or current in arbitrary units) vs [S] based on experimentally determined K_m and V_{max} values for 2OG and racemic 4-methyl-2OG. The "Single 4-m2OG Enantiomer" line shows the expected activity profile if only one 4-methyl-2OG enantiomer is catalytically active. The initial and final concentration values indicate the expected activity (current) for each substrate based on the conditions used in panel A if 500 µM of each substrate was consumed locally at the stationary electrode surface/inside the electrode nanopores during a voltammetric scan. The predicted changes in catalytic rate (Single 4-m2OG Enantiomer: –46%; Racemic 4-m2OG: –22%; 2OG: –9%) agree with the results observed in panel A and suggest that only one 4-methyl-2OG enantiomer is catalytically active with IDH1 R132H.

expected at low substrate concentrations as the *local* substrate concentration decreases at the electrode surface/in the electrode pores as it is consumed, the rates of depletion between two substrates at equivalent concentrations, and at comparable faradaic currents, should be roughly the same. As can be seen in **Figure 30A**, this is not the case. To explain this observation, it was hypothesized that only one enantiomer of the racemic mixture of the 2OG analogues was being consumed by IDH1 R132H (2OG is achiral).

To help test this hypothesis, a simple model was constructed to predict the catalytic rates (and thus electrical current) of both 2OG and 4-methyl-2OG reduction catalyzed by IDH1 R132H at different concentrations using measured Michaelis-Menten values for each substrate[54] (**Figure 30B**). In the case of 4-methyl-2OG, two curves were simulated, one

assuming that both enantiomers exhibited equal activity ("racemic 4-m2OG", black line), and another where only one enantiomer was active ("single 4-m2OG enantiomer", red line). Looking at the rate vs [S] curves in **Figure 30B**, it is apparent that a decrease in substrate concentration will have a much larger effect on the enzyme turnover rate (electrical current) if only one 4-methyl-2OG enantiomer is active, as can be seen if a hypothetical 500 µM of substrate is consumed (locally at the electrode surface/inside the pores) in each case. In the cyclic voltammetry experiment, the IDH1 R132H faradaic "coupled" current dropped by 43% for 4-methyl-2OG during the course of the scan compared to only a 10% drop in activity for 2OG even though the peak magnitudes of the coupled currents were roughly the same (**Figure 30A**). The simulated Michaelis-Menten curves (**Figure 30B**) show that the expected enzyme activity (current at a stationary electrode) should decrease by the following percentages if a hypothetical 500 µM substrate is consumed locally at the electrode surface: 46% for a single active 4-methyl-2OG enantiomer, 22% if both 4-methyl-2OG enantiomers are active, and 9% for 2OG. Overall, the electrochemical results with both 2OG derivatives fit much better with the single enantiomer hypothesis; further experiments in dilute solution reinforce this by showing that only half of each 2OG derivative tested was consumed and that a single diastereomer product was obtained even in the presence of excess NADPH.[54]

2.3.6.3 Observation of Substrate Competition Between 2OG and 3-methyl-2OG

Having shown that 2OG derivatives can be better substrates for IDH1 R132H compared to 2OG, an experiment was carried out to test whether substrate competition could be observed between 2OG and a 2OG derivative (**Figure 31**). First, a background trace was recorded with only 20 µM NADPH present in the reaction solution (black trace); 2OG was

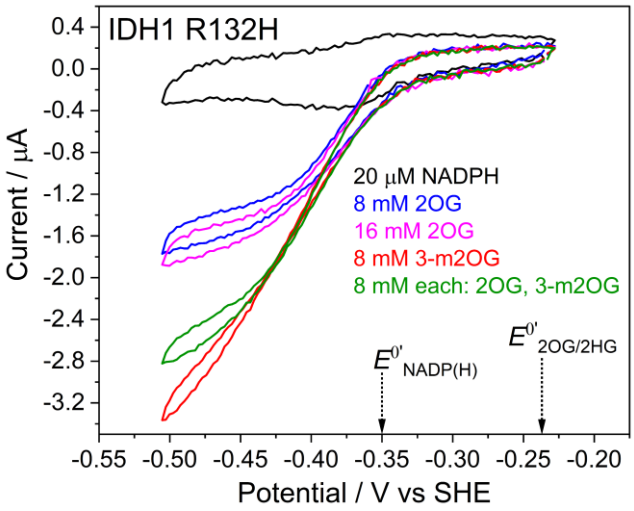


Figure 31. Substrate competition can be observed between the tighter-binding 2OG and the more active 3-methyl-2OG. The plot shows that 8 mM 3-methyl-2OG turns over much faster than both 8 and 16mM 2OG. Injecting 8 mM of 2OG with 8 mM 3-methyl-2OG already present results in a slightly lower current than 8 mM 3-methyl-2OG alone (current is slightly reduced due to substrate competition). Conditions: Stationary 0.03 cm^2 (FNR+$IDH1_{R132H}$)@ITO/PGE electrode, scan rate 2 mV s^{-1}, volume 2.5 mL, temperature 25 °C, pH = 8 (100 mM HEPES, 150 mM NaCl), 10 mM $MgCl_2$, 20 µM NADPH, Enzyme loading ratios (molar): FNR/$IDH1_{R132H}$; 1/2.

then injected into the solution (8 mM final concentration) and another trace recorded (blue trace). A second aliquot of 2OG was injected into the solution (16 mM final concentration, magenta trace) resulting in only a slight increase in coupled current. These voltammograms were important as they established baseline activities. A buffer exchange was then performed (the reaction solution was removed, and the electrode was rinsed and placed back into the electrochemical cell containing fresh buffer solution with Mg^{2+} and NADPH) and 8 mM 3-methyl-2OG was injected into the reaction solution, giving rise to a much larger catalytic current than either 8 or 16 mM 2OG (red trace). Finally, 8 mM 2OG was injected into the solution resulting in a decrease in catalytic activity but maintaining a current that was still well above that obtained with 16 mM 2OG. This decrease in current following addition of 2OG is attributable to substrate competition between the tighter-binding 2OG (K_m = 0.85 mM, k_{cat} = 0.72 s^{-1}) and the weaker-binding but overall better substrate,

3-methyl-2OG (K_m = 3.7 mM, k_{cat} = 6.9 s^{-1}).[54] Thus, 2OG is able to more efficiently bind the enzyme, blocking binding of the catalytically superior 3-methyl-2OG substrate. A repeat experiment yielded an identical result, and further controls showed good stability of the 3-methyl-2OG reaction if no 2OG was added.

2.3.7 Complex Interactions between IDH1 R132C/S280F and Mg^{2+}

It has been proposed that inhibitors of IDH1 variants primarily bind allosterically at the dimer interface, inducing/stabilizing a conformational change following which the enzyme is unable to bind Mg^{2+} ions[35] (the mechanism of IDH1 variant inhibition will be explored in detail in **Chapter IV**). Furthermore, because Mg^{2+} binding is required for IDH1 variants to efficiently bind 2OG, and the Mg^{2+}-isocitrate complex is proposed to be the true substrate of the wildtype enzyme,[35] it is important to understand how Mg^{2+} interacts with *both* reactions that the IDH1 variants catalyze (2OG reduction and isocitrate oxidation). To this end, chronoamperometry experiments were performed under both oxidizing (**Figure 32**) and reducing (**Figure 33**) conditions for IDH1 R132C/S280F with $MgCl_2$ titrated into the reaction solution at increasing concentrations. The IDH1 R132C/S280F variant was chosen because it performs both reactions efficiently compared to other IDH1 variants.

When Mg^{2+} was titrated into solution under oxidizing conditions in the presence of $NADP^+$ and isocitrate, the activity of IDH1 R132C/S280F initially exhibited the expected response before showing signs of substrate inhibition at higher Mg^{2+} concentrations (**Figure 32**). Fitting the Michaelis-Menten equation for a substrate inhibited enzyme (Eq. 9) resulted in an extremely good fit ($R^2 > 0.99$) with a $K_{m(nano)}$ = 1.35 mM. This Michaelis constant value cannot be compared to a standard value because the equivalent experiment cannot be

performed in dilute solution due to the immediate consumption of the 2OG and NADPH products (the neomorphic reaction). However, wildtype IDH1 also exhibits substrate inhibition when isocitrate is titrated into dilute solution, and there appears to be a complex relationship between concentrations of Mg^{2+}, isocitrate, and $NADP^+$ that could be due to

$$v = \frac{V_{max}[S]}{K_m + [S] + \frac{[S]^2}{K_i}} \quad \text{(Eq. 9)}$$

either the binding order or the presence of half-site reactivity (see **Chapter III** for further discussion). The presence of substrate inhibition when either Mg^{2+} or isocitrate is titrated into solution could also be due to the higher concentration component binding the enzyme on its own and blocking binding of the Mg^{2+}-isocitrate complex, the true substrate of the wildtype enzyme (and likely that of the IDH1 variants which retain wildtype activity).[35]

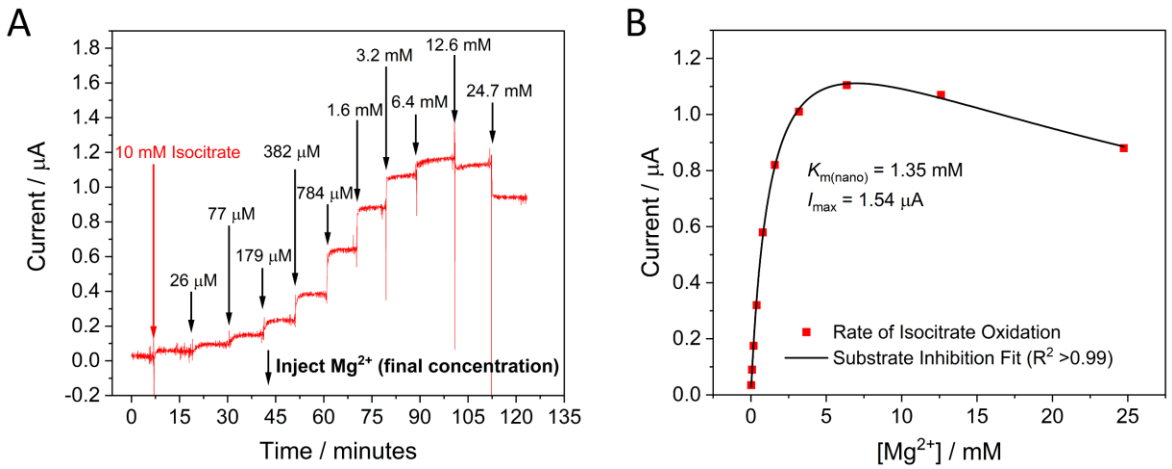


Figure 32. IDH1 R132C/S280F isocitrate oxidation activity as $MgCl_2$ is titrated into the reaction solution. (A) Chronoamperometry showing IDH1 R132H activity as $MgCl_2$ is titrated into the reaction solution at increasing concentrations (arrows show the final cumulative concentration of isocitrate after each injection). (B) Plot showing the steady-state R132C/S280F activity at each $MgCl_2$ concentration fitted by the Michaelis-Menten equation for a substrate inhibited enzyme (Eq. 9). Conditions: (FNR+IDH1$_{R132C/S280F}$)@ITO/PGE electrode, electrode area 0.03 cm^2, electrode rotated at 1000 rpm, 25 °C, pH = 8 (50 mM HEPES), 10 mM isocitrate (injection shown in panel A), 10 µM $NADP^+$, 4 mL cell volume, E = 0 V vs SHE, enzyme loading ratios (molar): FNR/IDH1$_{R132C/S280F}$; 2/5.

Interestingly, when $MgCl_2$ was titrated into solution under reducing conditions in the presence of NADPH and 2OG, IDH1 R132C/S280F also initially gave the expected catalytic response and exhibited substrate inhibition (see inlaid figures in **Figure 33A**, **B**); however, as increasing concentrations of Mg^{2+} were continued to be added to the reaction solution, the current (enzyme activity) began to increase again, ultimately reaching a level that was roughly two-fold greater than the initial maximum value before substrate inhibition was observed (**Figure 33A**). The same surprising result was obtained upon repeating the experiment with activity measured at more concentrations of Mg^{2+} (**Figure 33B**) yielding a clearer picture of the enzyme behavior: an initial maximum activity is reached—with substrate inhibition (see inlaid figure)—followed by a second rise in activity that overcomes the substrate inhibition. The Michaelis-Menten model clearly cannot describe this behavior. The only tested model which seemed to fit the data, and which fits very well ($R^2 > 0.99$), was the "isoenzyme model", which describes the expected reaction rates for experiments in which two isozymes (enzymes which perform the same reaction but with different catalytic efficiencies)[65] are present in the same solution (Eq. 10). Note that the isoenzyme model fits

$$v = \frac{V_{\max 1}[S]}{K_{m1}+[S]} + \frac{V_{\max 2}[S]}{K_{m2}+[S]} \qquad \text{(Eq. 10)}$$

better with **Figure 33A** than **Figure 33B** because substrate inhibition is not accounted for in the isoenzyme model and panel B has more data points in the substrate inhibited region.

This odd behavior, which has not been previously reported, is not due to effects of the e-Leaf system as other experiments have been run at very high $MgCl_2$ concentrations (50 mM and above) without any impact on current. Thus, the currents observed here are in fact due to IDH1 R132C/S280F-catalyzed reduction of 2OG. Based on the isoenzyme model fit to the data in **Figure 33A**, the IDH1 R132C/S280F variant seems to have two apparent

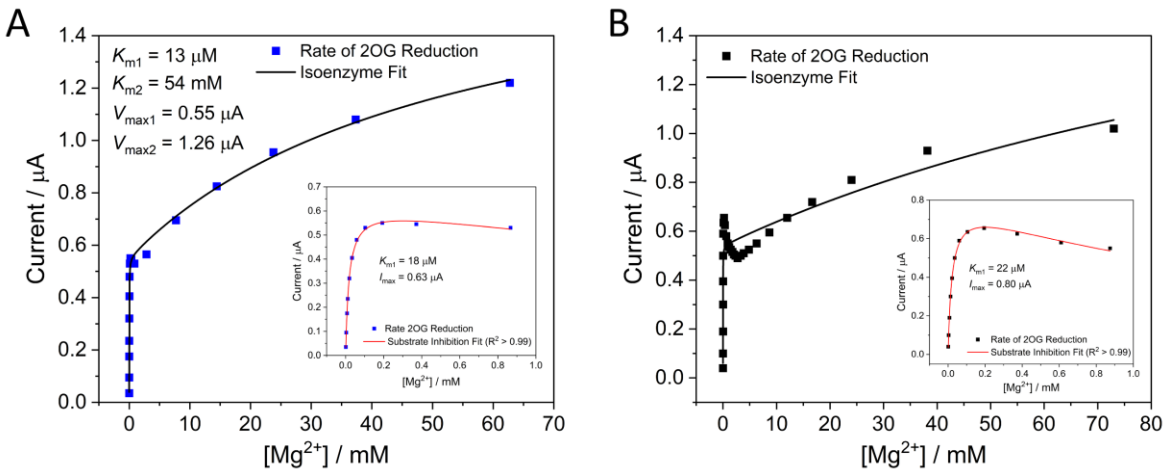


Figure 33. Plots showing IDH1 R132C/S280F-catalyzed 2OG reduction activity as $MgCl_2$ is titrated into the reaction solution fitted by the "isoenzyme" equation (Eq. 10). Panels A and B are repeat experiments performed under the same conditions. The experiment in panel A fits the model with $R^2 > 0.99$; the experiment in panel B does not fit the equation as well because the enzyme is substrate (Mg^{2+}) inhibited and extra data points were included to confirm this (the isoenzyme model does not account for substrate inhibition). The inlays in each figure show the data at low [Mg^{2+}] fit by the Michaelis-Menten equation for substrate inhibited enzymes (Eq. 9) (both $R^2 > 0.99$). Conditions: (FNR+IDH1$_{R132C/S280F}$)@ITO/PGE electrode, electrode area 0.03 cm^2, electrode rotated at 1000 rpm, 25 °C, pH = 8 (50 mM HEPES), 10 mM 2OG, 10 µM NADPH, 4 mL cell volume, E = –0.50 V vs SHE, enzyme loading ratios (molar): FNR/IDH1$_{R132C/S280F}$; 2/5.

K_m values for Mg^{2+} for the 2OG reduction reaction: one at a very low concentration (K_{m1} = 13 µM) and a second at a much higher concentration ($K_{m2} \approx$ 54 mM). Previous kinetic experiments performed with the IDH1 R132C/S280F variant in dilute solution measured a K_m = 237 µM for Mg^{2+}.[40] The subtle effects observed using the e-Leaf could have been missed in the cited work for several possible reasons including: (1) fewer measurements would have been made overall (typically only 7–10 concentrations are tested for standard solution kinetics) with a lack of sufficient measurements at very low Mg^{2+} concentrations being particularly important (for comparison see the inlaid figures in **Figure 33**); (2) enzyme turnover rates measured using spectrophotometric assays exhibit much greater variance between replicates compared to electrochemical measurements, especially measurements of low enzyme activity: using an electrochemical system, a single enzyme sample in/on an

electrode is used against all substrate concentrations under the exact same conditions (substrate is simply titrated into solution) eliminating the vast majority of experimental error—note the beautiful electrochemical data exhibiting near-ideal Michaelis-Menten kinetics (**Figure 14**, **Figure 15**, **Figure 32**, **Figure 49**).

This work is ongoing and the mechanism has not yet been resolved; two possible explanations for how such an activity profile (two apparent K_m values) could be achieved are: (1) if IDH1 R132C/S280F exhibits half-site reactivity for the 2OG reduction reaction (similar to the wildtype enzyme for isocitrate oxidation), it is plausible that Mg^{2+} is able to bind with very high affinity to one monomer subunit of the active dimer, but that binding of a second Mg^{2+} ion at the other active site is much less favourable. In this case, the enzyme active sites would turn over one at a time, limited by the absence of Mg^{2+} at one active site at any given time. At very high Mg^{2+} concentrations, a second Mg^{2+} ion may be able to bind the other subunit, perhaps allowing the enzyme to exhibit "dual-site" activity. (2) It is also plausible that at low concentrations of Mg^{2+}, the binding of Mg^{2+} and 2OG is separate and ordered, perhaps resulting in a rate-limiting step, but that at higher Mg^{2+} concentrations, a Mg^{2+}-2OG complex forms that is capable of binding the enzyme directly as substrate (similar to the Mg^{2+}-isocitrate complex for the wildtype enzyme). It should also be noted that the binding/release dynamics of $NADP^+$/NADPH are also very important and likely affect (and are affected by) the binding of Mg^{2+} and 2OG.[32,35] Regardless of the mechanism, the huge difference in K_m values for Mg^{2+} between the two reactions (1.35 mM for isocitrate oxidation vs. 13 μM for 2OG reduction) with the same enzyme is very interesting as it indicates significant differences in how the enzyme interacts with the essential metal ion under different conditions.

2.4 Conclusions

Wildtype IDH1 and six IDH1 variants were incorporated into the e-Leaf, allowing their catalytic properties to be studied under different conditions. The ability to change the reaction solution multiple times for a single enzyme sample/electrode was exploited (e.g., changing pH, adding/removing substrates/metal cofactor), allowing more informative and direct comparisons between conditions than could otherwise be made using standard solution assays. Furthermore, the unique ability to control, on-demand, the redox environment inside the electrode, where the IDH1 enzymes reside, proved extremely useful as it enabled wildtype IDH1 to be driven in either direction, enabling investigation of the fundamental thermodynamics of the reactions catalyzed, and resulting in the creation of a Pourbaix diagram describing the conditions under which oncometabolite 2HG is formed. This tight redox control also made it possible to separately study the two different reactions, isocitrate oxidation and 2OG reduction, catalyzed by five important cancer-associated IDH1 variants, which is something that cannot be done in homogeneous solution using standard assays.

Despite IDH1 having been studied for decades as an important central carbon metabolic enzyme, the first application of electrochemical methods presented in this work provides a new perspective from which to view the IDH1 enzymes, which can now be studied and treated as *electrocatalysts*. Having established the fundamental behavior (thermodynamic and kinetic) of the IDH1 enzymes in the e-Leaf, the next two chapters focus on further exploiting the unique advantages of the e-Leaf system—simultaneous control and monitoring of activity coupled with enzyme nanoconfinement—to study the effects of

enzyme crowding on cofactor recycling and the kinetic mechanism of IDH1 variant inhibition by several high-profile inhibitors.

CHAPTER III

NADP(H)-DEPENDENT BIOCATALYSIS USING ONLY ENZYME-COPURIFIED NADP(H)

3 NADP(H)-dependent Biocatalysis Using only Enzyme-copurified NADP(H)

3.1 Abstract

Recombinant Isocitrate dehydrogenase I (IDH1) copurifies with a molecule of NADP(H) bound to each of the two active sites per dimer molecule. This special property was exploited to use IDH1 as a "shuttle" to carry NADP(H) into the electrode nanopores of an indium tin oxide electrode. Co-loaded alongside FNR, the resulting system is capable of functioning via the internal recycling of the IDH1-copurified NADP(H)—no added NADP(H) is required. Surprisingly, the system is stable for several days without the NADP(H) escaping the electrode nanopores; when scaled up, bulk electrolysis resulted in extremely high total turnover numbers for both the trapped NADP(H) cofactor (~160,000) and enzymes (~150,000). With NADP(H) being present only inside the electrode, it was possible to electrochemically quantify the trapped NADP(H) and thus the amount of IDH1 that carried it in. The results indicate that the enzymes are present in the electrode at extremely high concentrations ([FNR] + [IDH1] ≈ 2 mM) that likely approach the physical limit. This concentrating effect, coupled with the nanoconfinement of NADP(H), increases the efficiency of cascade catalysis by several orders of magnitude. Furthermore, the tight redox control of the electrode environment was used to measure the binding affinities of "resting" conformations of wildtype IDH1 and the cancer-associated R132H variant, yielding results that would be extremely difficult to obtain by other means. Together, the experiments presented in this Chapter quantify the advantage of nanoconfinement for cascade catalysis and provide an interesting perspective on enzyme behavior under

conditions of macromolecular crowding, which may be more representative of the in vivo environment than standard (often nanomolar) enzyme solution assays.

3.2 Introduction

3.2.1 Biological Nanoconfinement

Optimized over billions of years, cells have evolved to use many different strategies to tightly control, both spatially and temporally, the chemical reactions of metabolism. One such strategy, ubiquitous across all domains of life, is the use of nanoconfinement, which encompasses both volumetric confinement, i.e., physically enveloping enzymes within a membrane or protein shell (e.g., organelles/bacterial microcompartments)[66,67] and enzyme co-localization (e.g., metabolons).[68] Employing physical control over the intracellular spatial arrangement of enzymes/macromolecules can have several advantages, enabling cells to do useful things such as (1) separate competing enzymes/pathways, (2) create charge separation and/or concentration gradients, and (3) minimize the escape of unstable/toxic pathway intermediates (including recycled cofactors). The e-Leaf enables enzymes to be studied under conditions of nanoconfinement through the co-localization and entrapment of enzymes within a porous inorganic electrode material. This artificial nanoconfinement results in the rapid transfer of cascade intermediates between enzyme partners, mimicking biological nanoconfinement, and allowing non-electroactive enzymes to be treated as electrocatalysts.

3.2.2 Enzyme Copurification with Bound Nicotinamide

In general, the nicotinamide cofactors, NAD(H) and NADP(H), are mobile enzyme co-substrates that act as oxygen-insensitive electron sources/sinks for metabolic redox reactions. Although NAD(P)(H) is generally considered to be an *exchangeable* cofactor, an intriguing characteristic of both recombinant wildtype IDH1 and the cancer-associated IDH1 R132H variant is that they copurify as dimers with a molecule of NADP(H) tightly bound at

each monomer active site (**Figure 34**).[23,32,34–37] Although uncommon, this feature is not unique to the IDH1 enzymes, and other proteins have been reported to copurify with both NAD(H)[69–78] and NADP(H)[17,79–84] bound. An interesting subgroup of these proteins is the so-called "nicotinoproteins"[74–78,82,83,85] which use NAD(P)(H) as a permanent noncovalently bound prosthetic group (analogous to a flavin group) to perform a variety of reactions such

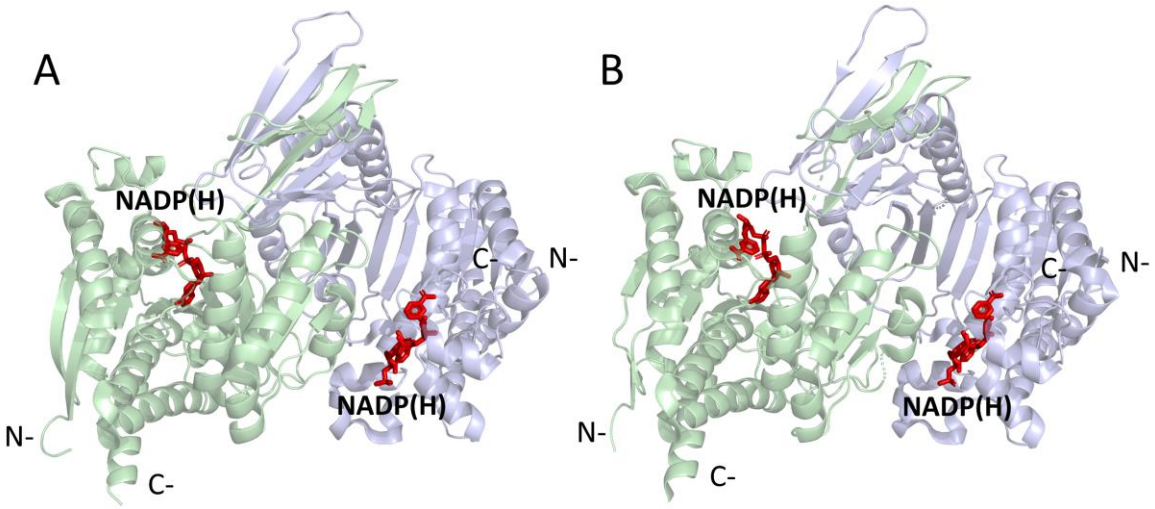


Figure 34. Crystal structures of dimeric IDH1 showing copurified NADP(H) bound at each monomer active site. (A) Wild-type IDH1 (PDB: 1T09).[34] (B) Cancer-associated IDH1 R132H variant (PDB: 3MAR).[37] Both enzymes were crystallized without added NADP(H)[34,37] and show IDH1 in the open inactive conformation.[32]

as the dismutation of aldehydes to their respective alcohols and carboxylic acids.[85] The limited number of NAD(P)(H)-dependent dehydrogenases reported to copurify with nicotinamide cofactors[69,70,78–81] suggest that such extremely tight binding is unusual.

It may seem that such tight binding of NAD(P)(H) would curtail its use as an exchangeable cofactor; however, enzymes are highly dynamic, and different enzyme conformations may have vastly different binding affinities for the cofactor. In the case of IDH1, the extremely tight binding that is required for the NADP(H)-enzyme complex to survive the purification process is not represented by measured Michaelis constant (K_m) values. These values range from 10–100 μM,[35,40] well within the range of other

dehydrogenases which do not copurify with NAD(P)(H). Despite this, copurified NADP(H) has been shown to remain bound to IDH1 even when the enzyme is diluted ~12 million-fold.[32] Only after Mg^{2+} and isocitrate (for the wildtype enzyme) bind is a conformational change induced that results in the release of approximately 50% of the bound NADP(H).[32] Thus, the extremely tight binding of NADP(H) to IDH1 is limited to the "open inactive" conformation of the enzyme, the conformation in which the enzyme naturally purifies (**Figure 34**). This property was exploited to create a system where all components, enzymes *and* cofactor, are trapped in the electrode nanopores of the e-Leaf. This is possible because IDH1 is able to carry the NADP(H) into the electrode pores as "cargo", only releasing it in the presence of substrate. This system presented an opportunity to carry out unique quantitative experiments investigating fundamental properties of enzyme nanoconfinement and its benefits for cascade catalysis.

3.2.3 Aims of this Chapter

To date, all e-Leaf experiments have required the addition of NADP(H) to the bulk reaction solution from where it can enter the electrode nanopores for use by trapped enzymes. However, the uncommon property of IDH1-NADP(H) copurification prompted the idea to try running the system without adding any NADP(H); thus, all catalytic components (enzymes and NADP(H) cofactor) would be trapped in the electrode nanopores. This Chapter aims to test the properties of such a system. Furthermore, it has been a longstanding goal to quantify the non-electroactive enzymes trapped in the e-Leaf electrode alongside FNR. The special properties of the FNR-IDH1-NADP(H) system offered an opportunity to quantify all components (including NADP(H)) trapped in the mesoporous ITO electrode.

3.3 Results and Discussion

3.3.1 IDH1 Enzymes Copurify with Bound NADP(H)

It was important to confirm that the in-house expressed and purified wildtype IDH1 and IDH1 R132H enzymes copurified with bound NADP(H). To do this, two independent experimental methods were used: ^{1}H NMR and non-denaturing mass spectrometry (also called native mass spectrometry). The ^{1}H NMR experiments showed that wildtype IDH1

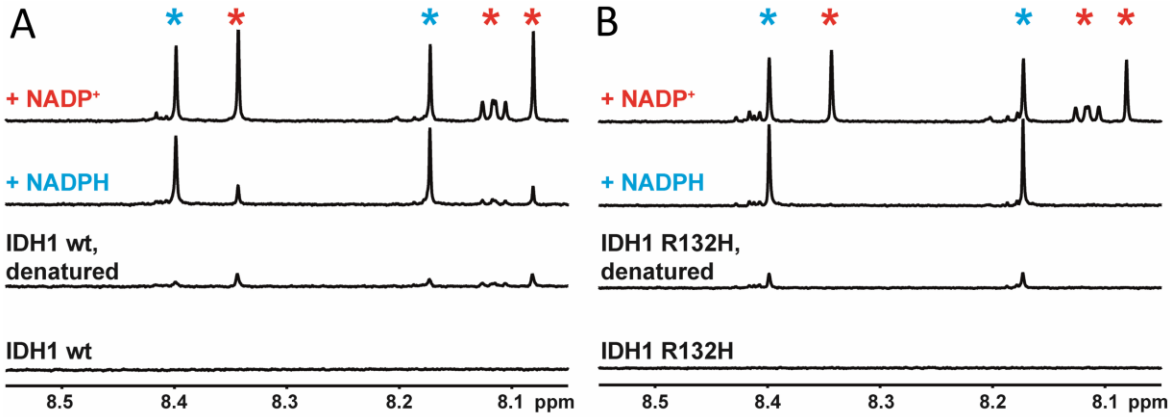


Figure 35. ^{1}H NMR data showing the release of copurified enzyme-bound NADP(H) from wildtype IDH1 (A) and IDH1 R132H (B) upon thermal denaturation (see **Figure 37** for the equivalent experiment with FNR). Starting from the lower spectra: (1) folded IDH1 protein—NADP(H) is initially enzyme-bound, hence not observed; (2) denaturation releases NADP(H) into solution. (A) Wild-type IDH1 copurifies with an approximately 2:1 mixture of $NADP^{+}$ (red asterisk) and NADPH (blue asterisk). (B) IDH1 R132H copurifies exclusively with NADPH.

copurified with a mixture of both $NADP^{+}$ and NADPH in an approximate ratio of 2:1 in favor of $NADP^{+}$ (**Figure 35A**). In contrast, IDH1 R132H copurified exclusively with NADPH (**Figure 35B**). Non-denaturing mass spectrometry experiments (**Figure 36**) revealed that wildtype IDH1 copurified with an average NADP(H) active site occupancy of 46%, meaning that each wildtype IDH1 dimer molecule carried (on average) one molecule of NADP(H) ($NADP(H)/IDH1_{dimer} \approx 1/1$). IDH1 R132H was shown to copurify with more

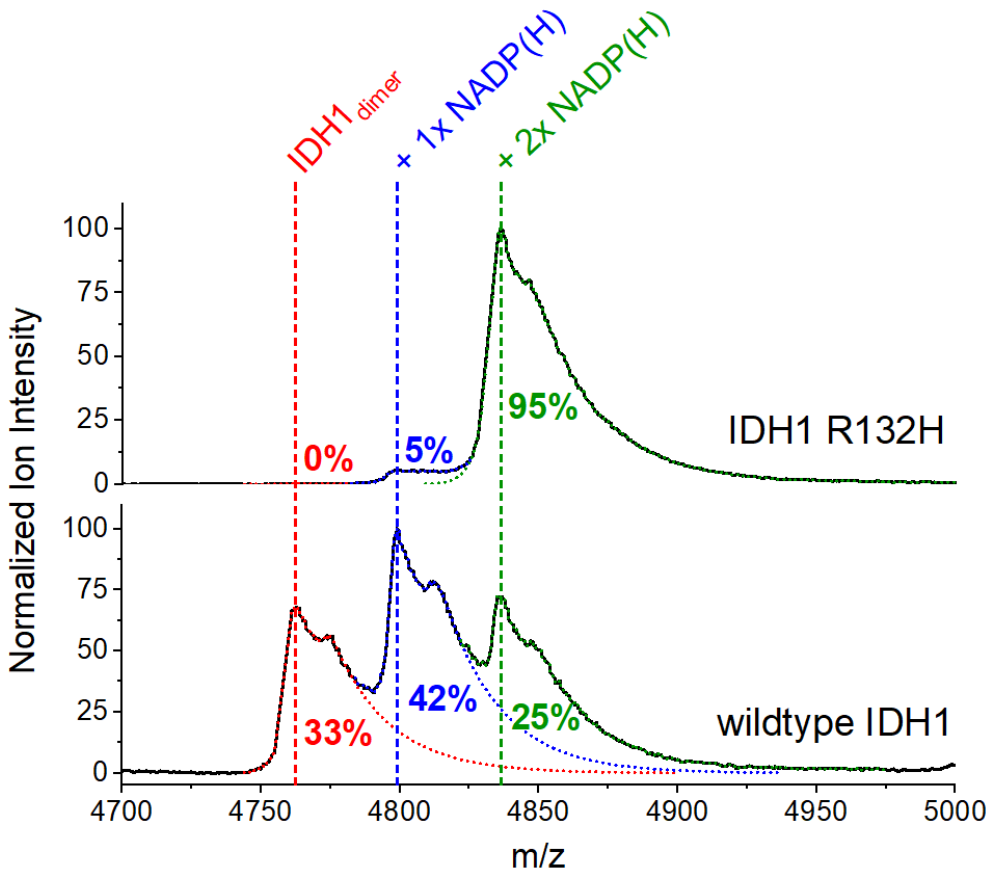


Figure 36. Non-denaturing mass spectrometry for IDH1 R132H (top) and wildtype IDH1 (bottom) showing the relative fractions of dimeric enzyme with 2 molecules of bound NADP(H) (green), one molecule of bound NADP(H) (blue), and no bound NADP(H) (red) after enzyme purification. To separate the overlapping peaks in the bottom panel (wildtype IDH1) and allow integration, the exponential parts of each peak were fit using an asymptotic exponential equation (approaching 0). The decay rate constant used to fit the first two peaks (red and blue) was determined by fitting the same exponential equation to the green peak (2 molecules of bound NADP(H)), the trailing tail of which does not overlap with other peaks.

NADPH bound, having an active site occupancy of approximately 97.5%, i.e., NADP(H)/IDH1 R132H$_{dimer}$ ≈ 1/2 (**Figure 36**). The active site occupancy values calculated from non-denaturing mass spectrometry experiments are consistent with the amount of NADP(H) that was detected by ^{1}H NMR, but the ^{1}H NMR quantification was less precise because the concentrations were very low. Interestingly, previous studies have reported that both the wildtype and R132H IDH1 enzymes copurify with an active site occupancy of ~90%.[35] Furthermore, there are conflicting reports about whether wildtype IDH1 copurifies

with a mixture of $NADP^+$ and NADPH[36] or exclusively NADPH.[32,35] These varied reports likely reflect differences in expression and purification methods/conditions, emphasizing the importance of verifying the status of copurified NADP(H) for the enzyme samples used in this work.

As a control, an equivalent ^1H NMR experiment was carried out with FNR to confirm that it did not copurify with any bound NADP(H) (**Figure 37**). Upon thermal denaturation, the release of its prosthetic group, FAD, was clearly visible, but no peaks associated with

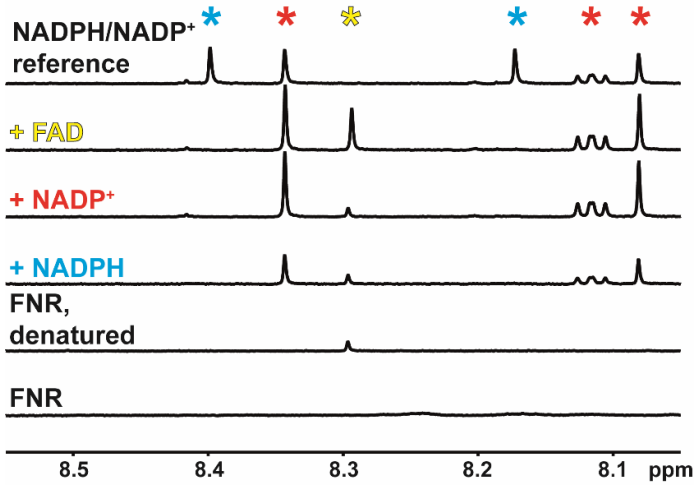


Figure 37. ^1H NMR data showing that no NADP(H) copurifies with FNR. The FAD cofactor only becomes visible after the enzyme is denatured, which was confirmed by adding additional FAD (100 µM) to the NMR tube containing the denatured FNR. Interestingly, the NADPH that was added to the sample (100 µM) was oxidized to $NADP^+$ despite the FNR being denatured. A control experiment (**Figure 38**) confirmed that "free" FAD in solution is able to directly oxidize NADPH.

NADP(H) were present. Interestingly, when NADPH was added to the NMR tube, peaks characteristic of $NADP^+$ were observed instead of NADPH even though FNR had already been denatured (**Figure 37**). To confirm that no active FNR was still present, a further control experiment was performed, confirming that "free" FAD is able to directly oxidize NADPH to $NADP^+$ in solution (**Figure 38**).

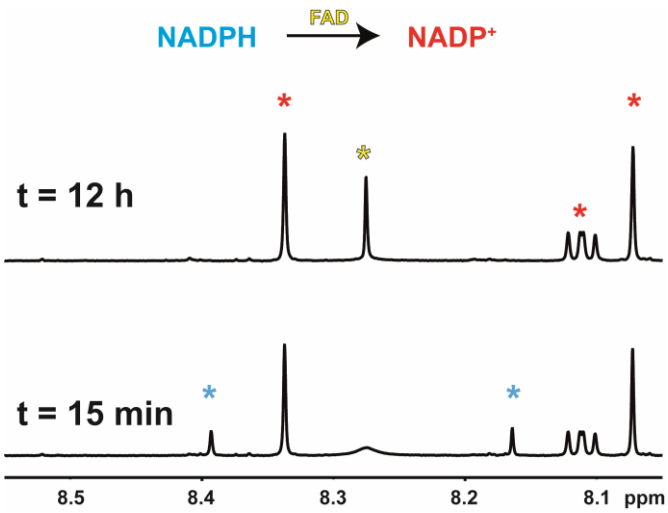


Figure 38. ^{1}H NMR control experiment showing that "free" FAD (100 μM) in solution is able to directly oxidize NADPH (100 μM) in solution. At the *t* = 15 minutes timepoint (bottom), the fully-oxidized FAD peak (yellow star) is much smaller and broader than expected likely due to much of it having been reduced by NADPH. After 12 hours (top), the oxidized FAD peak is present as expected, having been reoxidized by oxygen, alongside $NADP^+$ (no NADPH remains).

3.3.2 Copurified NADP(H) is Sufficient for Nanoconfined Enzyme Catalysis

Having shown that in-house expressed wildtype IDH1 and IDH1 R132H copurify with NADP(H), electrochemical experiments were performed to test if the copurifying NADP(H) by itself was able to sustain steady-state catalysis under conditions of nanoconfinement, i.e., whether the e-Leaf system could be run without adding any NADP(H) to the system other than that which naturally copurified bound to IDH1. As before, FNR and IDH1 were loaded together by placing a concentrated solution (4–5 μL) onto the electrode and incubating at room temperature for 30–45 minutes before rinsing with buffer to remove any enzyme which did not enter the electrode nanopores. Only a tiny fraction of the loaded enzyme actually enters the nanopores while the rest is removed by rinsing. This was confirmed by a control experiment in which three electrodes were loaded as described above: the electrode rinsing

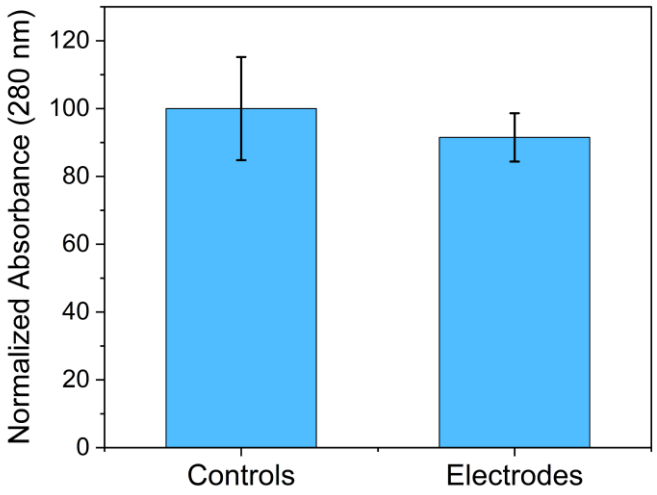


Figure 39. Bar chart showing no significant difference (p = 0.45; two-tailed t-test assuming unequal variances) in the amount of enzyme rinsed from 0.06 cm^2 electrodes (n = 3) after enzyme loading vs control samples (n = 3), where no electrode was used (directly diluted enzyme stock). The three electrodes were loaded with enzyme (1.27 nmoles total; FNR/IDH1 R132H$_{dimer}$; 1/2) following the typical dropcasting procedure (see **Methods**). The electrodes were rinsed using buffer (100 mM HEPES; pH = 8), and the rinsed solution was kept for comparison with three aliquots of the same amount of enzyme that was directly diluted into the same amount of buffer used for rinsing. Based on absorbance at 280 nm, the rinsed solution contained roughly the same amount of enzyme as the directly diluted stocks, confirming that only a tiny fraction of the enzyme used is actually taken up into the electrode nanopores. Error bars represent the standard deviation.

solution was shown to contain roughly the same amount of enzyme as the directly diluted enzyme stock used for loading (**Figure 39**).

When nanoconfined in the e-Leaf, both wildtype IDH1 and IDH1 R132H gave strong catalytic responses when their respective substrates were added into the cell solution even though no NADP(H) had been added (**Figure 40**). The current responses following substrate addition are consistent with previous results for both enzymes in the e-Leaf[26] (see **Chapter II**). Interestingly, initial injections of isocitrate to the wildtype reaction showed that there was an activation period which was not present following later additions (**Figure 40A**). At low concentrations of isocitrate, a sigmoidal cyclic voltammogram with wildtype IDH1 (blue trace, **Figure 40B**) shows that the current is limited by the rate of IDH1-catalyzed

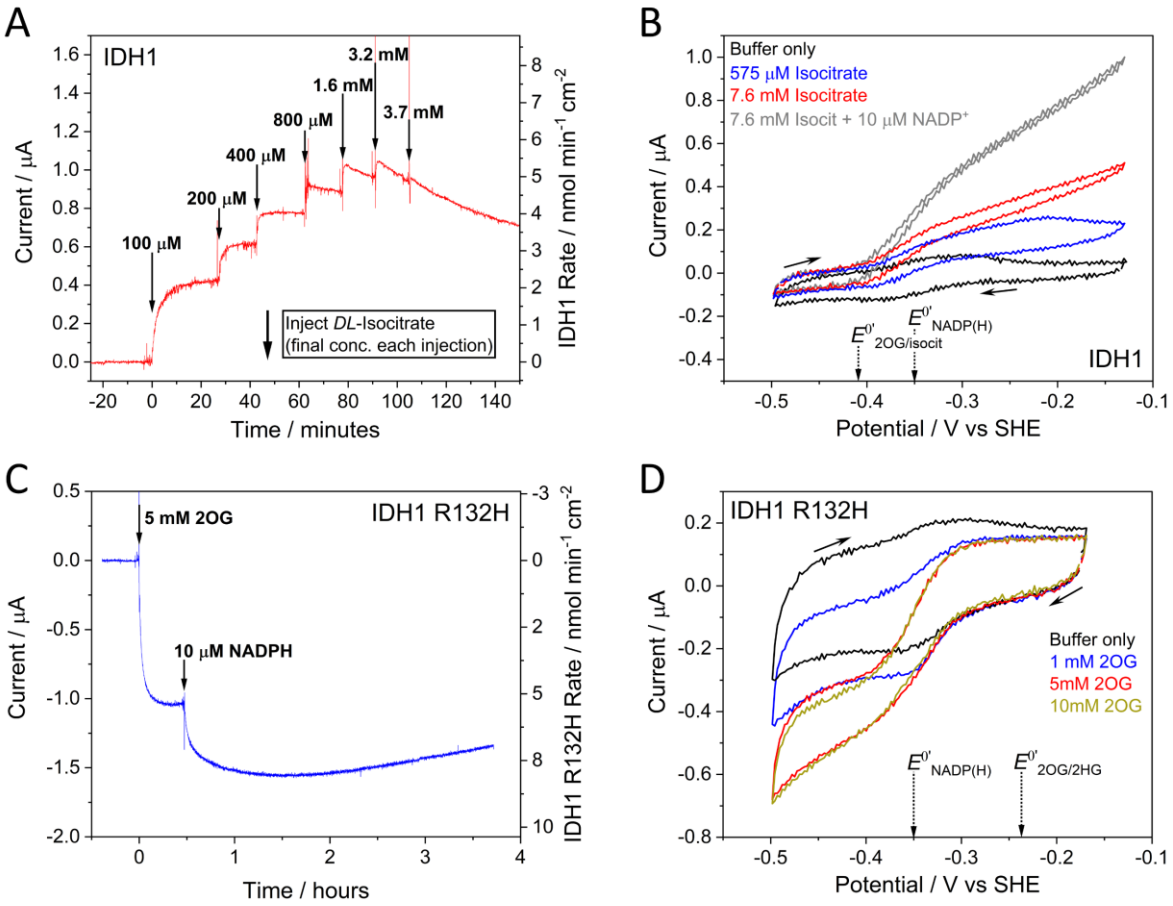


Figure 40. Electrochemical experiments demonstrating that wildtype IDH1 (panels A and B) and IDH1 R132H (panels C and D) are both active in the e-Leaf using only the NADP(H) which copurified bound to IDH1 (no NADP(H) was added unless indicated in the figure). (A) Chronoamperogram showing IDH1 activity as increasing concentrations of *DL*-isocitrate are titrated into the reaction solution. The values shown are the final concentrations of each addition of isocitrate (not cumulative). (B) Cyclic Voltammetry showing wildtype IDH1 activity at different concentrations of isocitrate. The grey trace shows IDH1 activity when 10 µM $NADP^+$ was added to the solution. (C) Chronoamperogram showing IDH1 R132H activity after 5 mM 2OG was injected into solution followed by an addition of 10 µM NADPH. (D) Cyclic voltammetry showing IDH1 R132H activity at different concentrations of 2OG. Conditions (all experiments): temperature 25 °C, volume 4 mL, pH = 8 (100 mM HEPES, 10 mM $MgCl_2$); (A and B) (FNR+IDH1)@ITO/PGE electrode, enzyme loading ratios (molar): FNR/IDH1; 2/1. (A): electrode area 0.06 cm^2, 1000 rpm, potential *E* (vs SHE) = +0.2 V. (B): 0.03 cm^2 electrode area, scan rate 1 mV s^{-1}, stationary electrode. (C and D): (FNR+$IDH1_{R132H}$)@ITO/PGE electrode, area 0.06 cm^2, enzyme loading ratios (molar): FNR/$IDH1_{R132H}$; 2/5. (C): 1000 rpm, potential *E* (vs SHE) = –0.5 V. (D): scan rate 1 mV s^{-1}, stationary electrode. Racemic *DL*-isocitrate was used for both A and B.

isocitrate oxidation. As was observed previously for the wildtype enzyme, high concentrations of isocitrate (red trace) give linear potential-dependent cyclic voltammograms indicating that the current is limited by the rate of electron transfer between the electrode and

FNR (**Figure 40B**). Voltammograms with IDH1 R132H (**Figure 40D**) show a similar trend, but the traces exhibit less potential-dependence than those for the wildtype. In both cases, additions of 10 μM NADP(H) (grey trace, **Figure 40B**; and **Figure 40C**) indicate that the system is limited by NADP(H)—this is not surprising considering that the only NADP(H) present is that which copurified bound to IDH1.

3.3.2.1 IDH1-Copurified NADP(H) is Detectable by Cyclic Voltammetry

Intriguingly, the "buffer only" voltammograms in panels B and D in **Figure 40** (black traces) are *not* those which would be expected for FNR alone. The peaks are present at a more positive value than expected for the FNR-bound FAD ($E^{0'}$ = –0.38 V) and the shapes of the peaks are also unexpected: there is a sharp reduction peak and a broader oxidation peak with a trailing tail. Such peaks are characteristic of NADP(H), which also has a formal potential of –0.35 V at pH = 8, the same as the average value of those observed in the "buffer only" voltammograms; therefore, the peaks must be the result of electrochemical cycling of the IDH1-copurified NADP(H). This means that the bound NADP(H) must be transiently released from IDH1 long enough to react with FNR. This property was exploited to quantify the NADP(H) (and thus IDH1) present in the electrode nanopores as will be shown later in this chapter.

3.3.3 Bulk Synthesis Using Only Enzyme-copurified NADP(H)

To see if the IDH1-copufied NADP(H) could be used for bulk electrolysis, and to investigate the stability of the system, a 4 cm^2 electrode (double-sided 1 x 2 cm ITO on titanium foil) was loaded with FNR and wildtype IDH1 following the standard dropcasting

procedure. The 4 cm^2 electrode, which had a 67-fold greater surface area than a standard 0.06 cm^2 analytical-scale electrode, was loaded with 4-fold more enzyme than the latter, resulting in ~2.4% of the FNR applied to the electrode being taken up by the electrode compared to only ~0.6% of applied FNR being taken up after loading a 0.06 cm^2 electrode (based on quantification by cyclic voltammetry). The larger electrode was needed to achieve currents capable of converting bulk isocitrate into 2OG.

The electrode, loaded with FNR and IDH1, was placed into a 3-chamber electrochemical cell (see **Methods**) containing 4 mL of buffer solution with 10 mM $MgCl_2$ already present. With an oxidizing potential applied (E = +0.2 V) and a stir bar supplying mass transport, 5 mM enantiopure *D*-isocitrate was injected into the reaction solution resulting in an oxidation current of 26 µA (**Figure 41A**); a sample of the solution was taken for NMR analysis (TP1). Over the course of approximately 55 hours, the current gradually dropped to 0 A. The integral of the chronoamperogram was taken (giving the "charge passed"), and it was calculated that 4.95 mM of 2OG product had been made indicating that all of the isocitrate had been consumed. Exhaustive conversion of substrate was confirmed by NMR analysis of a second solution sample (TP2, **Figure 41B**). Another aliquot of *D*-isocitrate was then added to the solution (1.5 mM final concentration), and a third sample was taken (TP3). Following the second addition of isocitrate, an oxidation current was again observed, indicating that the system was still active after 68 hours. The isocitrate was consumed again, and after ~115 hours, a final sample was taken (TP4). Again, the "charge passed" calculation matched very well with the NMR analysis, indicating that all of the added isocitrate had been oxidized to 2OG except for a small amount which had migrated across

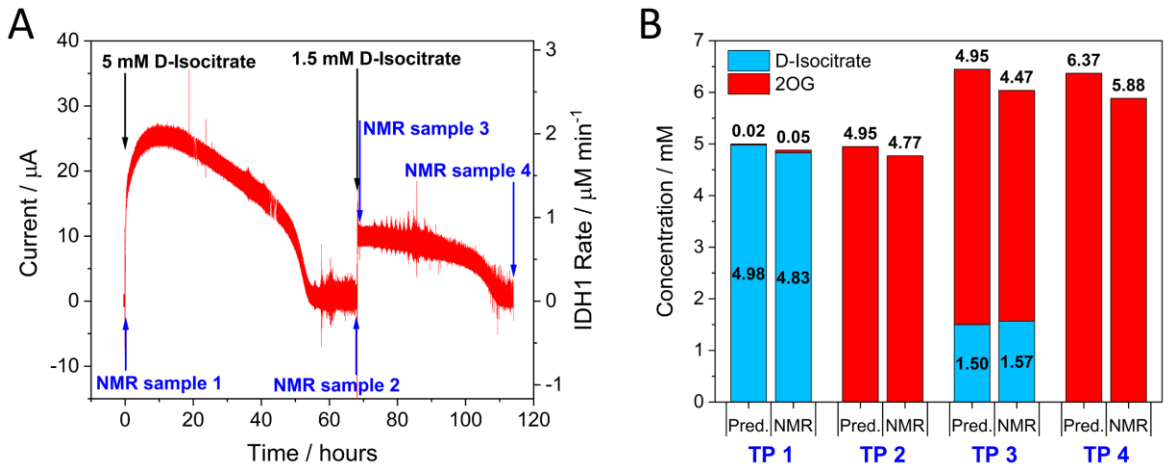


Figure 41. Scaled-up wildtype IDH1 experiment (4 cm^2 electrode, 4mL stirred solution) showing quantitative conversion of 6 mM *D*-isocitrate to 2OG using only IDH1-copurified NADP(H). (A) Chronoamperogram showing IDH1 activity over the course of five days. (B) Bar chart comparing predicted yields (based on charge passed) with ^{1}H NMR-quantified substrate (*D*-isocitrate) and product (2OG) at each time point (TP). The NMR measurements correspond to samples taken from the working electrode solution, and the concentrations shown are corrected for the volumes of samples taken/injections made. Conditions for (A): (FNR+IDH1)@ITO/Ti foil electrode, area 4 cm^2, solution agitated by stirring, temperature 25 °C, volume 4 mL, potential *E* (vs SHE) = +0.2 V, pH = 8 (100 mM HEPES, 10 mM $MgCl_2$). Enzyme loading ratios (molar): FNR/IDH1; 2/1.
*Note: After completion of the experiment, NMR analysis of the counter electrode solution showed that 0.78 µmoles of 2OG and 2.6 µmoles of isocitrate were present, having had crossed through the glass frit from the working electrode chamber during the experiment. The crossed-over 2OG was added to the timepoint 4 NMR value to calculate the total product made. When the isocitrate in the counter electrode solution is added to the calculation, the residual isocitrate (0.66 mM) + 2OG produced (5.88 mM) = 6.54 mM at timepoint 4, a value close to the total 6.5 mM of isocitrate initially added.

the glass frit that separated the working and counter electrode chambers (**Figure 41**). Incredibly, even though no NADP(H) had been added at any point, the nanoconfined IDH1-FNR-NADP(H) system was stable over a five-day period.

3.3.4 Quantification of FNR, IDH1, and NADP(H) in the Electrode Nanopores

3.3.4.1 The Longstanding Challenge of Non-electroactive Enzyme Quantification

It is straightforward to quantify the amount of (electroactive) FNR inside the electrode nanopores of the e-Leaf using cyclic voltammetry by integrating the average values of the oxidation and reduction non-turnover redox peaks resulting from the cooperative

two-electron transfer between the electrode and the FAD prosthetic group of FNR.[18] For example, based on eight 0.06 cm^2 electrodes loaded with FNR and wildtype IDH1 (2:1 molar ratio), the average FNR loading was 161 ± 19 pmoles cm^{-2} (± SD). However, the quantification of other enzymes has been a longstanding challenge that has gone unsolved. Dehydrogenases do not generally perform long-range electron transfer (they are not electroactive), and although indium tin oxide (ITO) is used commercially in touch-screen devices as a transparent conductive metal oxide, the mesoporous ITO layer of the e-Leaf is several microns thick and opaque, preventing analysis via spectroscopy. These limitations have led to a qualitative understanding of the relationship between the different e-Leaf enzymes which relies upon optimizing the enzyme molar loading ratios to achieve the desired performance.[1,26]

3.3.4.2 Thin-film Voltammetry Quantification of NADP(H) and IDH1

It was noted earlier that the "buffer only" voltammograms in **Figure 40B, D** did not exhibit the expected FNR non-turnover peaks but instead had peaks characteristic of NADP(H). This fact implies that the noncovalent IDH1-NADP(H) complex, although strongly biased toward the NADP(H) being bound at any given time, is in dynamic equilibrium. Thus, when transiently released from the enzyme, NADP(H) is able to be oxidized/reduced by an adjacent FNR molecule and measured as electrical current. Interestingly, this same property was previously exploited by Roman et al. to oxidize IDH1-copurified NADPH to $NADP^+$ via incubation of IDH1 alongside old yellow enzyme (which contains a flavin group that oxidizes NADPH) in order to generate a population of IDH1 molecules with only $NADP^+$ bound.[32]

The ability to detect the *finite* amount of IDH1-copurified NADPH via cyclic voltammetry offered a special opportunity to try to quantify the amount of NADP(H) present in the electrode nanopores; in doing so, it would also thus be straightforward to quantify the amount of IDH1 which carried the NADP(H) into the electrode. As mentioned, the amount of an adsorbed redox species (such as FNR) present in/on an electrode can be determined from the area under the non-turnover peaks of a cyclic voltammogram. However, NADP(H) is *not* an adsorbed redox-active species, and it has the additional complication of being in equilibrium with IDH1. Both of these facts indicate a time-dependency for measurement of non-adsorbed NADP(H). Therefore, the scan rate (the rate at which the applied potential is cycled) used will give different values for NADP(H), i.e., faster scan rates will allow less time for NADP(H) to reach an adjacent FNR molecule in the electrode to be measured and vice versa for slow scan rates. Although this may seem to make quantification more complicated, it is actually an advantage as it makes it possible to separate the FNR and NADP(H) signals—normally, the FNR and NADP(H) cyclic voltammetry redox signals are measured together as a single peak because their formal reduction potentials are close to one another (at pH = 8: $E^0{}'_{FNR}$ = –0.38 V, $E^0{}'_{NADP(H)}$ = –0.35 V) and because the peaks of non-adsorbed species (e.g., NADP(H)) are broader.

Using thin-film voltammetry, in which all redox-active species are present at the surface/inside of the electrode (i.e., a "thin film"), the nanoconfined IDH1-copurified NADP(H) was quantified. Dimeric wildtype IDH1 (0.85 nmoles) was loaded onto two 0.06 cm^2 electrodes with different amounts of FNR to give molar ratios of FNR/IDH1 = 2/1 and FNR/IDH1= 2/5 (**Figure 42** panels A and B, respectively). Cyclic voltammetry was then performed with each electrode at varied scan rates yielding scan rate-dependent apparent

electroactive coverages (termed Faradaic capacity) which represent the total amount of adsorbed FNR plus the amount of NADP(H) that was oxidized/reduced (**Figure 42A**, **B**) according to:

$$\text{Faradaic Capacity} = \Gamma_{FNR} + \Gamma^{*}_{NADP(H)}, \qquad \text{(Eq. 11)}$$

where Γ_{FNR} and $\Gamma^{*}_{NADP(H)}$ denote the FNR and NADP(H) coverages, respectively, in moles cm^{-2} (the NADP(H) term has an asterisk because it is not an adsorbed species and thus has a "coverage" that changes with the scan rate). As can be seen in **Figure 42A**, **B**, the Faradaic capacity of an electrode loaded only with FNR is not dependent on the scan rate because FNR is adsorbed. However, electrodes loaded with both FNR and IDH1 show higher coverages (FNR + NADP(H)) at low scan rates while the signal collapses to "FNR-only" at high scan rates in which there is not sufficient time to detect the transiently released, non-adsorbed NADP(H) (**Figure 42A**, **B**). Furthermore, the corresponding "trumpet plots", which show how the oxidation and reduction peak potentials change as a function of the scan rate, reflect the presence of NADP(H) only at low scan rates (**Figure 42C**, **D**): at a scan rate of 1 mV s^{-1}, electrodes loaded with both FNR and IDH1 (open circles) have a positive-shifted average redox peak potential of –0.35 V (the formal reduction potential of NADP(H)), but the peak potentials revert to values similar to the FNR-only electrode (solid squares) at higher scan rates (**Figure 42C**, **D**). Analogous experiments were carried out with an electrode co-loaded with FNR and IDH1 R132H which showed the same trends as the wildtype electrodes (**Figure 43**).

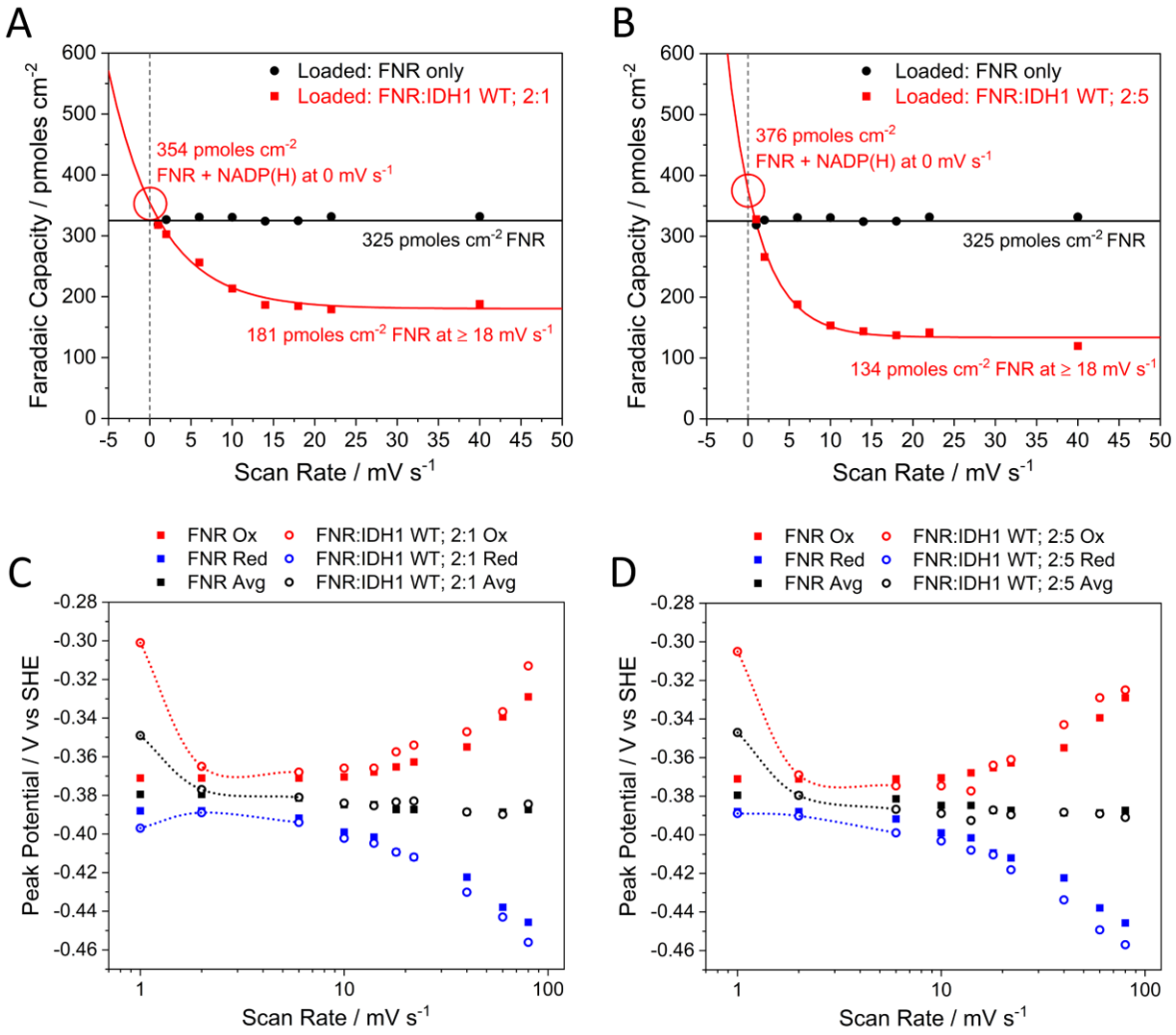


Figure 42. Scan rate-dependent Faradaic capacity (A and B) and trumpet plots (C and D) from thin-film voltammetry experiments using electrodes co-loaded with FNR and wildtype IDH1 compared to an FNR-only electrode. At low scan rates, the NADP(H) carried in with IDH1 can be detected; peaks collapse to the FNR-only signal at high scan rates. (A and B) Scan rate-dependent coverage plots fit by an asymptotic exponential equation to allow extrapolation to 0 mV s^{-1}. (C and D) Trumpet plots showing the changes in oxidation and reduction peak potentials as a function of scan rate (see trend lines). Conditions: stationary (FNR+IDH1)@ITO/PGE electrode (except for FNR-only data, which did not contain IDH1), electrode area 0.06 cm^2, temperature 25 °C, volume 4 mL, pH = 8 (100 mM HEPES), and enzyme loading ratios (molar): (A and C): FNR/IDH1; 2/1; (B and D): FNR/IDH1; 2/5.

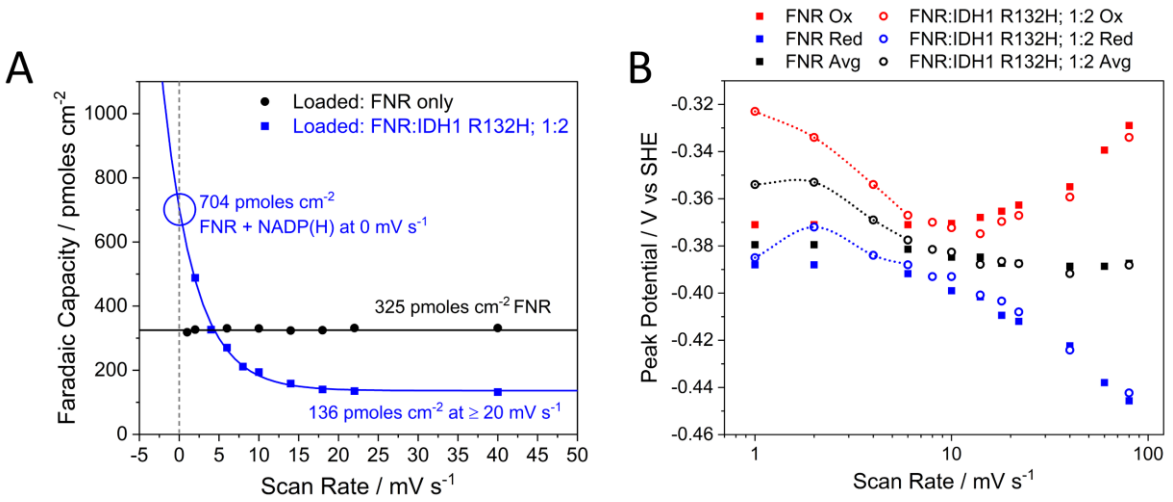


Figure 43. Scan rate-dependent Faradaic capacity (A) and trumpet plot (B) from thin-film voltammetry experiments using an electrode co-loaded with FNR and IDH1 R132H compared to an FNR-only electrode. At low scan rates, the NADP(H) carried into the electrode nanopores with IDH1 R132H can be detected; peaks collapse to the FNR-only signal at higher scan rates. (A) Scan rate dependent coverage plot fit by an asymptotic exponential equation to allow extrapolation to 0 mV s^{-1}. (B) Trumpet plot showing the changes in oxidation and reduction peak potentials as a function of scan rate (see trend lines). Conditions: stationary (FNR+$IDH1_{R132H}$)@ITO/PGE electrode (except for FNR-only data, which did not contain $IDH1_{R132H}$), electrode area 0.06 cm^2, temperature 25 °C, volume 4 mL, pH = 8 (100 mM HEPES), enzyme loading ratios (molar): FNR/$IDH1_{R132H}$; 1/2.

Importantly, the FNR-only electrode exhibited peak currents that varied linearly with the scan rate, ν, (**Figure 44**) as expected according to the equation describing the peak current of a voltammogram for an adsorbed redox-active species:[86]

$$I_{peak} = \frac{n^2 F^2 A \Gamma_{total} \nu}{4RT}, \qquad \text{(Eq. 12)}$$

where I_{peak} is the peak current, n is the number of electrons transferred, F is the Faraday constant, A is the electrode area, Γ_{total} is the total enzyme coverage, R is the ideal gas constant, and T is the temperature. In contrast, electrodes loaded with both FNR and IDH1 did not show peak currents that were linear with the scan rate (**Figure 44**). Together, these observations confirm that the copurified NADP(H) can be detected using cyclic voltammetry but only at sufficiently low scan rates that allow the NADP(H) to be transiently released by

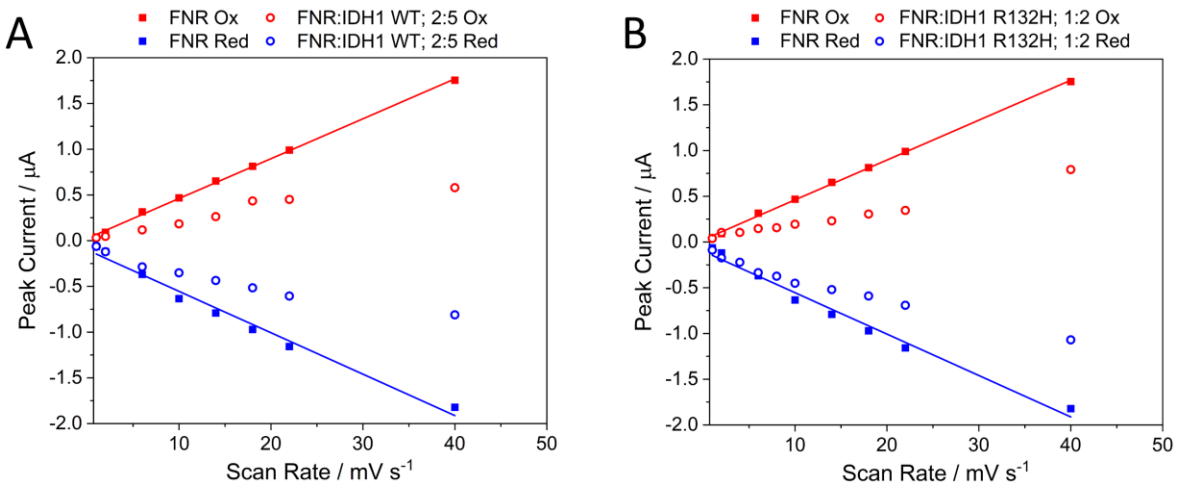


Figure 44. Cyclic voltammetry peak current values plotted against scan rate for an FNR only electrode (solid squares) and electrodes co-loaded with both FNR and IDH1 (open circles). The plots show that when FNR is loaded alone, the peak current is linear with scan rate as expected for an adsorbed electroactive protein (Eq. 12). However, when FNR is co-loaded with wild-type IDH1 (A) or IDH1 R132H (B), the peak current is not linear with scan rate indicating the presence of an electroactive species that is not adsorbed (NADP(H)).

IDH1 for oxidation/reduction by FNR.

Because there was no NADP(H) in the bulk solution, the total amount of NADP(H) present could be estimated by extrapolating the Faradaic capacity to a scan rate of 0 mV s^{-1}, a theoretical condition in which infinite time is allowed for each oxidation/reduction cycle ensuring that all NADP(H) is detected (**Figure 42A**, **B**). The amount of FNR present in each FNR/IDH1 electrode is determined from voltammograms at high scan rates where the Faradaic capacity collapses to the FNR-only signal; thus, this component of the Faradaic capacity can be subtracted out leaving only the component due to NADP(H) (Eq. 11). With the ability to separately quantify FNR and the nanoconfined NADP(H) carried in by IDH1, it was possible to calculate the amount of IDH1 present based on the measured NADP(H) active site occupancies (**Figure 36**). The amounts of FNR, NADP(H), and IDH1 present in four different electrodes are shown in **Table 2**.

3.3.4.3 Estimating Enzyme and NADP(H) Concentrations in the Electrode Nanopores

Having determined the total amount of FNR, NADP(H), and IDH1 present in the electrode, it was of interest to estimate the concentration of each species inside the nanopores of the electrode. Estimating concentrations required two assumptions: (1) that the electrode was 3–6 μm thick—this is a reasonable assumption based on previous scanning electron microscopy (SEM) measurements using the same e-Leaf electrode fabrication procedure[18] and (2) that the ITO has a 50% packing volume, i.e., 50% of the available space within the 3–6 μm layer is occupied by the ITO particles.[4,87] With these assumptions, the internal

Table 2. Enzymes and NADP(H) Quantified in the Electrode Nanopores and their Estimated Nanoconfined Concentrations

Enzymes present	Loading Ratio	FNR/ pmol cm^{-2}	NADP(H)/ pmol cm^{-2}	$IDH1_{dimer}$/ pmol cm^{-2}	$[FNR]_{pore}$/ mM	$[NADP(H)]_{pore}$/ mM	$[IDH1_{dimer}]_{pore}$/ mM
FNR	–	325	–	–	1.08–2.17	–	–
FNR, IDH1	2:1	181	173	188	0.60–1.21	0.58–1.15	0.63–1.25
FNR, IDH1	2:5	134	242	263	0.45–0.89	0.81–1.61	0.88–1.75
FNR, R132H	1:2	136	568	291	0.45–0.91	1.89–3.79	0.97–1.94

Note: Concentrations of species in the electrode nanopores ($[X]_{pore}$) were calculated assuming a 3 to 6-μm thick ITO layer and a 50% packing volume (see text). $IDH1_{dimer}$ values were calculated from quantified NADP(H) based on the measured NADP(H):$IDH1_{dimer}$ stoichiometry (46% active site occupancy for wildtype IDH1 and 97.5% occupancy for IDH1 R132H) (see text, **Figure 36**). Approximate maximum error limits are as follows: FNR coverage, ±10%; NADPH coverage, ±15%; IDH1 coverage ±20%; and concentrations ±25%.

volume of a 0.06 cm^2 mesoporous ITO electrode was estimated to be 9–18 nL (150–300 nL for a 1 cm^2 electrode). This volume range was used to estimate the nanoconfined concentrations of each species (**Table 2**).

The values in **Table 2** indicate that the enzymes are extremely concentrated inside the nanopores of the electrode. Being within the millimolar range, both FNR and IDH1 must be approaching their maximum theoretical concentrations; for example, the average center-to-center distance of a 1 mM solution is 11.8 nm.[88] Further evidence of the enzymes reaching a possible concentration limit is the observation that changing the enzyme loading ratio, e.g., reducing the amount of FNR while keeping IDH1 constant, resulted in changes in the amounts of quantified FNR and IDH1 in a manner consistent with the loading ratio used, suggesting that the enzymes compete for space in the electrode (**Table 2**). Maximum theoretical enzyme concentrations can be estimated if the enzymes are treated as perfect spheres with a diameter that is equivalent to their longest dimension according to the simple equation:[4,88]

$$[\mathrm{E}]_{\max} = \left(\frac{1.18}{d}\right)^3, \qquad \text{(Eq. 13)}$$

where $[\mathrm{E}]_{\max}$ is the maximum theoretical enzyme concentration (M) and d is the average center-to-center distance between molecules (nm). In the case of FNR and IDH1, which have maximum lengths of approximately 5.5 and 7.8 nm, respectively, their maximum theoretical solution concentrations are thus 9.9 mM for FNR and 3.5 mM for IDH1 (wildtype and variant). An alternative maximum theoretical concentration can be estimated using crystallographic unit cells; in the case of FNR and wildtype IDH1, the concentrations are 4.6 and 0.8 mM, respectively.[4] Significantly, these values are lower than the aforementioned concentrations due to the fact that protein crystals impose unit cell geometries that do not allow the most space-efficient packing. Taking average values for the range of concentrations given for each enzyme in **Table 2** (the condition where the ITO layer is 4.5 μm thick), the

total enzyme concentration in the electrode (i.e., [FNR] + [IDH1]) was approximately 2 mM in all cases where both FNR and IDH1 were loaded. At this concentration, the average enzyme center-to-center distance is 9.4 nm.

3.3.5 Estimating NADP(H) and Enzyme Total Turnover Numbers

It is astounding that the nanoconfined IDH1-FNR system was able to convert ~24 μmoles of isocitrate to 2OG using only the tiny amount of NADP(H) that copurified with IDH1 (**Figure 41**). Importantly, the nicotinamide cofactors (NAD(P)(H)), and sometimes the enzymes themselves, are among the most expensive inputs for cofactor-dependent biocatalytic applications.[89] As a result, cofactor recycling systems are generally employed, and the efficiency of the recycling system is measured by the total turnover number (TTN)[90] of the cofactor and/or the enzyme(s) according to Eq. 14.

$$\text{TTN} = \frac{\text{moles of product}}{\text{moles of cofactor/catalyst used}} \qquad \text{(Eq. 14)}$$

With the ability to quantify both the nanoconfined NADP(H) and enzymes (**Table 2**), it was thus possible to estimate the $TTN_{NADP(H)}$ and TTN_{Enzyme} for the scaled-up experiment in **Figure 41**. Using the data in **Table 2** as a guide, the amount of wildtype IDH1 present in the 4 cm^2 electrode was estimated by scaling-up from the 0.06 cm^2 electrode loaded with the same FNR/IDH1 ratio of 2/1 ratio. Adjusting for the lower FNR coverage on the larger 4 cm^2 electrode (40 pmol cm^{-2}), and assuming the same final FNR/IDH1 ratios were present in the electrode, the $IDH1_{dimer}$ coverage was estimated to be 41.5 pmol cm^{-2}. Based on the average IDH1 active site occupancy of 46% (**Figure 36**), the total amount of NADP(H) used in the reaction was estimated to be 153 pmoles. Taking the average value of 2OG product as

quantified by the total charge passed and by ^{1}H NMR (24.5 μmoles; **Figure 41B**), the $TTN_{NADP(H)} \approx 160{,}000$. The total turnover numbers for each of the enzymes are: $TTN_{FNR} \approx 153{,}000$ and $TTN_{IDH1} \approx 148{,}000$.

Taken together, the special nanoconfined IDH1-FNR-NADP(H) system is extremely efficient in terms of both the use of NAD(P)(H) and enzyme. In fact, a survey of the literature reveals that it is orders of magnitude more efficient (regarding the use of both enzyme and NADP(H)) than any other system reported to date.[89,91–93] It is also notable that the scaled-up experiment presented in **Figure 41** was the first of such experiments to be performed, i.e., there was no optimization, and the goal of the experiment was merely to test if bulk synthesis was possible using only copurified NADP(H). There is no doubt that higher total turnover numbers, perhaps approaching or exceeding 1,000,000, could be achieved through optimization and by extending the duration of the experiment.

3.3.5.1 A New Metric for Comparing the Efficiency of Cofactor Recycling Systems: the "Total Turnover Product"

Based on the aforementioned survey of the literature,[89,91–93] it was stated that the IDH1-FNR-NADP(H) system is more efficient than any other system reported in terms of the use of *both* enzyme and NADP(H). However, achieving very high total turnover numbers within a single domain (cofactor *or* enzyme), while still uncommon, is more straightforward because the other components can be used in large quantities; in doing so, the system becomes less efficient overall. For example, to my knowledge, there is only one other system with a reported $TTN_{NAD(P)(H)}$ that is within the same order of magnitude as that reported here: using a glutathione-based NADP(H) recycling system, a $TTN_{NADP(H)}$ of ~500,000 was

achieved.[94] However, this was only possible because the concentration of $NADP^+$ was reduced to 10 nM, increasing its efficiency of use, with the consequence being that higher enzyme concentrations were required to compensate. As a result, the highest TTN_{Enzyme} achieved within the cascade was 10,000 and the lowest TTN_{Enzyme} was just 2,500.[94]

As a means to improve comparisons made between cofactor recycling systems, I propose a new metric which takes into account the overall efficiency of the system, the total turnover product (TTP):

$$TTP = TTN_{Cofactor} \times TTN_{Catalyst}, \quad \text{(Eq. 15)}$$

where the $TTN_{Catalyst}$ can be any catalyst including an enzyme. For the TTP calculation, the least efficient (limiting) catalyst/enzyme $TTN_{Catalyst}$ value should be used. Based on the TTN values calculated for the experiment in **Figure 41**, the TTP (using the lower TTN_{IDH1}) is $2.4x10^{10}$, which is an order of magnitude larger than the $1.3x10^9$ achieved in the aforementioned study.

3.3.6 Enzymes *and* NADP(H) remain Nanoconfined Following Buffer Exchanges

Running the e-Leaf using only IDH1-copurified NADP(H) requires that the NADP(H) remains trapped in the electrode nanopores to be recycled locally. If the NADP(H) were to escape the pores and enter the bulk solution, it would be diluted to negligible levels and effectively no current would be measured. It was therefore surprising that system showed such long-term stability without added NADP(H) as demonstrated by the five-day scaled-up experiment (**Figure 41**). In contrast, other e-Leaf experiments with alcohol dehydrogenase (ADH) showed that NADP(H) can exchange between the electrode pores and the bulk

solution: following a buffer exchange, in which the reaction solution was removed and replaced with fresh buffer containing substrate but not NADP(H), the current quickly dropped to 0 A as a result of the residual NADP(H) in the electrode escaping into the bulk solution.[25] How then did the miniscule amount of NADP(H) that copurified bound to IDH1 remain trapped in the electrode for ~5 days once it was released from the enzyme after substrate binding and/or the first turnover?

To investigate if the mechanism by which NADP(H) remained trapped in the electrode nanopores relied on enzyme turnover, buffer exchange experiments were carried out for both wildtype IDH1 and IDH1 R132H (**Figure 45**). First, each reaction was initiated by the addition of substrate (isocitrate for wildtype and 2OG for R132H) and the reaction was allowed to reach a steady-state with electrode rotation maintaining a constant substrate flux. A "live" buffer exchange was then performed where the reaction solution was serially diluted (>1000-fold) using a solution with the same composition (also without any NADP(H)) in order to confirm that nothing in the bulk solution was contributing to the measured currents. The serial dilution was performed while carefully maintaining electrical contact so that the rate of the reaction could be monitored even during the procedure (**Figure 45**). Following the buffer exchange, the wildtype current dropped by ~15% likely as a result of some of the NADP(H) located close to the electrode surface being washed out of the electrode (**Figure 45A**). Interestingly, the current for the IDH1 R132H reaction remained unchanged (**Figure 45B**). Despite the small decrease in activity for the wildtype, the first buffer exchange confirmed that both the enzymes *and* NADP(H) are present *only* in the electrode nanopores. After again establishing a steady-state catalytic current, a second buffer exchange was performed, but this time the exchange buffer did not contain the enzyme substrate. The

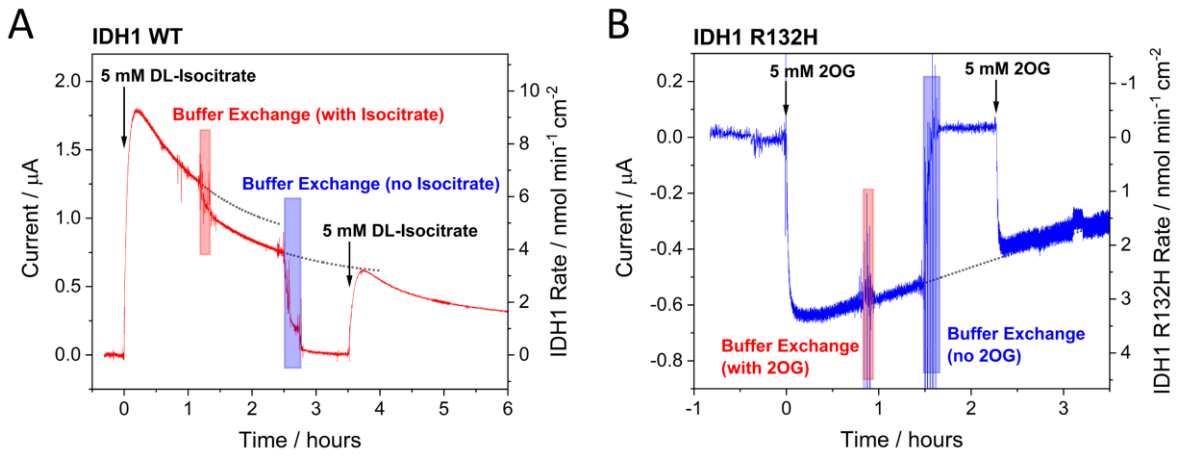


Figure 45. Chronoamperometry experiments showing steady-state catalysis by wildtype IDH1 (isocitrate oxidation to 2OG) and IDH1 R132H (2OG reduction to 2HG) using only copurified enzyme-bound NADP(H) interrupted by live buffer exchanges. The first buffer exchange (>1,000-fold dilution) used the starting buffer solution with 5 mM substrate (*DL*-isocitrate or 2OG) in order to maintain IDH1 catalysis. The second buffer exchange (~55,000-fold dilution) was performed using the starting buffer solution without any substrate present. Conditions: (FNR+E2)@ITO/PGE electrode (E2 represents wildtype or R132H IDH1), area 0.06 cm^2, electrode rotated at 1000 rpm, temperature 25 °C, volume 2.6 mL, pH = 8 (100 mM HEPES, 10 mM $MgCl_2$), potential *E* (vs SHE) = +0.2 V for wildtype IDH1 or –0.5 V for IDH1 R132H. Enzyme loading ratios (molar): FNR/$IDH1_{WT}$; 2/1 or FNR/$IDH1_{R132H}$; 1/2.

second buffer exchange without substrate resulted in the currents of both reactions to drop to 0 A as expected. This condition was used to test the hypothesis that coupled enzyme turnover, i.e., the internal rapid recycling of NADP(H) between FNR and IDH1, was what allowed the NADP(H) to remain nanoconfined. Without enzyme turnover, the electrode was left for ~45 minutes to allow any unbound NADP(H) to escape the electrode nanopores where it would be diluted to a negligible concentration in the bulk solution. Finally, enzyme substrate was added to the reaction solution to see if any activity remained. In both cases, the currents quickly resumed at the levels which would have been expected if no intervention had been made, indicating that the NADP(H) remains trapped in the electrode nanopores even when enzyme turnover is stopped (**Figure 45**). **Figure 46** shows examples of reactions without interventions that were used as models for the current extrapolation (dotted lines in **Figure 45**).

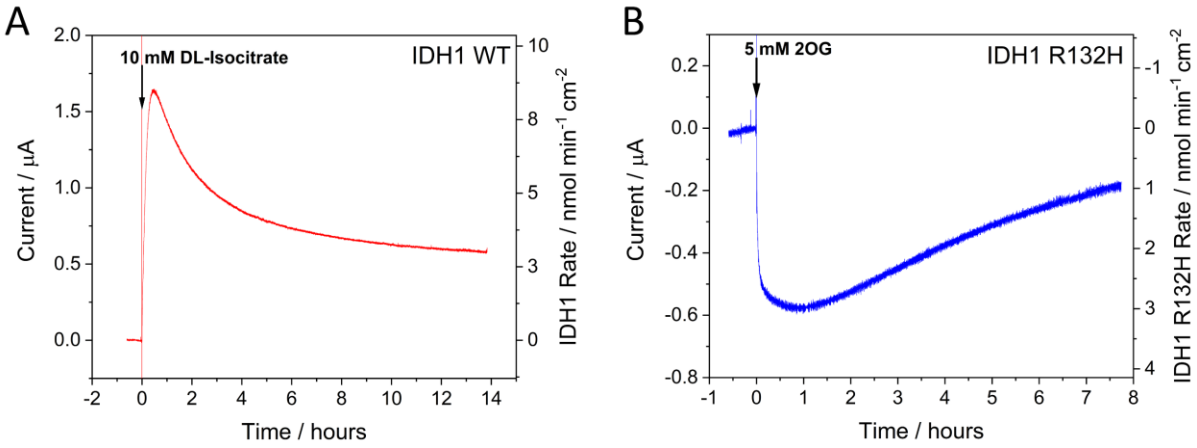


Figure 46. Electrochemical experiments showing the activity of wildtype IDH1 (A) and IDH1 R132H (B) upon injection of substrate without added NADP(H). Conditions (A and B): (FNR+E2)@ITO/PGE electrode (E2 represents wildtype or R132H IDH1), area 0.06 cm^2, temperature 25 °C, volume 4 mL, pH = 8 (100 mM HEPES, 10 mM $MgCl_2$, electrode rotated at 1000 rpm. (A): potential *E* (vs SHE) = +0.2 V, molar loading ratio: FNR/IDH1; 2/1. (B): potential *E* (vs SHE) = −0.5 V, molar loading ratio: FNR/IDH1 R132H; 1/2.

The buffer exchange experiments imply that, unlike other enzymes in the e-Leaf, wildtype IDH1 and IDH1 R132H are able to rebind $NADP^+$ and NADPH, respectively, in order to prevent it from escaping the electrode nanopores. Presumably, NADP(H) rebinding occurs between catalytic cycles when the enzyme is in the open inactive conformation which has a very high affinity for NADP(H) as assumed from copurification.[32] Significantly, the tightly bound NADP(H) is released again when substrate binds and/or turnover occurs allowing it to participate in cascade catalysis while remaining trapped in the electrode nanopores.

3.3.6.1 Wildtype IDH1 Tightly Rebinds both $NADP^+$ and NADPH while IDH1 R132H only Rebinds NADPH

Because wildtype IDH1 and IDH1 R132H catalyze different reactions, one being an oxidation and the other a reduction, a second set of buffer exchange experiments were

performed to see if the redox state of NADP(H) affected its rebinding by either enzyme during a pause in turnover (**Figure 47**). For the wildtype IDH1 experiment (**Figure 47A**), the same procedure as before was followed whereby the reaction was initiated by the addition of substrate followed by a buffer exchange using a buffer of identical composition to the reaction solution. Consistent with the previous set of experiments, the current for wildtype

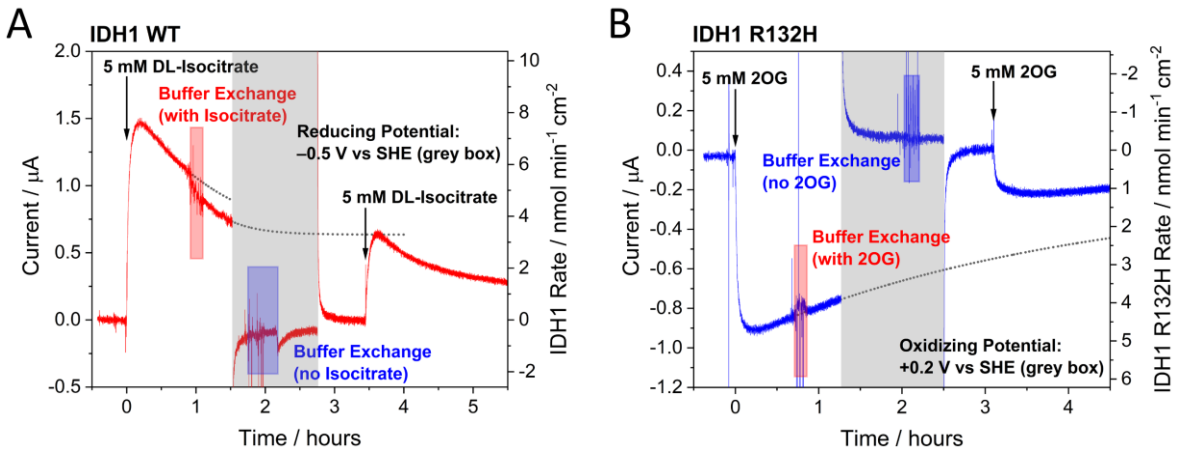


Figure 47. Chronoamperometry experiments showing steady-state catalysis by wildtype IDH1 and IDH1 R132H using only copurified enzyme-bound NADP(H), interrupted by live buffer exchanges and potential switches. The first buffer exchange (>1,000-fold dilution) used the starting buffer solution with 5 mM substrate (*DL*-isocitrate or 2OG) added to maintain IDH1 catalysis; the second buffer exchange (~55,000-fold dilution) was performed using the starting buffer solution without any added substrate. (A) the potential was switched from oxidizing (+0.2 V) to reducing (−0.5 V) (timespans indicated by grey boxes) to convert all of the nicotinamide in the pores to NADPH. (B) the potential was switched to an oxidizing value (+0.2 V). Conditions: (FNR+E2)@ITO/PGE electrode (where E2 represents wildtype IDH1 or IDH1 R132H), area 0.06 cm^2, electrode rotated at 1000 rpm, temperature 25 °C, volume 2.6 mL, potential *E* (vs SHE) = +0.2 V for wildtype IDH1 or –0.5 V for IDH1 R132H (except where potential switches are indicated by grey boxes), pH = 8 (100 mM HEPES, 10 mM $MgCl_2$). Enzyme loading ratios (molar): FNR/$IDH1_{WT}$; 2/1 or FNR/$IDH1_{R132H}$; 1/2.

IDH1 dropped by ~15% before again reaching a steady state. This time, however, before the second buffer exchange, the potential was switched from oxidizing (+0.2 V) to reducing (−0.5 V) to rapidly convert all of the $NADP^+$ in the electrode to NADPH. Once the current reached a steady state around 0 A (no reaction occurs because $NADP^+$ is no longer recycled for use by IDH1), the second ~55,000-fold dilution buffer exchange was performed without

isocitrate present. Again, the electrode was left for ~45 minutes to allow any unbound NADPH to escape the electrode pores before the electrode potential was switched back to oxidizing. Interestingly, when isocitrate was added back to the solution, the current resumed at the magnitude expected if no intervention had been made (**Figure 47A**) indicating that wildtype IDH1 is capable of rebinding both $NADP^+$ and NADPH between catalytic cycles (presumably in the open inactive conformation).

The same experiment was performed with IDH1 R132H except that the reducing potential used to drive 2OG reduction (–0.5 V) was switched to an oxidizing potential (+0.2 V) prior to the second buffer exchange in order to convert all of the NADPH in the electrode to $NADP^+$ (**Figure 47B**). Unlike the wildtype enzyme, however, when 2OG was added back into the reaction solution after the second buffer exchange, the current resumed at value that was less than 50% of the value expected from extrapolation (**Figure 47B**). This result suggests that IDH1 R132H does not rebind $NADP^+$ as efficiently as NADPH.

In order to confirm that wildtype IDH1 can rebind both $NADP^+$ and NADPH but IDH1 R132H can only efficiently rebind NADPH, a set of oscillating potential switch experiments were performed (**Figure 48**). These chronoamperometry experiments offer an alternative method to test the NADP(H) rebinding efficiency by switching the potential of the electrode between oxidizing and reducing at 30-minute intervals. Thus, under conditions where either enzyme did not rebind NADP(H), electrode rotation would cause any unbound NADP(H) to escape the pores and be lost to the bulk solution where it would not contribute to the current. For both enzymes, steady state current was first established following addition of enzyme substrate before the potential was oscillated causing enzyme turnover to stop and resume in cycles (**Figure 48**). In the case of wildtype IDH1, stopping catalysis and converting

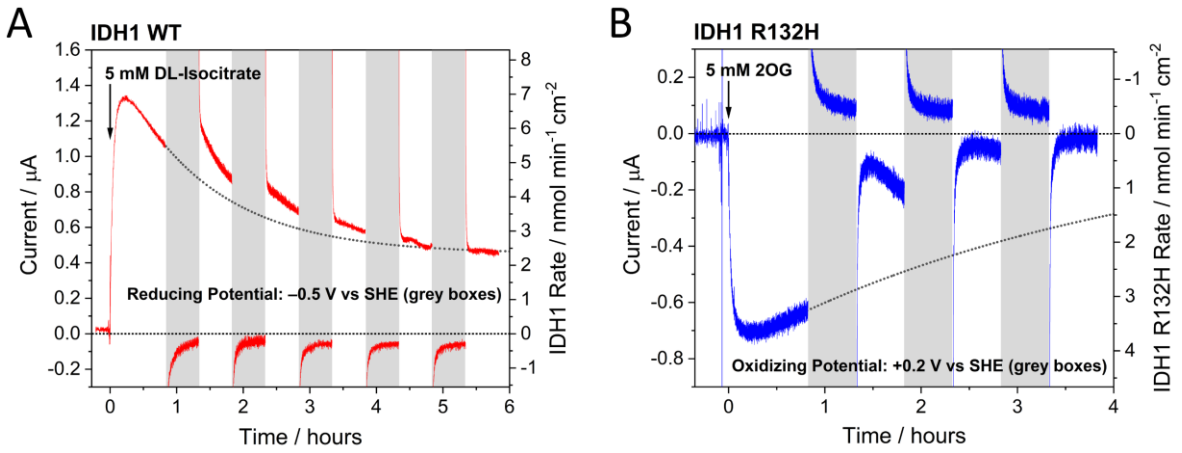


Figure 48. Oscillating potential switch chronoamperometry experiments showing steady-state catalysis by wildtype IDH1 (isocitrate oxidation to 2OG) and IDH1 R132H (2OG reduction to 2HG) using only copurified enzyme-bound NADP(H) interrupted by potential switches. (A) wildtype IDH1 can rebind both $NADP^+$ and NADPH. (B) IDH1 R132H has a much lower affinity for $NADP^+$ compared to NADPH. Conditions: (FNR+E2)@ITO/PGE electrode (where E2 represents wildtype IDH1 or IDH1 R132H), area 0.06 cm^2, electrode rotated at 1000 rpm, temperature 25 °C, pH = 8 (100 mM HEPES, 10 mM $MgCl_2$), volume 2.6 mL, potential *E* (vs SHE) = +0.2 V for wildtype IDH1 (A) or −0.5 V for IDH1 R132H (B) except where potential switches are indicated by grey boxes. Enzyme loading ratios (molar): $FNR/IDH1_{WT}$; 2/1 or $FNR/IDH1_{R132H}$; 1/2.

nanoconfined $NADP^+$ into NADPH did not result in a decrease in measured current when catalysis was resumed implying that the enzyme was able to efficiently rebind the NADPH formed during reductive periods (**Figure 48A**). In stark contrast, after the first oxidative period for IDH1 R132H, where nanoconfined NADPH was converted to $NADP^+$, the current dropped to a value of less than 50% the expected value. After two more cycles, the current was at 0 A (i.e., no IDH1 R132H activity was detected) meaning that IDH1 R132H was not able to efficiently rebind $NADP^+$ (**Figure 48B**). Both results are consistent with the experiments shown in **Figure 47**.

Together, the results show that wildtype IDH1, in the open inactive conformation, is able to efficiently rebind both $NADP^+$ and NADPH between catalytic cycles. As previously mentioned in this chapter, the open inactive conformation of IDH1 must have a very high affinity for NADP(H) that is not represented by reported K_m values for NADP(H)[35,40] because

such values reflect only the affinity of IDH1 conformations that pertain to enzyme turnover. In contrast to the wildtype, IDH1 R132H can only efficiently rebind NADPH. This is consistent with the ^{1}H NMR experiments, which showed that the wildtype enzyme copurified with a mixture of $NADP^{+}$ and NADPH but that IDH1 R132H copurified exclusively with NADPH (**Figure 35**). Furthermore, this cofactor selectivity is consistent with the reactions that each enzyme performs: wildtype IDH1 catalyzes the NADP(H)-dependent *bidirectional* isocitrate to 2OG, CO_2 reaction, while IDH1 R132H catalyzes the *unidirectional* NADPH-dependent 2OG to 2HG reaction. Interestingly, despite only binding NADPH with high efficiency, IDH1 R132H may have a higher affinity for NADPH than IDH1 does for either form of the cofactor. The ^{1}H NMR and non-denaturing mass spectrometry results showed that wildtype IDH1 copurified with less total NADP(H) than IDH1 R132H, which had an NADPH molecule bound to nearly every active site (46% active site occupancy versus 97.5%). Furthermore, a 15% drop in current was measured for the wildtype enzyme in two independent experiments following the first buffer exchange (**Figure 45** and **Figure 47**) whereas essentially 100% activity was maintained for R132H in both cases. The selectivity and extremely high affinity of "resting" IDH1 R132H for NADPH may thus have in vivo mechanistic importance by biasing the enzyme toward catalyzing the cancer-associated 2OG to 2HG reaction even under conditions where the NADPH/$NADP^{+}$ ratio is low or where NADPH is scarce.

3.3.7 Nanoconfinement Greatly Enhances NADP(H) Recycling Efficiency

An advantage of nanoconfinement for enzyme cascade catalysis is that intermediates and exchangeable cofactors are predominantly retained, i.e., intermediates/cofactors are

more likely to be consumed/recycled by an adjacent enzyme rather than escaping into the bulk solution. Capable of being run without any added NADP(H), the FNR-IDH1-NADP(H) system presented a special opportunity to quantify the nanoconfinement advantage.

Two experiments were carried out using a single electrode that was co-loaded with FNR and wildtype IDH1. The same electrode was used for both experiments to enable direct comparison by eliminating possible differences in the ITO layer thickness or the amount of enzyme present (**Figure 49A**, **B**). In the first experiment, $NADP^+$ was titrated into solution with isocitrate and Mg^{2+} already present; the measured current was thus proportional to the rate of isocitrate oxidation catalyzed by IDH1 with $NADP^+$ being recycled by FNR (**Figure 49A**). Additions of increasing concentrations of $NADP^+$ resulted in a rapid rise in current that reached a maximum before exhibiting slight substrate inhibition. After the first experiment, the electrode was removed from solution and thoroughly rinsed to remove any residual isocitrate and $NADP^+$ in the electrode. The reaction solution was then exchanged for buffer that did not contain Mg^{2+} or isocitrate, and the second experiment was performed. This time, NADPH was titrated into solution, but because no Mg^{2+} or isocitrate was present in the reaction solution, the current was solely due to the direct electrochemical oxidation of NADPH catalyzed by FNR, i.e., no NADP(H) recycling occurred within the electrode nanopores (**Figure 49B**). The experiment shown in **Figure 49B** was fit using a modified form of the Michaelis-Menten equation (see **Chapter VII** for derivation) that shows how the electrical current varies with the substrate concentration:

$$I = \frac{nAF\Gamma k_{cat(nano)}[S]}{K_{m(nano)} + [S]}, \qquad \text{(Eq. 16)}$$

where I is the measured current (A), n is the number of electrons transferred per molecule, A

is the electrode surface area (cm^2), F is the Faraday constant (96485 C), [S] is the substrate concentration, Γ is the enzyme coverage (moles cm^{-2}), $k_{cat(nano)}$ is the maximum turnover frequency (s^{-1}) of the rate-determining enzyme, and $K_{m(nano)}$ is the apparent Michaelis constant of a nanoconfined enzyme. The experiment carried out in **Figure 49A** exhibited substrate inhibition; therefore, Eq. 16 was modified (see **Chapter VII**) to account for the inhibitory effect (K_i) at high [$NADP^+$]:

$$I = \frac{nAF\Gamma k_{cat(nano)}[S]}{K_{m(nano)} + [S] + \frac{[S]^2}{K_i}}. \qquad \text{(Eq. 17)}$$

Upon comparing the experiments in panels A and B of **Figure 49**, it is immediately apparent that the experiment in panel A, which relied on nanoconfined NADP(H) recycling, used NADP(H) much more efficiently than the experiment in which NADPH was directly consumed by FNR. Specifically, $K_{m(nano)}$ for the "FNR-only" experiment was 670-fold higher than the IDH1-FNR cascade experiment (6.7 mM vs 10 μM). Importantly, the FNR-only current was still limited by the mass transport of NADPH even at an electrode rotation rate of 4000 rpm while the IDH1-FNR cascade experiment did not show increased current at rotation rates above 1000 rpm, consistent with internal NADP(H) recycling being rate limiting (**Figure 49**). The massive (670-fold) difference in NADP(H) usage efficiency is clear when the data sets are plotted together on a semi-log plot (**Figure 49C**). Significantly, unlike the Michaelis-Menten plots for nanoconfined enzymes shown in **Chapter II**, here it was possible to estimate the $k_{cat(nano)}$ values for nanoconfined IDH1 and FNR using the fitted equations because the enzyme coverages of FNR and IDH1 can now be determined (**Table 2**). The $k_{cat(nano)}$ values determined from fitting the data ($R^2 > 0.99$ for both data sets) were 13 s^{-1} for the data in **Figure 49A** and 36 s^{-1} for the data in **Figure 49B**, equating to the

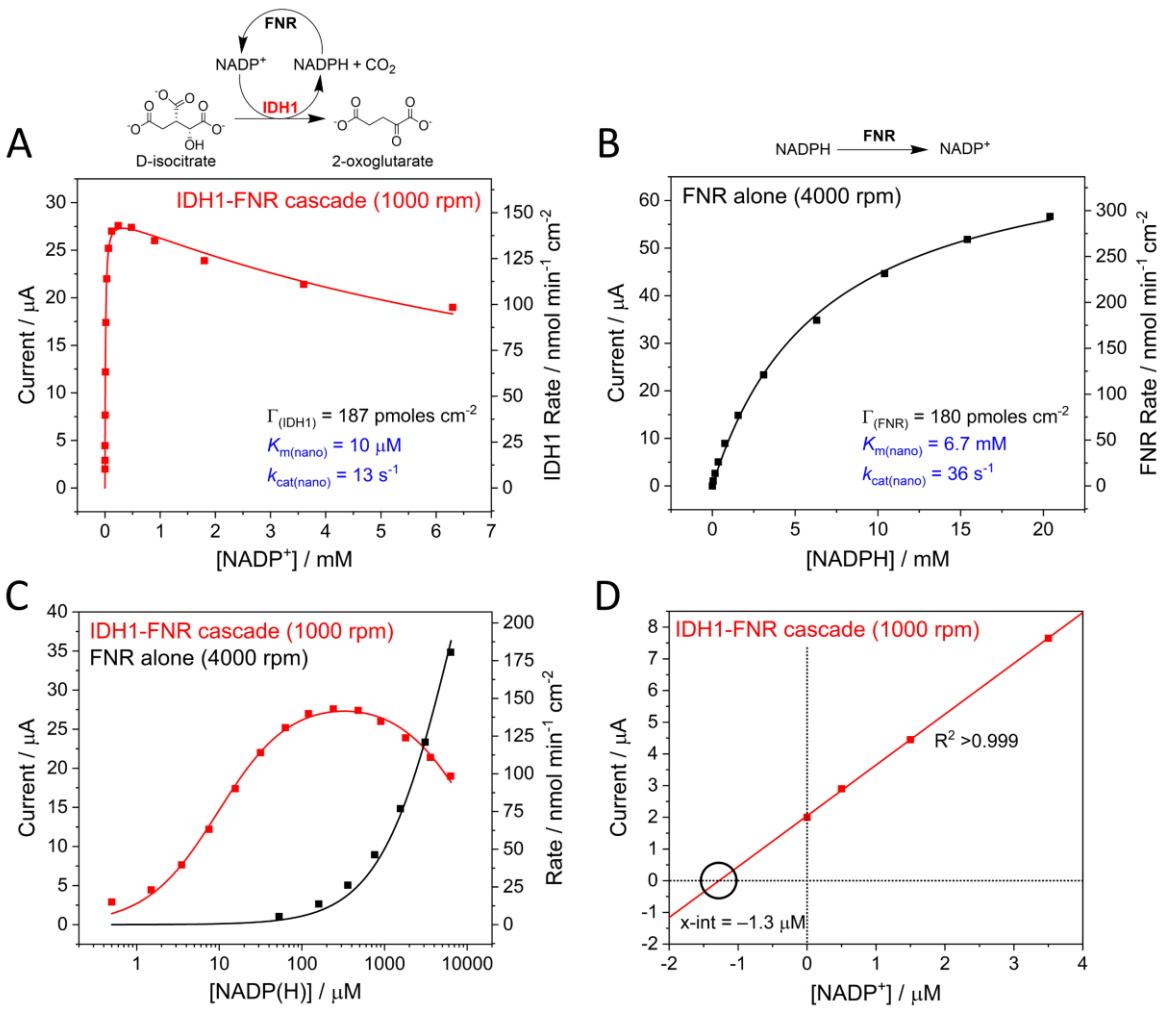


Figure 49. Nanoconfined electrochemical enzyme kinetics measuring the activity of the IDH1-FNR cascade (A) and FNR alone (B) fit by derived electrochemical-kinetic equations (Eq. 17 (A) and Eq. 16 (B)). The same electrode was used in both (A) and (B), which contained both FNR and IDH1 loaded in a 2:1 ratio. (A) Rate of isocitrate oxidation at increasing concentrations of $NADP^+$ (NADP(H) is recycled between IDH1 and FNR). (B) Rate of NADPH oxidation by nanoconfined FNR at increasing concentrations of NADPH. (A and B) The enzyme coverages (shown in black) were used as inputs for the fitted equations, while those in blue were determined by fitting the equations to the data. The data in (A) were fit using Eq. 17 to account for the slight substrate inhibition observed ($K_{i(nano)}$ = 11 mM). Both equations fit to the data sets had an $R^2 > 0.99$. (C) Data from (A) and (B) compared on a semi-log plot. (D) The first four data points in panel A extrapolated to the x-intercept to estimate the *effective* NADP(H) solution concentration of the nanoconfined IDH1-copurified NADP(H) (see text). Conditions (A and B): (FNR+IDH1)@ITO/PGE electrode, area 0.06 cm^2, temperature 25 °C, volume 4 mL, potential E (vs SHE) = +0.2 V, pH = 8 (100 mM HEPES), enzyme loading ratios (molar): FNR/IDH1; 2/1. (A): buffer also contained: 10 mM $MgCl_2$, 10 mM *DL*-isocitrate; electrode rotated at 1000 rpm. (B): electrode rotated at 4000 rpm.

maximum turnover frequencies of IDH1 and FNR, respectively, under nanoconfinement.

Under comparable conditions, standard solution assays yielded k_{cat} values of 86 s^{-1} for

IDH1[40] and 51 s^{-1} for FNR (**Figure 50**). The greater decrease in turnover rate for IDH1 under nanoconfinement compared to FNR (turnover is 6.6-fold faster in solution for IDH1 compared to 1.4-fold faster for FNR) could perhaps result from the highly crowded environment ([FNR] + [IDH1] ≈ 2 mM (**Table 2**)) hindering the larger conformational changes required for IDH1 turnover compared to FNR; however, further experiments would be needed to confirm this. Interestingly, the $K_{m(nano)}$ value measured for IDH1 in **Figure 49A** is very close to K_m values measured for IDH1 in dilute solution.[35,40] The $K_{m(nano)}$ and solution K_m values of IDH1 R132H for 2OG were also shown to be very similar in **Chapter II** (**Figure 14**).

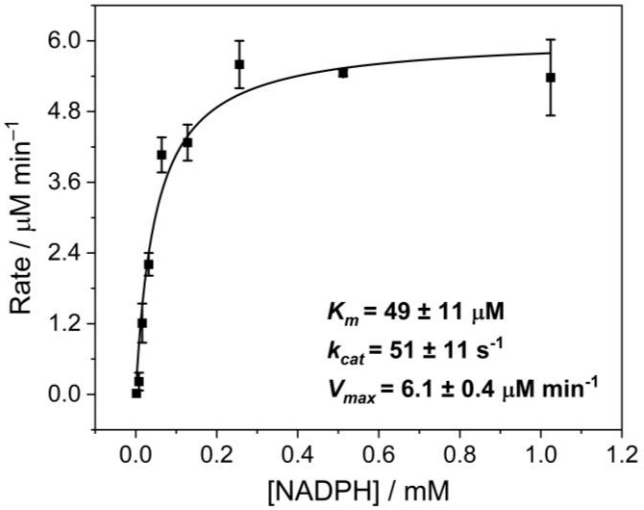


Figure 50. Rates of FNR-catalyzed NADPH oxidation in homogeneous solution measured spectrophotometrically by absorbance at 340 nm. The data were fit by the Michaelis-Menten equation. Benzyl viologen was used to rapidly reoxidize FNR. Conditions: 2 nM FNR, 100 mM HEPES (pH = 8), 5 mM benzyl viologen, 26 °C, [NADPH] was varied, 1 mL reaction volume, O_2 < 1 ppm. Reactions were carried out in duplicate.

Another way to understand the efficiency gain due to nanoconfinement of NADP(H) is to determine the factor by which NADP(H) is concentrated in the electrode nanopores from the bulk solution. Experimentally, it is not clear how this could be done, but an approximate value can be obtained from the experiment shown in **Figure 49A**. Importantly,

for the experiment in **Figure 49A**, in which $NADP^+$ was titrated into the solution, the first data point was measured without any added $NADP^+$. Normally, this would give a current value of 0 A; however, as shown before, IDH1-copurified NADP(H) can be used as the sole source of NADP(H) when nanoconfined in the e-Leaf. The current measured when isocitrate was added, before any $NADP^+$ had been added, was 2 μA; therefore, by extrapolating the first several data points with added NADP(H) back to the x-intercept, it should be possible to estimate the *effective* bulk solution $NADP^+$ concentration, i.e., the bulk solution concentration which would be required to achieve 2 μA current (since $I = 0$ when [S] = 0 and I α [S] when [S] << $K_{m(nano)}$; see Eq. 16). **Figure 49D** shows the extrapolated plot: the x-intercept indicates that the IDH1-copurified NADP(H) has an *effective* bulk solution concentration of 1.3 μM. Comparing this with the estimated concentration of 0.58–1.15 mM NADP(H) *inside* the electrode nanopores reveals that the nanoconfined IDH1-FNR system concentrates NADP(H) by 450–900-fold from the bulk solution, greatly increasing how efficiently it is used. This result is consistent with the 670-fold lower $K_{m(nano)}$ value measured for the IDH1-FNR cascade compared to the "FNR-only" condition.

3.3.8 IDH1-FNR Cascade Nanoconfined versus in Dilute Solution

A final set of experiments were performed to compare the rates of bulk chemical synthesis via cascade catalysis using only IDH1-copurified NADP(H) under conditions of nanoconfinement versus dilute (homogeneous) solution. Importantly, the comparison was based on the amount of product made normalized to both the amount of enzyme used and the reaction volume. The solution experiments involved using the same quantities of enzymes that were present in the electrode nanopores of an "analytical scale" electrode

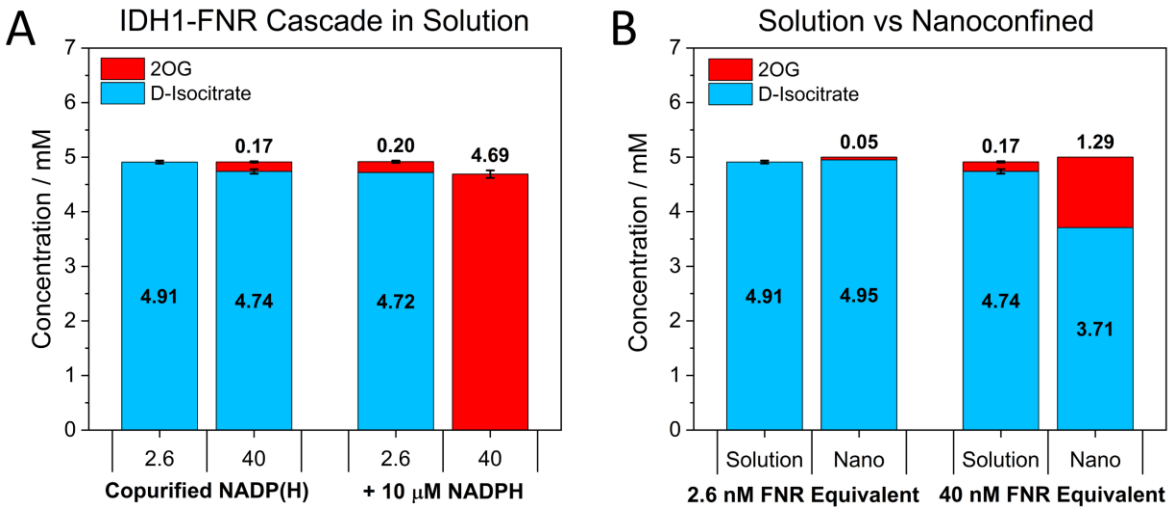


Figure 51. Comparing the IDH1-FNR cascade in solution vs under nanoconfinement. (A) Analysis by ^{1}H NMR (after heat quenching) showing the homogeneous solution-based conversion of isocitrate to 2OG after 12 hours. The numbers under each bar in the x-axis indicate the concentration (in nM) of FNR used. The molar ratio of FNR/IDH1$_{dimer}$ used was 1/1.04 ([IDH1] = 1.04 x [FNR]). The "Copurified NADP(H)" bars show experiments where no NADP(H) was added (only IDH1-copurified NADP(H) was present); the "+ 10 μM NADPH" bars show positive control experiments where 10 μM NADPH was added. Conditions: 400 μL volume, 100 mM HEPES (Ph 8), 10 mM $MgCl_2$, 5 mM D-isocitrate, 25 mM benzyl viologen. All of reactions were performed in triplicate; error bars represent the standard deviation. (B) Comparison of the IDH1-FNR cascade in solution vs under nanoconfinement in the e-Leaf without any added NADP(H). The "Copurified NADP(H)" solution experiments in (A) are compared with equivalent amounts of enzyme normalized to the reaction volume (4 mL) used in the analytical-scale electrochemical experiment from **Figure 46A** ("2.6 nM FNR Equivalent") and the scaled-up electrochemical experiment in **Figure 41** ("40 nM FNR Equivalent").

(A = 0.06 cm^2) and a large electrode (A = 4 cm^2); after 12 hours, the amount of 2OG generated was measured (**Figure 51A**). The IDH1-FNR cascade was driven in solution using a large excess of benzyl viologen (25 mM) in place of the electrode, oxidizing FNR and thus facilitating $NADP^+$ recycling. The large 4 cm^2 electrode, which contained a "solution equivalent" of 40 nM FNR and 41.5 nM IDH1$_{dimer}$ (see **Methods**, **Figure 51**), produced 8-fold more 2OG than the equivalent reaction in solution (**Figure 51B**). In fact, even the analytical-scale electrode, which only contained a solution equivalent of 2.6 nM FNR and 2.7 nM IDH1$_{dimer}$, produced 50 μM 2OG, while no 2OG was detected in the equivalent solution assay. Control experiments with 10 μM added NADPH confirmed that the enzyme

cascade was active in dilute solution, but that the catalytic components (particularly NADPH) were too dilute to achieve a substantial rate (**Figure 51A**). Therefore, despite the significant mass transport limitations of a heterogeneous system such as the e-Leaf, nanoconfinement can offer a significant kinetic advantage when the concentration of a recycled component is very low.

3.4 Conclusions

The discovery that enzyme-copurified NADP(H) is capable of supporting sustained catalysis under conditions of nanoconfinement is very interesting and unexpected. The rebinding of NADP(H) by IDH1 between catalytic cycles prevents NADP(H) from escaping the nanopores of the electrode, allowing the system to run without any redundant NADP(H), i.e., each NADP(H) molecule is always connected to the cascade, in contrast to the standard situation in which most of the NADP(H) is present in a bulk solution reservoir. Trapping both the enzymes *and* cofactor in the nanoporous electrode results in a massive increase in the overall efficiency of the system as shown by several different methods. Furthermore, the presence of a finite amount of NADP(H) in the system made it possible to quantify the amount of a non-electroactive enzyme present in the electrode nanopores for the first time, providing important new information about the e-Leaf system. Quantification, via thin-film voltammetry, showed that the enzymes and NADP(H) concentrate in the electrode relative to the bulk solution, giving rise to rate enhancements compared to cascade experiments in dilute solution. Interestingly, the turnover frequencies measured for nanoconfined enzymes ($k_{cat(nano)}$), present at millimolar levels, are within the same order of magnitude as turnover frequencies measured in dilute solution (k_{cat}), despite such concentrations approaching maximum theoretical levels.

The rebinding of NADP(H) by a "resting conformation" of IDH1, coupled with tight redox control of the electrode environment, made it possible to investigate whether the redox status of NADP(H) affected rebinding for both wildtype IDH1 and IDH1 R132H. The experiments yielded the interesting and likely mechanistically important result that "resting" IDH1 R132H has a much higher affinity for NADPH compared to $NADP^+$, a property that

is not observed for the wildtype enzyme. Significantly, the ability of IDH1 R132H to selectively and tightly rebind NADPH may facilitate catalysis of the cancer-associated 2OG to 2HG reaction even under conditions where the $NADP^+$/NADPH ratio is high or where concentrations of NADPH are very low. Obtaining similar information using other methods would be difficult due to the transient nature of different enzyme conformations.

On a final note, understanding how enzymes behave under conditions of enzyme crowding is important because such conditions likely more accurately represent the crowded in vivo environment compared to standard “dilute” solution (often nanomolar) enzyme assays.

CHAPTER IV

INVESTIGATING THE KINETIC MECHANISM OF ISOCITRATE DEHYDROGENASE INHIBITION

4 Investigating the Kinetic Mechanism of Isocitrate Dehydrogenase Inhibition

4.1 Abstract

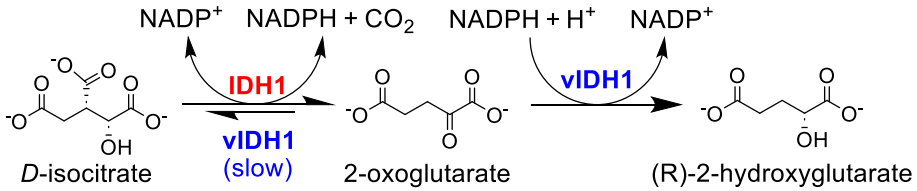
Isocitrate dehydrogenase 1 and 2 are important drug targets for which several selective inhibitors have been developed. However, the mechanism(s) of action of these inhibitors is not fully known, and even less is known about the rates of such processes. Exploiting the advantages of the e-Leaf for measuring real-time enzyme activity, the inhibition kinetics of the most common cancer-associated IDH1 variant, IDH1 R132H, were investigated using several clinically-relevant inhibitors, some of which have been FDA-approved. To facilitate electrochemical investigation, a new method and analytical framework were established enabling detailed kinetic and mechanistic information on IDH1 inhibition to be obtained. Notably, the IDH1 variant inhibition kinetics are very slow, following a two-stage process where rapid non-inhibitory binding is followed by a slower inhibitory step. Significantly, these details are not resolved using conventional steady-state kinetics or by techniques that only measure binding. Using data obtained from several inhibitors, a general kinetic mechanism for IDH1 inhibition is proposed which should also be relevant to IDH2 variant inhibitors. Importantly, despite the unusual environment for studying enzyme catalysis, data measured in the e-Leaf are consistent with experiments performed in dilute solution. The ability to interact with and control enzyme cascades entrapped in a nanoporous electrode material, facilitated by nanoconfined NADP(H) recycling via FNR, is shown to be a powerful tool for enzyme mechanistic studies.

This page contains redacted material that will become publicly available in December 2029.

4.2 Introduction

4.2.1 Isocitrate Dehydrogenase as a Drug Target

The isocitrate dehydrogenase 1/2 enzymes are the most frequently mutated metabolic genes associated with cancer.[29,38] Specifically, the single mutant IDH1 R132H/C variant enzymes are linked to numerous types of cancers including acute myeloid leukemia, chondrosarcoma, gliomas, and cholangiocarcinoma.[46] Instead of the wildtype $NADP^+$-dependent isocitrate oxidation reaction, the IDH1 variants primarily catalyze the NADPH-dependent reduction of 2OG, forming 2HG, a widely recognized oncometabolite (**Scheme 7**).[30,45] Many small molecules have been developed to inhibit variant IDH1 R132



Scheme 7. NADP(H)-dependent reactions of wildtype IDH1 and IDH1 variants (vIDH1). Note that the variant IDH1 enzymes also catalyze the wildtype reaction (isocitrate oxidation) but at a greatly reduced rate.[35,39,40] Molecules are presented as the forms dominating at pH = 7.

enzymes, with two drugs, Ivosidenib (AG-120) and Olutasidenib (FT-2102), having been recently FDA-approved to treat acute myeloid leukemia (AML)[51,52] and several others currently undergoing clinical trials.[29,44,50] Unfortunately, there have also recently been new variant IDH1 R132 enzymes detected in patients which show resistance to Ivosidenib. These drug-resistant IDH1 enzymes possess a second single amino acid substitution at the 280 residue in which the wildtype serine is replaced with phenylalanine (IDH1 R132H/C S280F).[40,63] Significantly, other inhibitors have recently been identified which are effective against the Ivosidenib-resistant double mutant variants.[40] The results presented in this chapter primarily focus on the mechanism of inhibition of IDH1 R132H,

the most common IDH1 variant. This variant is commonly found in patients with AML, and it is associated with more than 80% of grade II/III gliomas.[30,47–49]

4.2.2 Current Knowledge of the Mechanism of Allosteric IDH1 Inhibition

Ivosidenib and other IDH1 inhibitors are proposed to function by binding noncovalently at the IDH1 dimer interface, stabilizing an open inactive conformation (**Figure 52**).[35,40,41,95–99] These allosteric inhibitors are extremely potent, having IC_{50} values (the concentration of inhibitor required to reduce activity by 50%) that approach the enzyme

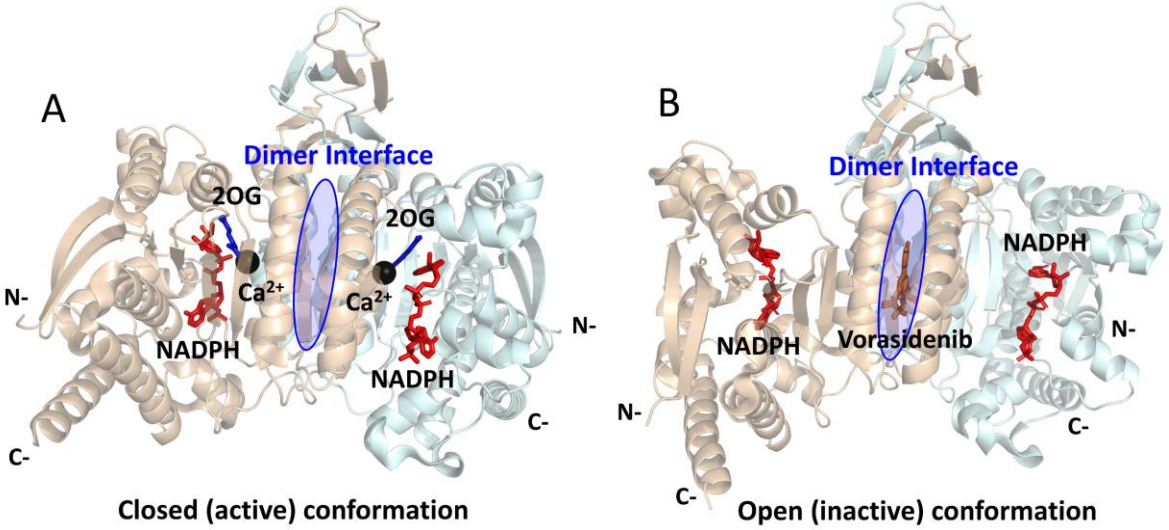


Figure 52. Crystal structure views of (A) the closed (active) conformation with 2OG, NADP(H), and inhibitory Ca^{2+} (substituting for Mg^{2+}) bound at the active site of each monomer (PDB: 4KZO)[36] and (B) the proposed open (inactive) conformation with one molecule of an inhibitor, Vorasidenib, bound at the dimer interface and a molecule of NADP(H) bound at the active site of each monomer (PDB: 6ADG).[100]

concentrations themselves (usually < 100 nM).[29,35,40] Importantly, it has been shown that inhibitor binding at the dimer interface, which stabilizes an inactive enzyme conformation, results in the enzyme losing the ability to bind Mg^{2+} at the active site, which is required for both catalysis and efficient 2OG binding.[35] Conversely, when Mg^{2+} and 2OG are bound to

the enzyme, forming the closed active conformation (**Figure 52A**), the inhibitor is apparently unable to bind the enzyme; thus, inhibition is competitive with respect to Mg^{2+}.[35] Notably, it is the competitive behavior of the inhibitors that make them selective for the IDH1 variants over the wildtype enzyme: the IDH1 variants have a much lower affinity for Mg^{2+} than the wildtype enzyme,[35,40] resulting in lower concentrations of inhibitor being able to disrupt productive Mg^{2+} binding for the variant compared to the wildtype. The lower affinity for Mg^{2+} is likely influenced by the fact that the wildtype IDH1 substrate is actually the Mg^{2+}-isocitrate complex, whereas IDH1 variants appear to bind Mg^{2+} and 2OG separately.[35]

Wildtype IDH1 and IDH1 R132H are structurally very similar (**Figure 53**), which is perhaps unsurprising as they only differ by a single amino acid substitution. Both enzymes are purified in the open inactive conformation (**Figure 53A**), and binding of substrate (isocitrate or 2OG) and Mg^{2+} give nearly identical closed active conformations (**Figure 53B**). As shown in **Figure 53C**, the inactive conformation resulting from inhibitor binding is the same as the open inactive conformation. Interestingly, despite apparent mutually exclusive inhibitor/Mg^{2+} binding to IDH1 R132H,[35] it was recently shown that some IDH1 variant inhibitors, including Ivosidenib, *bind* to both wildtype IDH1 and IDH1 variants with roughly equal affinity while only *inhibiting* the variant.[101] This important observation implies that multiple enzyme-inhibitor complexes/conformations must exist, including some where the enzyme is still capable of turnover. This concept will reappear many times throughout this Chapter.

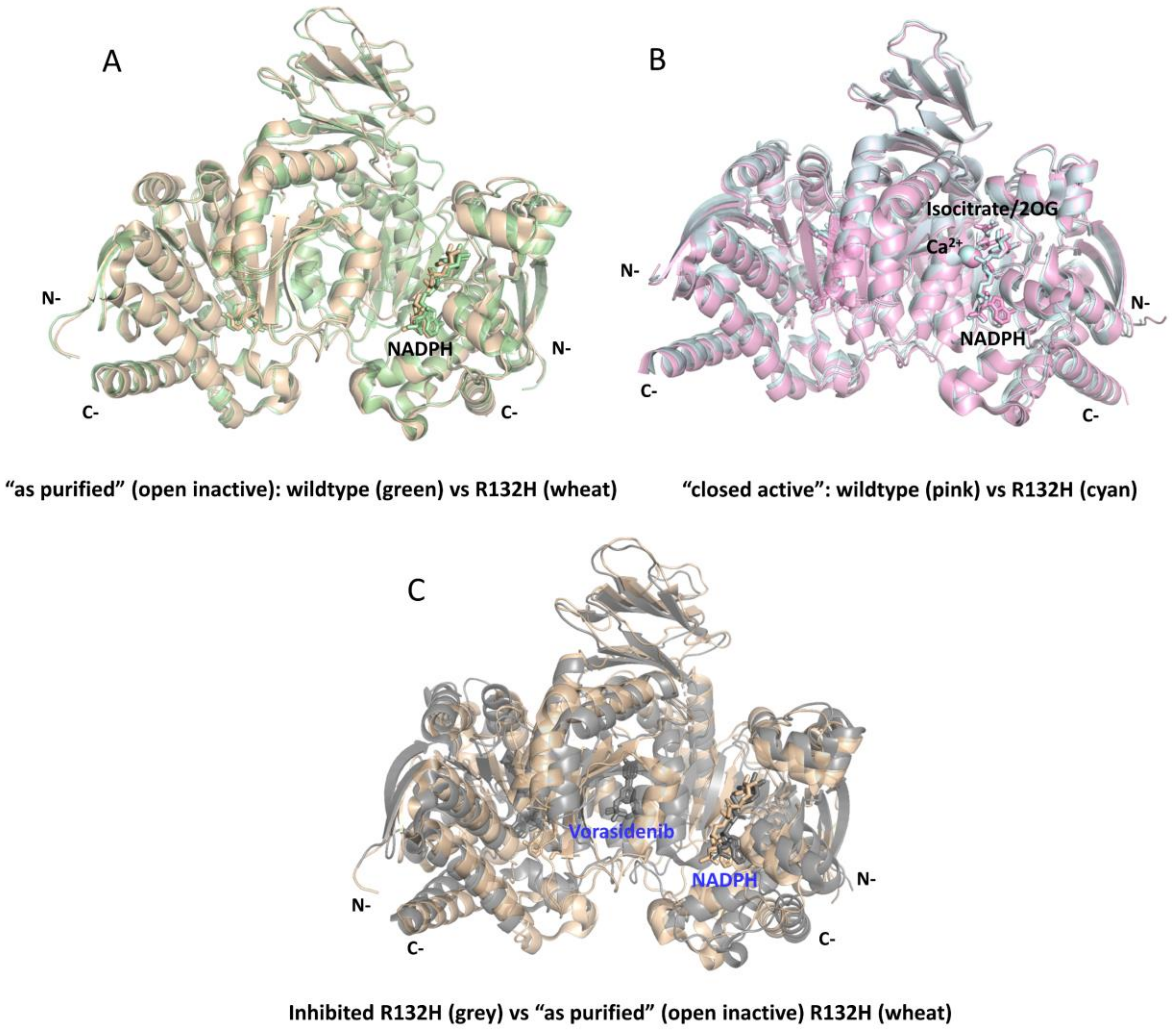


Figure 53. Crystal structure overlays of different IDH1 conformational states. (A) Wildtype IDH1 in the open inactive conformation (PDB: 1T09)[34] overlaid with IDH1 R132H in the open inactive conformation (PDB: 3MAR).[37] (B) Wildtype IDH1 in the closed active conformation (PDB: 1T0L)[34] with NADP(H), inhibitory Ca^{2+} (in place of Mg^{2+}) and isocitrate bound overlaid with IDH1 R132H in the closed active conformation (PDB: 4KZO)[36] with NADP(H), inhibitory Ca^{2+} (in place of Mg^{2+}) and 2OG bound. (C) IDH1 R132H with an inhibitor, Vorasidenib, bound at the dimer interface (PDB: 6ADG)[100] overlaid with IDH1 R132H in the open inactive conformation (PDB: 3MAR).[37]

4.2.3 IDH1 Inhibition Kinetics

Despite having been FDA-approved, there are no detailed kinetic data for Ivosidenib in the literature. Instead, work on IDH1 inhibitors has primarily focused on measuring IC_{50} (or EC_{50}) values,[40,50,102] or binding using non-denaturing mass spectrometry, NMR, surface

plasmon resonance (SPR), and isothermal titration calorimetry.[35,40,101] However, it has been shown that allosteric IDH1 inhibitors can bind without inhibiting,[101] implying that the data available in the literature, mostly focused on *binding*, may not necessarily be representative of productive *inhibitory* complexes.

Obtaining kinetic data for tight-binding inhibitors, such as those for IDH1, is difficult because the very low IC_{50} values are often below the experimentally practical enzyme concentrations required to measure activity. To date, there have been three studies which have presented kinetic data for IDH1/2 inhibitors: two focused on IDH2 inhibitors[95,97] and one focused on an IDH1 inhibitor.[103] Each of these studies has shown that the tested IDH1/2 inhibitors are slow-binding, but no detailed analysis has been done beyond obtaining basic on/off rates. A consequence of the slow kinetics is that IC_{50} measurements require that the inhibitor is pre-incubated with the enzyme for a specified period before initiating the reaction (the inhibitor thus binds under non-turnover conditions).[97,102] However, these incubation periods are not standardized, and it has been shown by Deng et al. that the length of incubation time (literature values range from 12 min.[40] to 30 min.[50,103] to 16 hours[97,102]) for an inhibitor can strongly affect its apparent IC_{50} value.[41] Consequently, it is important to allow enough time for the enzyme-inhibitor complex to reach equilibrium before adding substrate and no kinetic information is obtained.

4.2.4 The Importance of Enzyme Inhibition Kinetics

Enzyme inhibitors are often compared based on their K_i or IC_{50} values, both of which give an indication of potency. However, such values do not account for differences in kinetics, mechanism of inhibition, or how inhibition is affected by different enzyme

conformational states, i.e., when the enzyme is undergoing turnover and is thus present in different conformations that may affect drug binding. Detailed kinetic data such as the association rate constant, k_{on}, dissociation rate constant, k_{off}, drug residence time, $t_r = 1/k_{off}$ and complex dissociation half-life, $t_{1/2} = \ln(2)/k_{off}$, are often omitted when screening for inhibitors despite the fact that such drug-target kinetic data are often even more informative than binding affinity values in predicting in vivo efficacy—this is especially true when the duration of the pharmacological effect is important.[104–107] For obvious reasons, these data, measured under enzyme turnover conditions, are especially important for slow-acting inhibitors[104] and enzymes which are conformationally dynamic such as IDH1.[33]

4.2.5 Advantages of the e-Leaf for Measuring Inhibition Kinetics

In contrast to standard kinetic methods, such as surface plasmon resonance (SPR), the e-Leaf displays the rate of the enzyme reaction directly as current; thus, transient effects, i.e., changes to the steady-state rate, are detected immediately in real time. A huge advantage of using the e-Leaf to investigate drug-enzyme interactions is that any data obtained (e.g., k_{on}, k_{off}, drug residence time, and K_d) is done so under steady-state *turnover conditions*. Such conditions (with substrate(s) and cofactor(s) present) more closely mimic inhibition in vivo because the data will automatically reflect any differences in binding/inhibition mechanisms that are present (e.g., competitive inhibition, conformational selection, induced fit binding) and which may be missed if inhibition is performed under non-turnover conditions. In the latter case, standard techniques measuring binding affinity (IC_{50}, K_d) or binding kinetics (surface plasmon resonance (SPR)) are performed using non-turnover conditions. These data measure affinity/rates of binding to inactive enzyme. Measurements under turnover

conditions are especially important if an inhibitor can only bind (or bind preferentially) to particular enzyme conformations/states, or if binding can occur without inhibition as is the case for IDH1.[35,95,97,103]

Another advantage of the e-Leaf system is that inhibition can be monitored as a pseudo first-order process. Importantly, despite the enzymes being present at millimolar concentrations within the electrode nanopores,[23] the total amount of enzyme present is tiny compared to the amount of inhibitor present in the bulk solution reservoir (**Figure 54**). Therefore, with constant resupply of inhibitor to the electrode facilitated by electrode rotation, the inhibitor concentration remains constant throughout the duration of the experiment and inhibition is pseudo first-order.

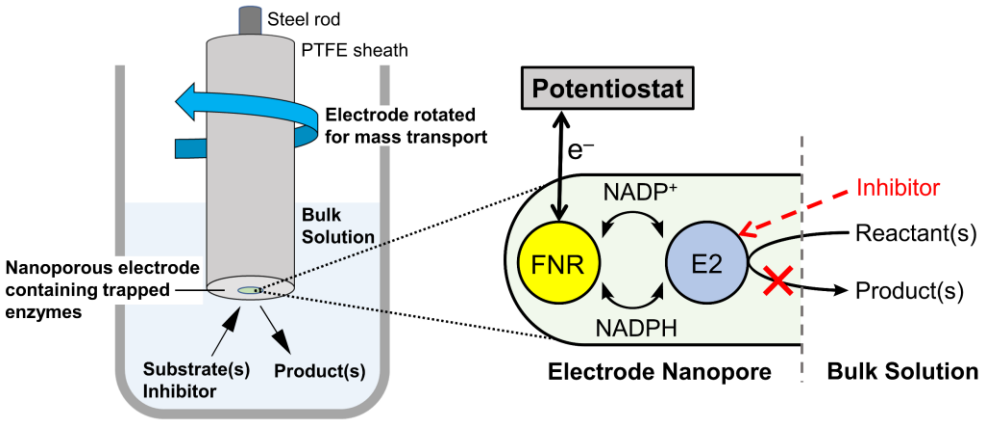


Figure 54. Physical setup of the e-Leaf when used as an analytical tool to study enzyme inhibition. E2 is an NADP(H)-dependent dehydrogenase. The electrode is rotated to optimize substrate/inhibitor mass transport. The expanded electrode nanopore shows the tightly-channeled chemical-to-electrical information flow.

4.2.6 Aims of this Chapter

Isocitrate dehydrogenase enzymes are important drug targets,[30,46] for which inhibitors have been developed and several have been approved for clinical use. Despite this, many open questions remain about the inhibitory mechanism of action, and little is known about the inhibition kinetics. This is particularly important because the studies which have investigated the properties of IDH inhibitors have shown that their behavior is very complex: they bind allosterically but are competitive with active-site binding substrate/metal ions;[29,35,40] furthermore, they can also apparently bind in modes which are non-inhibitory.[101] Likewise, preliminary kinetic work[95,97,103] has shown that these inhibitors bind and dissociate slowly, but no detailed kinetic studies have been done. This Chapter aims to establish a new method and analytical framework to obtain detailed kinetic and mechanistic information on IDH1 inhibition by exploiting the unique advantages of the e-Leaf for investigating slow, tight-binding inhibitors.

4.3 Results and Discussion

4.3.1 Measuring Real-time Inhibition of IDH1 R132H by an FDA-approved Drug

An initial experiment was carried out to test if rates of inhibition of IDH1 R132H could be observed in real time (**Figure 55**). The electrode was loaded with FNR and IDH1 R132H and placed into a solution already containing 10 µM NADPH and 10 mM $MgCl_2$. The reaction was initiated by the addition of 10 mM 2OG. After steady-state enzyme turnover had been observed for ~20 minutes, an aliquot of Ivosidenib dissolved in DMSO was injected into the bulk solution. During the experiment, the electrode was rotated at 1000 rpm to ensure that a constant supply of 2OG substrate and Ivosidenib reached the R132H enzyme. The addition of inhibitor resulted in an immediate decrease in the reaction rate (note that

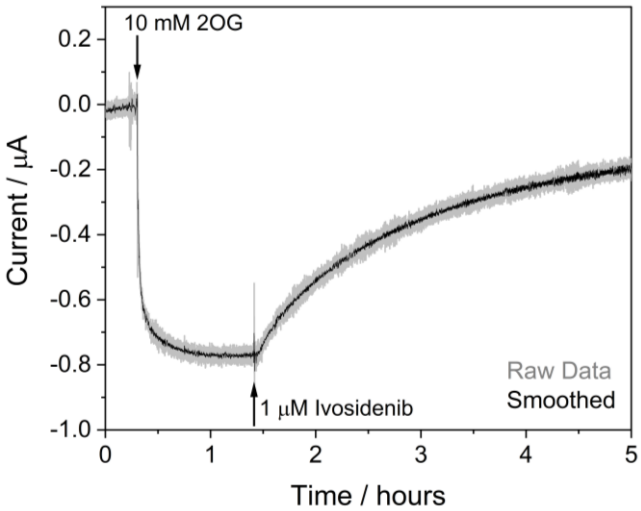


Figure 55. Chronoamperogram showing Ivosidenib inhibition of IDH1 R132H. The grey trace shows the raw data before smoothing. Conditions: (FNR+$IDH1_{R132H}$)@ITO/PGE electrode, electrode area 0.06 cm^2, electrode rotated at 1000 rpm, temperature 25 °C, E = –0.513 V vs SHE, mixed buffer (pH = 8): 20 mM each: MES, TAPS, CHES, 10 mM $MgCl_2$, 10 µM NADPH, 10 mM 2OG, volume 4 mL. Enzyme loading ratios (molar): FNR/$IDH1_{R132H}$; 2/5. Ivosidenib was injected as a solution in DMSO at the time indicated to give a final concentration of 1 µM. The grey data was smoothed using the Savitzky-Golay method (4 points left/right) to obtain the black trace.

current α enzyme rate), but inhibition was very slow with a half-life ($t_{1/2}$) ≈ 1 h. The inhibition plot appeared to exhibit pseudo first-order kinetics (this will be proven later in this Chapter), though it was clear that inhibition was not complete, i.e., the rate approached a non-zero equilibrium value. Importantly, this proof-of-concept experiment showed that, using the e-Leaf, it is possible to monitor, in real time, the *transient* kinetics of enzyme inhibition during *steady-state* catalysis.

4.3.2 Dual Enzyme Monitoring: Selective Inhibition of "side-by-side" Enzymes

As shown in **Chapter II**, the e-Leaf is able to measure the rates of two opposing reactions (oxidation and reduction) in a single experiment: wildtype IDH1 was driven bidirectionally to investigate reaction thermodynamics, and rates of isocitrate oxidation and 2OG reduction catalyzed by IDH1 variants were compared. Extending this concept, and utilizing the ability to load multiple enzymes into the porous e-Leaf electrode, it should thus be possible to monitor two different reactions (oxidation and reduction), catalyzed by *separate enzymes* within a single experiment. Conveniently, wildtype IDH1 and the IDH1 variants catalyze reactions that are linked to NADP(H) in opposite directions (isocitrate oxidation versus 2OG reduction, respectively). Therefore, by loading *both* wildtype IDH1 and IDH1 R132H into the same electrode alongside FNR, it should be possible to measure each of their turnover rates independent of the other using cyclic voltammetry. Such an experiment should make it possible to *directly* test the selective action of an inhibitor/activator.

An electrode loaded with both wildtype IDH1 and IDH1 R132H (optimized to compensate for the much faster wildtype enzyme) was used to test the selectivity of

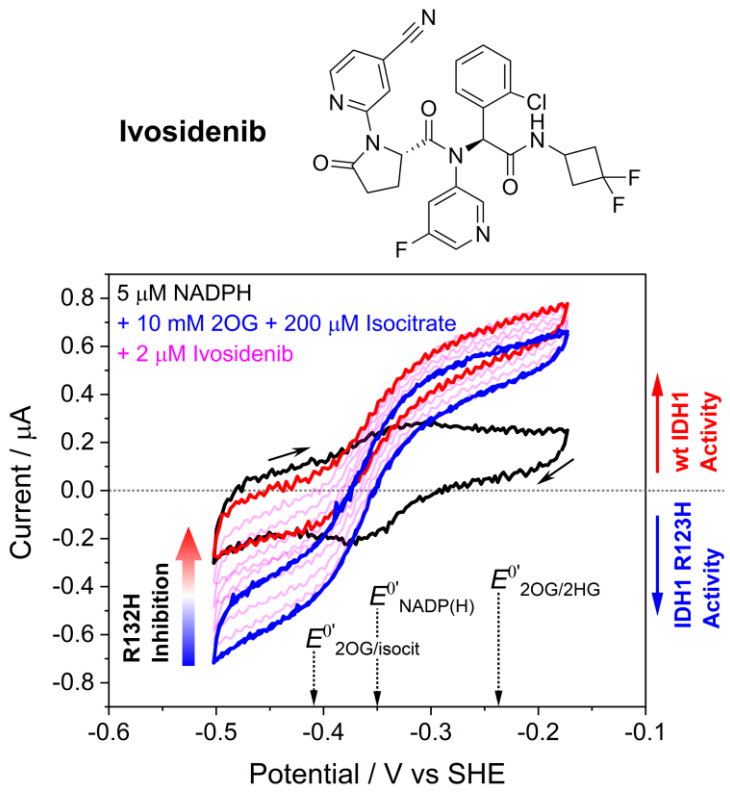


Figure 56. Dual enzyme monitoring to demonstrate inhibitor selectivity. Cyclic voltammograms show simultaneous effects on wildtype IDH1 and IDH1 R132H catalysis after introducing Ivosidenib: only IDH1 R132H is inhibited. Black trace: 5 μM NADPH (without isocitrate or 2OG present). Blue traces: two consecutive traces overlaid (to show system stability) with 10 mM 2OG and 0.2 mM enantiopure *D*-isocitrate. The pink traces show changes to rates after addition of Ivosidenib (2 μM). Importantly, the oxidation current is only due to wildtype IDH1 isocitrate oxidation activity and the reduction current is only due to IDH1 R132H 2OG reduction activity (see text and **Figure 57** for control experiments). Conditions: (FNR+IDH1$_{WT}$+IDH1$_{R132H}$)@ITO/PGE electrode, electrode area 0.06 cm^2, electrode rotation rate 1000 rpm, scan rate 1 mV s^{-1}, temperature 25 °C, O_2 < 1 ppm, volume 4 mL, pH = 8 (100 mM HEPES), 10 mM $MgCl_2$, 5 μM NADPH, enzyme loading ratios (molar): FNR/IDH1$_{WT}$/IDH1$_{R132H}$; 2/1/5.

Ivosidenib for IDH1 R132H inhibition over the wildtype enzyme (**Figure 56**). First, with only 5 μM NADPH present and with electrode rotation to facilitate mass transport, an initial voltammogram (black trace) was recorded without either IDH1 substrate present to show the background FNR-catalyzed cycling of NADP(H). Next, 10 mM 2OG was added to the bulk solution to initiate IDH1 R132H catalysis. Isocitrate was then slowly titrated into the solution until the oxidation and reduction currents were approximately equal (i.e., the rates of each

enzyme were roughly the same). Two consecutive voltammograms were recorded (blue traces) to show initial activities and stability of the system. Ivosidenib (2 μM final concentration) was then added to the solution, and successive voltammograms (pink traces) were recorded to monitor any changes to wildtype and R132H IDH1 activity over time. Significantly, the data show that, when presented with a mixed population of wildtype IDH1 and an IDH1 variant as would be the case in a cancer cell, Ivosidenib *selectively inhibits* IDH1 R132H (current at a potential negative of the $NADP^+$ reduction peak) while leaving wildtype IDH1 activity unaffected (current positive of the NADPH oxidation peak) (**Figure 56**). Selective inhibition occurs despite Ivosidenib being able to *bind* to both wildtype IDH1 and R132H with roughly equal affinity.[101] The red trace (final voltammogram) shows that wildtype IDH1 isocitrate oxidation activity was not inhibited and instead actually slightly increased during the experiment. Interestingly, this increase is also attributable to the inhibition of IDH1 R132H, which slightly competes with FNR for NADPH, i.e., a minor alternate NADP(H) recycling pathway (between wildtype IDH1 and IDH1 R132H) was removed when R132H was inhibited.

For such a complex experiment, it was important to confirm that the interpereted outcome was actually what occured. To this end, control experiments were carried out to test the stability of IDH1 R132H catalysis (i.e., that what was perceived to be inhibiton was not the loss of enzyme activity for an unrelated reason) and that the measured oxidation current was solely due to wildtype IDH1 isocitrate oxidation activity and the reduction current was solely due to IDH1 R132H 2OG reduction activity (**Figure 57**). **Figure 57A** confirms the stability of IDH1 R312H catalysis in the e-Leaf by showing 10 consecutive voltammograms

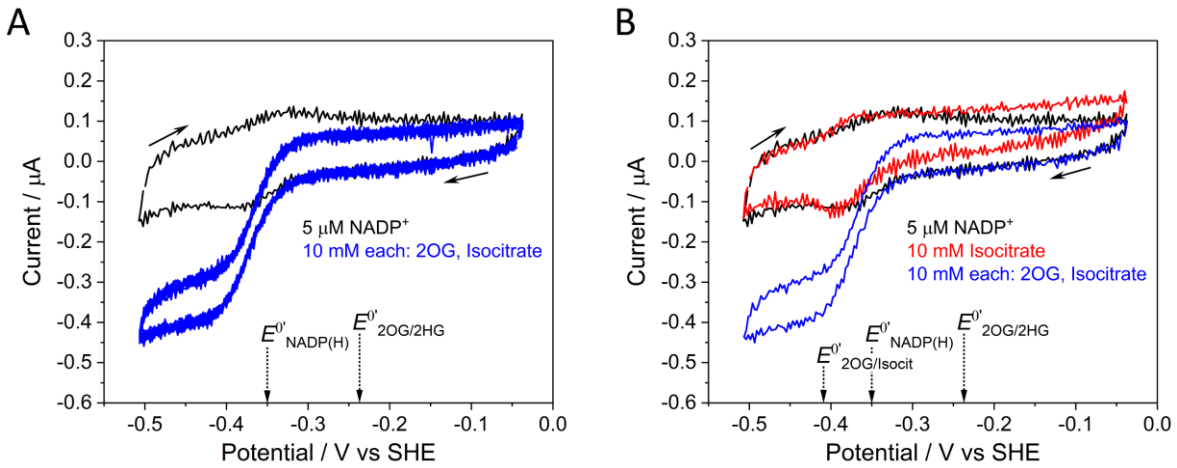


Figure 57. Control experiments for the experiment shown in **Figure 56**. (A) Cyclic voltammetry showing the stability of IDH1 R132H 2OG reduction activity over time: 10 consecutive traces (blue) at a scan rate of 1 mV s^{-1} equate to >2.6 hours of stable enzyme catalysis. (B) The minor IDH1 R132H isocitrate oxidation activity is only detected in the absence of 2OG. Isocitrate oxidation activity of IDH1 R132H was first measured with 10 mM *DL*-isocitrate present; after 2OG was added, isocitrate oxidation activity was no longer detected.[26,40] Conditions: stationary (FNR+$IDH1_{R132H}$)@ITO/PGE electrode, electrode area 0.03 cm^2, scan rate 1 mV s^{-1}, temperature 25 °C, O_2 < 1 ppm, volume 4 mL, pH 8 (20 mM each: MES, TAPS, CHES), 10 mM $MgCl_2$, 5 μM $NADP^+$, enzyme loading ratios (molar): FNR/$IDH1_{R132H}$; 2/5.

at a scan rate of 1 mV s^{-1} equating to over 2.6 hours of stable measurement. Voltammograms in **Figure 57B** confirm that the small amount of IDH1 R132H isocitrate oxidation activity (red trace) is not measured when 2OG is present,[26,40] as was previously shown in **Chapter II**. Wildtype IDH1 did not contribute to any of the measured reduction current because it requires high [CO_2] (or rapid in situ supply of CO_2) to convert 2OG to isocitrate.[26] The exciting ability to study multiple enzymes independently within a single system may prove invaluable in myriad other areas of enzymology. For IDH1 specifically, this technique should be useful for studying the activities of wildtype/variant heterodimers, which are likely clinically relevant, but which are understudied.[29]

4.3.3 Comparing Rates of Inhibition with Inhibitor Potency

Following a successful initial set of inhibition experiments (and some experimental optimization), six IDH1 inhibitors (**Figure 58**) were tested under the same conditions to compare their rates of action (**Figure 59A**). Like the experiment in **Figure 55**, the reaction was initiated by the addition of 10 mM 2OG with 10 μM NADPH and 10 mM $MgCl_2$ already

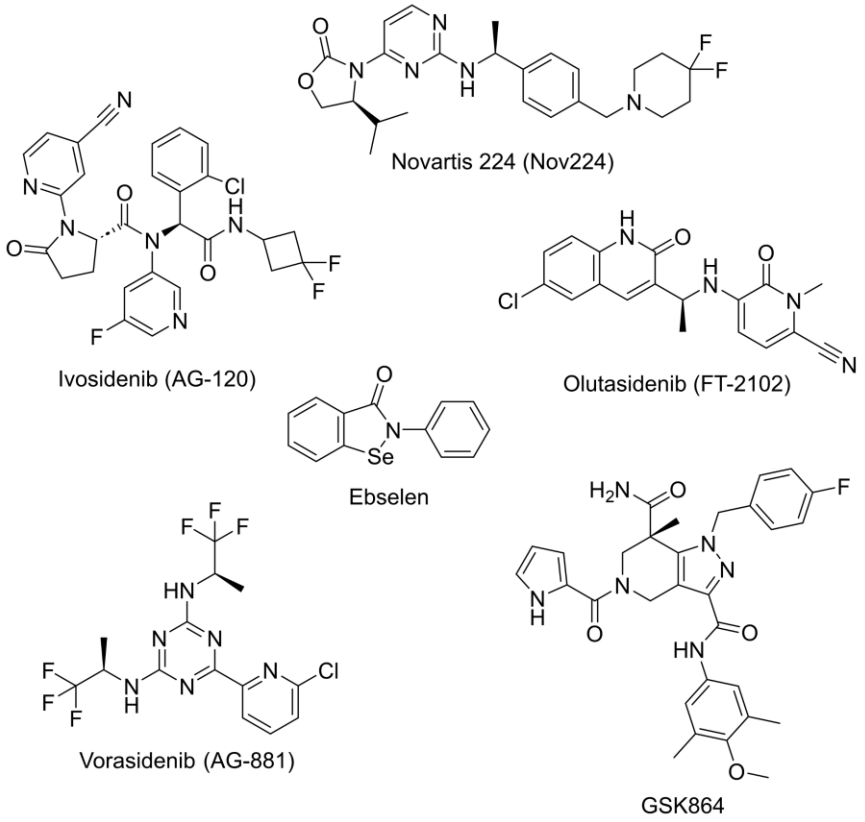


Figure 58. Structures of the IDH1 variant inhibitors used in this work.

in the bulk solution. Three independent experiments were performed for each inhibitor/control, with **Figure 59A** showing representative chronoamperometry (timecourse) data for each of the six inhibitors following injection into the bulk cell solution (at $t = 0$) as a 2.5 μL aliquot dissolved in DMSO. The control experiment had DMSO added without inhibitor. The plot in **Figure 59A** was extended to 2.5 hours in order to show the slow

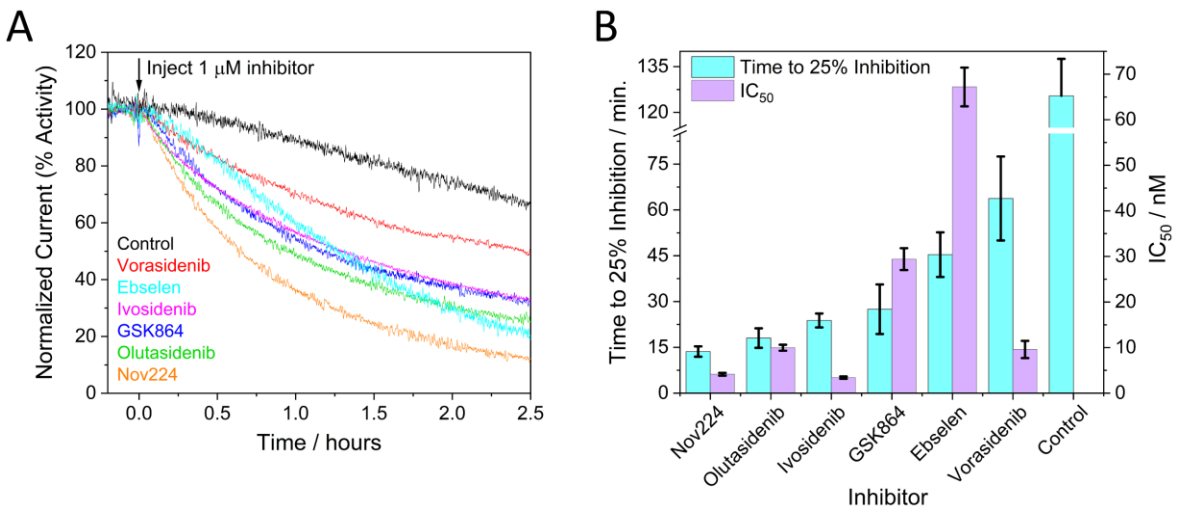


Figure 59. Kinetic vs equilibrium-based measurements of IDH1 R132H inhibition. (A) Representative chronoamperometry (timecourse) experiments comparing the rates of inhibition of five selective IDH1 variant inhibitors under the same conditions following injection of 1 μM inhibitor (final concentration). The control experiment had DMSO added without inhibitor. Three independent experiments were carried out for each inhibitor/control. (B) Comparison between *rates* of inhibition (time to 25% inhibition) and measured *equilibrium*-based IC_{50} values (inhibitor concentration required to reduce the initial enzyme turnover rate by 50% following a 12-minute inhibitor-enzyme incubation). The metric "time to 25% inhibition" was chosen over the more standard half-life to account for the fact that the system exhibited a slow decay in activity over time (termed "film loss", see **Methods**). Importantly, both metrics (half-life and "time to 25% inhibition") show the same trends. Conditions: (FNR+$IDH1_{R132H}$)@ITO/PGE electrode, electrode area 0.06 cm^2, electrode rotated at 1000 rpm, temperature 25 °C, E = –0.513 V vs SHE, mixed buffer (pH = 8): 20 mM each: MES, TAPS, CHES, 10 mM $MgCl_2$, 10 μM NADPH, 10 mM 2OG, volume 4 mL. Enzyme loading ratios (molar): FNR/$IDH1_{R132H}$; 2/5. Inhibitor was injected as a solution in DMSO (2.5 μL) at t = 0. The data were smoothed using the Savitzky-Golay method (4 points left/right). The IC_{50} measurements were performed by Raphael Reinbold.

approach to a non-zero equilibrium value indicating incomplete inhibition for all of the selective IDH1 variant inhibitors. To confirm that the rates of inhibition were not limited by an artifact of the e-Leaf system, a control experiment using $CaCl_2$, an active-site binding inhibitor,[35] was performed; the result shows that the system is capable of measuring rapid inhibition (**Figure 60**). Note that other experiments in this Chapter show that inhibition data measured using the e-Leaf are consistent with values measured in dilute solution. **Figure 59B** shows how the *rates* of IDH1 R132H inhibition (time to 25% inhibition) compare with measured *equilibrium*-based IC_{50} values. The latter measurement represents the inhibitor

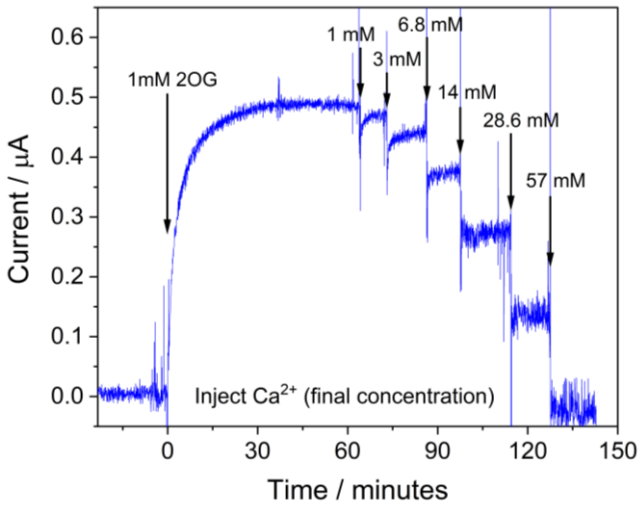


Figure 60. Control experiment showing fast inhibition of IDH1 R132H in the e-Leaf following injections of increasing concentrations of $CaCl_2$. Note that the concentrations shown represent the *cumulative* concentration of $CaCl_2$ following each injection. Conditions: (FNR+IDH1$_{R132H}$)@ITO/PGE electrode, electrode area 0.06 cm^2, electrode rotated at 1000 rpm, temperature 25 °C, E = –0.5 V vs SHE, O_2 < 1 ppm, volume 4 mL, pH = 8 (20 mM of each: MES, TAPS, CHES), 10 µM NADPH, 10 mM $MgCl_2$, 1 mM 2OG, enzyme loading ratios (molar): FNR/IDH1$_{R132H}$; 2/5.

concentration required to reduce the initial enzyme turnover rate by 50% following inhibitor-enzyme incubation. Interestingly, the kinetic and equilibrium-based inhibition data show some correlation, but the results for Ebselen and Vorasidenib are notably different. Ebselen is not a specific IDH1 variant inhibitor, and it reacts with cysteine residues and can react at multiple sites on a single enzyme.[108] As a result, it is likely that Ebselen is able to inhibit FNR in addition to IDH1. The likely non-specific inhibitor, Ebselen, was included in the data because it exhibits different kinetics from the other selective IDH1 variant inhibitors as represented by it cutting vertically across the other inhibition timecourse data (**Figure 59A**). In contrast, Vorasidenib is a selective IDH1 variant inhibitor; the relative disagreement between very low rates of inhibition despite it apparently being a highly potent inhibitor is interesting with respect to the other four tested selective IDH1 variant inhibitors. The IC_{50} requirement for inhibitor-enzyme incubation prior to measuring turnover means that

inhibition/binding occurs under non-turnover conditions. In contrast, e-Leaf inhibition measurements occur during enzyme turnover. Thus, differences observed (i.e., lack of correlation) between the apparent potency of inhibitors and their relative rates of inhibition may reflect differences in inhibitor preference for binding particular conformational states of the enzyme.

Instead of the more standard half-life, i.e., time to 50% inhibition, the time to 25% inhibition was used to account for the fact that the system exhibited a slow decay in activity over time (termed "film loss", discussed later). Importantly, by the time most inhibitors had reached 25% inhibition, the control enzyme activity was still at ~98%. Regardless, both metrics showed the same trends. For an inhibition reaction involving the binding of a single molecule of inhibitor to the enzyme, and assuming the reaction is pseudo first-order with respect to the active enzyme (this will be proven later), the rate of the inhibition reaction is given by:

$$\text{Rate} = k_{\text{obs}}[\text{E}], \qquad \text{(Eq. 18)}$$

where k_{obs} is the pseudo first-order observed rate constant (s^{-1}). Therefore, the time taken to reach 25% inhibition, i.e., the time after which 75% activity remains ($t_{3/4}$), can be used to obtain k_{obs} with the derived equation:

$$k_{\text{obs}} = \frac{\ln\left(\frac{4}{3}\right)}{t_{3/4}}. \qquad \text{(Eq. 19)}$$

The calculated rate constant values are presented in **Table 3**, and can be used to predict the time taken to reach X% inhibition (using a suitably derived equation) more accurately than by directly taking the values from the timecourse plot in **Figure 59A** because the gradual background loss in activity convolutes the signal over long time periods. Thus, Eq. 20 and

Eq. 21 were used to predict the time that would be required to reach 50% ($t_{1/2}$) and 90% ($t_{1/10}$) inhibition, respectively, for each selective IDH1 variant inhibitor (**Table 3**). Note that these predicted time values assume an approach to 0, i.e., complete inhibition.

$$t_{1/2} = \frac{\ln(2)}{k_{obs}} \quad \text{(Eq. 20)}$$

$$t_{1/10} = \frac{\ln(10)}{k_{obs}} \quad \text{(Eq. 21)}$$

The calculated inhibition time values (**Table 3**) emphasize the slow binding kinetics and the kinetic differences between inhibitors. Furthermore, these data strongly imply that the IDH1 inhibitors bind the enzyme differently under turnover versus non-turnover conditions. For example, the IC_{50} values presented in **Figure 59B** were determined by measuring the initial

Table 3. Pseudo First-order Observed Rate Constants for IDH1 Variant Inhibitors

Inhibitor	Time to 25% inhibition ($t_{3/4}$)/ min.	k_{obs}/ 10^{-4} s^{-1}	*Predicted* time to 50% inhibition ($t_{1/2}$)/ min.	*Predicted* time to 90% inhibition ($t_{1/10}$)/ min.
Novartis 224	13.6 ± 1.7	3.5 ± 0.44	32.82 ± 4.06	109.0 ± 13.5
Olutasidenib (FT-2102)	18.0 ± 3.2	2.7 ± 0.47	43.46 ± 7.67	144.4 ± 25.5
Ivosidenib (AG-120)	23.8 ± 2.3	2.0 ± 0.19	57.33 ± 5.47	190.5 ± 18.2
GSK864	27.5 ± 8.1	1.7 ± 0.52	66.22 ± 19.58	220.0 ± 65.0
Ebselen*	45.4 ± 7.3*	–	–	–
Vorasidenib (AG-881)	63.7 ± 13.8	0.75 ± 0.16	153.60 ± 33.14	510.2 ± 110.1
Control	125.4 ± 12.1	–	–	–

*Note: Ebselen is not a selective IDH1 variant inhibitor and can react with an enzyme multiple times (i.e., it does not exhibit pseudo first-order kinetics)

enzyme activity after only a 12-minute inhibitor-enzyme incubation. Thus, more than 50% inhibition must have been achieved for all inhibitors in under 12 minutes. Importantly, it will be shown later that e-Leaf-measured rates of inhibition are not limited by mass transport of inhibitor and that measured kinetic values are consistent with those measured in dilute solution. With this in mind, it is striking that, under conditions of enzyme turnover, it would take Vorasidenib ~2.5 h to reach 50% inhibition and ~8.5 h to reach 90% inhibition. Even the fastest-acting inhibitor, Novartis 224, would require ~33 and ~109 minutes to reach 50% and 90% inhibition, respectively. Such contrasting results make clear the need for pairing affinity-based measurements such as IC_{50}, EC_{50}, K_d, etc., with kinetic data in order to better predict inhibition in vivo, where the enzyme will usually be under turnover conditions.

4.3.4 Real-time Measurement of Inhibitor Binding *and* Dissociation in a Single Experiment

Despite their high affinities (IC_{50} < 100 nM), the fact that the IDH1 inhibitors bind noncovalently suggest that binding is reversible. To test this, a series of experiments were carried out using similar conditions to those in the previous section. This time, however, the buffer was exchanged live during the experiment with buffer that was free of inhibitor (**Figure 61**). At low inhibitor concentrations, dissociation of two IDH1 variant inhibitors, Ivosidenib and Novartis 224 (Nov224), was observed in real time after the buffer was changed, with rates of the process represented by a clear increase in enzyme activity over time (**Figure 61**). Consistent with having slower "on" (inhibition) kinetics, rates of Ivosidenib dissociation appeared to be more complete (**Figure 61A**) than the equivalent experiments with Nov224 (**Figure 61B**). Estimating the first-order dissociation rate constant (k_{off}) using these data is slightly more difficult than estimating the forward rate constant

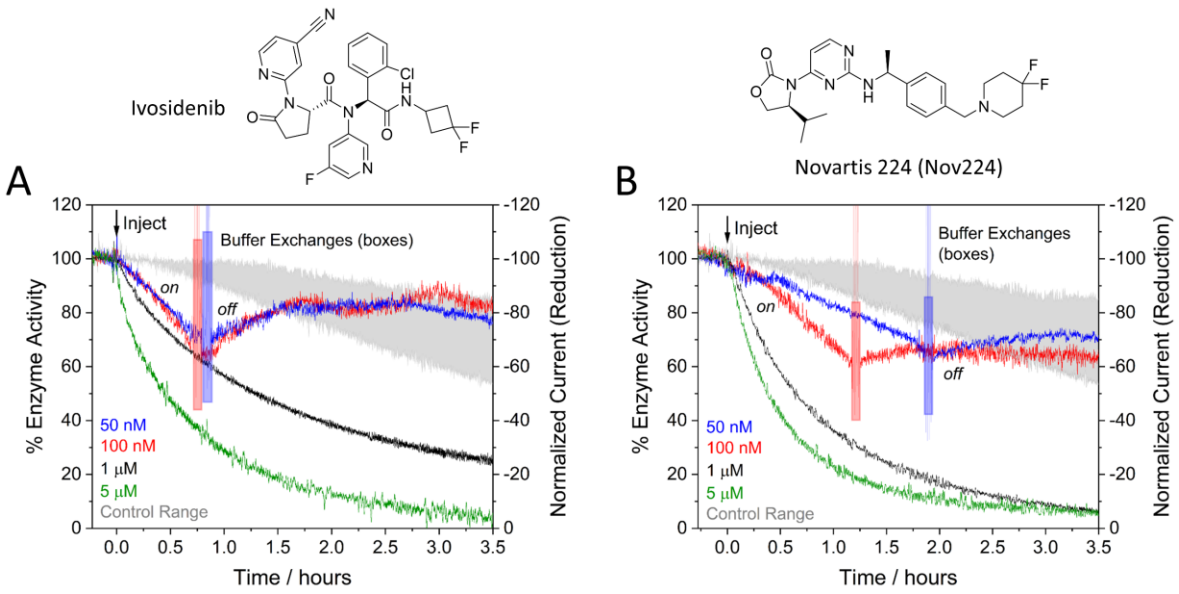


Figure 61. IDH1 R132H inhibition by Ivosidenib (A) or Novartis 224 (Nov224) (B) followed by inhibitor removal (50 and 100 nM) by solution exchange to show recovery of enzyme activity. Conditions: (FNR+IDH1$_{R132H}$)@ITO/PGE electrode, area 0.06 cm^2, electrode rotated at 1000 rpm, temperature 25 °C, E = −0.513 V vs SHE, mixed buffer (pH = 8): 20 mM each: MES, TAPS, CHES, 10 mM $MgCl_2$, 10 µM NADPH, 10 mM 2OG, volume 4 mL. Enzyme loading ratio (molar): FNR/IDH1$_{R132H}$; 2/5. Inhibitor (2.5 µL of various concentrations in DMSO) was injected at t = 0. The shaded region shows the range for 3 DMSO controls.

(k_{obs}) because the background decay of the system (film loss) has as stronger effect on the former (see section on film-loss correction in **Chapter VII** for details). With this in mind, the k_{off} for both inhibitors was estimated to be roughly 1–3x10^{-4} s^{-1}, equating to a complex dissociation half-time ($t_{1/2}^{off}$), the time required for 50% of the inhibitor to dissociate, of 0.6−2 hours.

To investigate whether the inhibition experiments were detecting specific interactions between the inhibitor and IDH1 R132H, a control experiment was carried out using Enasidenib (AG-221), a specific inhibitor for mitochondrial IDH2 variants[97] (**Figure 62**): the reported IC$_{50}$ values for Enasidenib against IDH1 R132H are 78 µM after 1 h and 48 µM after 16 h of incubation with IDH1 R132H.[97] For comparison, IC$_{50}$ values measured for

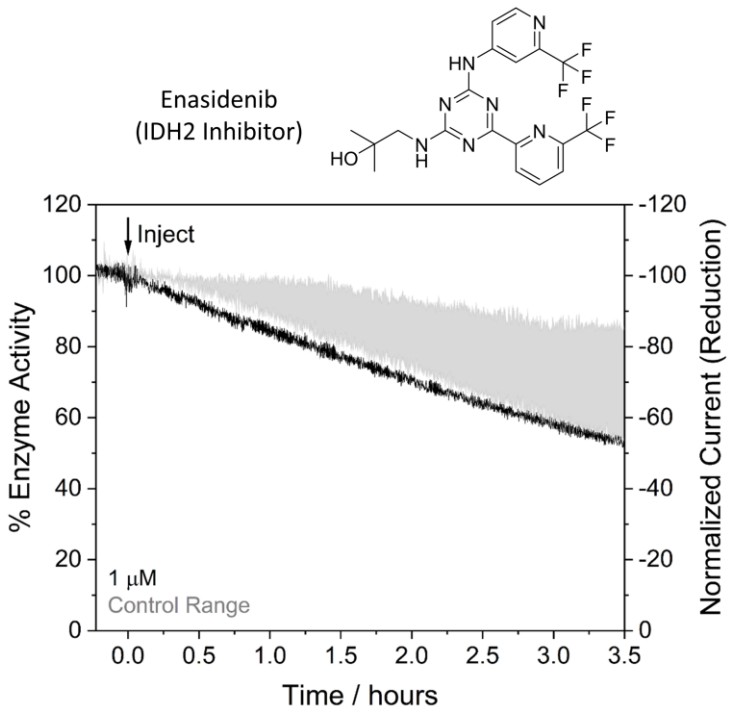


Figure 62. Control experiment using Enasidenib (AG-221), a specific IDH2 variant inhibitor. Conditions: (FNR+$IDH1_{R132H}$)@ITO/PGE electrode, area 0.06 cm^2, electrode rotated at 1000 rpm, temperature 25 °C, $E = -0.513$ V vs SHE, mixed buffer (pH = 8): 20 mM each: MES, TAPS, CHES, 10 mM $MgCl_2$, 10 μM NADPH, 10 mM 2OG, volume 4 mL. Enzyme loading ratio (molar): FNR/$IDH1_{R132H}$; 2/5. Inhibitor (2.5 μL in DMSO) was injected at $t = 0$. The shaded region shows the range for 3 DMSO controls.

Ivosidenib and Nov224 were 3.4 ± 0.3 and 4.2 ± 0.3 nM (±standard error) following a 12 minute incubation (**Figure 59B**). The very slow decrease in current, just above the control, is compelling evidence that the results with Ivosidenib and Nov224 reflect specific enzyme-inhibitor interactions.

Importantly, these experiments also show that the rate of inhibition varies with the concentration of inhibitor used, and that, even at very low (nanomolar) inhibitor concentrations, the reaction is pseudo first-order. These features were exploited to obtain detailed kinetic information as will be described in subsequent sections.

4.3.5 Obtaining Pseudo First-order Kinetics at Nanomolar Inhibitor Concentrations

Building on the kinetic experiments in the preceding sections, my goal was to develop an analytical framework that would allow extraction of more detailed kinetic information that could inform on the mechanism of IDH1 variant inhibition. Early on, by thinking carefully about the experimental setup and plotting the inhibition timecourse data in different ways, I realized that the data exhibited pseudo first-order kinetics, even at *nanomolar* inhibitor concentrations, and that this offered a significant advantage over solution-based kinetics for studying slow, tight-binding inhibitors such as those for IDH1 (kinetic experiments using inhibitor concentrations approaching the enzyme concentration are not pseudo first-order in homogeneous solution). The next several sections in this Chapter leverage this property to capture detailed kinetic information that would be very difficult to obtain using standard methods, ultimately resulting in a working kinetic mechanism of IDH1 variant inhibition.

Inhibition chronoamperometry (timecourse) experiments were performed over a range of Ivosidenib concentrations showing inhibitor-induced changes to the rate of IDH1 R132H-catalyzed 2OG reduction over time (i.e., the rate of change of enzyme rate) (**Figure 63A**). As before, the electrode was rotated to facilitate mass transport of substrate and inhibitor, and, consistent with previous experiments, higher concentrations of inhibitor resulted in faster inhibition. In all cases, inhibition approached an equilibrium value indicating incomplete inhibition. It was also clear that the rate of inhibition approached a maximum value at high inhibitor concentrations (the significance of this will be shown later). To test whether the data were pseudo first-order, the data were plotted in semi-log form

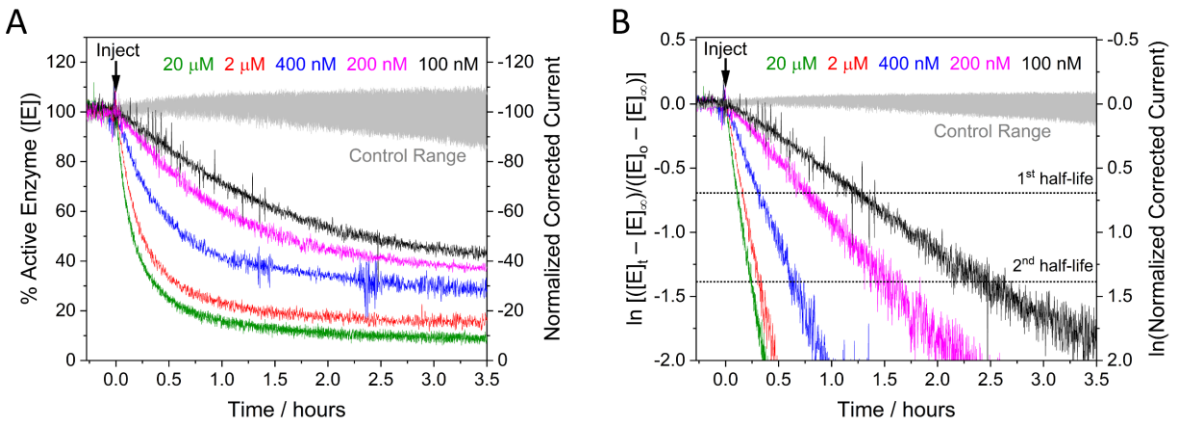


Figure 63. Plots of IDH1 R132H inhibition at different concentrations of Ivosidenib showing pseudo first-order behavior. (A) Different concentrations of Ivosidenib (0.1–20 µM) induce changes in the amount of active IDH1 R132H over time (using enzyme rate/current as a proxy, see **Methods**). The data in panel A were corrected for film loss (see **Methods**); uncorrected data are presented in the **Appendix**. (B) Data from panel A plotted logarithmically according to Eq. 22 showing that inhibition exhibits pseudo first-order reaction kinetics for >2 half-lives. The equilibrium value for each data set was obtained from the film loss corrected plot (panel A). Conditions: (FNR+IDH1$_{R132H}$)@ITO/PGE electrode, electrode area 0.06 cm^2, electrode rotation rate 1000 rpm, temperature 25 °C, E = –0.5 V vs SHE, O_2 < 1 ppm, volume 4 mL, pH = 8 (20 mM each of: MES, TAPS, CHES), 10 µM NADPH, enzyme loading ratios (molar): FNR/IDH1$_{R132H}$; 2/5.

(**Figure 63B**) based on the integrated rate law for a pseudo first-order reversible reaction (see **Chapter VII** for derivation):

$$\ln\left(\frac{[\mathrm{E}]_t - [\mathrm{E}]_\infty}{[\mathrm{E}]_\mathrm{o} - [\mathrm{E}]_\infty}\right) = -(k_{\mathrm{obs}})t\,, \qquad \text{(Eq. 22)}$$

where the subscripts o, t, and ∞ represent enzyme concentrations at t = 0, t = variable, and t = infinity (equilibrium), respectively. The linear data in **Figure 63B** confirm that all of the reactions, from 0.1 µM up to 20 µM inhibitor, exhibit pseudo first-order kinetics for more than two half-lives. Notably, the pseudo first-order observed rate constant (k_{obs}) can be obtained from the slope of each data set in the semi-log plot (see Eq. 22). The ability to analyze such a large range of inhibitor concentrations under pseudo first-order conditions is possible because the total amount IDH1 R132H enzyme present (~17 pmoles)[23] is much lower than the total amount of inhibitor in the bulk solution reservoir (0.4–80 nmoles for

these experiments). Furthermore, mass transport of small molecules (substrate, inhibitor, etc.) *within* the ITO layer is not limiting, except for very fast reactions[109] (see **Treatment of Primary Data** in the **Methods** for an extended discussion). As a result, the inhibitor concentration does not change during the experiment and pseudo first-order conditions apply. It should be noted that the timecourse data show the *transient* (i.e., approach to equilibrium) kinetics of inhibition during *steady-state* enzyme catalysis.

4.3.6 Obtaining k_{on}, k_{off}, and K_d Values from Timecourse Data

Although the observed rate constant (k_{obs}) can be determined from the slope of the semi-log plot (**Figure 63B**), the preferred method was to directly fit a first-order exponential decay equation (see **Methods**) to corrected timecourse data such as those in **Figure 63A**. This method was used because, like the Guggenheim method,[110–112] the equilibrium value of uninhibited enzyme ($[E]_\infty$) does not need to be known resulting in a simpler analytical procedure. Importantly, values obtained by direct fitting of the data were consistent with those derived using both the Guggenheim and semi-log slope methods.

A large number of experiments were carried out to test how the observed rate constant (k_{obs}) varied with different concentrations of Ivosidenib, 2OG, and Mg^{2+} (**Figure 64**). The measured k_{obs} values vary linearly with low concentrations of inhibitor ([I] < 1 μM). Importantly, in both cases, the gradients of the lines depend on the concentrations of 2OG and Mg^{2+}, but the lines meet at a common intercept. For each line, the behavior is characteristic of a reversible reaction between inhibitor, I, and enzyme, E,

$$E + I \underset{k_{off}}{\overset{k_{on}}{\rightleftharpoons}} EI, \qquad \text{(Eq. 23)}$$

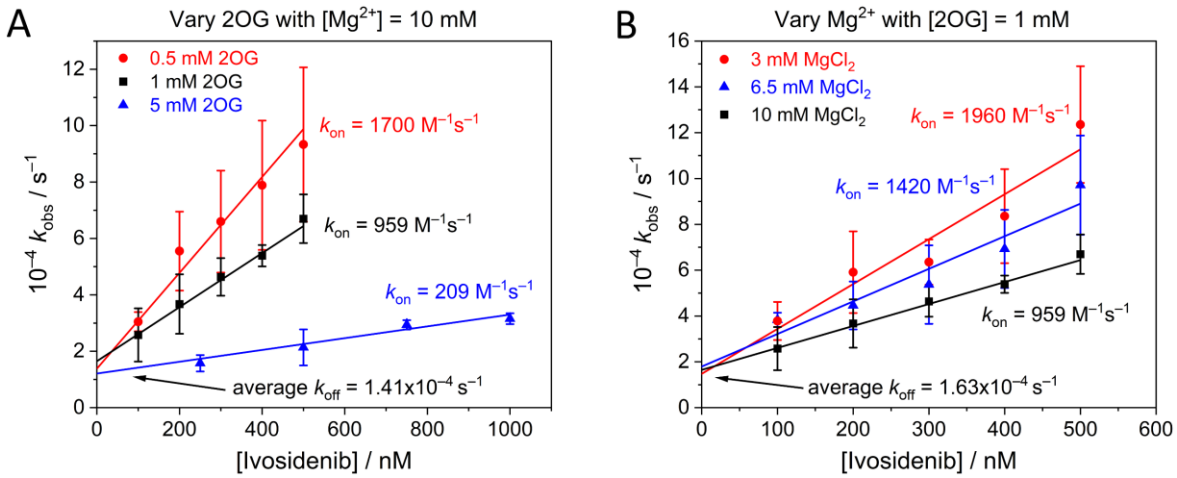


Figure 64. Observed rate constant (k_{obs}) values for IDH1 R132H inhibition at different Ivosidenib concentrations and with varied concentrations of 2OG (A) and $MgCl_2$ (B). The plotted k_{obs} values were determined by fitting a first-order exponential decay equation to timecourse inhibition experiments like those presented in **Figure 63A**. The slope = k_{on}, the intercept = k_{off}, and intercept/slope = K_d (see Eq. 24). Each data point represents 2–3 independent experiments. Conditions: (FNR+IDH1$_{R132H}$)@ITO/PGE electrode, electrode area 0.06 cm^2, electrode rotation rate 1000 rpm, temperature 25 °C, E = –0.5 V vs SHE, O_2 < 1 ppm, volume 4 mL, pH = 8 (20 mM of each: MES, TAPS, CHES), 10 µM NADPH, enzyme loading ratios (molar): FNR/IDH1$_{R132H}$; 2/5. The data in panel A were measured at $MgCl_2$ = 10 mM; the data in panel B were measured at 2OG = 1 mM. Note: data in black in panels A and B are the same.

where the observed rate constant, k_{obs}, can be plotted against the inhibitor concentration to obtain the second-order "on" and first-order "off" rate constants (k_{on} and k_{off}, respectively) according to:

$$k_{obs} = k_{on}[\mathrm{I}] + k_{off} \,. \qquad \text{(Eq. 24)}$$

Therefore, the slopes of the lines in **Figure 64** give the apparent k_{on} values at different concentrations of 2OG/Mg^{2+}, and the intercept gives k_{off}. Furthermore, the inhibitory equilibrium constant, K_d^{I}, is given by k_{off}/k_{on}. Similar experiments carried out with Nov224 at three different concentrations of 2OG (**Figure 65**) showed the same trends as those for Ivosidenib.

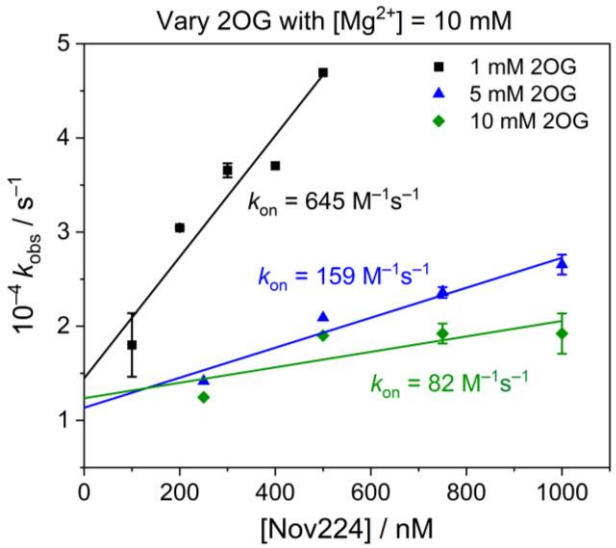


Figure 65. Observed rate constant (k_{obs}) values for Nov224 inhibition of IDH1 R132H with varied concentrations of 2OG. The plotted k_{obs} values were determined by curve fitting a first-order exponential decay equation to timecourse inhibition experiments like those presented in **Figure 63A**. Each data point represents 1–3 independent experiments. Conditions: (FNR+IDH1$_{R132H}$)@ITO/PGE electrode, electrode area 0.06 cm^2, electrode rotation rate 1000 rpm, temperature 25 °C, E = –0.5 V vs SHE, O_2 < 1 ppm, volume 4 mL, pH = 8 (20 mM of each: MES, TAPS, CHES), 10 µM NADPH, enzyme loading ratios (molar): FNR/IDH1$_{R132H}$; 2/5.

4.3.6.1 IDH1 Variant Inhibitors are Competitive with 2OG and Mg^{2+}

The flatter slopes at increasing 2OG and Mg^{2+} concentrations in **Figure 64** and **Figure 65** indicate that Ivosidenib and Nov224 are competitive with respect to both 2OG and Mg^{2+}; this is consistent with studies using standard methods.[35,50] Furthermore, the common intercepts (k_{off}) indicate that rates of inhibitor dissociation are *independent* of the presence of 2OG and Mg^{2+}. Taking the average of the intercepts for the five data sets for Ivosidenib and three data sets for Nov224 give k_{off} values of 1.50×10^{-4} s^{-1} and 1.27×10^{-4} s^{-1}, respectively. Interestingly, these values are not significantly different ($p = 0.15$; two-tailed t-test), suggesting that the rates of inhibitor dissociation could be gated by a process inherent to the enzyme, though more data with additional inhibitors would be needed to confirm this. A more detailed presentation of the kinetic data, compared with literature values for other

IDH inhibitors, is presented later in **Table 4**.

The fact that inhibition is competitive but dissociation is independent is interesting because 2OG and Mg^{2+} bind at the active site whereas Ivosidenib and Nov224 are allosteric inhibitors, binding at the IDH1 dimer interface.[35,40] Importantly, both observations are consistent with the proposed mechanism of inhibition. Competitive binding is consistent with results showing mutually exclusive Ivosidenib/Mg^{2+} binding,[35] in part owing to the enzyme adopting different conformations when either an inhibitor or 2OG/Mg^{2+} are bound. Similarly, once the enzyme is bound by the inhibitor, stabilizing the open inactive conformation of the enzyme, rates of changes between different enzyme conformational states should be dictated by the kinetics of inhibitor dissociation, which are apparently unaffected by 2OG/Mg^{2+} concentrations.

These data were used to derive a simplified mechanism of competitive inhibition, where the binding of either a molecule or ion X (2OG or Mg^{2+}), with a dissociation constant of K_d^X, prevents the enzyme from being inhibited by Ivosidenib or Nov224. The reactions are:

$$\mathrm{E} + \mathrm{I} \overset{k_{on}}{\rightarrow} \mathrm{EI} \qquad \text{(Eq. 25)}$$

$$\mathrm{E} + \mathrm{X} \overset{K_d^X}{\rightleftharpoons} \mathrm{EX} \qquad \text{(Eq. 26)}$$

from which it is derived that (see **Chapter VII**)

$$k_{on} = \frac{k_{on}^0 K_d^X}{K_d^X + [\mathrm{X}]}, \qquad \text{(Eq. 27)}$$

where k_{on}^0 is the second-order rate constant at [X] = 0. Taking reciprocals gives:

$$\frac{1}{k_{on}} = \frac{1}{k_{on}^{0}} + \frac{[X]}{k_{on}^{0}\, K_{d}^{X}} . \qquad \text{(Eq. 28)}$$

As evident from Eq. 28, plots of $1/k_{on}$ vs [2OG] or [Mg^{2+}] should be linear, with slope $=1/k_{on}^{0}K_{d}^{X}$, and intercept $=1/k_{on}^{0}$. As a result, the dissociation constants K_{d}^{X} for 2OG (at a specified Mg^{2+}concentration) or for Mg^{2+} (at a specified 2OG concentration) are obtained from the ratio intercept/gradient (**Figure 66)**. The derived values (K_{d}^{2OG}= 0.124 mM; $K_{d}^{Mg^{2+}}$ = 3.4 mM) agree with corresponding K_m values determined using standard solution-based assays (K_{m}^{2OG} = 0.40 mM; $K_{m}^{Mg^{2+}}$ = 4 mM for Mg^{2+}).[40] Again, the

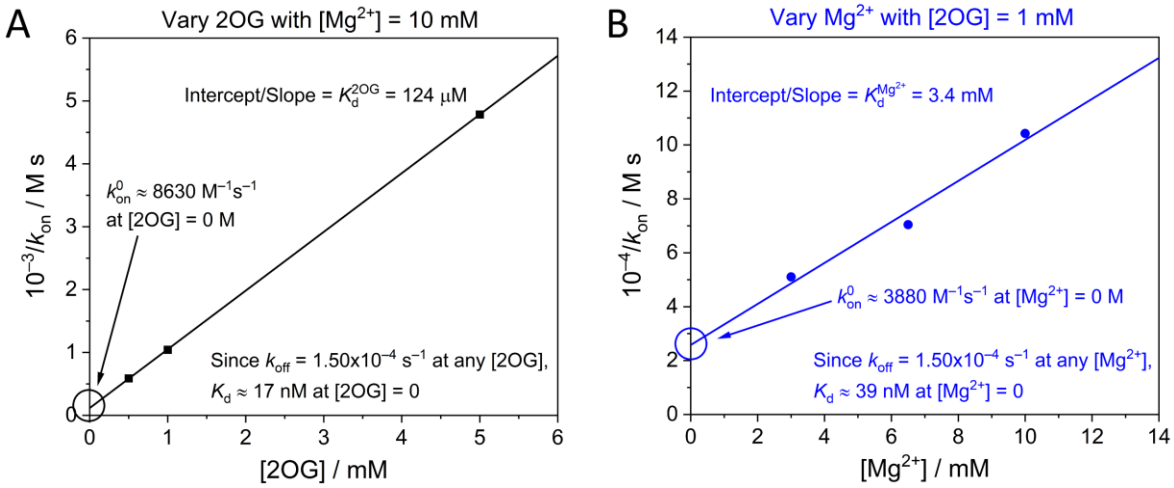


Figure 66. Reciprocal plots of k_{on} values obtained from the lines of best fit in **Figure 64A** and **B** according to Eq. 28 to obtain limiting Ivosidenib k_{on}^{0} values where [2OG] (A) and [Mg^{2+}] (B) equal 0 M. The plots also allow the k_{on} (and thus K_{d}^{I} as k_{off} is constant) to be estimated at any value of [2OG] or [Mg^{2+}] within the range of data collected.

results with Nov224 (**Figure 67**) were consistent with those for Ivosidenib**.** Significantly, the plots in **Figure 66** and **Figure 67** make it possible to predict values of k_{on} (and thus values of K_{d}^{I} as k_{off} is constant) for Ivosidenib or Nov224 over a range of concentrations of 2OG/Mg^{2+}. In the case of Ivosidenib, for example, at [2OG] = 0 (when $K_{d}^{I} = k_{off}/k_{on}^{0}$),

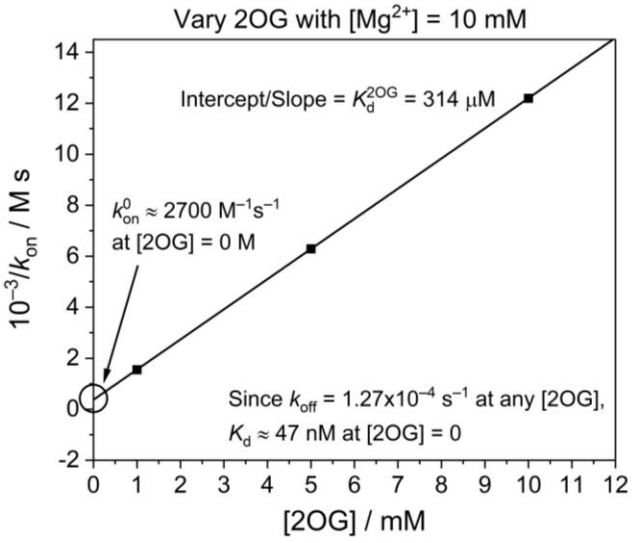


Figure 67. Reciprocal plot of k_{on} values obtained from the lines of best fit in **Figure 65** according to Eq. 28 to obtain limiting Nov224 k_{on}^{0} values where [2OG] equals 0 M. The plot also allows the k_{on} (and thus K_d^I as k_{off} is constant) to be estimated at any value of [2OG] within the range of data collected.

K_d^I = 17 nM; and when [Mg^{2+}] = 0, K_d^I = 39 nM. Significantly, these data are in agreement with IC_{50} values determined after enzyme-inhibitor pre-incubation (performed without either 2OG or Mg^{2+} present).[29,40,50,102] As the concentrations of 2OG or Mg^{2+} increase, inhibition of IDH1 R132H is suppressed, consistent with inhibition being competitive. Interestingly, Ivosidenib inhibition appears to be affected more strongly by changes in 2OG rather than Mg^{2+} concentrations, consistent with 2OG having a much lower K_d than Mg^{2+}. However, because Mg^{2+} is required for 2OG to bind the enzyme efficiently,[35] and since the K_d^{2OG} value (and all K_m values) must be measured with Mg^{2+} present, the effect of 2OG and Mg^{2+} are not able to be assessed separately.

4.3.7 IDH1 Variant Inhibitors Bind the Enzyme Before Inhibiting

It was noted before that the observed rate constant of the IDH1 inhibition reaction is linear with respect to low concentrations of inhibitor ([I] < 1 μM). However, as the

concentration of inhibitor is increased, the rate of inhibition eventually reaches a limiting value. **Figure 68A** shows k_{obs} values plotted over an extended range of Ivosidenib concentrations at two concentrations of Mg^{2+} (3 and 10 mM). The data imply that the observed rate constant, k_{obs}', simplified to account for only the forward reaction (see **Derivation of Equations**, **Chapter VII**), is dependent on [I] in a hyperbolic manner according to the empirical equation:

$$k_{obs}' = \frac{a[I]}{b + [I]}, \qquad \text{(Eq. 29)}$$

for which two mechanisms are possible involving the formation of a *non-inhibitory* pre-equilibrium complex (see **Chapter VII** for further discussion). The two options are: (1) inhibition is linear, involving the rapid and reversible formation of an initial enzyme-inhibitor complex in which the enzyme is still active, followed by a first-order (intramolecular) isomerization step that results in inhibition of the enzyme; (2) the inhibitor can bind in two different modes, one forming an inhibitory enzyme-inhibitor complex, and the other forming a complex in which the enzyme is still active but which blocks the binding of other inhibitor molecules (a so-called "dead-end" complex, see **Chapter VII**). Both mechanisms are consistent with Eq. 29, meaning neither option can be fully ruled out. However, mechanism 1 is well-established for slow, tight binding inhibitors.[104,107,113,114] and would be a simpler explanation for the observed behavior. Moving forward with mechanism 1, the first step is the rapid and reversible formation of a non-inhibitory enzyme-inhibitor complex according to:

$$E + I \overset{K^{pre}}{\rightleftharpoons} E \sim I' \qquad \text{(Eq. 30)}$$

where K^{pre} is the pre-equilibrium constant. This step is then followed by a first-order

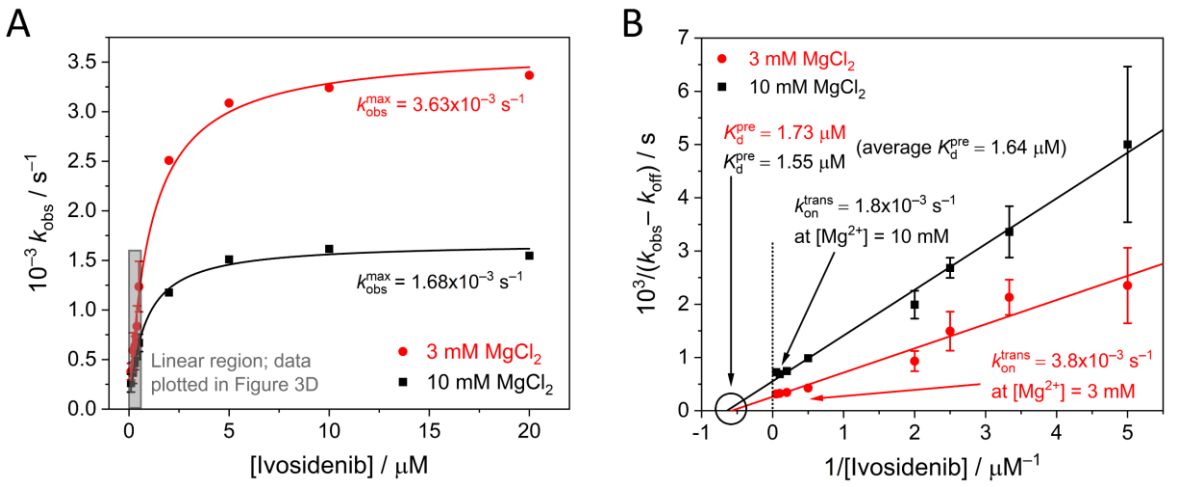


Figure 68. Data showing that Ivosidenib inhibits by a (at least) two-step mechanism. (A) Extended k_{obs} plot at two concentrations of Mg^{2+} ([2OG] = 1 mM) shows that the rate of inhibition exhibits a hyperbolic dependence on the concentration of Ivosidenib according to Eq. 29: inhibition is initially linear with inhibitor concentrations but reaches a limiting value that is Mg^{2+} dependent. The grey rectangle re-shows the data from **Figure 64B**. The k_{obs} values outside of the linear region were measured under the same experimental conditions as those described in **Figure 64B** (2OG = 1 mM); each of these data points represents a single experiment. (B) Data from **Figure 68A** plotted according to Eq. 33 to obtain k_{on}^{trans} and K_d^{pre} values.

(intramolecular) *trans*formative step giving the enzyme-inhibitor complex in which the enzyme is inhibited:

$$E \sim I \underset{k_{off}^{trans}}{\overset{k_{on}^{trans}}{\rightleftharpoons}} EI\,, \qquad \text{(Eq. 31)}$$

where k_{on}^{trans} and k_{off}^{trans} represent first-order rate constants for the reversible isomerization reaction. Assuming that $k_{off}^{trans} = k_{off}$ (this is reasonable because k_{off}^{trans} should be the rate-limiting step in that direction), the approach of Morrison and Walsh[114] can be used to derive (see **Chapter VII**):

$$k_{obs} - k_{off} = \frac{k_{on}^{trans}[I]}{K_d^{pre} + [I]}\,. \qquad \text{(Eq. 32)}$$

Taking the reciprocal of Eq. 32 gives:

$$\frac{1}{(k_{obs} - k_{off})} = \frac{1}{k_{on}^{trans}} + \frac{K_d^{pre}}{k_{on}^{trans}} \bullet \frac{1}{[I]}. \quad \text{(Eq. 33)}$$

According to Eq. 33, a straight line should be obtained for a plot of $1/(k_{obs} - k_{off})$ vs 1/[I]. Importantly, such a plot has a y-intercept = $1/k_{on}^{trans}$ and an x-intercept = $-1/K_d^{pre}$ (**Figure 68B**). Notably, the two data sets in **Figure 68B**, representing experiments carried out at different concentrations of Mg^{2+} have a common x-intercept but cut through the y-axis at different points. This means that initial binding of inhibitor to the enzyme (non-inhibitory), represented by K_d^{pre} with a measured value of 1.64 µM, is unaffected by Mg^{2+}. In contrast, the second (inhibitory, rate-limiting) step (k_{on}^{trans}) is Mg^{2+}-dependent, with higher Mg^{2+} concentrations slowing the rate of inhibition, consistent with the reaction being competitive with Mg^{2+}.

Results with Nov224 were consistent with those observed for Ivosidenib (**Figure 69**), suggesting that these kinetic features are likely present in other allosteric inhibitors of IDH. The reciprocal plot in **Figure 69B** shows the data for Nov224 and Ivosidenib measured under the same conditions; interestingly, the data appear to converge at a common x-intercept, indicating that the formation of the initial (non-inhibitory) enzyme-inhibitor complex may be limited by a process inherent to the enzyme. However, data for more than two inhibitors would be required to confirm this.

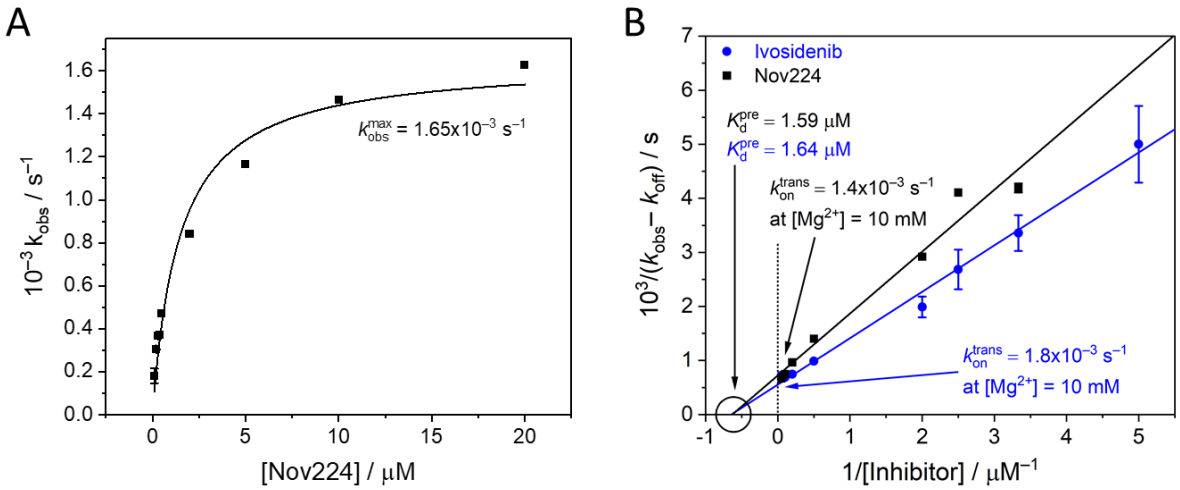


Figure 69. Data showing that Nov224 inhibits by a (at least) two-step mechanism. (A) Extended k_{obs} plot from the black data set presented in **Figure 65** ([2OG] = 1 mM) showing that inhibition exhibits a hyperbolic dependence on the concentration of Nov224 according to Eq. 29. Conditions were otherwise the same as those for experiments with Ivosidenib. (B) Data from panel A plotted according to Eq. 33 to obtain k_{on}^{trans} and K_d^{pre} values for Nov224 (black) for comparison with data for Ivosidenib inhibiton (blue) at [2OG] = 1 mM, [Mg^{2+}] = 10 mM.

4.3.8 Enzyme Inhibition Kinetics Under Concentrated versus Dilute Enzyme Conditions

To see how kinetic measurements of IDH1 R132H inhibition using the e-Leaf compare with values obtained in dilute solution, an experiment was designed to try to measure the kinetics of inhibition in solution (**Figure 70**). Within this context, it was of interest to see what type of information could be obtained under more conventional homogeneous conditions. Care was taken to keep as many of the conditions the same as possible to ensure a fair comparison between the e-Leaf- and solution-derived data. In order to study the *transient* kinetics of enzyme inhibition under conditions of *steady-state* enzyme turnover (like the e-Leaf), it was important that the rate of the IDH1 R132H reaction, monitored by depletion of NADPH (absorbance at 340 nm), was constant for an extended period of time. This was achieved for over 30 minutes using conditions of 10 mM Mg^{2+}, 1 mM 2OG and a

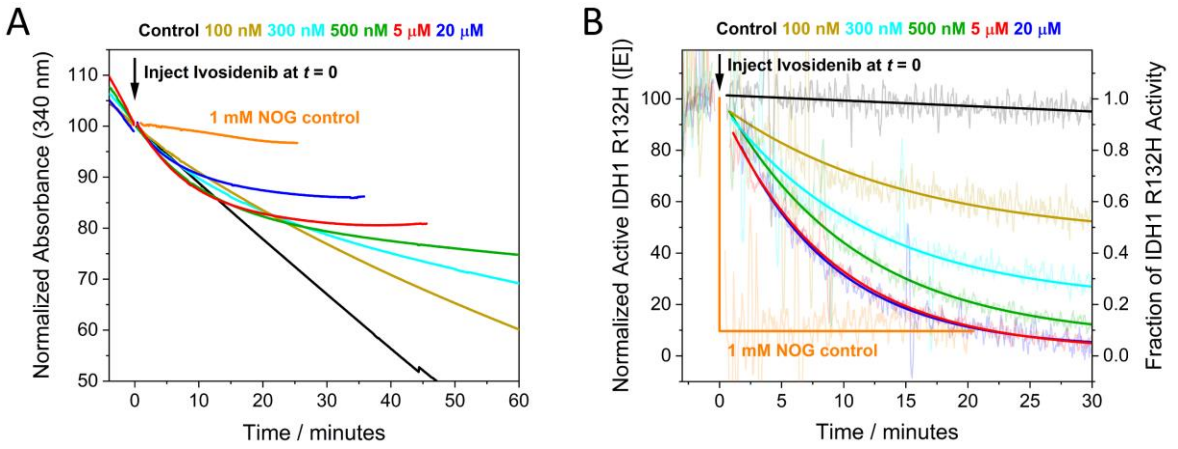


Figure 70. Kinetics of IDH1 R132H inhibition by Ivosidenib measured in dilute solution. (A) Normalized absorbance (at 340 nm to monitor [NADPH]) versus time showing how the rate is affected by different concentrations of Ivosidenib injected at t = 0. Ivosidenib was added to the reaction as a concentrated 1 µL solution in DMSO; the control experiment used DMSO without inhibitor. (B) First-derivative plot of the data in panel A (i.e., enzyme rate vs time) to measure the rate of inhibitor-induced changes to the enzyme rate and the extent of inhibition at different concentrations of inhibitor. Note: experiments at 2 and 10 µM Ivosidenib showed roughly the same rate of inhibition as 5 and 10 µM but were omitted for clarity.

IDH1 R132H solution concentration of 100 nM, which is ~10,000-fold less concentrated than the estimated *local* 1–2 mM IDH1 R132H concentration in the electrode nanopores.[23] **Figure 70A** shows the normalized absorbance plotted against time after additions of different concentrations of Ivosidenib into the solution. Note that the control experiment without inhibitor (black) is roughly linear for the duration of the experiment indicating that the turnover rate is constant. A control experiment was also performed to ensure that the slow rates of inhibition observed were representative of the kinetics of the inhibitor. In this case, an active-site binding inhibitor, N-oxalylglycine (NOG), a catalytically-inactive 2OG analogue,[35,54] was used, resulting in ~90% inhibition within seconds (**Figure 70**).

To better enable comparison with the e-Leaf results, the data in **Figure 70A** were converted into a first-derivative plot to show the inhibitor-induced "rate of change of enzyme rate" (**Figure 70B**); the resulting plot is analogous to the chronoamperometry (timecourse)

data obtained using the e-Leaf (**Figure 63A**). It is clear from **Figure 70B** that low concentrations of Ivosidenib do not fully inhibit the enzyme, consistent with the e-Leaf data. Furthermore, higher inhibitor concentrations give faster inhibition, but a limiting rate is eventually reached. As was done for the timecourse e-Leaf plots, a first-order exponential equation was fit to the data in **Figure 70B** to see how the observed rate constant (k_{obs}) varied with inhibitor concentration (**Figure 71**). In dilute solution, however, the experiments at low

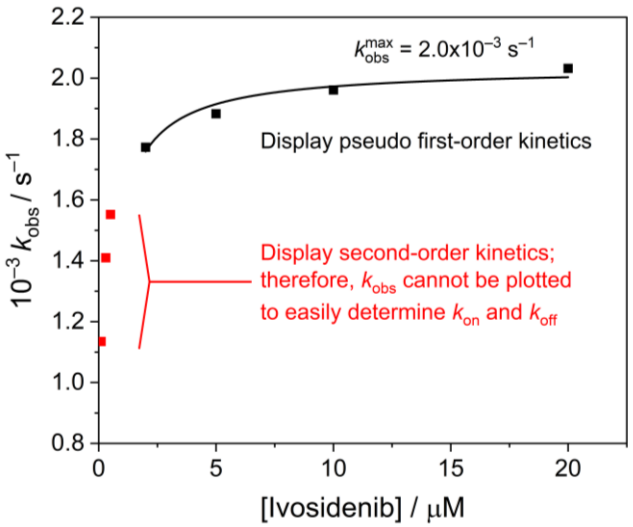


Figure 71. Plot of k_{obs} values against different Ivosidenib concentrations for inhibition experiments performed in dilute solution ([IDH1 R132H] = 100 nM). The k_{obs} values were determined by fitting a first-order exponential decay equation to enzyme rate vs time plots shown in **Figure 70B**. Note: the experiments at 2 and 10 μM Ivosidenib shown here are not shown in **Figure 70B** as they had roughly the same rate of inhibition as 5 and 20 μM (as shown in this figure).

concentrations of Ivosidenib were not obtained under pseudo first-order conditions ([IDH1 R132H] = 100 nM) meaning that, in contrast to the e-Leaf data, the solution data could not be used to obtain k_{on} and k_{off} values (**Figure 71**). Importantly, at higher concentrations of Ivosidenib (2–20 μM), pseudo first-order conditions applied, and thus the maximum rate of inhibition could still be derived using the solution data. Significantly, the value obtained from the solution data, 2.0x10^{-3} s^{-1} (half-time of 5.8 min.), is in very good agreement with the limiting value measured using the e-Leaf: 1.68x10^{-3} s^{-1} (half-time of

6.9 min.). The inhibition experiments in dilute solution give compelling evidence that the maximum (limiting) rate of inhibition observed electrochemically is not an artifact of the nanoconfined environment but a true property of the enzyme-inhibitor dynamics. Together, the data strongly imply the formation of a pre-equilibrium complex prior to the formation of the final inactive enzyme-inhibitor complex. Furthermore, the very good agreement between the crowded nanoconfined and dilute solution environments suggest that the e-Leaf environment does not substantially affect the kinetics of inhibition.

4.3.9 Comparison of e-Leaf Kinetic Data with Other Kinetic Data for IDH1/2 Inhibitors

Although no other kinetic data exists for Ivosidenib or Nov224 inhibition of any IDH1/2 enzymes, three studies provide kinetic data for other IDH1/2 inhibitors: one study, using surface plasmon resonance (SPR), measured ML309 binding to IDH1 R132H,[103] and two others, using a solution-based assay, measured Enasidenib (AG-221) and AGI-6780 inhibition of IDH2 R140Q.[95,97] It is important to note the significant difference between measuring *binding* versus *inhibition* because several IDH1 inhibitors (and presumably IDH2 inhibitors) can bind to both the IDH1 variants and the wildtype enzyme with roughly equal affinity while only inhibiting the variant.[101] The kinetic binding/inhibition data are compared in **Table 4**. Like Ivosidenib and Nov224, the other inhibitors (ML309, Enasidenib, and AGI-6780) bind allosterically[95–97] and exhibit slow binding/inhibition kinetics that are similar to those measured using the e-Leaf. Notably, measurements using SPR (ML309)[103] gave much faster on and off rate constants than activity-based assays measuring enzyme *inhibition* (solution assays[95,97] and this work), indicating that perhaps the SPR experiments were measuring, in part, the formation of the weakly bound pre-equilibrium complex

Table 4. Comparing IDH1/2 Inhibition Kinetics (Turnover Conditions) and Binding Kinetics (Non-turnover Conditions)

Inhibitor	Enzyme	k_{on}/M^{-1} s^{-1}	k_{off}/ s^{-1}	K_d/ μM	[Mg^{2+}]/ mM	[2OG]/ mM	Method	Turnover conditions	Ref.
Ivosidenib	**IDH1 R132H**	959	$1.50x10^{-4}$	0.156	10	1	e-Leaf	Yes	This work
Nov224 (IDH224)	**IDH1 R132H**	645	$1.27x10^{-4}$	0.197	10	1	e-Leaf	Yes	This work
Enasidenib	**IDH2 R140Q**	1480	$4.72x10^{-3}$	3.19	Not stated	Not stated	Solution	Yes	[97]
Ivosidenib	**IDH1 R132H**	322	$1.50x10^{-4}$	0.466	10	3.2	e-Leaf	Yes	This work
Nov224 (IDH224)	**IDH1 R132H**	241	$1.27x10^{-4}$	0.527	10	3.2	e-Leaf	Yes	This work
AGI-6780	**IDH2 R140Q**	967	$1.38x10^{-4}$	0.143	10	3.2	Solution	Yes	[95]
Ivosidenib	**IDH1 R132H**	8630	$1.50x10^{-4}$	0.017	10	0	e-Leaf	Yes	This work
Nov224 (IDH224)	**IDH1 R132H**	2700	$1.27x10^{-4}$	0.048	10	0	e-Leaf	Yes	This work
ML309	**IDH1 R132H**	32,000	$1.5x10^{-3}$	0.048	0	0	SPR	No	[103]

Note: Data presented here using turnover conditions measure activity-based enzyme *inhibition* kinetics. Non-turnover conditions (surface plasmon resonance (SPR)) measure the kinetics of inhibitor binding/release: binding does not result in immediate inhibition in the case of IDH1 (see text, **Figure 72**). The [Mg^{2+}] and [2OG] values are the concentrations under which inhibition/binding was measured. Ivosidenib values measured in this work were obtained from **Figure 64** and **Figure 66** to match the 2OG/Mg^{2+} concentrations used in the cited studies. Nov224 values were obtained from **Figure 65** and **Figure 67**.

convoluted by the presence of the slower isomerization step that results in a more stable final complex.

4.3.10 Further Testing the Proposed Model

To further test whether the data fit with the proposed two-step kinetic mechanism of inhibition, the overall inhibitor dissociation constant, K_d^I, was calculated by two different methods: (1) using data obtained at low (≤500 nM) Ivosidenib concentrations (**Figure 64B**) and (2) using data obtained at very high (extrapolated to infinity) Ivosidenib concentrations

(**Figure 68B**). At low Ivosidenib concentrations, the K_d^I is simply the ratio k_{off}/k_{on}. At high Ivosidenib concentration, the overall dissociation constant, K_d^I, is given by the product of the dissociation constants for each step:

$$K_d^I = \frac{k_{off} K_d^{pre}}{k_{on}^{trans}}. \quad \text{(Eq. 34)}$$

When calculated using data at low Ivosidenib concentrations (**Figure 64B**), the K_d^I values are 76 nM and 156 nM at 3 mM and 10 mM Mg^{2+}, respectively; the corresponding K_d^I values obtained from experiments at high Ivosidenib concentrations (**Figure 68B**) are 65 nM and 136 nM at 3 mM and 10 mM Mg^{2+}, respectively. These values are in very good agreement.

4.3.11 Bringing the Data Together: A Kinetic Mechanism of IDH1 Inhibition

The experiments in this Chapter have revealed new details about the kinetics of IDH1 R132H inhibition. Bringing the data together, a working kinetic mechanism of IDH1 variant inhibition is proposed (**Figure 72**). The rates shown are those for Ivosidenib, which was used as a case study. Importantly, however, as discussed throughout the text, the results with Nov224 were consistent with those for Ivosidenib, with slight differences in rates, suggesting that the mechanism presented here is generalizable to other allosteric IDH1 inhibitors. By extension, this mechanism is probably also relevant to allosteric IDH2 inhibitors, which bind the structurally analogous IDH2 variants at the dimer interface.[95,97]

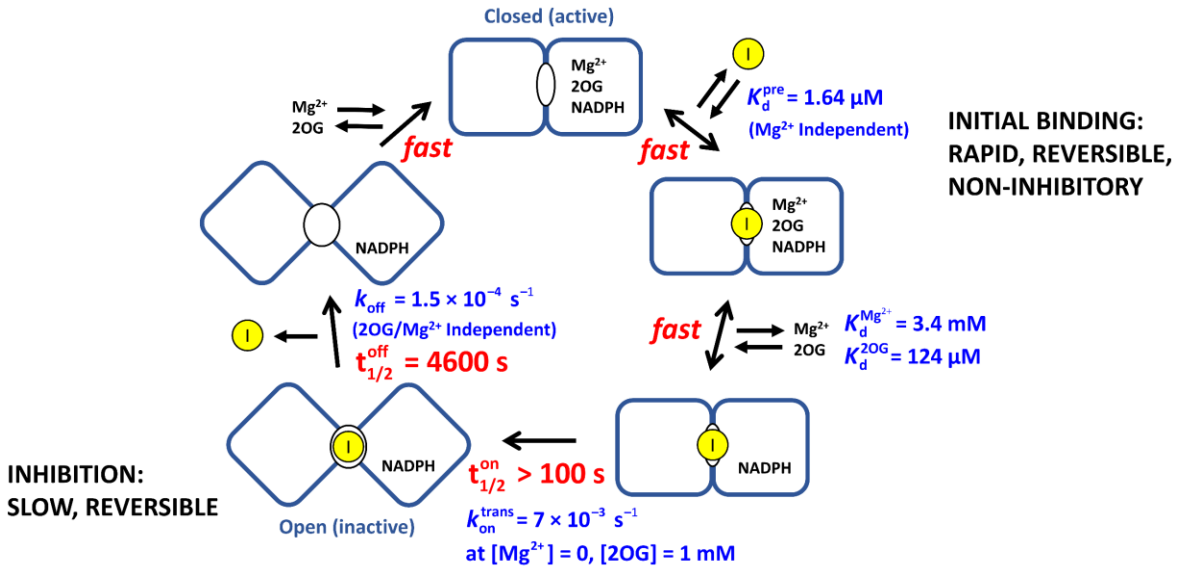


Figure 72. Kinetic mechanism for the inhibition of IDH1 R132H by Ivosidenib. It is likely that this kinetic mechanism is generally relevant to other allosteric dimer interface-binding IDH1/2 inhibitors. For simplicity, the binding/dissociation steps for 2OG and Mg^{2+} are shown at a single monomer active site (though there is likely half-site reactivity).[32] The pre-equilibrium dissociation constant, K_d^{pre}, was measured from data shown in **Figure 68B**. The K_d^{2OG} and $K_d^{Mg^{2+}}$ values were determined from data shown in **Figure 66** panels A and B, respectively. For the subsequent slow steps, the $t_{1/2}$ values are first-order complex half-times calculated using the rate constants given in blue for each step. The k_{on}^{trans} value presented is the limiting (fastest) rate, determined by plotting the Mg^{2+}-dependent k_{on}^{trans} values measured in **Figure 68B** against [Mg^{2+}] and extrapolating to [Mg^{2+}] = 0 M.

4.3.11.1 Timeline for an Average IDH1 R132H Molecule in the Inhibition Cycle

The inhibition cycle (**Figure 72**) involves multiple steps that occur on different timescales. To obtain an intuitive understanding of the process, it is a useful exercise to consider the inhibition process as experienced by a single statistically average enzyme molecule: (Stage 1) in the presence of inhibitor, a pre-equilibrium complex is formed between the inhibitor and enzyme; binding/dissociation is rapid, with the average enzyme molecule being bound 50% of the time at an inhibitor concentration of 1.64 µM (K_d^{pre}). Importantly, the enzyme remains catalytically active during this stage. (Stage 2) At an opportune moment, when the enzyme is transiently free of Mg^{2+} (and perhaps also 2OG), the

enzyme-inhibitor complex undergoes an isomerization reaction which stabilizes the enzyme in an inactive conformation, likely the open inactive form as has been observed by crystallography,[35,40,100] with a rate constant, k_{on}^{trans}. Binding is now 10–100-fold tighter than it was in the pre-equilibrium enzyme-inhibitor complex (**Table 4**). Importantly, this process also occurs much slower than the initial binding, on the order of 100 s (**Figure 72**) up to several minutes for the average molecule depending on the concentration of Mg^{2+} (and likely also 2OG) present. (Stage 3) Inhibitor dissociation, i.e., *reversal* of the latter step to reform the active enzyme molecule, represented by the first-order dissociation constant, k_{off}, is the slowest step of all. Notably, the kinetics are no longer affected by other components in the solution (i.e., 2OG or Mg^{2+}), and the enzyme will take ~4600 s (1.3 h) to become active again.

4.3.12 Discussion on General Mechanistic Features of IDH1/2 Variant Inhibition

4.3.12.1 Does the Oxidation State of IDH1-bound NADP(H) Affect Rates of Inhibition?

An interesting observation is that only NADP(H) is bound to the enzyme (at both active sites) for nearly every crystal structure of IDH1/2 which also has an inhibitor bound at the dimer interface. This was observed for GSK321,[99] ML309,[103] an analogue of BAY-1436032,[115] and Vorasidenib[100] bound to variants of IDH1, AG-6780[95] and AG-221[97] bound to variants of IDH2, and DS-1001B[40] bound to IDH1 R132C/S280F. It was also shown that the ML309 inhibitor had a very low affinity for the enzyme without NADPH present, but bound with high affinity when NADPH was added.[103] These repeat observations for different inhibitors of IDH1/2 variants thus pose the question: is it a general requirement for NADP(H) to be bound at the active site of each monomer in order for the inhibitor to

bind (i.e., uncompetitive inhibition with respect to NADP(H))? If so, does the oxidation state of the bound NADP(H) affect the ability of the inhibitor to bind the enzyme?

To test this using the e-Leaf, a chronoamperometry experiment was carried out with a potential switch during enzyme inhibition (**Figure 73**). Like other inhibition experiments before, Ivosidenib was injected in the reaction solution during steady-state IDH1 R132H

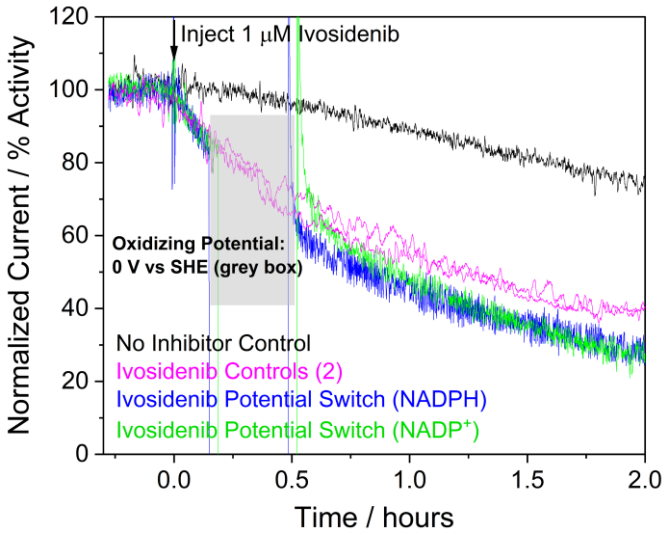


Figure 73. Chronoamperometry experiments to test whether changing the electrode potential (from reducing to oxidizing) affects rates of IDH1 R132H inhibition by altering the redox status of nanoconfined NADP(H) (see text). Conditions: (FNR+IDH1$_{R132H}$)@ITO/PGE electrode, area 0.06 cm^2, electrode rotated at 1000 rpm, temperature 25 °C, E = −0.51 V vs SHE (except when the potential was shifted to 0 V vs SHE for the blue and green traces (grey box)), mixed buffer (pH = 8): 20 mM each: MES, TAPS, CHES, 10 mM $MgCl_2$, 10 mM 2OG, volume 4 mL. The bulk solution contained 10 μM NADPH except for the green trace, which contained 10 μM NADP$^+$. Enzyme loading ratios (molar): FNR/IDH1$_{R132H}$; 2/5. 1 μM Ivosidenib (final concentration) was injected at t = 0. The control had DMSO injected without inhibitor.

catalysis. This time, however, after allowing the experiment to run for ~10 minutes to confirm IDH1 R132H inhibition, the potential was switched from reducing (−0.51 V) to oxidizing (0 V vs SHE) in order to convert all of the NADP(H) in the electrode nanopores to NADP$^+$, shutting down IDH1 R132H turnover in the process (grey box, **Figure 73**). During this time, IDH1 R132H would be forced to rebind NADP$^+$ or be without any NADP(H) bound, all whilst in the presence of Ivosidenib. The goal was to see if a significant change in

the rate of inhibition occurs under oxidizing conditions. After 20 minutes at an oxidizing potential, the potential was shifted back to reducing. Interestingly, the current resumed at a level that was roughly what would have been expected if no intervention had been made based on two Ivosidenib controls for which the potential was not adjusted (magenta traces). The same experiment was repeated with only $NADP^+$ present in the bulk solution (blue trace), but this also showed that the rates of inhibition were apparently unaffected by a change in the electrode potential. Although these experiments did not show that the rates of IDH1 R132H inhibition are affected by the redox state of the bound nicotinamide, they do not rule out that possibility, and it remains to be fully understood whether NADP(H) binding is required for the IDH1/2 enzymes to be inhibited.

4.3.12.2 Does the Reaction Being Catalyzed Affect Inhibition?

As discussed, the proposed mechanism of IDH1 variant inhibition involves the disruption of Mg^{2+} binding. This mechanism is what makes the inhibitors selective because the wildtype IDH1 enzyme has a much higher affinity for the Mg^{2+}-isocitrate complex than the variant enzymes do for Mg^{2+}, which binds separately from 2OG.[35] With this in mind, an experiment was carried out to test whether Ivosidenib is able to inhibit an IDH1 variant during catalysis of isocitrate oxidation instead of 2OG reduction (**Figure 74**). The experiment was carried out under similar conditions to other inhibition experiments, except that an oxidizing potential was applied to recycle $NADP^+$, and isocitrate was used in place of 2OG. Furthermore, the IDH1 R132C variant was used because it is capable of catalyzing isocitrate oxidation much faster than IDH1 R132H (see **Chapter II**).[40] Importantly, Ivosidenib is roughly equally effective against IDH1 R132C as the R132H variant.[40]

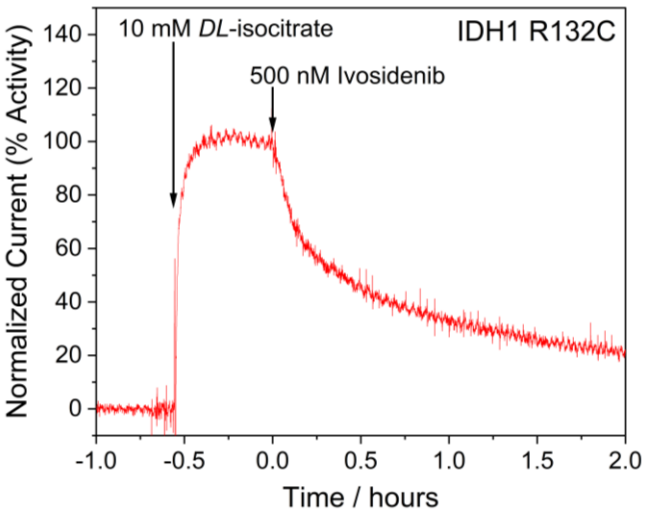


Figure 74. Ivosidenib inhibition of IDH1 R132C during catalysis of the wildtype reaction, isocitrate oxidation, instead of 2OG reduction. Conditions: (FNR+IDH1$_{R132C}$)@ITO/PGE electrode, area 0.06 cm^2, electrode rotated at 1000 rpm, temperature 25 °C, E = 0 V vs SHE, mixed buffer (pH = 8): 20 mM each: MES, TAPS, CHES, 10 mM $MgCl_2$, 10 μM $NADP^+$, 10 mM *DL*-isocitrate, volume 4 mL. Enzyme loading ratios (molar): FNR/IDH1$_{R132C}$; 2/5. Inhibitor (2.5 μL in DMSO) was injected at t = 0.

Despite the IDH1 R132C enzyme catalyzing isocitrate oxidation, strong inhibition was still observed (**Figure 74**).

4.3.12.3 Inhibitor Binding Stoichiometry

In this work, IDH1 inhibitors have been treated assuming a 1:1 binding stoichiometry with dimeric IDH1. Significantly, however, results obtained using non-denaturing mass spectrometry have shown that several inhibitors (GSK864, Nov224, DS-1001B, and Olutasidenib) predominantly bind IDH1 R132H twice;[35,40] in contrast, only one molecule of Ivosidenib binds to the enzyme.[35] It is not clear if the 2:1 binding stoichiometry (for some inhibitors) actually occurs in solution, where the inhibitor is much more dilute; however, two molecules of DS-1001B were shown to bind at the dimer interface, the proposed site of binding for IDH inhibitors, of the IDH1 double mutant, IDH1 R132C/S280F.[40] In this work,

the e-Leaf results with Nov224 (reported to bind twice) appear to exhibit pseudo first-order kinetics, following the same inhibitory mechanism as Ivosidenib (which only binds IDH1 R132H once) involving the rapid formation of a pre-inhibitory complex followed by a slow (reversible) inactivation of the enzyme. Based on these results, the following two scenarios are possible for Nov224 inhibition: (1) the enzyme is inhibited after the first molecule of Nov224 binds, rendering the second binding constant undetectable by an activity-based assay such as the e-Leaf; (2) Nov224 only binds the enzyme twice when it is present at high concentration (as is the case for non-denaturing mass spectrometry and crystallography). Importantly, both of these scenarios would be consistent with the results presented in this work for Nov224.

4.3.13 *This redacted material will be publicly available in December 2029*

This page contains redacted material that will become publicly available in December 2029.

This page contains redacted material that will become publicly available in December 2029.

This page contains redacted material that will become publicly available in December 2029.

This page contains redacted material that will become publicly available in December 2029.

This page contains redacted material that will become publicly available in December 2029.

4.4 Conclusions

Using a high-profile enzyme drug target, IDH1 R132H, as a case study, this Chapter presents a new method for investigating the kinetics of slow-acting enzyme inhibitors. Unlike conventional enzyme kinetics, the e-Leaf displays the steady-state enzyme rate directly as electrical current, enabling transient effects, i.e., *changes* to the steady-state rate, to be immediately detected and quantified. Notably, the e-Leaf is able to obtain pseudo first-order inhibition kinetics at very low (nanomolar) inhibitor concentrations, whereas this is not possible in homogenous solution assays in which the enzyme is also present at nanomolar (or greater) levels. Detailed kinetic data are obtained under steady-state turnover conditions (with substrate(s) and cofactor(s) present), yielding information on important processes such as inhibitor binding/dissociation, rates of intramolecular reorganization, and the formation of non-inhibitory enzyme-inhibitor complexes. Importantly, the requirement of turnover conditions implies that the data will automatically reflect differences in binding/inhibition mechanisms (e.g., competitive inhibition, conformational selection, induced fit binding). In contrast, standard techniques measuring binding affinity (IC_{50}, K_d) or binding kinetics (surface plasmon resonance (SPR)) are performed under non-turnover conditions, measuring affinity/rates of binding to inactive enzyme—these values are likely less predictive of in vivo efficacy, especially if the enzyme is conformationally dynamic and/or if the inhibitor can only bind (or binds preferentially) particular enzyme conformations/states as is likely the case for IDH1/2.[35,95,97,103] Importantly, despite the enzymes being concentrated to millimolar levels inside an inorganic material,[23] the data for Ivosidenib are consistent with experiments carried out in dilute solution and are within the range of other reported IDH1/2 inhibitors.

Through careful adaptation of established kinetic equations, coupled with unique advantages of the e-Leaf for studying slow tight-binding inhibitors, it was possible to establish a working kinetic mechanism of IDH1 variant inhibition. Briefly, inhibitor *binding* appears to occur in two steps, one fast (non-inhibitory) and one slower, the slower step being competitive with 2OG/Mg^{2+}; inhibitor *dissociation* is a very slow process, occurring on the timescale of hours, and it appears to be independent of the presence of 2OG/Mg^{2+}. The improved mechanistic understanding of how these allosteric inhibitors function should prove useful for designing more potent and selective drugs. Kinetic features can also be selected for: overall slow binding/dissociation kinetics can be an advantage, allowing a drug to have fewer "off-target" interactions if the drug-enzyme complex lifetime can be extended to outlive the functional lifetime of the enzyme in vivo.

CHAPTER V

5 This material will be available in December 2029.

This page contains redacted material that will become publicly available in December 2029.

This page contains redacted material that will become publicly available in December 2029.

This page contains redacted material that will become publicly available in December 2029.

This page contains redacted material that will become publicly available in December 2029.

This page contains redacted material that will become publicly available in December 2029.

This page contains redacted material that will become publicly available in December 2029.

This page contains redacted material that will become publicly available in December 2029.

This page contains redacted material that will become publicly available in December 2029.

This page contains redacted material that will become publicly available in December 2029.

This page contains redacted material that will become publicly available in December 2029.

This page contains redacted material that will become publicly available in December 2029.

This page contains redacted material that will become publicly available in December 2029.

This page contains redacted material that will become publicly available in December 2029.

This page contains redacted material that will become publicly available in December 2029.

This page contains redacted material that will become publicly available in December 2029.

This page contains redacted material that will become publicly available in December 2029.

This page contains redacted material that will become publicly available in December 2029.

This page contains redacted material that will become publicly available in December 2029.

This page contains redacted material that will become publicly available in December 2029.

This page contains redacted material that will become publicly available in December 2029.

This page contains redacted material that will become publicly available in December 2029.

This page contains redacted material that will become publicly available in December 2029.

CHAPTER VI

CONCLUSIONS AND FUTURE PERSPECTIVES

6 Conclusions and Future Perspectives

6.1 Nanoconfined Cascade Catalysis

The results in this work, particularly those in **Chapter III** in which an NADP(H)-dependent cascade was run using only enzyme-copurified NADP(H), show that nanoconfinement can be exploited to dramatically increase (by orders of magnitude) the efficiency of cascade catalysis. The ability to keep NADP(H) trapped in the electrode nanopores or other confined spaces alongside enzymes may not be possible for many systems which do not contain an enzyme like IDH1, which can rebind it between catalytic cycles. However, the unique cofactor-efficient experiments set a new benchmark for what is possible: ~160,000 $TTN_{NADP(H)}$ without any experimental optimization. The experiments showing extreme cascade efficiency emphasize why nanoconfinement has evolved to be such a prevalent strategy in biology—these experiments also have conceptual relevance to pre-cellular evolution in which the first organic molecules may have been synthesized within the nanospaces between minerals.[134,135]

Significantly, the presence of only a finite amount of NADP(H) in the IDH1-FNR-NADP(H) system made it possible to quantify the amount of a non-electroactive enzyme present in an e-Leaf electrode for the first time. Quantification showed that the enzymes and NADP(H) both concentrate in the electrode relative to the bulk solution, ultimately reaching millimolar levels. Interestingly, despite the approximate 10,000-fold difference in concentration, the turnover frequencies measured for nanoconfined enzymes ($k_{cat(nano)}$) are within the same order of magnitude as turnover frequencies measured in homogeneous solution (k_{cat}). Such high concentrations give rise to a “cluster channeling”

effect whereby a cascade intermediate can be processed by any one of multiple copies of the next enzyme locally within the electrode.[4,136] Indeed, at total nanoconfined enzyme concentrations ([FNR] + [IDH1]) around 2 mM, the center-to-center distance between enzymes is only 9.4 nm, indicating that a cascade intermediate only needs to diffuse a few nanometers before reaching another enzyme. This cluster channeling effect is what allows non-electroactive enzymes to be treated as electrocatalysts by drastically reducing the lag time between sequential ordered reactions. Furthermore, these high local enzyme concentrations increase the efficiency of cascade catalysis by preventing the escape of intermediates because they are more likely to be consumed rather than diffuse out of the electrode.[1]

6.2 The Kinetic Mechanism of Isocitrate Dehydrogenase Inhibition

A large part of this work focuses on developing new methods to investigate the kinetic mechanism of IDH1 variant inhibition. Despite being a high-profile drug target for which two FDA-approved drugs have been developed, there is a glaring lack of kinetic information available in the literature on the kinetics of IDH1 variant inhibition. This is especially surprising considering that preliminary experiments[95,97,103] have shown that the IDH1/2 inhibitors generally exhibit very slow kinetics which affect apparent IC_{50} values.[41]

After establishing the fundamental behavior (thermodynamic and kinetic) of the IDH1 enzymes in the e-Leaf (**Chapter II**), the unique advantages of the e-Leaf for studying slow tight-binding inhibitors were exploited. Using the most common cancer-associated IDH1 variant, IDH1 R132H, and the first FDA-approved IDH1 inhibitor, Ivosidenib, as a model system, an e-Leaf experimental method and analytical framework were developed, ultimately leading to a kinetic mechanism of inhibition. The kinetic mechanism is as follows: *inhibition* occurs in two steps, one rapid (non-inhibitory) and one slower (inhibitory), on the order of several minutes; importantly, the slower step is competitive with 2OG/Mg^{2+}. Inhibitor *dissociation* is a very slow process, occurring on the timescale of hours; significantly, this process appears to be independent of the presence of 2OG/Mg^{2+}. The same kinetic mechanism was observed for both Ivosidenib and another IDH1 variant inhibitor, Novartis 224, suggesting that the mechanism has general relevance for IDH1/2 allosteric inhibition. Significantly, results with a wildtype IDH1 inhibitor indicate that it also likely follows the same mechanism but with even slower overall kinetics.

This work constitutes the first significant investigation into the kinetics of IDH1 variant inhibition. The resulting improved mechanistic understanding of allosteric IDH1 inhibition emphasizes the importance of obtaining kinetic inhibition data *under conditions of enzyme turnover* alongside equilibrium binding data. In the case of IDH1, this is especially important because the inhibitors can bind the enzymes in non-inhibitory conformations, rendering binding-only methods unreliable. Furthermore, it is likely that the very slow kinetics are relevant to in vivo efficacy. The observation of competition between inhibitor and 2OG/Mg^{2+} for the (inhibitory) isomerization reaction but not initial inhibitor binding or inhibitor dissociation is also significant and may affect how the drug behaves in vivo where 2OG/Mg^{2+} are present. As proposed at the conclusion of **Chapter IV**, it should be possible to select for desired kinetic features using a suitable assay. Inhibitors exhibiting overall slow binding/dissociation kinetics may result in fewer off-target interactions if the drug-enzyme complex lifetime is longer than the functional lifetime of the enzyme in vivo.

6.3 The e-Leaf as an Analytical Tool for Investigating Enzyme Mechanisms

In contrast to conventional solution-based kinetics, the e-Leaf displays the steady-state enzyme rate directly as electrical current. This allows transient effects, i.e., *changes* to the steady-state rate, to be detected and quantified in real time. Significantly, because the e-Leaf operates using a tiny amount of enzyme (pmole scale) and the inhibitor is present in the bulk solution at any desired volume, the kinetics of inhibition are observed as a pseudo first-order process even at very low (nanomolar) inhibitor concentrations; in contrast, this is not possible for homogenous solution assays in which the enzyme is also present at nanomolar levels as is quite common. As demonstrated by the experiments in **Chapter III** focusing on NADP(H) rebinding by wildtype IDH1 and an IDH1 variant, the ability to tightly control the redox environment in which the enzymes reside can yield information which would be extremely difficult to obtain using other methods.

Another significant advantage of the e-Leaf is that it is an activity-based assay, meaning that all data are obtained under steady-state enzyme turnover conditions. The consequence is that the data obtained will automatically reflect differences in inhibition mechanisms that may be present between inhibitors (e.g., competitive inhibition, conformational selection, induced fit binding). On the other hand, standard techniques measuring affinity (IC_{50}, K_d) or binding kinetics (surface plasmon resonance (SPR)) are performed under non-turnover conditions. Such values are less likely to be representative of in vivo efficacy, especially if the enzyme is conformationally dynamic and/or if the inhibitor binds preferentially to particular enzyme states. Importantly, the e-Leaf kinetic inhibition

data for Ivosidenib with IDH1 R132H were shown to be consistent with experiments carried out in dilute solution despite the significant differences in environment.

An obvious next step is to scale-up the e-Leaf technology by incorporating it into a multi-electrode array (multiplexing). The ability to monitor dozens to hundreds of reactions in parallel would greatly improve experimental throughput, making the technology relevant for large-scale screening applications including, but not limited to, drug discovery, enzyme engineering (directed evolution), and biosensing.

6.4 This material will be available in December 2029

CHAPTER VII

METHODS AND DERIVATION OF EQUATIONS

7 Methods and Derivation of Equations

7.1 Materials and Methods

7.1.1 Enzyme Expression and Purification

Ferredoxin-$NADP^+$ reductase (FNR) from *Chlamydomonas reinhardtii* was produced as previously described.[40] Briefly, FNR production was induced in BL21(DE3)plysS *E. coli* cells by adding 1 mM IPTG and allowing the cultures to grow for a further 4 hours (37 °C). The cells were harvested by centrifugation; the pellets were resuspended in a small volume of cold buffer (50 mM HEPES, 150 mM NaCl, 1 mM DTT; pH 7.4) and stored overnight at −80 °C. The cells were thawed and lysed using a french press at 20 psi, and the lysate was centrifuged at 4 °C using an ultracentrifuge (Beckman L8-70M Ultracentrifuge). FNR was purified from the supernatant using a Ni^{2+} HisTrap HP affinity column (GE Healthcare Life Sciences) and eluted from the column using an imidazole gradient (final concentration of 250 mM imidazole). Fractions containing FNR were selected based on the absorbance at 280 nm and 460 nm. The fractions containing FNR were combined and concentrated using Amicon Ultra-4 mL Centrifugal filters (10 kDa) to a final volume of around 2 mL. The concentrated FNR solution was then applied to a desalting column (PD-10; GE Healthcare) to remove the imidazole. The enzyme was separated into single-use aliquots, flash-frozen in liquid nitrogen, then stored at −80 °C. Glutamate dehydrogenase (*E.* coli) was expressed and purified following the same procedure as above.

7.1.2 Expression and Purification of Recombinant *Hs* IDH1 and *Hs* IDH1 Variants

Human wildtype or IDH1 variants were expressed and purified as described.[40] Briefly, cells were grown at 37 °C until they reached OD_{600} = 0.6–0.8. Expression was induced with 1 mM IPTG at 18 °C for 12 hours. After centrifugation [Beckman-Coulter, J-Lite® JLA-10.500, 500 mL centrifuge tubes, 11,876 g (8,000 rpm), 10 min. cycles, 6°C], cells were resuspended in 50 mL of lysis buffer (20 mM Tris-HCl, 500 mM NaCl, pH 7.4) supplemented with DNase I, TCEP, lysozyme and a tablet of EDTA-free protease inhibitors (Merck). Cells were then lysed by sonication (Cole-Parmer, 60 % amplitude, 9.9 s on, 9.9 s off) on ice. After centrifugation [Beckman-Coulter, JA-25.50, 50 mL tubes, 69,486 g (24,000 rpm), 30 min cycles, 6°C], cell lysates were loaded onto a 5 mL HisTrap HP column (GE Healthcare Life Sciences, Little Chalfont, UK), with 50 mM Tris-HCl, 500 mM NaCl, pH 7.4, containing 20 mM imidazole, then eluted with an imidazole gradient (up to 500 mM imidazole). Fractions containing recombinant IDH1 were further purified using a Superdex S200 column (300 mL) equilibrated with 20 mM Tris-HCl, pH 7.4, 100 mM NaCl. Fractions containing the purified protein were concentrated by centrifugal ultra-filtration. The *apo*-proteins were generated by overnight treatment at 4 °C with ethylenediaminetetraacetic acid (EDTA) (2000x molar excess of protein), followed by purification by PD-10 desalting column. The purity of the resulting proteins was assessed as >95% (by SDS-PAGE) and their concentrations were determined using a ND-1000 NanoDrop spectrophotometer.

7.1.3 ITO/PGE Electrode Fabrication

Nanoporous indium tin oxide (ITO) electrodes were prepared by electrophoretic deposition of ITO nanoparticles (<50 nm particle size, Sigma-Aldrich) onto pyrolytic graphite edge (PGE) rotating disc electrodes as described.[23,24,26] Briefly, ITO nanoparticles were deposited from a suspension of ITO (0.02 g) with I_2 (0.01 g) dissolved in acetone (20 mL) that had been sonicated for ~1 hour. The electrode and a conductive support were held in parallel orientation in the ITO suspension (approximately 1 cm apart), and a voltage of 10 V was applied (zero current) for 6 minutes with the PGE electrode connected to the negative terminal. After six minutes, the ITO electrode was allowed to dry and was visually inspected. If the nanoporous ITO layer appeared thin (more blue/green than green/yellow), it was placed back in the solution with the same voltage applied for up to an additional 4 minutes. The electrode was rinsed with water before use. The same procedure was used for Ti foil electrodes, except both sides of the electrode were electrodeposited (6 minutes each side). The mechanism for electrophoretic deposition of metal oxide films has been described by Koura et al.[137]

7.1.4 Enzyme Loading (Dropcasting)

Enzymes were loaded onto the electrode by dropcasting a concentrated 4–7 µL solution onto the ITO electrode and allowing it to incubate at room temperature >30 minutes as described.[26] In all cases, 0.85 nmol (homodimer basis) of IDH1 (wildtype or variant) was used and the corresponding amounts of other enzymes were adjusted to give the desired molar enzyme ratios. Generally, four-fold more enzyme was used to load 4 cm^2 Ti foil electrode (unless otherwise stated). Enzyme molar ratios were calculated based on IDH1

homodimers. Electrodes were rinsed thoroughly using buffer before use in an experiment to ensure that no enzyme was introduced into the cell solution.

7.1.5 Electrochemical Quantification of Adsorbed FNR

Electroactive FNR adsorbed on the electrode was quantified by integrating and averaging the FNR-bound FAD redox peaks (non-turnover peaks) from cyclic voltammograms and using the equation

$$\Gamma = \frac{\text{Peak Area}}{nFA\nu}, \qquad \text{(Eq. 35)}$$

where Γ is the amount (in moles) of electroactive FNR per unit area (mol cm^{-2}), Peak Area is the average area of the integrated FNR-bound FAD reduction and oxidation peaks (in units AV or J s^{-1}), ν is the scan rate (V s^{-1}), F is the Faraday constant (96485 C per mole of electrons), A is the electrode surface area (cm^2), and n is the number of electrons transferred (2 electrons per molecule of FNR).

7.1.6 Electrochemical Experiments

Electrochemical experiments were performed in an anaerobic (O_2 < 1 ppm) glove box (Braun Technologies) with a nitrogen atmosphere. An Autolab PGSTAT 10 potentiostat was used with Nova software. Experiments carried out under aerobic conditions used a PalmSense Potentiostat with PSTrace software. In-house custom glass electrochemical cells were used for all experiments. A two-chamber glass cell was used for experiments with an ITO/PGE rotating disc electrode (the working electrode and platinum counter electrode were in the same chamber).[5,26] A three-chamber glass cell was used for scaled-up experiments

(4 cm^2 electrode) in which the working, counter, and reference electrodes were housed in separate chambers.[18] The working electrode chamber was surrounded by a water jacket to control the temperature. For scaled-up experiments (three-chamber cell), the counter electrode and working electrode chambers were separated by a glass frit and contained the same buffer solution. In all experiments, the reference electrode chamber contained 0.1 M NaCl and was connected to the working electrode chamber via a Luggin capillary. Electrode potentials were measured against either a saturated calomel electrode (SCE) or a Ag/AgCl (3 M KCl) electrode and converted to SHE using a SCE to SHE conversion table ($E_{SHE} = E_{SCE}$ + 0.241 V at 25 ºC)[26] or the following equation $E_{SHE} = E_{Ag/AgCl}$ + 0.21 V.

7.1.7 Live Buffer Exchange Protocol

Live buffer exchanges (i.e., where current is continuously monitored during the buffer exchange) were performed as previously described,[26] except that different volumes of exchange buffer were used depending on how much dilution was required. Briefly, a 1 mL syringe was used to reduce the reaction volume to ~1.5 mL while making sure that the electrode was always submerged in order to maintain electrical contact. A 60 mL syringe containing fresh buffer solution was then used to slowly inject 8 mL of buffer into the cell. The syringe was removed, and a 20 mL syringe was then used to remove 8 mL of buffer from the cell now containing the diluted starting buffer. Once the buffer volume was reduced to ~1.5 mL again, 8 mL of buffer solution was again added to the cell, and the process was repeated until all of the exchange buffer was used and the final cell volume was equal to the starting volume. The electrode rotation (1000 rpm) provided adequate solution agitation to ensure mixing during the procedure.

7.1.8 Enzyme Reactions in Homogeneous Solution

7.1.8.1 Wildtype IDH1 and IDH1 R132H Spectrophotometric Assays

Solution assays were conducted as previously described.[26] Briefly, reactions were carried out in a buffer containing 100 mM Tris base, 10 mM $MgCl_2$, 0.2 mM DTT, Tween-20 (0.005 % (C_V)), and 0.1 mg/mL BSA. The pH was adjusted to 6.0, 7.0, 8.0, or 9.0 using HCl or NaOH. Wild-type *Hs* IDH1 (2.5 nM) was allowed to warm up to room temperature, and the reaction was initiated by addition of 0.3 mM isocitrate and 0.1 mM $NADP^+$. *Hs* IDH1 R132H (200 nM) was allowed to warm up to room temperature, and the reaction was initiated by addition of 1.5 mM 2OG and 0.3 mM NADPH. The turnover of NADPH was observed by measuring the absorbance at 340 nm using a PHERAstar FS Microplate Reader. Activities were normalized to pH 8 for each enzyme. IDH1 molar enzyme concentrations were calculated based on their respective homodimers.

7.1.8.2 IC_{50} Measurement

IC_{50} values were measured as described.[26] Briefly, measurements were performed at pH 8 in a buffer containing 100 mM Tris base, 10 mM $MgCl_2$, 0.2 mM DTT, Tween-20 (0.005 % (C_V)), and 0.1 mg/mL BSA. *Hs* IDH1 R132H (15 nM) was incubated with inhibitor for 12 minutes before the reaction was initiated by addition of 1.5 mM 2OG and 0.3 mM NADPH. IC_{50} values were calculated using non-linear regression (GraphPad Prism). All experiments were conducted in triplicate. The molar enzyme concentration for IDH1 R132H was calculated based on the R132H homodimer.

7.1.8.3 IDH1-FNR Experiments in Homogeneous Solution

IDH1-FNR homogeneous solution cascade experiments were carried out as described.[23] Briefly, the isocitrate oxidation activity of the IDH1-FNR cascade was measured in dilute solution both with added NADPH (positive control) and without (only IDH1-copurified NADP(H) present) over 12 hours for comparison with the same cascade reaction nanoconfined in electrodes. Two experiments were carried out at different enzyme concentrations based on the amount of FNR and $IDH1_{dimer}$ that was quantified on individual small (0.06 cm^2) and large (4 cm^2) electrodes used in experiments (see **Figure 51** for details), equivalent to 2.6 (2.7) and 40 (41.5) nM of FNR (parentheses denote [$IDH1_{dimer}$]) in a 4 mL solution. The solution reactions were allowed to run at 25 °C for 12 h before heat quenching and analysis by ^{1}H NMR. $NADP^+$ was recycled by FNR for use by IDH1, with a large excess of benzyl viologen in solution (25 mM) to continuously re-oxidize FNR in place of the electrode. The cascade activity in solution was determined based on the amount of product made (2OG) in the solution over a 12-hour period (quantified by ^{1}H NMR after heat quenching). The molar ratio of FNR:$IDH1_{dimer}$ used was 1:1.04 ([IDH1] = 1.04 x [FNR]), the same ratio that was quantified in the electrode nanopores for the relevant electrochemical experiments using the FNR:$IDH1_{dimer}$ = 2:1 loading ratio (**Table 2**). Other conditions: 400 µL reaction volume, 100 mM HEPES (pH 8), 10 mM $MgCl_2$, 5 mM *D*-isocitrate, 25 mM benzyl viologen, 25 °C. All reactions were performed in triplicate with error bars representing the standard deviation.

7.1.8.4 FNR Solution Assay

FNR solution assays were carried out as described.[23] Briefly, the NADPH oxidation activity of FNR in homogeneous solution was determined in an anaerobic glovebox (Belle Technologies) (O_2 < 1 ppm) by measuring the absorbance of reduced benzyl viologen (Sigma-Aldrich) at 560 nm (isosbestic point of monomeric and dimeric reduced benzyl viologen)[138] using an Ocean Optics S2000 Fiber Optic spectrophotometer with OOIBase32 software (Ocean Optics, Inc.). An extinction coefficient of 7800 M^{-1} cm^{-1} was used for $1e^-$ reduced (radical) benzyl viologen[139] (two molecules of benzyl viologen are reduced for every molecule of NADPH oxidized). Reaction conditions: 2 nM FNR, 100 mM HEPES (pH = 8), 5 mM benzyl viologen, 26 °C, [NADPH] was varied, 1 mL reaction volume.

7.1.8.5 Solution Enzyme Inhibition Kinetic Assays

Inhibition experiments were carried out as described.[24] Briefly, experiments were carried out in homogeneous solution for comparison with inhibition experiments measured under the nanoconfined conditions in the e-Leaf. The IDH1 R132H reaction rate (reduction of 2OG to 2HG coupled to NADPH oxidation) was monitored by measuring the change in NADPH concentration (absorbance at 340 nm) over time via UV-vis spectroscopy (PerkinElmer UV/VIS/NIR Lambda 19 Spectrometer). The reaction was carried out under nearly identical conditions to the electrochemical inhibition experiments: the solution had a pH = 8 (20 mM each: MES, TAPS, CHES) and contained 10 mM $MgCl_2$, 1 mM 2OG, and 100 μM NADPH. The reaction temperature was 25 °C and was initiated by addition of 100 nM IDH1 R132H (concentration based on the dimeric form). A concentration of 100 nM IDH1 R132H was chosen because it afforded a long-lived steady-state reaction that allowed

the effect of a slow-acting inhibitor to be observed (i.e., 100 nM enzyme gave a near constant reaction rate for > 30 minutes). Once a steady-state reaction rate was achieved (i.e., the decrease in [NADPH] was linear), the cuvette was removed, and inhibitor was added (1 µL solution in DMSO at $t = 0$); the solution was mixed, and measurement was resumed. Control experiments had DMSO added without inhibitor.

7.1.9 e-Leaf Inhibition Kinetic Experiments

7.1.9.1 Treatment of Primary Data: Assumptions Required for Obtaining Inhibition Kinetic Parameters

In order to derive useful kinetic information on inhibition from a typical chronoamperometry experiment (measuring electric current over time at a fixed applied potential), two assumptions must be made to allow current to act as a proxy for the amount of active IDH1 R312H present in the electrode (as shown in **Figure 63A**): (1) the measured current is directly proportional to the rate of IDH1 R132H turnover under conditions where IDH1 R132H activity is limiting; (2) the specific activity (turnover rate) of each IDH1 R132H molecule is roughly equal throughout the 3–6 µM thick nanoporous ITO layer under the steady-state conditions achieved using a rotating disc electrode. Assumption 1 has previously been shown to be correct for IDH1 R132H[26] and several other E2 enzymes.[4,23,25] The second assumption is supported by a recent modelling study showing that, for an E2 enzyme with a dilute solution $k_{cat} = 1000\ s^{-1}$, the activities of the most deeply buried and the least buried enzyme molecules should be the same within a 5 µm-thick nanoporous ITO electrode, i.e., an enzyme molecule buried at 5 µm depth has the same turnover rate as an enzyme molecule near the electrode surface.[109] The solution k_{cat} of IDH1 R132H is

approximately 1–2 s^{-1},[35,40,54] thus the activity profile of R132H molecules can be assumed to be approximately homogeneous within the nanoporous electrode. With these two assumptions fulfilled, the measured current is thus proportional to the amount of active IDH1 R132H in the electrode nanopores.

The final crucial point enabling analysis is that, even at nanomolar concentrations, the inhibitor in the 4 mL bulk solution is present at much higher absolute quantities (0.4−80 nmoles for concentrations of 100 nM to 20 µM, respectively) than the concentrated IDH1 R132H enzyme that is trapped within the electrode nanopores (around 17 pmoles).[23] Because of this, the inhibitor is maintained at an effectively constant concentration throughout the experiment. With sufficient electrode rotation to maintain a constant local inhibitor concentration at the electrode, the reaction will exhibit pseudo first-order kinetics and can be analyzed accordingly.

7.1.9.2 Determining k_{obs} From Timecourse Experiments

Observed rate constant values (k_{obs}) for the inhibition of IDH1 R132H were determined by fitting a first-order exponential decay equation ("ExpDec1" fit using OriginLabs software) to chronoamperometry experiments that showed the rate of loss of enzyme activity over time (see **Treatment of Primary Data** above for details on how the measured electrical current is directly proportional to the amount of active IDH1 R132H enzyme present). The exponential decay equation was fit to the data for at least two half-lives of inhibition. The primary data were "film-loss corrected" (see below for details) before curve fitting to correct for the slight loss in enzyme activity during the course of an experiment. Obtaining k_{obs} values via direct curve fitting was preferred over using the slope of the semi-log plot

(example shown in **Figure 63B**) as it was both more convenient and more reliable than the slope method: curve fitting does not require the equilibrium concentration of free enzyme ($[E]_\infty$) to be known, and this value is convoluted by the film loss observed during experiments. Determining the k_{obs} using curve fitting is similar to the Guggenheim method,[110–112] which does not require equilibrium values to be known. Guggenheim analysis was also performed on the electrochemical inhibition data for comparison; rate constants measured using this alternative method were virtually identical to those obtained via direct curve fitting.

7.1.9.3 Film Loss Correction

Prior to curve fitting to obtain k_{obs} values, the inhibition timecourse (chronoamperometry) data were corrected to account for the small background decrease in enzyme activity over time (termed "film loss" in protein film electrochemistry). This was done despite the background loss in activity only having a marginal effect on measured kinetic constants (similar values are obtained when fitting the corrected and uncorrected data). To do this, eight control experiments were conducted at different 2OG and Mg^{2+} concentrations with DMSO injected into the solution (no inhibitor) to measure the average background loss in activity over time. The background activity loss did not correlate with different concentrations of 2OG or Mg^{2+} and was roughly linear after steady-state enzyme activity was established. The average decrease in activity over a 5-hour period for eight control experiments was 44 ± 5% (i.e., 56% activity remained after 5 hours on average). To correct for this, the average decay rate per data point measured (every 3 seconds) was added back as a percentage of the current measured at that timepoint. In other words, every three

seconds, the background decrease in activity was 0.007375%; this value was multiplied by the current measured at each timepoint, and this new value was added to the next current data point measured, in a cumulative fashion (i.e., each preceding background decay data point calculation was also added to the raw data point to obtain the corrected data point). Despite the background activity loss not having a large effect on measured kinetic parameters, the correction method proved effective, with control experiments maintaining a percent activity near 100% for > 2 hours—importantly, most inhibition kinetic data were obtained in less than one hour.

As noted above, the data correction did not substantially affect the measured rate constants. This is because the most important data was obtained within the first 20–60 minutes of measurement (depending on inhibitor/2OG/Mg^{2+} concentration) during which time control experiments lost an average of only 3–9% of activity. Importantly, because film loss appears as a roughly linear percentage of activity lost over time, and because the (exponential) rate of enzyme inhibition is fastest just after injection of inhibitor (when [E] is highest), the percentage of total initial enzyme activity lost due to film loss for inhibition experiments is far less than that for control experiments (i.e., film loss accounts for significantly less than 3–9% of the decrease in activity observed in inhibition experiments over the first 20–60 minutes).

The plot in **Figure 63A** was extended to 3.5 hours to show the approach to equilibrium, i.e., to show that inhibition is incomplete and there is active enzyme remaining. Although, the rate of film loss is low on the timescale of the initial enzyme inhibition, it does obscure visualization of the approach to equilibrium, hence the choice to correct the data. Importantly, measuring the observed rate constant (by fitting an exponential equation or

Guggenheim analysis) does not require the equilibrium value to be known. **Figure 87** in the **Appendix** shows data before and after film-loss correction.

7.1.10 ^{1}H Nuclear Magnetic Resonance (NMR) Experiments

NMR spectra were obtained as previously described[23] using a Bruker AVIII 700 MHz NMR spectrometer equipped with an inverse 5mm TCI $^{1}H/^{13}C/^{15}N$ cryoprobe. The water signal was suppressed by excitation sculpting. For copurification experiments, proteins were buffer exchanged into NMR buffer (50 mM Tris-d_{11}, 100 mM NaCl, 10 % D_2O, pH 7.5) using Micro Bio-Spin 6 columns (Bio-Rad) according to the manufacturer's protocol. The final protein concentrations were 50 µM for FNR and IDH1 R132H and 124 µM for wildtype IDH1 (a higher concentration was required to compensate for the weaker NADP(H) signal intensity due to copurification with both $NADP^+$ and NADPH). A ^{1}H spectrum (NS: 64, relaxation delay: 2 s) of this solution was obtained before the protein was denatured by heat (2 min, 100 °C). A spectrum of the denatured protein sample was recorded and the copurifying molecules identified by spiking with 100 µM of NADPH, $NADP^+$, or FAD.

A control experiment to investigate oxidation of NADPH to $NADP^+$ in the presence of FAD was set up according to the same parameters. The sample was composed of FAD (1 mM) and NADPH (1 mM) in NMR buffer. An equivalent experiment was set up with benzyl viologen (1 mM) and NADPH (1 mM).

For quantitative NMR experiments, 80 µL of a sample from electrochemical experiments in 100 mM HEPES was mixed with 16 µL D_2O (final 10% concentration), 16 µL 3-(Trimethylsilyl)propionic-2,2,3,3-d_4 acid sodium salt solution (TSP; final: 1 mM), 48 µL MQ water. The concentration of *D*-isocitrate and 2OG was calculated using the

concentration of the internal standard TSP. The number of scans was 32, and D1 was 30 s. If the sample concentration was small, the number of scans was increased to 128. The water signal was suppressed by excitation sculpting.

7.1.11 Non-denaturing Mass Spectrometry Experiments

Non-denaturing mass spectrometry studies were conducted as previously reported.[40] In brief, the protein samples were exchanged into buffer (ammonium acetate, 200 mM, pH 7.5) with Micro Bio-Spin 6 Columns (Bio-Rad). The samples were analyzed at a concentration of 20 µM on a quadrupole-TOF (Waters Synapt G2Si) instrument and an Advion Triversa Nanomate chip-based ESI autosampler. The parameters were as follows: 1.7-1.8 kV, spray backing gas pressure 0.6 psi, inlet pressure 3.7 mbar; cone voltages 100V and 5.2 V.

7.1.12 Data Smoothing

Some IDH1 R132H chronoamperometry traces were smoothed using the Nova software Savitzky-Golay method (polynomial order 2, 4 points left/right). The figure caption will indicate if smoothing was used. See **Figure 55** for an example of an IDH1 R132H trace before and after smoothing.

7.2 Derivation of Equations

7.2.1 Derivation of Equations for Chapter III

In order to derive an equation giving the current for an electroactive enzyme as a function of substrate concentration, we start with the equation describing the current from an electroactive enzyme,

$$I = nAF\Gamma k_T, \qquad \text{(Eq. 36)}$$

where I is the current (Amps), n is the number of electrons transferred per molecule, A is the electrode surface area (cm^2), F is the Faraday constant (96,485 C per mole of electrons), Γ is the enzyme coverage (moles cm^{-2}), and k_T is the enzyme turnover frequency (s^{-1}). Because the enzyme turnover frequency, k_T, changes with substrate concentration as described by the Michaelis-Menten equation (this equation also can be fitted to currents measured for nanoconfined enzymes in the e-Leaf), the substrate-dependent Michaelis-Menten turnover frequency must be substituted for k_T. When written in the form,

$$\nu = \frac{k_{cat}[S]}{K_m + [S]}[E], \qquad \text{(Eq. 37)}$$

the Michaelis-Menten turnover frequency is:

$$k_T = \frac{k_{cat}[S]}{K_m + [S]}. \qquad \text{(Eq. 38)}$$

Combining Eq. 36 and Eq. 38 gives Eq. 39, where k_{cat} and K_m have been renamed as $k_{cat(nano)}$ and $K_{m(nano)}$ to indicate that they are values for nanoconfined enzymes, not values for enzymes in dilute solution.

$$I = \frac{nAF\Gamma k_{\text{cat(nano)}}[\text{S}]}{K_{\text{m(nano)}} + [\text{S}]} \quad \text{(Eq. 39)}$$

(where $\frac{k_{\text{cat(nano)}}[\text{S}]}{K_{\text{m(nano)}}+[\text{S}]} = k_{\text{T}}$)

Eq. 40 is a modified form of Eq. 39 that was derived to account for substrate inhibition. It was derived the same way as Eq. 39, except that k_{T} in Eq. 36 was replaced by $\frac{k_{\text{cat}}[S]}{K_{\text{m}}+[S]+\frac{[S]^2}{K_i}}$, the Michaelis-Menten turnover frequency for a substrate inhibited enzyme, where K_i is the substrate inhibition constant.

$$I = \frac{nAF\Gamma k_{\text{cat(nano)}}[S]}{K_{\text{m(nano)}} + [S] + \frac{[S]^2}{K_i}} \quad \text{(Eq. 40)}$$

7.2.2 Derivation of Equations for Chapter IV

7.2.2.1 Derivation of the Pseudo First-order Reversible Integrated Rate Law

For the reversible enzyme inhibition reaction,

$$\text{E} + \text{I} \underset{k_{\text{off}}}{\overset{k_{\text{on}}}{\rightleftharpoons}} \text{EI}, \quad \text{(Eq. 41)}$$

the rate equation is:

$$-\frac{d[\text{E}]}{dt} = k_{\text{on}}[\text{E}][\text{I}] - k_{\text{off}}[\text{EI}]. \quad \text{(Eq. 42)}$$

Under pseudo first-order conditions, where [I] is constant throughout the experiment, the rate equation becomes:

$$-\frac{d[\text{E}]}{dt} = k_{\text{on}}^{\text{app}}[\text{E}] - k_{\text{off}}[\text{EI}] \quad \text{(Eq. 43)}$$

where

$$k_{on}^{app} = k_{on}[\mathrm{I}]. \qquad \text{(Eq. 44)}$$

The pseudo first-order rate equation (Eq. 42) can then be treated in the same manner as a first-order reversible rate equation using the *apparent* first-order forward rate constant in place of the second-order forward rate constant. Therefore,

$$[\mathrm{E}]_o = [\mathrm{E}]_t + [\mathrm{EI}]_t = [\mathrm{E}]_\infty + [\mathrm{EI}]_\infty, \qquad \text{(Eq. 45)}$$

and at equilibrium,

$$K = \frac{k_{on}^{app}}{k_{off}} = \frac{[\mathrm{EI}]_\infty}{[\mathrm{E}]_\infty}, \qquad \text{(Eq. 46)}$$

where the subscripts o, t, and ∞ represent concentrations at time t = 0, t = variable, and t = infinity (concentration at equilibrium), respectively. Subtituting Eq. 45 into Eq. 46 and solving for $[\mathrm{EI}]_t$ gives

$$[\mathrm{EI}]_t = \frac{k_{on}^{app}[\mathrm{E}]_\infty}{k_{off}} + [\mathrm{E}]_\infty - [\mathrm{E}]_t. \qquad \text{(Eq. 47)}$$

Substituting Eq. 47 into Eq. 43 gives the rate law for a pseudo first-order reversible reaction:

$$-\frac{d[\mathrm{E}]}{dt} = ([\mathrm{E}]_t - [\mathrm{E}]_\infty)(k_{on}^{app} + k_{off}). \qquad \text{(Eq. 48)}$$

Integration of Eq. 48 gives

$$\ln\left(\frac{[\mathrm{E}]_t - [\mathrm{E}]_\infty}{[\mathrm{E}]_o - [\mathrm{E}]_\infty}\right) = -(k_{on}^{app} + k_{off})t. \qquad \text{(Eq. 49)}$$

Substituting Eq. 44 into Eq. 49 gives the final integrated rate law for a pseudo first-order reversible reaction:

$$\ln\left(\frac{[\mathrm{E}]_t - [\mathrm{E}]_\infty}{[\mathrm{E}]_o - [\mathrm{E}]_\infty}\right) = -(k_{on}[\mathrm{I}] + k_{off})t \qquad \text{(Eq. 50)}$$

where

$$k_{obs} = k_{on}[\mathrm{I}] + k_{off}\,. \qquad \text{(Eq. 51)}$$

Therefore, plotting $\ln\left(\frac{[\mathrm{E}]_t - [\mathrm{E}]_\infty}{[\mathrm{E}]_o - [\mathrm{E}]_\infty}\right)$ against t using gives a straight line with a slope of $-k_{obs}$ (see **Figure 63B**).

7.2.2.2 Derivation of Rate Law for Competition Between Ivosidenib and 2OG/Mg^{2+}

For the forward enzyme-inhibitor reaction (ignoring the slow dissociation step),

$$\mathrm{E} + \mathrm{I} \xrightarrow{k_{on}} \mathrm{EI}\,, \qquad \text{(Eq. 52)}$$

where the enzyme also binds rapidly and reversibly to agent X (X = 2OG or Mg^{2+}), preventing the inhibitor from reacting with the enzyme, according to:

$$\mathrm{E} + \mathrm{X} \overset{K^{\mathrm{X}}}{\rightleftharpoons} \mathrm{EX}\,, \qquad \text{(Eq. 53)}$$

then

$$K_d^{\mathrm{X}} = \frac{[\mathrm{E}][\mathrm{X}]}{[\mathrm{EX}]}\,. \qquad \text{(Eq. 54)}$$

Because

$$[\mathrm{EX}] = [\mathrm{E}]_o - [\mathrm{E}]\,, \qquad \text{(Eq. 55)}$$

therefore

$$K_d^{\mathrm{X}} = \frac{[\mathrm{E}][\mathrm{X}]}{[\mathrm{E}]_o - [\mathrm{E}]}\,. \qquad \text{(Eq. 56)}$$

Rearranging gives:

$$K_d^{\mathrm{X}}[\mathrm{E}]_o = [\mathrm{E}][\mathrm{X}] + K_d^{\mathrm{X}}[\mathrm{E}]\,, \qquad \text{(Eq. 57)}$$

and solving for [E] gives:

$$[\mathrm{E}] = \frac{K_\mathrm{d}^\mathrm{X}[\mathrm{E}]_\mathrm{o}}{K_\mathrm{d}^\mathrm{X} + [\mathrm{X}]}. \qquad \text{(Eq. 58)}$$

Therefore, the rate of an enzyme-inhibitor reaction with a competing reaction between the enzyme and agent X is given by:

$$\text{rate} = k_\mathrm{on}[\mathrm{E}][\mathrm{I}] = \frac{k_\mathrm{on}K_\mathrm{d}^\mathrm{X}[\mathrm{E}]_\mathrm{o}[\mathrm{I}]}{K_\mathrm{d}^\mathrm{X} + [\mathrm{X}]}, \qquad \text{(Eq. 59)}$$

where k_on is the observed second-order rate constant that depends on [X] which lowers the concentration of active enzyme. The form of the dependence (the attenuation of rate as [X] is increased) is obtained by noting that when [X] = 0, $k_\mathrm{on} = k_\mathrm{on}^0$. Therefore,

$$\text{rate} = k_\mathrm{on}[\mathrm{E}][\mathrm{I}] = \frac{k_\mathrm{on}^0 K_\mathrm{d}^\mathrm{X}[\mathrm{E}]_\mathrm{o}[\mathrm{I}]}{K_\mathrm{d}^\mathrm{X} + [\mathrm{X}]}, \qquad \text{(Eq. 60)}$$

and noting further that $[\mathrm{E}] = [\mathrm{E}]_\mathrm{o}$ and dividing each side by $[\mathrm{E}]_\mathrm{o}[\mathrm{I}]$ we obtain

$$k_\mathrm{on} = \frac{k_\mathrm{on}^0 K_\mathrm{d}^\mathrm{X}}{K_\mathrm{d}^\mathrm{X} + [\mathrm{X}]}, \qquad \text{(Eq. 61)}$$

in which k_on is independent of the point at which measurement is made, i.e., it is independent of [E]. The resulting rate equation thus has one dependent variable (k_on), one independent variable ([X]) and two constants (k_on^0 and K_d^X). Setting [X] = 0 in Eq. 61, we see that $k_\mathrm{on} = k_\mathrm{on}^0$ as required. Taking the reciprocal of Eq. 61 gives the linear equation:

$$\frac{1}{k_\mathrm{on}} = \frac{1}{k_\mathrm{on}^0} + \frac{[\mathrm{X}]}{k_\mathrm{on}^0 K_\mathrm{d}^\mathrm{X}}. \qquad \text{(Eq. 62)}$$

7.2.2.3 Relating the Observed Rate Constant to Pre-equilibrium Binding and the Rate-determining Inhibition Step

Adopting the approach of Morrison and Walsh[114] for a two-step inhibition mechanism according to the reaction scheme

$$E + I \underset{k_2}{\overset{k_1}{\rightleftharpoons}} EI \underset{k_4}{\overset{k_3}{\rightleftharpoons}} EI^*, \qquad \text{(Eq. 63)}$$

where the first step is a rapid equilibrium (k_1, k_2 >> k_3, k_4) followed by a slow, intramolecular isomerization reaction, the observed rate constant is equal to:

$$k_{obs} = \frac{k_3[I]}{K_i + [I]} + k_4, \qquad \text{(Eq. 64)}$$

where $K_i = k_2/k_1$. Using the nomenclature presented in this work, and assuming that $k_{off}^{trans} = k_{off}$ (since k_{off}^{trans} will be rate-determining step for the dissociation process), Eq. 64 is equivalent to:

$$k_{obs} = \frac{k_{on}^{trans}[I]}{K_d^{pre} + [I]} + k_{off}. \qquad \text{(Eq. 65)}$$

Rearranging gives:

$$k_{obs} - k_{off} = \frac{k_{on}^{trans}[I]}{K_d^{pre} + [I]}, \qquad \text{(Eq. 66)}$$

and taking the reciprocal gives:

$$\frac{1}{(k_{obs} - k_{off})} = \frac{1}{k_{on}^{trans}} + \frac{K_d^{pre}}{k_{on}^{trans}} \bullet \frac{1}{[I]}. \qquad \text{(Eq. 67)}$$

Therefore, a plot of $\frac{1}{(k_{obs} - k_{off})}$ versus 1/[I] gives a linear plot with a y-intercept = $1/k_{on}^{trans}$ and an x-intercept = $-1/K_d^{pre}$. An alternative method to derive Eq. 65 is given in the next

section, where initially, the reverse kinetic step, k_{off}^{trans}, is ignored for simplicity (and because the reverse rate is very slow compared to the forward rate). This method yields Eq. 82, which is equivalent to Eq. 65 except that the y-intercept for Eq. 82 will equal 0 (because this equation does not account for the reverse reaction). To correct for this, the *off* rate constant, k_{off}, can be added to the right hand side of Eq. 82 so that the y-intercept is equal to the off rate constant (assuming that $k_{off}^{trans} = k_{off}$ since k_{off}^{trans} will be the rate-determining step in the reverse direction). Following this, Eq. 65 and Eq. 82 are equivalent, and Eq. 67 can be derived in the same manner as above.

7.2.2.4 Derivation of Equations Describing the Hyperbolic Dependence of the Inhibition Rate on [I]

The hyperbolic dependence of k_{obs} on [I], i.e., describing the rate reaching a limiting value, is given by the empirical formula:

$$\text{rate}' = \frac{a[\text{E}][\text{I}]}{b + [\text{I}]}, \qquad \text{(Eq. 68)}$$

where rate´ ignores the small contribution from the off rate constant (the intercept obtained at low [I]). Since, for a pseudo first-order inhibition reaction (where [I] is constant),

$$\text{rate} = k_{obs}[\text{E}], \qquad \text{(Eq. 69)}$$

we can obtain the pseudo first-order rate constant by dividing both sides of Eq. 69 by the enzyme concentration [E] (the value of k_{obs} does not depend on [E], but the term has to be extracted out) to give:

$$k_{obs}' = \frac{a[\text{I}]}{b + [\text{I}]}, \qquad \text{(Eq. 70)}$$

where k_{obs}' ignores the small contribution from the final off rate constant (the intercept obtained at low [I]). There are (at least) three ways that this rate law can arise:

(1) The inhibitor associates (rapidly) to form a non-inhibitory pre-equilibrium complex,

$$E + I \overset{K^{pre}}{\rightleftharpoons} E \sim I, \qquad \text{(Eq. 71)}$$

which is followed by an intramolecular isomerization reaction that results in inhibition (this step is also reversible, although we simplify by ignoring the back reaction as the intercept correction is very small).

$$E \sim I \underset{k_{off}^{trans}}{\overset{k_{on}^{trans}}{\rightleftharpoons}} EI \qquad \text{(Eq. 72)}$$

Using the pre-equilibrium approach, the initial pre-equilibrium is given by

$$K_d^{pre} = \frac{[E][I]}{[E \sim I]}. \qquad \text{(Eq. 73)}$$

Since

$$[E] = [E]_o - [E \sim I], \qquad \text{(Eq. 74)}$$

we obtain

$$K_d^{pre} = \frac{([E]_o - [E \sim I])[I]}{[E \sim I]}, \qquad \text{(Eq. 75)}$$

and since

$$K_d^{pre}[E \sim I] = [E]_o[I] - [E \sim I][I], \qquad \text{(Eq. 76)}$$

and

$$K_d^{pre}[E \sim I] + [E \sim I][I] = [E]_o[I], \qquad \text{(Eq. 77)}$$

it follows that

$$[\mathrm{E} \sim \mathrm{I}] = \frac{[\mathrm{E}]_o[\mathrm{I}]}{K_d^{pre} + [\mathrm{I}]}. \quad \text{(Eq. 78)}$$

Since

$$\mathrm{rate}' = k_{on}^{trans}[\mathrm{E} \sim \mathrm{I}], \quad \text{(Eq. 79)}$$

the rate is given by:

$$\mathrm{rate}' = k_{on}^{trans}[\mathrm{E} \sim \mathrm{I}] = \frac{k_{on}^{trans}[\mathrm{E}]_o[\mathrm{I}]}{K_d^{pre} + [\mathrm{I}]}. \quad \text{(Eq. 80)}$$

The rate can also be described by:

$$\mathrm{rate}' = k_{obs}[\mathrm{E}] = \frac{k_{on}^{trans}[\mathrm{E}]_o[\mathrm{I}]}{K_d^{pre} + [\mathrm{I}]}, \quad \text{(Eq. 81)}$$

and since k_{obs} is independent of the point at which measurement is made, i.e., it is independent of [E], we obtain:

$$\mathrm{rate}'/[\mathrm{E}]_o = k_{obs} = \frac{k_{on}^{trans}[\mathrm{I}]}{K_d^{pre} + [\mathrm{I}]}. \quad \text{(Eq. 82)}$$

Thus, the terms *a* and *b* are as follows: $a = k_{on}^{trans}$ and $b = K_d^{pre}$.

(2) The inhibitor associates (more weakly) with the enzyme to form a complex that remains active and does not eventually become the inhibited state. The complex is thus a "dead end" complex,

$$\mathrm{E} + \mathrm{I} \overset{K_d^{dead\ end}}{\rightleftharpoons} \mathrm{E} \sim \mathrm{I}. \quad \text{(Eq. 83)}$$

The free enzyme that remains reacts with I by another pathway to give the inhibited state in a second-order step

$$\mathrm{E} + \mathrm{I} \underset{k_{\mathrm{off}}}{\overset{k_{\mathrm{on}}}{\rightleftharpoons}} \mathrm{EI}\,. \qquad \text{(Eq. 84)}$$

Using the competing equilibrium approach, the competing equilibrium is given by

$$K_{\mathrm{d}}^{\text{dead end}} = \frac{[\mathrm{E}][\mathrm{I}]}{[\mathrm{E} \sim \mathrm{I}]}\,. \qquad \text{(Eq. 85)}$$

Since

$$[\mathrm{E} \sim \mathrm{I}] = [\mathrm{E}]_{\mathrm{o}} - [\mathrm{E}], \qquad \text{(Eq. 86)}$$

we obtain

$$K_{\mathrm{d}}^{\text{dead end}} = \frac{[\mathrm{E}][\mathrm{I}]}{[\mathrm{E}]_{\mathrm{o}} - [\mathrm{E}]}, \qquad \text{(Eq. 87)}$$

and since

$$K_{\mathrm{d}}^{\text{dead end}}[\mathrm{E}]_{\mathrm{o}} - K_{\mathrm{d}}^{\text{dead end}}[\mathrm{E}] = [\mathrm{E}][\mathrm{I}], \qquad \text{(Eq. 88)}$$

and

$$K_{\mathrm{d}}^{\text{dead end}}[\mathrm{E}]_{\mathrm{o}} = [\mathrm{E}]([\mathrm{I}] + K_{\mathrm{d}}^{\text{dead end}}), \qquad \text{(Eq. 89)}$$

it follows that

$$[\mathrm{E}] = \frac{K_{\mathrm{d}}^{\text{dead end}}[\mathrm{E}]_{\mathrm{o}}}{K_{\mathrm{d}}^{\text{dead end}} + [\mathrm{I}]}\,. \qquad \text{(Eq. 90)}$$

Therefore,

$$\text{rate}' = k_{\mathrm{on}}[\mathrm{E}][\mathrm{I}] = \frac{k_{\mathrm{on}} K_{\mathrm{d}}^{\text{dead end}}[\mathrm{E}]_{\mathrm{o}}[\mathrm{I}]}{K_{\mathrm{d}}^{\text{dead end}} + [\mathrm{I}]}\,. \qquad \text{(Eq. 91)}$$

As before, the rate can also be described by:

$$\text{rate}' = k_{\mathrm{obs}}[\mathrm{E}] = \frac{k_{\mathrm{on}} K_{\mathrm{d}}^{\text{dead end}}[\mathrm{E}]_{\mathrm{o}}[\mathrm{I}]}{K_{\mathrm{d}}^{\text{dead end}} + [\mathrm{I}]}, \qquad \text{(Eq. 92)}$$

and since k_{obs} is independent of the point at which measurement is made, i.e., it is independent of [E], we obtain:

$$\text{rate}'/[\text{E}] = k_{obs} = \frac{k_{on}K_d^{\text{dead end}}[\text{I}]}{K_d^{\text{dead end}} + [\text{I}]}. \qquad \text{(Eq. 93)}$$

Thus, the terms *a* and *b* are: $a = k_{on}K_d^{\text{dead end}}$ and $b = K_d^{\text{dead end}}$

(3) The initial state of the enzyme must first adopt an alternative conformation E* in a reaction given by forward and reverse rate constants k_{con+} and k_{con-}

$$\text{E} \underset{k_{con-}}{\overset{k_{con+}}{\rightleftharpoons}} \text{E}^* \qquad \text{(Eq. 94)}$$

where only the alternative conformation reacts with the inhibitor, in a second-order process.

$$\text{E}^* + \text{I} \underset{k_{off}}{\overset{k_{on}}{\rightleftharpoons}} \text{EI} \qquad \text{(Eq. 95)}$$

We use the steady-state approach. Note that since [E*] is now very small, it follows that $[\text{E}] = [\text{E}]_o$, i.e., there is no need to correct for the amount of complexed enzyme. Therefore,

$$\frac{d[\text{E}^*]}{dt} = 0 = k_{con+}[\text{E}] - k_{con-}[\text{E}^*] - k_{on}[\text{E}^*][\text{I}]. \qquad \text{(Eq. 96)}$$

Thus,

$$[\text{E}^*] = \frac{k_{con+}[\text{E}]}{k_{con-} + k_{on}[\text{I}]}, \qquad \text{(Eq. 97)}$$

and

$$\text{rate}' = k_{on}[\text{E}^*][\text{I}] = \frac{k_{on}k_{con+}[\text{E}][\text{I}]}{k_{con-} + k_{on}[\text{I}]}. \qquad \text{(Eq. 98)}$$

As before, the rate can also be described by:

$$\text{rate}' = k_{obs}[E] = \frac{k_{on}k_{con+}[E][I]}{k_{con-} + k_{on}[I]}, \quad \text{(Eq. 99)}$$

and thus

$$\text{rate}'/[E] = k_{obs} = \frac{k_{on}k_{con+}[I]}{k_{con-} + k_{on}[I]}. \quad \text{(Eq. 100)}$$

Finally, dividing each term in the right-hand side by k_{on} gives:

$$\text{rate}'/[E] = k_{obs} = \frac{k_{con+}[I]}{\frac{k_{con-}}{k_{on}} + [I]}. \quad \text{(Eq. 101)}$$

Thus, the terms a and b are as follows: $a = k_{con+}$, $b = k_{con+}/k_{on}$. In the context of IDH1 inhibition by Ivosidenib and other allosteric IDH inhibitors, option 3 can be ruled out as it does not account for any non-inhibitory binding modes.

APPENDIX

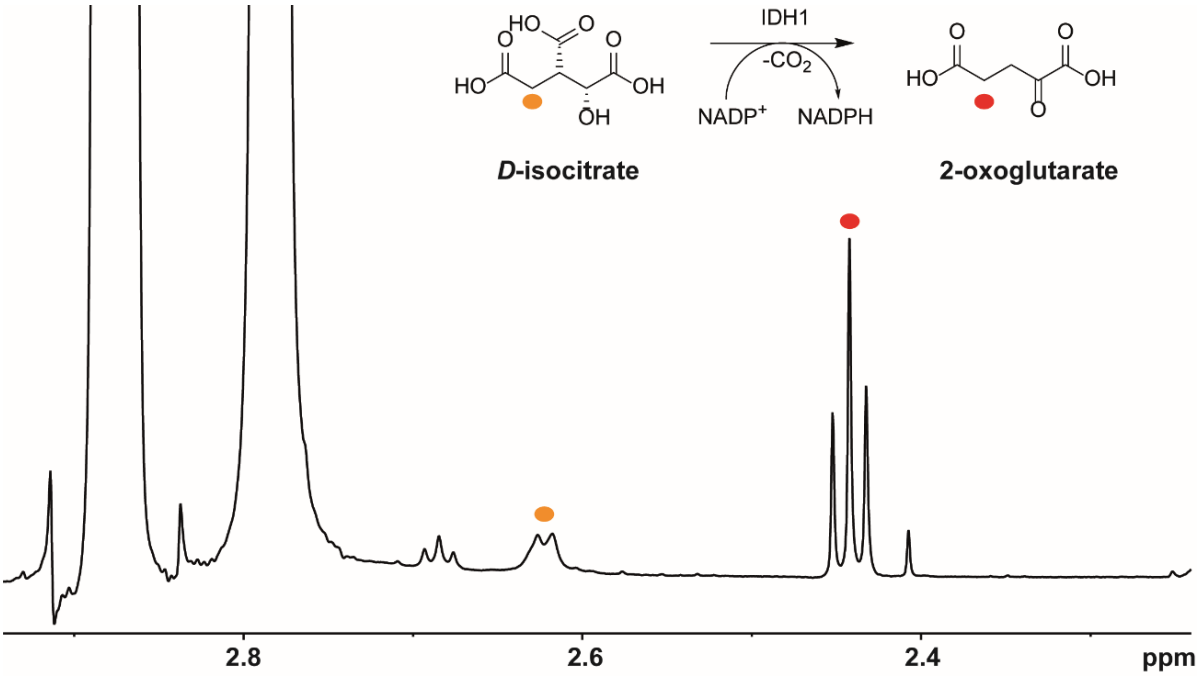


Figure 86. ^{1}H NMR peak identification for isocitrate and 2OG.

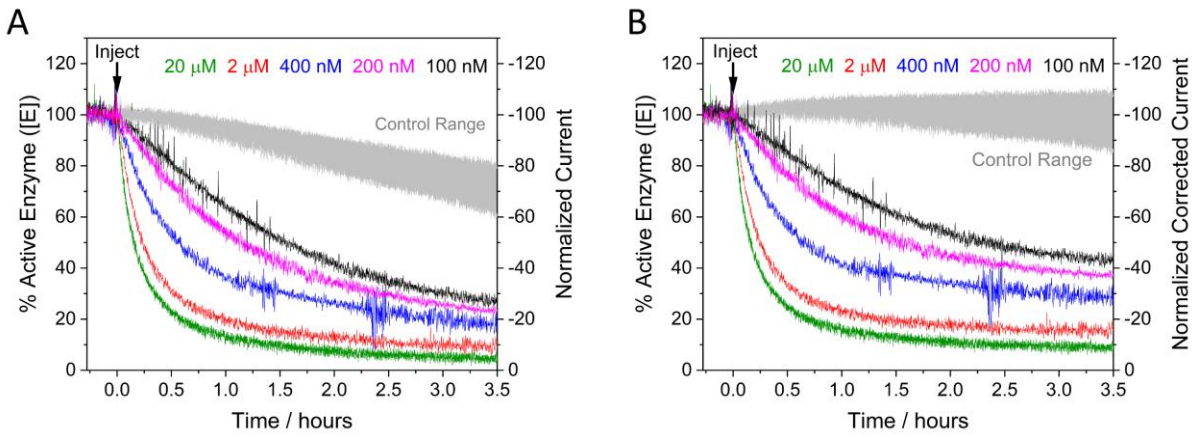


Figure 87. Inhibition timecourse data before and after film loss correction. (A) Uncorrected inhibition timecourse data for the plot presented in **Figure 63A** (and panel B in this figure). (B) Plot of the data in panel A after correcting for film loss. Note that the main parameter affected by film loss correction is the equilibrium value; the data from which observed rate constants are most dependent (first 20–60 minutes) are largely unaffected by the data correction procedure (see **Methods** section on film-loss correction for extended discussion).

REFERENCES

(1) Morello, G.; Megarity, C. F.; Armstrong, F. A. The Power of Electrified Nanoconfinement for Energising, Controlling and Observing Long Enzyme Cascades. *Nat. Commun.* **2021**, *12* (1), 340.

(2) Armstrong, F. A. Probing Metalloproteins by Voltammetry. In *Bioinorganic Chemistry. Structure and Bonding*; Springer-Verlag: Berlin/Heidelberg, 1990; pp 137–221.

(3) A. Armstrong, F.; A. Heering, H.; Judy Hirst. Reaction of Complex Metalloproteins Studied by Protein-Film Voltammetry. *Chem. Soc. Rev.* **1997**, *26* (3), 169–179.

(4) Armstrong, F. A.; Cheng, B.; Herold, R. A.; Megarity, C. F.; Siritanaratkul, B. From Protein Film Electrochemistry to Nanoconfined Enzyme Cascades and the Electrochemical Leaf. *Chem. Rev.* **2023**, *123* (9), 5421–5458.

(5) Evans, R. M.; Armstrong, F. A. Electrochemistry of Metalloproteins: Protein Film Electrochemistry for the Study of E. Coli [NiFe]-Hydrogenase-1. In *Methods in Molecular Biology*; Humana Press Inc., 2014; Vol. 1122, pp 73–94.

(6) Armstrong, F. A.; Hirst, J. Reversibility and Efficiency in Electrocatalytic Energy Conversion and Lessons from Enzymes. *Proc. Natl. Acad. Sci. U. S. A.* **2011**, *108* (34), 14049–14051.

(7) Armstrong, F. A.; Evans, R. M.; Hexter, S. V.; Murphy, B. J.; Roessler, M. M.; Wulff, P. Guiding Principles of Hydrogenase Catalysis Instigated and Clarified by Protein Film Electrochemistry. *Acc. Chem. Res.* **2016**, *49* (5), 884–892.

(8) Armstrong, F. A. Some Fundamental Insights into Biological Redox Catalysis from the Electrochemical Characteristics of Enzymes Attached Directly to Electrodes. *Electrochim. Acta* **2021**, *390*, 138836.

(9) Léger, C.; Bertrand, P. Direct Electrochemistry of Redox Enzymes as a Tool for Mechanistic Studies. *Chem. Rev.* **2008**, *108* (7), 2379–2438.

(10) Hirst, J. Elucidating the Mechanisms of Coupled Electron Transfer and Catalytic Reactions by Protein Film Voltammetry. *Biochim. Biophys. Acta - Bioenerg.* **2006**, *1757* (4), 225–239.

(11) Yates, N. D. J.; Fascione, M. A.; Parkin, A. Methodologies for “Wiring” Redox

Proteins/Enzymes to Electrode Surfaces. *Chem. – A Eur. J.* **2018**, *24* (47), 12164–12182.

(12) Page, C. C.; Moser, C. C.; Chen, X.; Dutton, P. L. Natural Engineering Principles of Electron Tunnelling in Biological Oxidation–Reduction. *Nat. 1999 4026757* **1999**, *402* (6757), 47–52.

(13) Léger, C.; Jones, A. K.; Albracht, S. P. J.; Armstrong, F. A. Effect of a Dispersion of Interfacial Electron Transfer Rates on Steady State Catalytic Electron Transport in [NiFe]-Hydrogenase and Other Enzymes. *J. Phys. Chem. B* **2002**, *106* (50), 13058–13063.

(14) Armstrong, F. A.; Wilson, G. S. Recent Developments in Faradaic Bioelectrochemistry. *Electrochim. Acta* **2000**, *45* (15–16), 2623–2645.

(15) Megarity, C. F.; Siritanaratkul, B.; Herold, R. A.; Morello, G.; Armstrong, F. A. Electron Flow between the Worlds of Marcus and Warburg. *J. Chem. Phys.* **2020**, *153* (22), 225101.

(16) Kurisu, G.; Kusunoki, M.; Katoh, E.; Yamazaki, T.; Teshima, K.; Onda, Y.; Kimata-Ariga, Y.; Hase, T. Structure of the Electron Transfer Complex between Ferredoxin and Ferredoxin-NADP+ Reductase. *Nat. Struct. Biol. 2001 82* **2001**, *8* (2), 117–121.

(17) Deng, Z.; Aliverti, A.; Zanetti, G.; Arakaki, A. K.; Ottado, J.; Orellano, E. G.; Calcaterra, N. B.; Ceccarelli, E. A.; Carrillo, N.; Karplus, P. A. A Productive NADP+ Binding Mode of Ferredoxin-NADP + Reductase Revealed by Protein Engineering and Crystallographic Studies. *Nat. Struct. Biol.* **1999**, *6* (9), 847–853.

(18) Siritanaratkul, B.; Megarity, C. F.; Roberts, T. G.; Samuels, T. O. M.; Winkler, M.; Warner, J. H.; Happe, T.; Armstrong, F. A. Transfer of Photosynthetic NADP+/NADPH Recycling Activity to a Porous Metal Oxide for Highly Specific, Electrochemically-Driven Organic Synthesis. *Chem. Sci.* **2017**, *8* (6), 4579–4586.

(19) Gorton, L.; Domínguez, E. Electrochemistry of NAD(P)+/NAD(P)H. *Encycl. Electrochem.* **2002**.

(20) Jaegfeldt, H. A Study of the Products Formed in the Electrochemical Reduction of Nicotinamide-Adenine-Dinucleotide. *J. Electroanal. Chem. Interfacial Electrochem.* **1981**, *128* (C), 355–370.

(21) Elving, P. J.; Schmakel, C. O.; Santhanam, K. S. V; Zuman, P.; Schmakel, C. 0;

Laboratories, A.; Chicago, N.; Santhanam, I. K. S. V. Nicotinamide-Nad Sequence: Redox Processes and Related Behavior: Behavior and Properties of Intermediate and Final Products. *C R C Crit. Rev. Anal. Chem.* **1976**, *6* (1), 1–67.

(22) Schmakel, C. O.; Santhanam, K. S. V.; Elving, P. J. Nicotinamide Adenine Dinucleotide (NAD+) and Related Compounds. Electrochemical Redox Pattern and Allied Chemical Behavior. *J. Am. Chem. Soc.* **1975**, *97* (18), 5083–5092.

(23) Herold, R. A.; Reinbold, R.; Schofield, C. J.; Armstrong, F. A. NADP(H)-Dependent Biocatalysis without Adding NADP(H). *Proc. Natl. Acad. Sci.* **2023**, *120* (1), e2214123120.

(24) Herold, R. A.; Schofield, C. J.; Armstrong, F. A. Electrochemical Nanoreactor Provides a Comprehensive View of Isocitrate Dehydrogenase Cancer-Drug Kinetics. *Angew. Chemie Int. Ed.* **2023**, e202309149.

(25) Megarity, C. F.; Siritanaratkul, B.; Heath, R. S.; Wan, L.; Morello, G.; FitzPatrick, S. R.; Booth, R. L.; Sills, A. J.; Robertson, A. W.; Warner, J. H.; Turner, N. J.; Armstrong, F. A. Electrocatalytic Volleyball: Rapid Nanoconfined Nicotinamide Cycling for Organic Synthesis in Electrode Pores. *Angew. Chemie Int. Ed.* **2019**, *58* (15), 4948–4952.

(26) Herold, R. A.; Reinbold, R.; Megarity, C. F.; Abboud, M. I.; Schofield, C. J.; Armstrong, F. A. Exploiting Electrode Nanoconfinement to Investigate the Catalytic Properties of Isocitrate Dehydrogenase (IDH1) and a Cancer-Associated Variant. *J. Phys. Chem. Lett.* **2021**, *12* (26), 6095–6101.

(27) Rosenthal, R. G.; Ebert, M.-O.; Kiefer, P.; Peter, D. M.; Vorholt, J. A.; Erb, T. J. Direct Evidence for a Covalent Ene Adduct Intermediate in NAD(P)H-Dependent Enzymes. *Nat. Chem. Biol.* **2014**, *10* (1), 50–55.

(28) Megarity, C. F.; Weald, T. R. I.; Heath, R. S.; Turner, N. J.; Armstrong, F. A. A Nanoconfined Four-Enzyme Cascade Simultaneously Driven by Electrical and Chemical Energy, with Built-in Rapid, Confocal Recycling of NADP(H) and ATP. *ACS Catal.* **2022**, 8811–8821.

(29) Liu, S.; Cadoux-Hudson, T.; Schofield, C. J. Isocitrate Dehydrogenase Variants in Cancer — Cellular Consequences and Therapeutic Opportunities. *Curr. Opin. Chem. Biol.* **2020**, *57*, 122–134.

(30) Losman, J.-A.; Kaelin, W. G. What a Difference a Hydroxyl Makes: Mutant IDH, (R)-2-Hydroxyglutarate, and Cancer. *Genes Dev.* **2013**, *27* (8), 836–852.

(31) Zhao, S.; Lin, Y.; Xu, W.; Jiang, W.; Zhai, Z.; Wang, P.; Yu, W.; Li, Z.; Gong, L.; Peng, Y.; Ding, J.; Lei, Q.; Guan, K. L.; Xiong, Y. Glioma-Derived Mutations in IDH1 Dominantly Inhibit IDH1 Catalytic Activity and Induce HIF-1α. *Science (80-.).* **2009**, *324* (5924), 261–265.

(32) Roman, J. V.; Melkonian, T. R.; Silvaggi, N. R.; Moran, G. R. Transient-State Analysis of Human Isocitrate Dehydrogenase I: Accounting for the Interconversion of Active and Non-Active Conformational States. *Biochemistry* **2019**, *58* (52), 5366–5380.

(33) Sabo, K. A.; Albekioni, E.; Caliger, D.; Coleman, N. J.; Thornberg, E.; Avellaneda Matteo, D.; Komives, E. A.; Silletti, S.; Sohl, C. D. Capturing the Dynamic Conformational Changes of Human Isocitrate Dehydrogenase 1 (IDH1) upon Ligand and Metal Binding Using Hydrogen-Deuterium Exchange Mass Spectrometry. *Biochemistry* **2023**, *62* (6), 1145–1159.

(34) Xu, X.; Zhao, J.; Xu, Z.; Peng, B.; Huang, Q.; Arnold, E.; Ding, J. Structures of Human Cytosolic NADP-Dependent Isocitrate Dehydrogenase Reveal a Novel Self-Regulatory Mechanism of Activity. *J. Biol. Chem.* **2004**, *279* (32), 33946–33957.

(35) Liu, S.; Abboud, M. I.; John, T.; Mikhailov, V.; Hvinden, I.; Walsby-Tickle, J.; Liu, X.; Pettinati, I.; Cadoux-Hudson, T.; McCullagh, J. S. O.; Schofield, C. J. Roles of Metal Ions in the Selective Inhibition of Oncogenic Variants of Isocitrate Dehydrogenase 1. *Commun. Biol. 2021 41* **2021**, *4* (1), 1–16.

(36) Rendina, A. R.; Pietrak, B.; Smallwood, A.; Zhao, H.; Qi, H.; Quinn, C.; Adams, N. D.; Concha, N.; Duraiswami, C.; Thrall, S. H.; Sweitzer, S.; Schwartz, B. Mutant IDH1 Enhances the Production of 2-Hydroxyglutarate Due to Its Kinetic Mechanism. *Biochemistry* **2013**, *52* (26), 4563–4577.

(37) Yang, B.; Zhong, C.; Peng, Y.; Lai, Z.; Ding, J. Molecular Mechanisms of "off-on Switch" of Activities of Human IDH1 by Tumor-Associated Mutation R132H. *Cell Res. 2010 2011* **2010**, *20* (11), 1188–1200.

(38) Oermann, E. K.; Wu, J.; Guan, K.-L.; Xiong, Y. Alterations of Metabolic Genes and Metabolites in Cancer. *Semin. Cell Dev. Biol.* **2012**, *23* (4), 370–380.

(39) Dang, L.; White, D. W.; Gross, S.; Bennett, B. D.; Bittinger, M. A.; Driggers, E. M.; Fantin, V. R.; Jang, H. G.; Jin, S.; Keenan, M. C.; Marks, K. M.; Prins, R. M.; Ward, P. S.; Yen, K. E.; Liau, L. M.; Rabinowitz, J. D.; Cantley, L. C.; Thompson, C. B.; Vander Heiden, M. G.; Su, S. M. Cancer-Associated IDH1 Mutations Produce 2-Hydroxyglutarate. *Nature* **2009**, *462* (7274), 739–744.

(40) Reinbold, R.; Hvinden, I. C.; Rabe, P.; Herold, R. A.; Finch, A.; Wood, J.; Morgan, M.; Staudt, M.; Clifton, I. J.; Armstrong, F. A.; McCullagh, J. S. O.; Redmond, J.; Bardella, C.; Abboud, M. I.; Schofield, C. J. Resistance to the Isocitrate Dehydrogenase 1 Mutant Inhibitor Ivosidenib Can Be Overcome by Alternative Dimer-Interface Binding Inhibitors. *Nat. Commun.* **2022**, *13* (1), 4785.

(41) Deng, G.; Shen, J.; Yin, M.; McManus, J.; Mathieu, M.; Gee, P.; He, T.; Shi, C.; Bedel, O.; McLean, L. R.; Le-Strat, F.; Zhang, Y.; Marquette, J. P.; Gao, Q.; Zhang, B.; Rak, A.; Hoffmann, D.; Rooney, E.; Vassort, A.; Englaro, W.; Li, Y.; Patel, V.; Adrian, F.; Gross, S.; Wiederschain, D.; Cheng, H.; Licht, S. Selective Inhibition of Mutant Isocitrate Dehydrogenase 1 (IDH1) via Disruption of a Metal Binding Network by an Allosteric Small Molecule. *J. Biol. Chem.* **2015**, *290* (2), 762–774.

(42) Golub, D.; Iyengar, N.; Dogra, S.; Wong, T.; Bready, D.; Tang, K.; Modrek, A. S.; Placantonakis, D. G. Mutant Isocitrate Dehydrogenase Inhibitors as Targeted Cancer Therapeutics. *Front. Oncol.* **2019**, *9*, 417.

(43) Chowdhury, R.; Yeoh, K. K.; Tian, Y.; Hillringhaus, L.; Bagg, E. A.; Rose, N. R.; Leung, I. K. H.; Li, X. S.; Woon, E. C. Y.; Yang, M.; McDonough, M. A.; King, O. N.; Clifton, I. J.; Klose, R. J.; Claridge, T. D. W.; Ratcliffe, P. J.; Schofield, C. J.; Kawamura, A. The Oncometabolite 2-hydroxyglutarate Inhibits Histone Lysine Demethylases. *EMBO Rep.* **2011**, *12* (5), 463–469.

(44) Ye, D.; Guan, K.-L.; Xiong, Y. Metabolism, Activity, and Targeting of D- and L-2-Hydroxyglutarates. *Trends in Cancer* **2018**, *4* (2), 151–165.

(45) Ward, P. S.; Patel, J.; Wise, D. R.; Abdel-Wahab, O.; Bennett, B. D.; Coller, H. A.; Cross, J. R.; Fantin, V. R.; Hedvat, C. V.; Perl, A. E.; Rabinowitz, J. D.; Carroll, M.; Su, S. M.; Sharp, K. A.; Levine, R. L.; Thompson, C. B. The Common Feature of Leukemia-Associated IDH1 and IDH2 Mutations Is a Neomorphic Enzyme Activity Converting α-Ketoglutarate to 2-Hydroxyglutarate. *Cancer Cell* **2010**, *17* (3), 225–

234.

(46) Cadoux-Hudson, T.; Schofield, C. J.; McCullagh, J. S. O. Isocitrate Dehydrogenase Gene Variants in Cancer and Their Clinical Significance. *Biochem. Soc. Trans.* **2021**, *49* (6), 2561–2572.

(47) Balss, J.; Meyer, J.; Mueller, W.; Korshunov, A.; Hartmann, C.; von Deimling, A. Analysis of the IDH1 Codon 132 Mutation in Brain Tumors. *Acta Neuropathol.* **2008**, *116* (6), 597–602.

(48) Chang, C.-M.; Xu, K.; G., H.-K. The Role of Isocitrate Dehydrogenase Mutations in Glioma Brain Tumors. In *Molecular Targets of CNS Tumors*; InTech, 2011.

(49) Cohen, A. L.; Holmen, S. L.; Colman, H. IDH1 and IDH2 Mutations in Gliomas. *Curr. Neurol. Neurosci. Rep.* **2013**, *13* (5), 1–7.

(50) Urban, D. J.; Martinez, N. J.; Davis, M. I.; Brimacombe, K. R.; Cheff, D. M.; Lee, T. D.; Henderson, M. J.; Titus, S. A.; Pragani, R.; Rohde, J. M.; Liu, L.; Fang, Y.; Karavadhi, S.; Shah, P.; Lee, O. W.; Wang, A.; McIver, A.; Zheng, H.; Wang, X.; Xu, X.; Jadhav, A.; Simeonov, A.; Shen, M.; Boxer, M. B.; Hall, M. D. Assessing Inhibitors of Mutant Isocitrate Dehydrogenase Using a Suite of Pre-Clinical Discovery Assays. *Sci. Rep.* **2017**, *7* (1).

(51) Dhillon, S. Ivosidenib: First Global Approval. *Drugs* **2018**, *78* (14), 1509–1516.

(52) Kang, C. Olutasidenib: First Approval. *Drugs* **2023**, *83* (4), 341–346.

(53) Kim, E. S. Enasidenib: First Global Approval. *Drugs* **2017**, *77* (15), 1705–1711.

(54) Liu, X.; Reinbold, R.; Liu, S.; Herold, R. A.; Rabe, P.; Duclos, S.; Yadav, R. B.; Abboud, M. I.; Thieffine, S.; Armstrong, F. A.; Brewitz, L.; Schofield, C. J. Natural and Synthetic 2-Oxoglutarate Derivatives Are Substrates for Oncogenic Variants of Human Isocitrate Dehydrogenase 1 and 2. *J. Biol. Chem.* **2023**, *299* (2), 102873.

(55) Buckel, W.; Miller, S. L. Equilibrium Constants of Several Reactions Involved in the Fermentation of Glutamate. *Eur. J. Biochem.* **1987**, *164* (3), 565–569.

(56) Zhang, W.; Zhang, M.; Gao, C.; Zhang, Y.; Ge, Y.; Guo, S.; Guo, X.; Zhou, Z.; Liu, Q.; Zhang, Y.; Ma, C.; Tao, F.; Xu, P. Coupling between D-3-Phosphoglycerate Dehydrogenase and D-2-Hydroxyglutarate Dehydrogenase Drives Bacterial L-Serine Synthesis. *Proc. Natl. Acad. Sci. U. S. A.* **2017**, *114* (36), E7574–E7582.

(57) Cheng, B.; Wan, L.; Armstrong, F. A. Progress in Scaling up and Streamlining a

Nanoconfined, Enzyme-catalysed Electrochemical Nicotinamide Recycling System for Biocatalytic Synthesis. *ChemElectroChem* **2020**, celc.202001166.

(58) Choe, S.; Wang, H.; DiNardo, C. D.; Stein, E. M.; de Botton, S.; Roboz, G. J.; Altman, J. K.; Mims, A. S.; Watts, J. M.; Pollyea, D. A.; Fathi, A. T.; Tallman, M. S.; Kantarjian, H. M.; Stone, R. M.; Quek, L.; Konteatis, Z.; Dang, L.; Nicolay, B.; Nejad, P.; Liu, G.; Zhang, V.; Liu, H.; Goldwasser, M.; Liu, W.; Marks, K.; Bowden, C.; Biller, S. A.; Attar, E. C.; Wu, B. Molecular Mechanisms Mediating Relapse Following Ivosidenib Monotherapy in IDH1-Mutant Relapsed or Refractory AML. *Blood Adv.* **2020**, *4* (9), 1894–1905.

(59) Hexter, S. V.; Grey, F.; Happe, T.; Climent, V.; Armstrong, F. A. Electrocatalytic Mechanism of Reversible Hydrogen Cycling by Enzymes and Distinctions between the Major Classes of Hydrogenases. *Proc. Natl. Acad. Sci. U. S. A.* **2012**, *109* (29), 11516–11521.

(60) Wan, L.; Heath, R. S.; Megarity, C. F.; Sills, A. J.; Herold, R. A.; Turner, N. J.; Armstrong, F. A. Exploiting Bidirectional Electrocatalysis by a Nanoconfined Enzyme Cascade to Drive and Control Enantioselective Reactions. *ACS Catal.* **2021**, *11* (11), 6526–6533.

(61) Yang, J.; Zhu, H.; Zhang, T.; Ding, J. Structure, Substrate Specificity, and Catalytic Mechanism of Human D-2-HGDH and Insights into Pathogenicity of Disease-Associated Mutations. *Cell Discov. 2020 71* **2021**, *7* (1), 1–17.

(62) Schafer, F. Q.; Buettner, G. R. Redox Environment of the Cell as Viewed through the Redox State of the Glutathione Disulfide/Glutathione Couple. *Free Radical Biology and Medicine*. Pergamon June 1, 2001, pp 1191–1212.

(63) Intlekofer, A. M.; Shih, A. H.; Wang, B.; Nazir, A.; Rustenburg, A. S.; Albanese, S. K.; Patel, M.; Famulare, C.; Correa, F. M.; Takemoto, N.; Durani, V.; Liu, H.; Taylor, J.; Farnoud, N.; Papaemmanuil, E.; Cross, J. R.; Tallman, M. S.; Arcila, M. E.; Roshal, M.; Petsko, G. A.; Wu, B.; Choe, S.; Konteatis, Z. D.; Biller, S. A.; Chodera, J. D.; Thompson, C. B.; Levine, R. L.; Stein, E. M. Acquired Resistance to IDH Inhibition through Trans or Cis Dimer-Interface Mutations. *Nature* **2018**, *559* (7712), 125–129.

(64) Oltvai, Z. N.; Harley, S. E.; Koes, D.; Michel, S.; Warlick, E. D.; Nelson, A. C.; Yohe, S.; Mroz, P. Assessing Acquired Resistance to IDH1 Inhibitor Therapy by Full-Exon

IDH1 Sequencing and Structural Modeling. *Mol. Case Stud.* **2021**, *7* (2), a006007.

(65) Brown, S.; Muhamad, N.; Pedley, K. C.; Simcock, D. C. The Kinetics of Enzyme Mixtures. *Mol. Biol. Res. Commun.* **2014**, *3* (1), 21–32.

(66) Kerfeld, C. A.; Aussignargues, C.; Zarzycki, J.; Cai, F.; Sutter, M. Bacterial Microcompartments. *Nat. Rev. Microbiol. 2018 165* **2018**, *16* (5), 277–290.

(67) Stewart, A. M.; Stewart, K. L.; Yeates, T. O.; Bobik, T. A. Advances in the World of Bacterial Microcompartments. *Trends Biochem. Sci.* **2021**, *46* (5), 406–416.

(68) Sweetlove, L. J.; Fernie, A. R. The Role of Dynamic Enzyme Assemblies and Substrate Channelling in Metabolic Regulation. *Nat. Commun.* **2018**, *9* (1), 2136.

(69) Conway, A.; Koshland, D. E. Negative Cooperativity in Enzyme Action. Binding of Diphosphopyridine Nucleotide to Glyceraldehyde-3-Phosphate Dehydrogenase. *Biochemistry* **1968**, *7* (11), 4011–4023.

(70) Grant, G. A.; Hu, Z.; Xu, X. L. Cofactor Binding to Escherichia Coli D-3-Phosphoglycerate Dehydrogenase Induces Multiple Conformations Which Alter Effector Binding. *J. Biol. Chem.* **2002**, *277* (42), 39548–39553.

(71) Mohapatra, S. B.; Manoj, N. Structural Basis of Catalysis and Substrate Recognition by the NAD(H)-Dependent α-d-Glucuronidase from the Glycoside Hydrolase Family 4. *Biochem. J.* **2021**, *478* (4), 943–959.

(72) Fjeld, C. C.; Birdsong, W. T.; Goodman, R. H. Differential Binding of NAD+ and NADH Allows the Transcriptional Corepressor Carboxyl-Terminal Binding Protein to Serve as a Metabolic Sensor. *Proc. Natl. Acad. Sci. U. S. A.* **2003**, *100* (16), 9202–9207.

(73) Sickmier, E. A.; Brekasis, D.; Paranawithana, S.; Bonanno, J. B.; Paget, M. S. B.; Burley, S. K.; Kielkopf, C. L. X-Ray Structure of a Rex-Family Repressor/NADH Complex Insights into the Mechanism of Redox Sensing. *Structure* **2005**, *13* (1), 43–54.

(74) Schenkels, P.; Duine, J. A. Nicotinoprotein (NADH-Containing) Alcohol Dehydrogenase from Rhodococcus Erythropolis DSM 1069: An Efficient Catalyst for Coenzyme-Independent Oxidation of a Broad Spectrum of Alcohols and the Interconversion of Alcohols and Aldehydes. *Microbiology* **2000**, *146* (4), 775–785.

(75) Norin, A.; Piersma, S. R.; Duine, J. A.; Jörnvall, H. Nicotinoprotein (NAD+-

Containing) Alcohol Dehydrogenase: Structural Relationships and Functional Interpretations. *Cell. Mol. Life Sci. C. 2003 605* **2003**, *60* (5), 999–1006.

(76) Zhang, Q.; Shirley, N.; Lahnstein, J.; Fincher, G. B. Characterization and Expression Patterns of UDP-d-Glucuronate Decarboxylase Genes in Barley. *Plant Physiol.* **2005**, *138* (1), 131–141.

(77) Thoden, J. B.; Frey, P. A.; Holden, H. M. Crystal Structures of the Oxidized and Reduced Forms of UDP-Galactose 4-Epimerase Isolated from Escherichia Coli. *Biochemistry* **1996**, *35* (8), 2557–2566.

(78) Tanaka, N.; Kusakabe, Y.; Ito, K.; Yoshimoto, T.; Nakamura, K. T. Crystal Structure of Formaldehyde Dehydrogenase from Pseudomonas Putida: The Structural Origin of the Tightly Bound Cofactor in Nicotinoprotein Dehydrogenases. *J. Mol. Biol.* **2002**, *324* (3), 519–533.

(79) Bhabha, G.; Tuttle, L.; Martinez-Yamout, M. A.; Wright, P. E. Identification of Endogenous Ligands Bound to Bacterially Expressed Human and E. Coli Dihydrofolate Reductase by 2D NMR. *FEBS Lett.* **2011**, *585* (22), 3528–3532.

(80) Cheng, Y. S.; Sacchettini, J. C. Structural Insights into Mycobacterium Tuberculosis Rv2671 Protein as a Dihydrofolate Reductase Functional Analogue Contributing to Para-Aminosalicylic Acid Resistance. *Biochemistry* **2016**, *55* (7), 1107–1119.

(81) Bezsudnova, E. Y.; Petrova, T. E.; Artemova, N. V.; Boyko, K. M.; Shabalin, I. G.; Rakitina, T. V.; Polyakov, K. M.; Popov, V. O. NADP-Dependent Aldehyde Dehydrogenase from Archaeon Pyrobaculum Sp.1860: Structural and Functional Features. *Archaea* **2016**, *2016*.

(82) Van Ophem, P. W.; Van Beeumen, J.; Duine, J. A. Nicotinoprotein [NAD(P)-Containing] Alcohol/Aldehyde Oxidoreductases. *Eur. J. Biochem.* **1993**, *212* (3), 819–826.

(83) Hektor, H. J.; Kloosterman, H.; Dijkhuizen, L. Identification of a Magnesium-Dependent NAD(P)(H)-Binding Domain in the Nicotinoprotein Methanol Dehydrogenase from Bacillus Methanolicus. *J. Biol. Chem.* **2002**, *277* (49), 46966–46973.

(84) Monchietti, P.; López Rivero, A. S.; Ceccarelli, E. A.; Catalano-Dupuy, D. L. A New Catalytic Mechanism of Bacterial Ferredoxin-NADP+ Reductases Due to a Particular

NADP+ Binding Mode. *Protein Sci.* **2021**, *30* (10), 2106–2120.

(85) Oppenheimer, N. J. NAD+ and NADP+ as Prosthetic Groups for Enzymes. In *eLS*; Wiley, 2010.

(86) Compton, R. G.; Banks, C. E. *Understanding Voltammetry*; World Scientific Publishing Co. Ltd., 2018; Vol. 3.

(87) Torquato, S.; Truskett, T. M.; Debenedetti, P. G. Is Random Close Packing of Spheres Well Defined? *Phys. Rev. Lett.* **2000**, *84* (10), 2064.

(88) Erickson, H. P. Size and Shape of Protein Molecules at the Nanometer Level Determined by Sedimentation, Gel Filtration, and Electron Microscopy. *Biol. Proced. Online* **2009**, *11* (1), 32–51.

(89) Sharma, V. K.; Hutchison, J. M.; Allgeier, A. M. Redox Biocatalysis: Quantitative Comparisons of Nicotinamide Cofactor Regeneration Methods. *ChemSusChem* **2022**, *15* (22), e202200888.

(90) Chenault, H. K.; Simon, E. S.; Whitesides, G. M. Cofactor Regeneration for Enzyme-Catalysed Synthesis. *Biotechnol. Genet. Eng. Rev.* **1988**, *6* (1), 221–270.

(91) Wang, X.; Saba, T.; Yiu, H. H. P.; Howe, R. F.; Anderson, J. A.; Shi, J. Cofactor NAD(P)H Regeneration Inspired by Heterogeneous Pathways. *Chem* **2017**, *2* (5), 621–654.

(92) Fukuzumi, S.; Lee, Y. M.; Nam, W. Catalytic Recycling of NAD(P)H. *Journal of Inorganic Biochemistry*. Elsevier Inc. October 1, 2019, p 110777.

(93) Vanita Uppada, S. B. and S. B. N. Cofactor Regeneration – an Important Aspect of Biocatalysis. *Curr. Sci.* **2014**, *106* (7), 946–957.

(94) Angelastro, A.; Dawson, W. M.; Luk, L. Y. P.; Allemann, R. K. A Versatile Disulfide-Driven Recycling System for NADP+ with High Cofactor Turnover Number. *ACS Catal.* **2017**, *7* (2), 1025–1029.

(95) Wang, F.; Travins, J.; DeLaBarre, B.; Penard-Lacronique, V.; Schalm, S.; Hansen, E.; Straley, K.; Kernytsky, A.; Liu, W.; Gliser, C.; Yang, H.; Gross, S.; Artin, E.; Saada, V.; Mylonas, E.; Quivoron, C.; Popovici-Muller, J.; Saunders, J. O.; Salituro, F. G.; Yan, S.; Murray, S.; Wei, W.; Gao, Y.; Dang, L.; Dorsch, M.; Agresta, S.; Schenkein, D. P.; Biller, S. A.; Su, S. M.; De Botton, S.; Yen, K. E. Targeted Inhibition of Mutant IDH2 in Leukemia Cells Induces Cellular Differentiation. *Science (80-.).* **2013**, *340*

(6132), 622–626.

(96) Merk, A.; Bartesaghi, A.; Banerjee, S.; Falconieri, V.; Rao, P.; Davis, M. I.; Pragani, R.; Boxer, M. B.; Earl, L. A.; Milne, J. L. S.; Subramaniam, S. Breaking Cryo-EM Resolution Barriers to Facilitate Drug Discovery. *Cell* **2016**, *165* (7), 1698–1707.

(97) Yen, K.; Travins, J.; Wang, F.; David, M. D.; Artin, E.; Straley, K.; Padyana, A.; Gross, S.; DeLaBarre, B.; Tobin, E.; Chen, Y.; Nagaraja, R.; Choe, S.; Jin, L.; Konteatis, Z.; Cianchetta, G.; Saunders, J. O.; Salituro, F. G.; Quivoron, C.; Opolon, P.; Bawa, O.; Saada, V.; Paci, A.; Broutin, S.; Bernard, O. A.; de Botton, S.; Marteyn, B. S.; Pilichowska, M.; Xu, Y.; Fang, C.; Jiang, F.; Wei, W.; Jin, S.; Silverman, L.; Liu, W.; Yang, H.; Dang, L.; Dorsch, M.; Penard-Lacronique, V.; Biller, S. A.; Su, S.-S. M. AG-221, a First-in-Class Therapy Targeting Acute Myeloid Leukemia Harboring Oncogenic IDH2 Mutations. *Cancer Discov.* **2017**, *7* (5), 478–493.

(98) Konteatis, Z.; Artin, E.; Nicolay, B.; Straley, K.; Padyana, A. K.; Jin, L.; Chen, Y.; Narayaraswamy, R.; Tong, S.; Wang, F.; Zhou, D.; Cui, D.; Cai, Z.; Luo, Z.; Fang, C.; Tang, H.; Lv, X.; Nagaraja, R.; Yang, H.; Su, S. S. M.; Sui, Z.; Dang, L.; Yen, K.; Popovici-Muller, J.; Codega, P.; Campos, C.; Mellinghoff, I. K.; Biller, S. A. Vorasidenib (AG-881): A First-in-Class, Brain-Penetrant Dual Inhibitor of Mutant IDH1 and 2 for Treatment of Glioma. *ACS Med. Chem. Lett.* **2020**, *11* (2), 101–107.

(99) Okoye-Okafor, U. C.; Bartholdy, B.; Cartier, J.; Gao, E. N.; Pietrak, B.; Rendina, A. R.; Rominger, C.; Quinn, C.; Smallwood, A.; Wiggall, K. J.; Reif, A. J.; Schmidt, S. J.; Qi, H.; Zhao, H.; Joberty, G.; Faelth-Savitski, M.; Bantscheff, M.; Drewes, G.; Duraiswami, C.; Brady, P.; Groy, A.; Narayanagari, S. R.; Antony-Debre, I.; Mitchell, K.; Wang, H. R.; Kao, Y. R.; Christopeit, M.; Carvajal, L.; Barreyro, L.; Paietta, E.; Makishima, H.; Will, B.; Concha, N.; Adams, N. D.; Schwartz, B.; McCabe, M. T.; Maciejewski, J.; Verma, A.; Steidl, U. New IDH1 Mutant Inhibitors for Treatment of Acute Myeloid Leukemia. *Nat. Chem. Biol. 2015 1111* **2015**, *11* (11), 878–886.

(100) Ma, R.; Yun, C.-H. Crystal Structures of Pan-IDH Inhibitor AG-881 in Complex with Mutant Human IDH1 and IDH2. *Biochem. Biophys. Res. Commun.* **2018**, *503* (4), 2912–2917.

(101) Liu, S.; Abboud, M.; Mikhailov, V.; Liu, X.; Reinbold, R.; Schofield, C. J. Differentiating Inhibition Selectivity and Binding Affinity of Isocitrate

Dehydrogenase 1 Variant Inhibitors. *J. Med. Chem.* **2023**, *66*, 17.

(102) Popovici-Muller, J.; Lemieux, R. M.; Artin, E.; Saunders, J. O.; Salituro, F. G.; Travins, J.; Cianchetta, G.; Cai, Z.; Zhou, D.; Cui, D.; Chen, P.; Straley, K.; Tobin, E.; Wang, F.; David, M. D.; Penard-Lacronique, V.; Quivoron, C.; Saada, V.; De Botton, S.; Gross, S.; Dang, L.; Yang, H.; Utley, L.; Chen, Y.; Kim, H.; Jin, S.; Gu, Z.; Yao, G.; Luo, Z.; Lv, X.; Fang, C.; Yan, L.; Olaharski, A.; Silverman, L.; Biller, S.; Su, S. S. M.; Yen, K. Discovery of AG-120 (Ivosidenib): A First-in-Class Mutant IDH1 Inhibitor for the Treatment of IDH1 Mutant Cancers. *ACS Med. Chem. Lett.* **2018**, *9* (4), 300–305.

(103) Davis, M. I.; Gross, S.; Shen, M.; Straley, K. S.; Pragani, R.; Lea, W. A.; Popovici-Muller, J.; DeLaBarre, B.; Artin, E.; Thorne, N.; Auld, D. S.; Li, Z.; Dang, L.; Boxer, M. B.; Simeonov, A. Biochemical, Cellular, and Biophysical Characterization of a Potent Inhibitor of Mutant Isocitrate Dehydrogenase IDH1. *J. Biol. Chem.* **2014**, *289* (20), 13717–13725.

(104) Lu, H.; Tonge, P. J. Drug–Target Residence Time: Critical Information for Lead Optimization. *Curr. Opin. Chem. Biol.* **2010**, *14* (4), 467–474.

(105) Bernetti, M.; Cavalli, A.; Mollica, L. Protein–Ligand (Un)Binding Kinetics as a New Paradigm for Drug Discovery at the Crossroad between Experiments and Modelling. *Medchemcomm* **2017**, *8* (3), 534–550.

(106) Bernetti, M.; Masetti, M.; Rocchia, W.; Cavalli, A. Kinetics of Drug Binding and Residence Time. *Annu. Rev. Phys. Chem.* **2019**, *70*, 143–171.

(107) Copeland, R. A.; Pompliano, D. L.; Meek, T. D. Drug–Target Residence Time and Its Implications for Lead Optimization. *Nat. Rev. Drug Discov. 2006 59* **2006**, *5* (9), 730–739.

(108) Thun-Hohenstein, S. T. D.; Suits, T. F.; Malla, T. R.; Tumber, A.; Brewitz, L.; Choudhry, H.; Salah, E.; Schofield, C. J. Structure-Activity Studies Reveal Scope for Optimisation of Ebselen-Type Inhibition of SARS-CoV-2 Main Protease. *ChemMedChem* **2022**, *17* (4), e202100582.

(109) Siritanaratkul, B. Design Principles for a Nanoconfined Enzyme Cascade Electrode via Reaction–Diffusion Modelling. *Phys. Chem. Chem. Phys.* **2023**, *25* (13), 9357–9363.

(110) Guggenheim, E. A. XLVI. On the Determination of the Velocity Constant of a Unimolecular Reaction. *London, Edinburgh, Dublin Philos. Mag. J. Sci.* **1926**, *2* (9), 538–543.

(111) Niebergall, P. J.; Sugita, E. T. Utilization of the Guggenheim Method in Kinetics. *J. Pharm. Sci.* **1968**, *57* (10), 1805–1808.

(112) Cornish-Bowden, A. *Fundamentals of Enzyme Kinetics*, 4th ed.; Wiley, 2012.

(113) Morrison, J. F. The Slow-Binding and Slow, Tight-Binding Inhibition of Enzyme-Catalysed Reactions. *Trends Biochem. Sci.* **1982**, *7* (3), 102–105.

(114) Morrison, J. F.; Walsh, C. T. The Behavior and Significance of Slow-Binding Enzyme Inhibitors. In *Advances in enzymology and related areas of molecular biology*; John Wiley & Sons, Ltd, 1988; Vol. 61, pp 201–301.

(115) Pusch, S.; Krausert, S.; Fischer, V.; Balss, J.; Ott, M.; Schrimpf, D.; Capper, D.; Sahm, F.; Eisel, J.; Beck, A. C.; Jugold, M.; Eichwald, V.; Kaulfuss, S.; Panknin, O.; Rehwinkel, H.; Zimmermann, K.; Hillig, R. C.; Guenther, J.; Toschi, L.; Neuhaus, R.; Haegebart, A.; Hess-Stumpp, H.; Bauser, M.; Wick, W.; Unterberg, A.; Herold-Mende, C.; Platten, M.; von Deimling, A. Pan-Mutant IDH1 Inhibitor BAY 1436032 for Effective Treatment of IDH1 Mutant Astrocytoma in Vivo. *Acta Neuropathol.* **2017**, *133* (4), 629–644.

(116) Gonthier, K.; Weidmann, C.; Berthiaume, L.; Jobin, C.; Lacouture, A.; Lafront, C.; Harvey, M.; Neveu, B.; Loehr, J.; Bergeron, A.; Fradet, Y.; Lacombe, L.; Riopel, J.; Latulippe, É.; Atallah, C.; Shum, M.; Lambert, J. P.; Pouliot, F.; Pelletier, M.; Audet-Walsh, É. Isocitrate Dehydrogenase 1 Sustains a Hybrid Cytoplasmic–Mitochondrial Tricarboxylic Acid Cycle That Can Be Targeted for Therapeutic Purposes in Prostate Cancer. *Mol. Oncol.* **2023**.

(117) Wan, L.; Heath, R. S.; Siritanaratkul, B.; Megarity, C. F.; Sills, A. J.; Thompson, M. P.; Turner, N. J.; Armstrong, F. A. Enzyme-Catalysed Enantioselective Oxidation of Alcohols by Air Exploiting Fast Electrochemical Nicotinamide Cycling in Electrode Nanopores. *Green Chem.* **2019**, *21* (18), 4958–4963.

(118) Megarity, C. F.; Siritanaratkul, B.; Cheng, B.; Morello, G.; Wan, L.; Sills, A. J.; Heath, R. S.; Turner, N. J.; Armstrong, F. A. Electrified Nanoconfined Biocatalysis with Rapid Cofactor Recycling. *ChemCatChem* **2019**, *11* (23), 5662–5670.

(119) Morello, G.; Siritanaratkul, B.; Megarity, C. F.; Armstrong, F. A. Efficient Electrocatalytic CO2 Fixation by Nanoconfined Enzymes via a C3-to-C4 Reaction That Is Favored over H2 Production. *ACS Catal.* **2019**, *9* (12), 11255–11262.

(120) Islam, M. S.; Leissing, T. M.; Chowdhury, R.; Hopkinson, R. J.; Schofield, C. J. 2-Oxoglutarate-Dependent Oxygenases. *https://doi.org/10.1146/annurev-biochem-061516-044724* **2018**, *87*, 585–620.

(121) Martinez, S.; Hausinger, R. P. Catalytic Mechanisms of Fe(II)- and 2-Oxoglutarate-Dependent Oxygenases. *J. Biol. Chem.* **2015**, *290* (34), 20702–20711.

(122) Cook, D. J.; Finnigan, J. D.; Cook, K.; Black, G. W.; Charnock, S. J. Cytochromes P450: History, Classes, Catalytic Mechanism, and Industrial Application. *Adv. Protein Chem. Struct. Biol.* **2016**, *105*, 105–126.

(123) Guengerich, F. P. Mechanisms of Cytochrome P450-Catalyzed Oxidations. *ACS Catal.* **2018**, *8* (12), 10964–10976.

(124) Omura, T. Forty Years of Cytochrome P450. *Biochem. Biophys. Res. Commun.* **1999**, *266* (3), 690–698.

(125) Montgomery, S. L.; Mangas-Sanchez, J.; Thompson, M. P.; Aleku, G. A.; Dominguez, B.; Turner, N. J. Direct Alkylation of Amines with Primary and Secondary Alcohols through Biocatalytic Hydrogen Borrowing. *Angew. Chemie Int. Ed.* **2017**, *56* (35), 10491–10494.

(126) Hewitson, K. S.; Granatino, N.; Welford, R. W. D.; McDonough, M. A.; Schofield, C. J. Oxidation by 2-Oxoglutarate Oxygenases: Non-Haem Iron Systems in Catalysis and Signalling. *Philos. Trans. R. Soc. A Math. Phys. Eng. Sci.* **2005**, *363* (1829), 807–828.

(127) Yin, X.; Zabriskie, T. M. VioC Is a Non-Heme Iron, α-Ketoglutarate-Dependent Oxygenase That Catalyzes the Formation of 3S-Hydroxy-L-Arginine during Viomycin Biosynthesis. *ChemBioChem* **2004**, *5* (9), 1274–1277.

(128) Ju, J.; Ozanick, S. G.; Shen, B.; Thomas, M. G. Conversion of (2S)-Arginine to (2S,3R)-Capreomycidine by VioC and VioD from the Viomycin Biosynthetic Pathway of Streptomyces Sp. Strain ATCC11861. *ChemBioChem* **2004**, *5* (9), 1281–1285.

(129) Helmetag, V.; Samel, S. A.; Thomas, M. G.; Marahiel, M. A.; Essen, L. O. Structural

Basis for the Erythro-Stereospecificity of the l-Arginine Oxygenase VioC in Viomycin Biosynthesis. *FEBS J.* **2009**, *276* (13), 3669–3682.

(130) Plug, C. M.; Dekker, D.; Bult, A. Complex Stability of Ferrous Ascorbate in Aqueous Solution and Its Significance for Iron Absorption. *Pharm. Weekbl. Sci. Ed.* **1984**, *6* (6), 245–248.

(131) Kuiper, C.; Vissers, M. C. M. Ascorbate as a Cofactor for Fe-and 2-Oxoglutarate Dependent Dioxygenases: Physiological Activity in Tumour Growth and Progression. *Frontiers in Oncology*. Frontiers Media S.A. December 10, 2014, p 359.

(132) Brillas, E.; Sirés, I.; Oturan, M. A. Electro-Fenton Process and Related Electrochemical Technologies Based on Fenton's Reaction Chemistry. *Chem. Rev.* **2009**, *109* (12), 6570–6631.

(133) Casado, J.; Fornaguera, J.; Galán, M. I. Mineralization of Aromatics in Water by Sunlight-Assisted Electro-Fenton Technology in a Pilot Reactor. *Environ. Sci. Technol.* **2005**, *39* (6), 1843–1847.

(134) Martin, W.; Russell, M. J.; Horner, D.; Blankenship, R.; Cavalier-Smith, T.; Nisbet, E. On the Origins of Cells: A Hypothesis for the Evolutionary Transitions from Abiotic Geochemistry to Chemoautotrophic Prokaryotes, and from Prokaryotes to Nucleated Cells. *Philos. Trans. R. Soc. London. Ser. B Biol. Sci.* **2003**, *358* (1429), 59–85.

(135) Deamer, D. The Role of Lipid Membranes in Life's Origin. *Life* **2017**, *7* (1), 5.

(136) Pareek, V.; Sha, Z.; He, J.; Wingreen, N. S.; Benkovic, S. J. Metabolic Channeling: Predictions, Deductions, and Evidence. *Mol. Cell* **2021**, *81* (18), 3775–3785.

(137) Koura, N.; Tsukamoto, T.; Shoji, H.; Hotta, T. Preparation of Various Oxide Films by an Electrophoretic Deposition Method: A Study of the Mechanism. *Jpn. J. Appl. Phys.* **1995**, *34* (3R), 1643–1647.

(138) Mayhew, S. G.; Muller, F. Dimerization of the Radical Cation of Benzyl Viologen in Aqueous Solution. *Biochem. Soc. Trans.* **1982**, *10* (3), 176–177.

(139) Bastian, N. R.; Kay, C. J.; Barber, M. J.; Rajagopalan, K. V. Spectroscopic Studies of the Molybdenum-Containing Dimethyl Sulfoxide Reductase from Rhodobacter Sphaeroides f. Sp. Denitrificans. *J. Biol. Chem.* **1991**, *266* (1), 45–51.